ACS SYMPOSIUM SERIES 1062

Interfaces and Interphases in Analytical Chemistry

EDITED BY
Robin Hellburn and Mark F. Vitha

Interfaces and Interphases in Analytical Chemistry

In Interfaces and Interphases in Analytical Chemistry; Helburn, R., et al.;
ACS Symposium Series; American Chemical Society: Washington, DC, 2011.

ACS SYMPOSIUM SERIES **1062**

Interfaces and Interphases in Analytical Chemistry

Robin Helburn, Editor
St. Francis College

Mark F. Vitha, Editor
Drake University

Sponsored by the
ACS Division of Analytical Chemistry

American Chemical Society, Washington, DC

Distributed in print by Oxford University Press, Inc.

Library of Congress Cataloging-in-Publication Data

Interfaces and interphases in analytical chemistry / Robin Helburn, editor, Mark F. Vitha, editor ; sponsored by the ACS Division of Analytical Chemistry.
p. cm. -- (ACS symposium series ; 1062)
Includes bibliographical references and index.
ISBN 978-0-8412-2604-3 (alk. paper)
1. Surface chemistry--Congresses. 2. Biological interfaces--Congresses. 3. Chemistry, Analytic--Congresses. I. Helburn, Robin. II. Vitha, Mark F. III. American Chemical Society. Division of Analytical Chemistry.
QD506.A1I553 2010
543--dc22

2011003051

The paper used in this publication meets the minimum requirements of American National Standard for Information Sciences—Permanence of Paper for Printed Library Materials, ANSI Z39.48n1984.

Distributed in print by Oxford University Press, Inc.

PRINTED IN THE UNITED STATES OF AMERICA

Foreword

The ACS Symposium Series was first published in 1974 to provide a mechanism for publishing symposia quickly in book form. The purpose of the series is to publish timely, comprehensive books developed from the ACS sponsored symposia based on current scientific research. Occasionally, books are developed from symposia sponsored by other organizations when the topic is of keen interest to the chemistry audience.

Before agreeing to publish a book, the proposed table of contents is reviewed for appropriate and comprehensive coverage and for interest to the audience. Some papers may be excluded to better focus the book; others may be added to provide comprehensiveness. When appropriate, overview or introductory chapters are added. Drafts of chapters are peer-reviewed prior to final acceptance or rejection, and manuscripts are prepared in camera-ready format.

As a rule, only original research papers and original review papers are included in the volumes. Verbatim reproductions of previous published papers are not accepted.

ACS Books Department

Preface

An interfacial layer and the chemistry that occurs there are at the heart of many analytical methods and techniques. From electrochemical sensing to chromatography to analyses based on surface spectroscopy, interfaces are where the critical chemistry in the method takes place. In this book, we look at ten diverse examples of *interfaces* and *interphases*, new and old, in which the authors design, build, characterize or use an analytically relevant interfacial system. The topics are organized according to the composition of the interphase (or interface) as distinct from a method-based classification. These composition-based groupings are: 1 alkyl chain assemblies, 2 materials other than alkyl chain assemblies including gels, submicron sized silica, carbon nanotubes and layered materials, and 3 interfaces composed of bio-active substances.

Looking at analytical chemistry through this lens, *i.e.* from the view at the interface, we show common themes among interfacial layers used in different techniques as well as some trends. In the latter for example, advances in materials have resulted in parallel developments in the design and composition of sensing interfaces. Yet for the solvated interfacial layers in liquid chromatography where the constraints are considerable and the chemistry is harder to control, advances have been more measured, focused largely on stabilizing the existing interfacial chemistry.

As with any book, titles can be misleading especially when they contain cross–cutting words like 'interface' or 'analytical,' so it may be equally useful to establish what this book is *not* about. This is not a book about surface analysis. There may be places where that aspect seeps into a particular discussion on account of the need to examine or characterize a particular analytically relevant interphase. That is the nature of interdisciplinary science. This *is* a book about traditional analytical chemistry and the interfacial layers that comprise or could comprise some of those methods. In showing analytical chemistry from this perspective, we hope to draw persons specializing in different methodologies who may be searching for new ways to think about their discipline, both in research and education.

Acknowledgments

We deeply thank the authors for their patience and their contributions, and for giving us the latitude to present their work in the context of this book's theme. Everyone who gave an oral paper in the original small symposium at the 2008 Northeast Regional Meeting (NERM) of the American Chemical Society (ACS) entitled *Analytical Interfacial Science* has contributed a chapter. In addition,

In Interfaces and Interphases in Analytical Chemistry; Helburn, R., et al.;
ACS Symposium Series; American Chemical Society: Washington, DC, 2011.

there are chapters written by persons who were not at the symposium but who were invited to contribute to the book. We especially thank these individuals for their willingness to be part of this effort. We thank all those patient persons in the ACS Books division, Jessica Rucker, Bob Hauserman, Sherry Weisgarber, and especially Tim Marney, who tolerated us throughout the acquisition, design and production phases. We thank all the referees for the individual chapters and especially Kimberly Frederick at Skidmore College for assisting us at a moment's notice. We thank the Division of Analytical Chemistry for a small grant in support of the original symposium.

Robin Helburn

Department of Chemistry & Physics
St. Francis College
Brooklyn Heights, NY 11201

Mark F. Vitha

Department of Chemistry
Drake University
Des Moines, IA 50311

In Interfaces and Interphases in Analytical Chemistry; Helburn, R., et al.;
ACS Symposium Series; American Chemical Society: Washington, DC, 2011.

Chapter 1

The "Interface" in Analytical Chemistry: Overview and Historical Perspective

R. S. Helburn*

Department of Chemistry & Physics, St. Francis College, Brooklyn Heights, NY 11201
***rhelburn@stfranciscollege.edu**

Many of today's analytical methods and techniques, e.g.– chromatographic, electrochemical, spectroscopic,– involve an interface, a phase boundary where analyte and/or signal transfer occurs. Functioning as a transducer in a sensor or facilitating solute partitioning in a chromatographic column, the interface is that critical region whose chemistry we design so as to enhance analyte selectivity and sensitivity. There are common themes in the design of "interfacial regions" that cut across a range of intended analytical purpose. In this introductory chapter we highlight the objectives of a small symposium at the Northeast Regional Meeting of the American Chemical Society (ACS) entitled "Analytical Interfacial Science" which has since expanded into this book. This symposium was an opportunity to bring together researchers who specialize in different areas of analytical chemistry but who share a common interest in studying, characterizing and ultimately using interfaces to perform chemical analyses. In this chapter we trace a brief, non-comprehensive historical trajectory of interfaces in selected methodologies with an emphasis on common themes that span techniques in separations, electrochemical systems and sensing, and techniques associated with surface microarray and immunoassay. Our discussion parallels the chapter topics as we provide an overview of interfacial regions composed of 1 hydrocarbon chain assemblies, 2 gels, layered substrates, submicron and nanosized materials, and 3 immobilized bio-reactive agents. The individual chapters are highlighted throughout the discussion.

In Interfaces and Interphases in Analytical Chemistry; Helburn, R., et al.;
ACS Symposium Series; American Chemical Society: Washington, DC, 2011.

Introduction

The field of analytical chemistry encompasses numerous methods and technologies, many of which involve an interface or interfacial environment between two adjacent phases and the transfer of analyte or signal between those phases. Some examples are: 1 the partitioning of solutes between mobile and stationary phases in liquid chromatography (LC), 2 extraction of analytes from a sample headspace into a microextraction medium, 3 emission or reflection-absorption spectroscopy (RAS) of surface confined analytes and 4 analyte interactions at a sensor surface. In each case, it is the chemistry at the phase boundary and its effect on solute or signal transfer that determines the efficacy of the method. The intent of this symposium was to convene a small group to talk about a common focus – *interfaces* and *interphases*. This is the primary link among the chapters. Each paper involves a system containing a phase or pseudophase boundary coupled with solute interactions, and where the system under study serves an analytical purpose. Readers will find that the chapters are written in a mixture of review and research formats and that they are organized with respect to type of interface as opposed to a technique-based area of analytical chemistry. Interfaces in the context of high vacuum surface analysis while mentioned briefly in a historical context are not part of this chapter collection.

Historical Sketch

Analytical Chemistry

Analytical chemistry has always been about the development of methods and techniques used to identify and quantify chemical substances. It is about the tools and approaches that we use to solve qualitative and quantitative chemical problems. As analytical chemists, we think about fundamental chemical and physical knowledge and then ask how we might exploit a principle or chemical reaction to create a tool that solves a real and pressing chemical problem.

Many physical-chemical theories that were developed in the 19th and early 20th centuries have laid the groundwork for understanding today's well established analytical methods and techniques. For example, the phase rule discussed in the classic publication "Thermodynamic Principles Determining Equilibria" by Josiah Willard Gibbs (*1*, *2*) provided a foundation for chemical separations. Raoult's Law helped us to understand solute-stationary phase interactions and neutral analyte activity coefficients (γ^{∞}) in gas chromatography (*3*, *4*). Wolcott Gibbs applied electrodeposition quantitatively for the first time in 1864, an event that followed the work of Michael Faraday (*1*, *5*, *6*). Pioneering work on the definition and measurement of pH, starting as early as 1906 (*7*–*9*) was seminal in leading to that most important of macroscopic measures. Early spectroscopic studies also contain fundamental findings of relevance to modern analytical chemistry such as quantum theory (*10*–*13*), absorption coefficients (ε) (*14*) and the theory of indicators (*15*).

In Interfaces and Interphases in Analytical Chemistry; Helburn, R., et al.;
ACS Symposium Series; American Chemical Society: Washington, DC, 2011.

Surface Analysis

Interest in the characterization of chemical surfaces began with spectroscopy in 1887 when the photoelectric effect was first discovered (*16*). The photoelectric effect provided a basis for several high vacuum surface spectroscopy techniques such as X-ray photoelectron spectroscopy (XPS) and Auger electron spectroscopy (AES). The first XPS spectrum was recorded in 1954 by the Swedish scientist Kai Manne Börje Siegbahn (*17*) who later worked with Hewlett Packard to produce the first commercial XPS instrument in 1969. Other high vacuum surface analysis techniques such as ultraviolet photoelectron spectroscopy (UPS) and AES followed during that period (*18*, *19*).

Atmospheric pressure methodologies such as specular RAS based on both UV/vis and infrared (IR) radiation, including ellipsometry and total internal reflection methods (*20*) also appeared during the mid to latter 1900's. The development of UV/vis diffuse reflectance spectroscopy occurred in the 1960's (*21*). Diffuse reflectance in the IR mode was developed in 1978 by P.R. Griffiths and M.P. Fuller (*22*). With respect to UV/vis and IR, it is reasonable to say that prior to the early 1960's, transmission was the sole mechanism for obtaining absorbance data on an analyte.

Surface chemistry ultimately developed into its own discipline and separate area of research and study. However, the ability to study surfaces naturally spurred interest in the characterization of thin layers applied to surfaces as well as a host of other interfacial systems such as colloids, micelles, vesicles and lipid bilayers, and the notion of an *interfacial layer* (*23*, *24*) as distinct from an *interface* took shape.

The "Interface" in Analytical Chemistry

An overlap (of surface chemistry) with traditional analytical chemistry began as many of these surface spectroscopies were now being used to scrutinize "analytically relevant" interfaces (Figure 1) such as the electrode-solution interface and the "interphase" between mobile and stationary phases in reversed phase liquid chromatography (RPLC). With increasing ability to characterize these functional interfacial regions came a move to augment their diversity and complexity by introducing novel materials (Figure 1) so as to enhance their selectivity, sensitivity and maybe even their "smartness". All of this suggests that a symposium focused on this unifying aspect of analytical chemistry, *interfaces* and *interphases*, might be of interest.

Alkyl Chain Assemblies and the *Interphase*

One of the most important themes in interfacial chemistry that spans analytical methodologies in several technique-based areas is the solvated hydrocarbon chain assembly, sometimes referred to as an *interphase*. The term was first invoked by Flory and Dill (*23*, *24*) to define an interfacial zone between two immiscible phases consisting of a densely organized and solvated alkyl chain assembly. Their early lattice model representations (Figure 2) depict theoretically-derived views of

In Interfaces and Interphases in Analytical Chemistry; Helburn, R., et al.;
ACS Symposium Series; American Chemical Society: Washington, DC, 2011.

(a) micelles (b) surface polymeric systems and (c) the C_{18} RPLC interfacial region (*25–27*). We present this concept here not only for its historical significance but because it lays a unifying groundwork for the topics that comprise many of the chapters that follow such as: 1 micelles and vesicles in analytical separations, 2 lipid bilayers as a separation medium in planar electrophoresis, 3 amino terminated alkyl films on silicon wafers as a substrate for surface immunoassay, and 4 methodologies for synthesizing hydrocarbon bonded silica in RPLC.

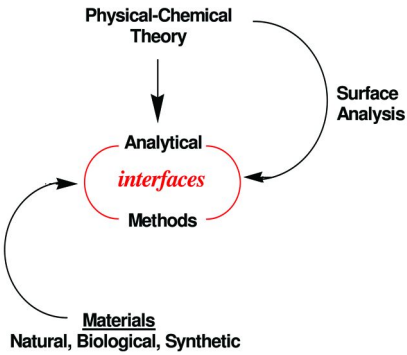

Figure 1. Developmental context in which to view the "interface" in analytical chemistry.

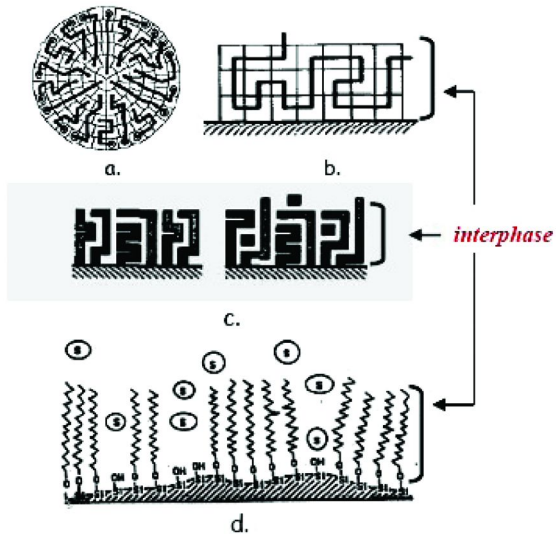

Figure 2. Modeled images for interphases as introduced by Dill and co-workers : (a) micelles, (b) condensed polymers, and (c) grafted chains in an RPLC stationary-mobile phase system (25), (d) a hand drawn version of a C_{18} –on-silica RPLC interphase is given for comparison; these theoretically based lattice model representations (a-c) are designed to illustrate the organized, semi-crystalline, constrained nature of interfacial chain molecules. Panels (a-c) are reproduced with permission from Reference (25).

In Interfaces and Interphases in Analytical Chemistry; Helburn, R., et al.;
ACS Symposium Series; American Chemical Society: Washington, DC, 2011.

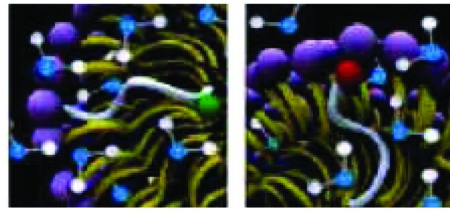

Figure 3. Schematic of micelle structures. Reproduced from Chapter 2, showing the locus of probe molecules in a micelle interior, green sphere (a), and near the surfactant polar head groups, red sphere (b). (see color insert)

More broadly speaking, an interphase, as distinct from an interface, is *any* region between two contacting bulk phases where the properties are significantly different from but related to those of the bulk phases (*28*). This more inclusive definition will be carried through subsequent chapters as we examine analytically relevant interphases comprised of layered materials, gel pseudophases, carbon nanotubes, colloidal silica and immobilized enzymes.

Characterizing the Micelle/Buffer Interface (CHs 2 and 3)

Since the first conceptual model of a micelle published by Hartley in 1936 (*29*) followed by the work of Dill et al. (1988) (*25*), self assembled alkyl chain phases have played a role in analytical methods, concentrating, organizing and mobilizing analytes. There have been several reviews of the role of micelles in analytical chemistry (*30*). Our focus in this book is on the interaction of micelles with the surrounding solution and with solutes, and the impact of those interfacial phenomena on the analytical process.

Chapter 2 of this book examines computational methods that have been used to probe the locus of solubilization of small molecules in micelles (Figure 3).

Visual concepts and questions of water penetration are part of the chapter discussion because they impact our understanding of solute-micelle interactions and the nature of a micelle's analytical interphase. Chapter 3 addresses the use of solvent-sensitive (solvatochromic) indicators (*31–33*) for characterizing the polarity of solubilization sites in micelles and vesicles. These indicator probes have been used to determine the parameters dipolarity/polarizability (π*), hydrogen-bond-donor (HBD) acidity(α), and hydrogen-bond-acceptor (HBA) basicity (β) for probe solvation sites from UV/vis absorption spectra of a partitioned or surface adsorbed probe. Also discussed in Chapter 3 are linear solvation energy relationships (LSERs) that can be used to correlate solute binding constants for micelles (K_p) (*34*) or a measured retention factor (k') in micellar electrokinetic chromatography (MEKC) (*35*) to the relative contribution of these parameters as expressed by the coefficients, *a*, *s* and *b* on the individual variables in the equation (see Eqn 1; C= a regression constant).

$$\text{Ln } k' = C + s\pi^* + a\Sigma\alpha_2 + b\Sigma\beta_2 \qquad \text{(Eqn. 1)}$$

In Interfaces and Interphases in Analytical Chemistry; Helburn, R., et al.;
ACS Symposium Series; American Chemical Society: Washington, DC, 2011.

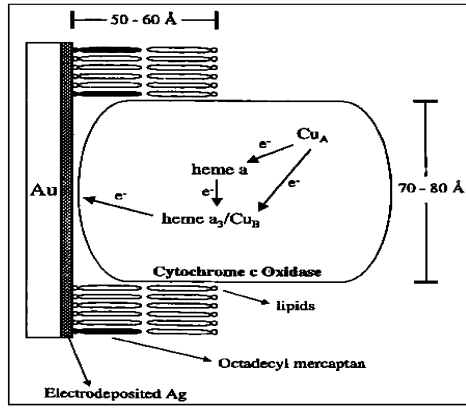

Figure 4. Silver electrode functionalized with the heme copper enzyme, cytochrome c-oxidase, embedded in a lipid bilayer. Reproduced with permission from Reference (42).

LSERs are relevant because they are quantitative tools for translating our understanding of interfacial analyte-micelle solvation into a method for optimizing an analytical chemical separation.

Mounted Bilayers (CH 4)

A natural extension of the use of micelles and vesicles is the surface mounted lipid bilayer in which nature's own biologically selective interphase is confined to a surface for the purpose of making measurements. For example, artificially constructed membranes (*36–38*) and natural cell membranes (*39*, *40*) have been mounted on silica in place of the more common C_{18}-on-silica interface in RPLC. Bilayers have been attached to electrodes to create natural biological environments for studying the electron transfer properties of redox active biomolecules. Figure 4 illustrates an engineered electrode-solution interface designed to probe the electron transfer properties of the heme–copper protein cytochrome c-oxidase (*41–43*). This layered interface simulates the enzyme's native mitochondrial environment within a bilayer while allowing the active site to make reproducible direct contact with a silver electrode (*41–43*). The design produced a Nernstian response in both cyclic voltammetry and potentiometric measurements without the use of mediators (*43*).

In Chapter 4, the supported bilayer is employed as a medium for the planar electrophoretic separation of membrane bound biomolecules such as lipids and proteins. As with the electrochemical system in Figure 4, the bilayer medium was selected to preserve the analytes' native conformation and function during a separation. Often, we think of planar electrophoresis as utilizing a cross linked gel where the mechanism of separation is a sized-based sieving process as opposed to one of differential interactions across a phase or pseudophase boundary. Here, the bilayer forms a distinct phase relative to the buffer. Moreover, the authors show that the bilayer phase can be doped with biomolecules such as cholesterol,

charged lipids, proteins and glycolipids, resulting in domains. Such doping is used to "tune" the mobility of migrating species by increasing the number of possible specific and non-specific interactions between the bilayer medium and an analyte. Figure 5, reproduced from Chapter 4, illustrates a biomolecule analyte as it spans the buffer and bilayer phases while migrating along the plane.

Bonded Monolayers (CHs 5 and 6)

Another analytically relevant alkyl chain assembly is the hydrocarbon monolayer formed through covalent bonding to a solid substrate. In many cases the monolayer is the final desired state. Alternatively, it is a vehicle for the covalent or non-covalent binding of additional substrates. One of the most frequently utilized monolayer bonded interfaces in LC is the C_{18} –on-silica interphase (Figure 1d) which has been the subject of intense scrutiny, having been characterized by NMR (*44–46*), Raman (*47*) and solvatochromic probe-based spectroscopies (*48–52*). Chapter 5 addresses the hydrolytic stability of conventional bonded silica interfaces that have a siloxane linkage (Figure 6a). The authors explore the synthesis and characterization of some allyl bonded monolithic phases that possess the more stable silicon-carbon bond (Figure 6b).

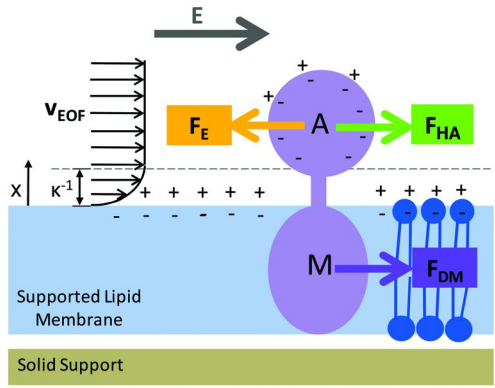

Figure 5. A biomolecule analyte existing in both buffer (as the charged "A" portion) and adjacent bilayer (as the neutral "M" part) in planar electrophoresis that utilizes a supported lipid bilayer as the separation medium. Reproduced from Chapter 4. (see color insert)

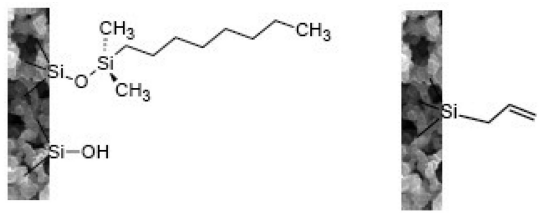

Figure 6. Conventional siloxane linkage (a), more stable silicon-carbon linkage (b). Reproduced from Chapter 5.

In Interfaces and Interphases in Analytical Chemistry; Helburn, R., et al.;
ACS Symposium Series; American Chemical Society: Washington, DC, 2011.

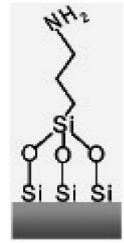

Figure 7. Silicon wafer modified with APTES. Reproduced from Chapter 6.

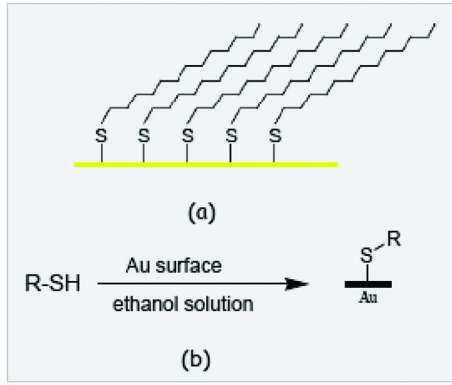

Figure 8. A self assembled monolayer (SAM) on a metal surface (a) created by reaction of a substitted thiol (R-SH; R= alkane chain) with an Au surface (b).

A hydrocarbon monolayer on silica can also be used in surface immunoassay. In this context, the hydrocarbons have a terminal reactive group that could be used to immobilize a biomolecule. In Chapter 6, a smooth silicon wafer is derivatized with 3-aminopropyltriethoxy silanes (APTES) to form an assembled hydrocarbon layer containing amino terminal groups. The preparation and the characterization of these APTES films (Figure 7) are presented.

We note that bonded hydrocarbon *monolayers* are equally prevalent in electrochemical interfacial regions where the common theme is the organized array of hydrocarbons bonded to gold (Au), silver (Ag) or platinum (Pt) via the relatively stable metal-sulfur bond (Figure 8). The result is a self assembled monolayer or thiol-SAM (*53*). Note that the bottom portion of the bilayer in Figure 4 is a thiol-SAM. The SAM in Figure 8 (for R=C_{18}) would be largely an insulator (*54*) and not capable of promoting charge transfer between an approaching small molecule and the electrode surface (*54*). To create a more conducting interface, the sulfur atom on the thiol could be substituted directly with conjugated or redox-active substituents such as benzene, porphyrin or quinone (*53*). Thiol-SAMs provide a relatively stable organic vehicle for mounting bio-recognition species such as enzymes or antibodies leading to selective *bio-sensing* interfaces (*53*). The immobilization of bio-reactive agents in analytical interfaces is a topic that we treat separately in a later section.

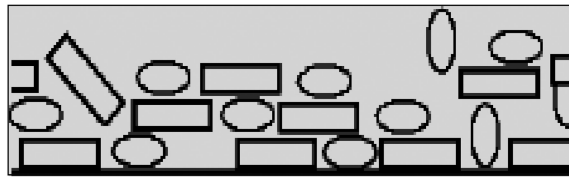

Figure 9. Concept image of an ITO with a surface film composed of POM and $TMPy4^{+}$. Reproduced from Chapter 7.

The Analytical Interface and *Materials*

It has been stated that new materials have much greater potential to transform or limit analytical chemistry than any advance in instrumentation or computer technology (*55*). In other words, it is the nature of the molecules and atoms at an interface functioning as a signal transducer in a sensor or enabling selective partition as in the case of chemical separations that ultimately defines the performance of an analytical technique (*55*). Thus, it is the interface and the materials situated there that are at the heart of these advances.

Materials have previously been classified as metals, semiconductors, polymers, ceramics or composites (*55*). The new materials that we speak of include hybrids and those whose physical features are defined at the submicron level. Where those features are less than 100 nm in dimension we can apply the term *nanomaterial*. A hybrid material comprises two or more integrating components that combine at the molecular or nanometer level (*55*, *56*). Lastly, it is important to recognize that old materials can sometimes become novel when used in a new application, and that structures such as micelles, colloids, bilayers, clays and gels are nature's own sub-micron, hybridized and ordered materials, respectively, that have been around for centuries. We simply observe and then attempt to mimic their behavior and utility. A number of the contributing chapters as well as discussions in this introductory chapter address materials (at an interface) in one or more of these contexts.

Layer-by-Layer (LBL) (CH 7)

The term layer-by-layer (LBL) refers to a hybrid technique in which two or more substrates are alternately deposited onto a surface. The resulting multilayer assembly is held together by the chemical interactions inherent among the species being deposited (*57*). Accordingly, this book includes a chapter on the cyclic voltammetry characterization of an indium tin oxide (ITO) electrode modified with alternating deposited layers of a tetra cationic porphyrin, 5,10,15,20-tetrakis(4-methylpyridinium) porphyrin ($TMPyP^{4+}$) and a negatively charged inorganic oxide cluster ($SiW_{12}O_{40}^{4-}$) also known as a polyoxometalate (POM), (Chapter 7). The $TMPyP^{4+}$ and POM, are held in place by electrostatic forces between the oppositely charged substrates. A concept image illustrating the author's proposed arrangement of the two components on the ITO surface is

In Interfaces and Interphases in Analytical Chemistry; Helburn, R., et al.;
ACS Symposium Series; American Chemical Society: Washington, DC, 2011.

shown in Figure 9. Porphyrins have sensing applications (*58*), and LBL methods present an approach for their surface immobilization.

Carbon Nanotubes (CH 8)

In Chapter 8, the temperature dependant resistance and magnetoresistance (MR) (*59*, *60*) are measured for an interface created by layering single wall carbon nanotubes (SWCNTs) onto hydrocarbon bonded quartz silica fibers (0.11 mm diameter). This potentially useful interface takes the same hybrid theme as that of bonded silicas used in RPLC but with an additional layer of SWCNTs (Figure 10). MR is a newly re-discovered physical property that is finding applications in sensing and biomolecular detection (*61*).

The Importance of Silica (CH 9)

With surfaces that are readily modified, silica is a most versatile inorganic material that has had a transforming effect on analytical interfacial chemistry. The uses of silica range from chromatographic stationary phases to cavity forming substrates on the front end of sensors, to modifiable silicon wafers and quartz silica fibers used in immunoassay, sensing or solid phase microextraction (SPME), respectively. In Chapter 9, the interfacial properties of submicron sized silica particles (Figure 11) are exploited for microarray analysis, a form of surface analysis that permits the fluorescence spectroscopic imaging of biomolecule interactions. Chapter 9 specifically addresses the uses of submicron silica particles as a plate substrate that enhances detection sensitivity by minimizing the background fluorescence signal.

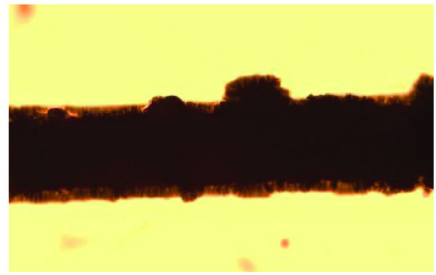

Figure 10. 200X magnification light micrograph of a phenyl bonded quartz fiber coated with SWCNTs and annealed. Reproduced from Chapter 8.

In Interfaces and Interphases in Analytical Chemistry; Helburn, R., et al.;
ACS Symposium Series; American Chemical Society: Washington, DC, 2011.

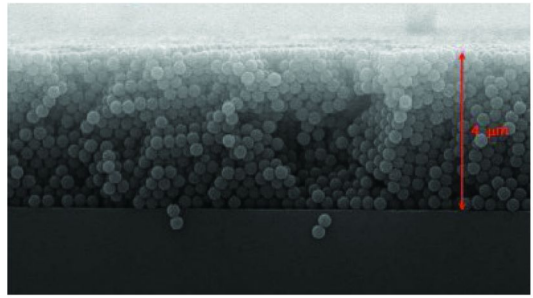

Figure 11. The interface on a protein microarray; cross section of the sub-micron silica particle substrate. Reproduced from Chapter 9; note the 4 um thickness of the film; packed particles used in silica-based LC columns range in diameter from 1-4 um. (see color insert)

Silica Substitutes: Group 4 Metal Oxides (CH 5 again)

While silica will remain an important material for creating analytically useful interfaces, oxides of the Group 4 metals zirconium and titanium (ZrO_2 and TiO_2 respectively) (*62*) are viable alternatives for creating normal phase LC and RPLC interphases. These inorganic supports fill a niche through their increased thermal and chemical stability, specifically in their tolerance for high pH mobile phases (*63*). Chapter 5, highlighted previously in our discussion of bonded hydrocarbon monolayers, devotes a section to the synthesis and characterization of monolithic normal phase LC interfaces based on zirconia and hafnia (HfO_2).

Gel Pseudophases (CH 10)

We have one chapter (Chapter 10) devoted to gels formed from the purine nucleoside guanosine (Figure 12a), and their use as a medium for the capillary electrophoretic separation of single stranded (ss) DNA. This is an example of an old material seen in a new light, as the guanosine (G) quartet (Figure 12b) which forms through hydrogen bonding between individual nucleobases was first identified in 1962 (*64*, *65*). The gel formation processs begins as the quartets assemble into a stack held together, in part, by π-π interactions. As the concentration of guanosine increases, the stacks organize into helical or columnar aggregates that eventually assume a higher ordered crystalline phase or gel (*65*, *66*). As with the bilayer electrophoresis discussed in Chapter 4, the electrophoresis of ss-DNA utilizing a G-gel as the separation medium shows that this too is system where specific analyte-"pseudophase" interactions provide for the separation mechanism. There is no "evidence of a sieving-gel mechanism. However, the nature of the G-gel aggregates in each individually optimized separation, as reported in the chapter, are not known at this time.

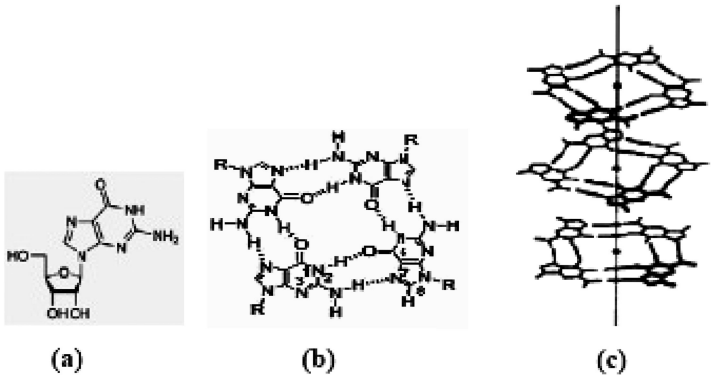

Figure 12. (a) Guanosine, (b) a G-tetrad formed from guanosine, R= ribose group, (c) three dimensional columnar network that comprises guanosine gels (G-gels). Panels (b-c) are adapted and reproduced from Chapter 10 and Reference (65).

Incorporating Bio-Reactive Materials into the Interface

With the increasing diversity of materials available for constructing analytically useful interphases, one could easily incorporate immobilized reactive biomolecules (*e.g.* enzymes, antibodies, microorganisms) into the preceding section on *materials*. We have already touched briefly on this type of system in our discussion of SAM-metal interfaces. However, the unique challenges associated with the use of these more delicate substrates as well as some of the new directions that this type of interface is moving in suggests that a separate section be devoted to the incorporation of these specialized materials.

History

The use of immobilized enzymes as a catalytic bio-recognition layer on a sensing surface (*i.e.* a biosensor) dates back to 1962 (*67*). Since enzymatic reactions usually involve small molecules such as O_2, many of these first interfaces consisted of biological material layered on top of an amperometric O_2 sensor. A classic example is the slice of banana on the surface of an O_2 electrode used for the detection of catecholamine neurotransmitters such as dopamine (*68*). Large amounts of the enzyme polyphenol oxidase in the flesh of the banana catalyze the degradation of dopamine in the presence of O_2, resulting in a measured decrease in ambient O_2 (*68*). The microorganism-based interface in Figure 13 detects compounds that are toxic to the microorganisms by measuring an increase in O_2, relative to that of a control interface, due to the compromised aerobic respiration on the part of immobilized aerobic bacteria (*69*).

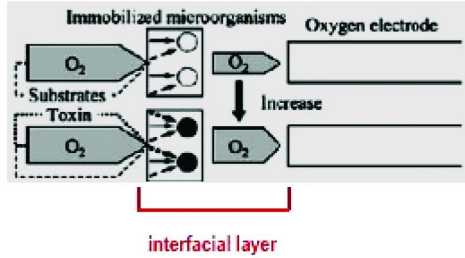

Figure 13. Sensing interface that utilizes aerobic microorganisms to detect compounds that are toxic to the microorganism; (top): response of sensor in the absence of the toxin, O_2 is consumed by the healthy metabolizing bacterium; (bottom): response of sensor in the presence of a toxic compound, microorganisms are poisoned and their respiration capabilities are compromised; the level of O_2 is not decreased. Reproduced with from Reference (69) (Figure 1) with kind permission of Springer Science + Business Media.

Over the years, advances in the fabrication of biosensing interfaces have paralleled developments in enzyme purification, mediator compounds (*70*), and materials science. These detecting interfaces have many requirements to meet in addition to the need to be tough and durable so that they can be deployed in the field or in vivo.

Biosensing Interfaces in Clinical Analysis (CH 11)

Clinical monitoring of physiologic analytes is a major application of biosensing where the challenges for today are to utilize materials to: 1 create robust environments for enzymes while maintaining their function, 2 enhance signal transfer at the electrode surface, and 3 simultaneously screen out interferents. Chapter 11 provides a review of some current technologies and approaches that are being used to address these issues in the construction of biosensing interphases for the amperometric detection of analytes such as glucose, nitric oxide (NO) and glutamate. As an example, Figure 14 illustrates, for an amperometric glucose oxidase biosensor, an interfacial layer comprised of multiple components such as metal nanoparticles, carbon nanotubes and a conducting polymer, in addition to the enzyme. Not shown but also needed in many biosensing interphases would be a protective surface membrane that screens small molecule interferents that are common in physiological systems.

Smart Interfacial Layers (CH 12)

Biosensing interfaces are moving towards becoming "smart" systems, *i.e.* those that carry out tasks in addition to serving as a detector. For example, the enzyme organophosphorus hydrolase (OPH) catalyzes the degradation of organophosphorus (OP) compounds such as the pesticide methyl parathion (*70*) as well as more toxic nerve agents such as sarin and soman (Figure 15). A sensing system built around OPH might engage in an additional self cleaning

In Interfaces and Interphases in Analytical Chemistry; Helburn, R., et al.;
ACS Symposium Series; American Chemical Society: Washington, DC, 2011.

or remediation step. Thus, a suite of durable layers fitted with OPH could be designed to completely degrade and sequester the reactants and products of the degradation reaction, thereby serving as a protective interface that mitigates risk of exposure by detecting and then decontaminating itself so that the material can be safely discarded (*71*, *72*).

The challenges here are immense. New nanostructured enzyme containing composites are being incorporated into textile materials (*73*) to create specialized reacting and sequestering layers. The final chapter in this book explores some of these challenges as the author steps us through the process of developing and testing a set of biosensing and self cleaning layers for the detection, degradation and sequestering of the OP toxin surrogate methyl parathion (MPT) and its reaction products. As an example, Figure 16c illustrates the "smart" interface created from OPH embedded poly-β-cyclodextrin (poly-β-CD) (16a) that has been coated onto a fabric. The mechanism of degradation and sequestration (16b-c) occurs as the incoming MPT preferentially binds the hydrophobic biocatalytic inclusion "pocket" of poly-β-CD, displacing the already formed yellow *p*-nitrophenol (pNP) degradation product (16b-c) until all of the target compound is decomposed and the products are sequestered.

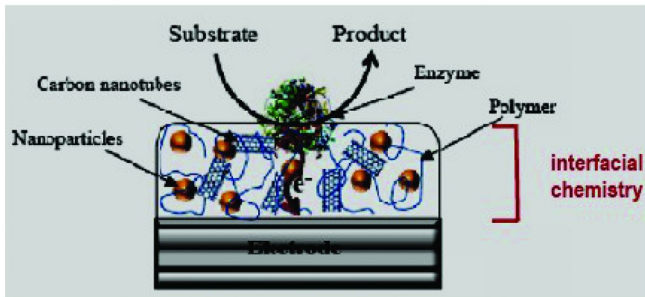

Figure 14. Graphic of a composite material designed to enhance sensitivity and signal transfer in an amperometric glucose sensor consisting of the enzyme glucose oxidase. Reproduced from Chapter 11. (see color insert)

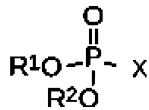

Figure 15. General OP structure; for sarin and soman x=F, R^1 and R^2= alkyl groups; the less toxic parathion surrogate (16b) contains P=S in place of P=O.

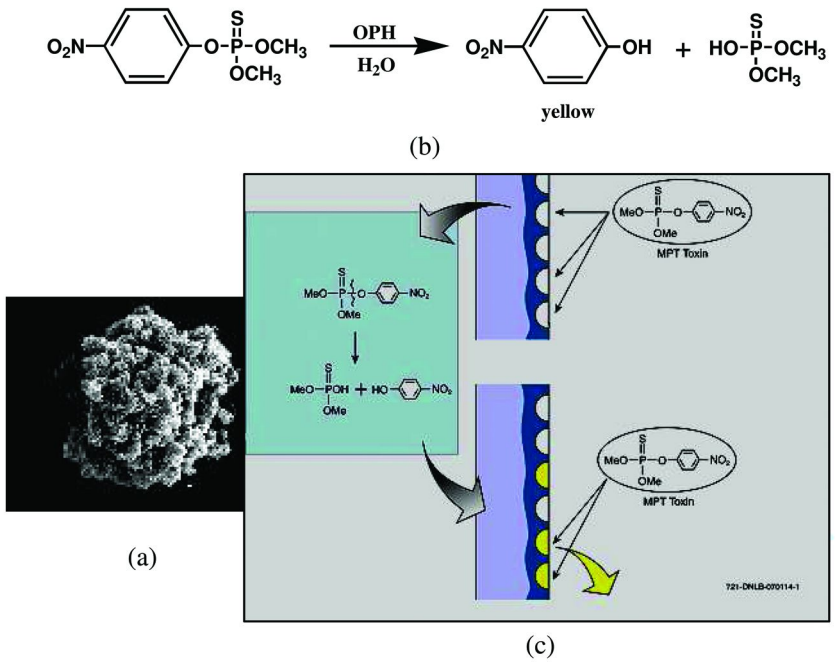

Figure 16. Reaction and degradation of MPT at the smart composite interface created from OPH treated poly-β-CD; SEM image of poly-β-CD (a); hydrolytic degradation of MPT to pNP (b); biocatalytic degradation and sequestration of products by the OPH- poly-β-CD composite (c). Adapted and reproduced from Chapter 12. (see color insert)

Concluding Remarks

In this introductory chapter, we have provided a framework in which to view the contributing chapters that follow. Our hope is that readers will see these topics and the chapters simply as examples of functional interfacial chemistry. Because at the heart of many (not all) analytical methods is the chemistry that occurs at an interface. The purpose of this book is to have analytical chemistry viewed from that perspective. The book is not comprehensive in this respect and one or more of the topics may stretch one's concept of an analytical interfacial system. However, we have aimed for breadth. We hope that this book will be both educational as well as a stimulus for new ideas in analytical chemistry thinking.

Acknowledgments

Many thanks go to Mark Vitha for valuable suggestions and for reviewing more than one version of this chapter.

In Interfaces and Interphases in Analytical Chemistry; Helburn, R., et al.;
ACS Symposium Series; American Chemical Society: Washington, DC, 2011.

References

1. Kolthoff, I. M. *Anal. Chem.* **1994**, *66* (4), 241A.
2. Gibbs, J. W. *Trans. Conn. Acad. Arts Sci.* **1874−78**, *3* (108), 343.
3. Bertrand, G. L.; Treiner, C. *J. Solution Chem.* **1984**, *13* (1), 43.
4. Kenworthy, S.; Miller, J.; Martire, D. E. *J. Chem. Ed.* **1963**, *40* (10), 541.
5. Williams, L. P. *Michael Faraday: A Biography*; Chapman & Hall: London, 1965.
6. Gibbs, W. *Z. Anal. Chem.* **1864**, *3*, 334.
7. Stock, J. T., Orna, M. V., Eds.; *Electrochemistry: Past and Present*; ACS Symposium Series 390; American Chemical Society: Washington, DC, 1989.
8. Cremer, M. *Z. Biol.* **1906**, *47*, 562.
9. Bates, G. R. *Determination of pH: Theory and Practice*; Wiley: Hoboken, NJ, 1973.
10. Planck, M. *Ann. Phys.* **1901**, *4*, 553.
11. Einstein, A. *Ann. Phys.* **1905**, *17*, 132.
12. Condon, E. U.; Shortley, G. H. *The Theory of Atomic Spectra*; Cambridge University Press: Cambridge, U.K., 1951.
13. Herzberg, G. *Molecular Spectra and Molecular Structure*; Van Nostrand & Reinhold: New York, 1950.
14. Beer, A. Bestimmung der Absorption des rothen lichts in farbig enlussigkeiten. *Annal. Phys. Chem.* **1852**, *86*, 78.
15. Noyes, A. A. *J. Am. Chem. Soc.* **1910**, 813.
16. Hertz, H. R. *Ann. Phys.* **1887**, *267* (7), 421.
17. Siegbahn, K. *Philos. Trans. R. Soc. London* **1970**, 33.
18. Rabalais J. W. *Principles of Ultraviolet Photoelectron Spectroscopy*; Wiley: Hoboken, NJ, 1977.
19. Turner D. W. *Molecular Photoelectron Spectroscopy*; Wiley: Hoboken, NJ, 1970.
20. Cardona, M.; Pollack, F.; Shaklee, K. *J. Phys. Soc. Jpn.* **1966**, *21*, 89.
21. Kortum, G. *Reflectance Spectroscopy*; Springer-Verlag: New York, 1969.
22. Fuller, M. P.; Griffiths, P. R. *Anal. Chem.* **1978**, *50* (13), 1906.
23. Flory, P. J. *J. Am. Chem. Soc.* **1962**, *84*, 2857.
24. Dill, K. A.; Flory, P. J. *Proc. Natl. Acad. Sci. U. S. A.* **1980**, *77* (6), 3115.
25. Dill, K. A.; Naghizadeh, J.; Marqusee, J. A. *Ann. Rev. Phys. Chem.* **1988** (39), 425.
26. Dill, K. A.; Flory, P. J. *Proc. Natl. Acad. Sci. U. S. A.* **1981**, *78* (2), 676.
27. Dorsey, J. G.; Dill, K. A. *Chem. Rev.* **1989**, *89* (2), 331.
28. *IUPAC Compendium of Chemical Terminology (Gold Book)*, 2nd ed.; McNaught, A. D., Wilkinson, A., Compilers; Blackwell Scientific Publications: Oxford, 1997.
29. Hartley, G. S. *Aqueous Solutions of Paraffin Chain Salts: A Study in Micelle Formation*; Hermann et Cie: Paris, 1936.
30. Cline Love, L. J.; Habarta, J. G.; Dorsey, J. *Anal. Chem.* **1984**, *56* (11), 1132A.
31. Kamlet, M. J.; Abboud, J. L.; Taft, R. W. *J. Am. Chem. Soc.* **1977**, *99*, 6027.

32. Kamlet, M. J.; Taft, R. W. *J. Am. Chem. Soc.* **1976**, *98*, 377.
33. Taft, R. W.; Kamlet, M. J. *J. Am. Chem. Soc.* **1976**, *98*, 2886.
34. Quina, F. H.; Alonso, E. O.; Farah, J. P. S. *J. Phys. Chem.* **1995**, *99*, 11708.
35. Trone, M. D.; Khaledi, M. G. *Anal. Chem.* **1999**, *71*, 1270.
36. Courtois, C.; Allais, C.; Constantieux, T.; Roderiguez, J.; Caldarelli, S.; Delaurent, C. *Anal. Bioanal. Chem.* **2008**, *392*, 1345.
37. Cohen, D. E.; Leonard, M. R. *J. Lipid Res.* **1995**, *36*, 2251.
38. Ogden, P. B.; Coym, J. W. *J. Chromatogr., A* **2009**, *1216*, 4713.
39. Moaddel, R.; Wainer, I. W. *Nat. Protoc.* **2009**, *4* (2), 197.
40. Lazaro, E.; Rafols, C.; Roses, M. *J. Chromatogr., A* **2008**, *1182*, 233.
41. Burgess, J. D.; Rhoten, M. C.; Hawkridge, F. M. *Langmuir* **1998**, *14*, 2467.
42. Su, L.; Kelly, J. B.; Hawkridge, F. M.; Rhoten, M. C.; Baskin, S. I. *J. Electroanal. Chem.* **2005**, *581*, 241.
43. Lewis, K. L.; Su, L.; Hawkridge, F. M.; Ward, K. R.; Rhoten, M. C. *IEEE Sens. J.* **2006** (2), 420.
44. Bliesner, D. M.; Sentell, K. B. *J. Chromatogr.* **1993**, *631*, 23.
45. Bliesner, D. M.; Sentell, K. B. *Anal. Chem.* **1993**, *65*, 1819.
46. Dawson, E. D.; Wallen, S. L. *J. Am. Chem. Soc.* **2002**, *124*, 14210.
47. Doyle, C. A.; Vickers, T. J.; Mann, C. K.; Dorsey, J. G. *J. Chromatogr.. A* **2000**, *877*, 41.
48. Helburn, R. S.; Rutan, S. C.; Pompano, J.; Mitchem, D.; Patterson, W. T. *Anal. Chem.* **1994**, *66*, 610.
49. Lu, H.; Rutan, S. C. *Anal. Chem.* **1996**, *68* (8), 1387.
50. Lu, H.; Rutan, S. C. *Anal. Chim. Acta* **1999**, *388* (3), 345.
51. Rutan, S. C.; Harris, J. M. *J. Chromatogr.* **1993**, *656* (1/2), 195.
52. Men, Y. D.; Marshall, D. B. *Anal. Chem.* **1990**, *62* (23), 2602.
53. Chen, D.; Li, J. *Surf. Sci. Rep.* **2006**, *61*, 445.
54. Maish, S.; Buckel, F.; Effenberger, F. *J. Am. Chem. Soc.* **2005**, *127*, 17315.
55. He, L.; Toh, C. *Anal. Chim. Acta* **2006**, *556*, 1.
56. Gomez-Romero, P.; Sanchez, C. *Functional Hybrid Materials*; Wiley VCH: Weinheim, Germany, 2004.
57. Zhang, X.; Chen, H.; Zhang, H. *Chem. Commun.* **2007**, 1395.
58. Rakow, N.; Suslick, K. S. *Nature* **2000**, *406*, 710.
59. Thomson, W. *Proc. R. Soc. London* **1856**, *8*, 546.
60. McGuire, T. R.; Potter, R. I. *IEEE Trans. Magn.* **1975**, *11* (4), 1018.
61. Osterfield, S. J.; Yu, H.; Gaster, R. S.; Caramuta, S.; Xu, L.; Han, S.-J.; Hall, D. A.; Wilson, R. J.; Sun, S.; White, R. L.; Davis, R. W.; Pourmand, N.; Wang, S. X. *Proc. Natl. Acad. Sci. U. S. A.* **2008**, *109* (52), 20637.
62. Nawrocki, J.; Dunlap, C.; McCormick, A.; Carr, P. W. *J. Chromatogr., A* **2004**, *1028*, 1.
63. Dunlap, C. J.; McNeff, C. V.; Stoll, D.; Carr, P. W. *Anal. Chem.* **2001**, *73*, 598A.
64. Gellert, M.; Lipsett, M.; Davies, D. *Proc. Natl. Acad. Sci. U. S. A.* **1962**, *48*, 2013.
65. Davis, J. T.; Spada, G. P. *Chem. Soc. Rev.* **2007**, *36*, 296.
66. Yu, Y.; Nakamura, D.; BeBoyace, K.; Nesius, A. W.; McGown, L. B. *J. Phys. Chem. B.* **2008**, *112*, 1130.

67. Clark, L. C.; Lyons, C. *Ann. NY Acad. Sci.* **1962**, *102*, 29.
68. Sidwell, J. S.; Rechnitz, G. A. *Biotechnol. Lett.* **1985**, *7* (6), 419.
69. Nakamura, H.; Shimomura-Shimizu, M.; Karube, I. *Adv. Biochem. Eng./ Biotechnol.* **2008**, *109*, 351.
70. Fultz, M. L; Durst, R. A. *Anal. Chim. Acta* **1982**, *140* (1), 1.
71. Singh, A.; Lee, Y.; Dressick, W. J. *Adv. Mater.* **2004** (23−24), 2112.
72. Telford, M. *Mater. Today* **2005**, *3*, 23.
73. Qian, L. *J. TATM* **2004**, *4* (1), 1.

Chapter 2

Defining the Micelle/Water Interface Using Computational and Experimental Results

Mark F. Vitha*

Drake University, Department of Chemistry, Des Moines, Iowa 50311
***Mark.vitha@drake.edu**

Surfactant micelles are used throughout analytical chemistry and in separation science specifically to improve the performance of a wide range of techniques. Within separation science, these improvements rely on the interaction of analytes with the micelles, which often occurs at the micelle/aqueous phase interface. It is therefore important to define and characterize the chemical nature of the interfacial region. In this chapter, we review computation and experimental methods to develop a working definition of the interface. In the following chapter, we examine these two specific approaches for characterizing the micelle/water interfacial region.

Introduction

The use of surfactant micelles in analytical chemistry has been the topic of several review articles and books (*1*–*6*). As a specific example, the addition of surfactant micelles to the mobile phase in liquid chromatography (known as micellar liquid chromatography, MLC) has been shown to offer unique selectivities arising from the interaction of solutes with micelles (*7*–*9*). Their use in capillary electrophoresis (referred to as micellar electrokinetic capillary chromatography, MEKC) helped to expand that technique to the analysis of neutral solutes (*7*, *10*, *11*). In these techniques, the efficacy of the micelles depends on the extent of interaction between the micelles and the solutes of interest. It is therefore important to understand, in a quantitative manner, the fundamental chemical forces governing the solute-micelle interactions so as to be able to explain and predict the influence of micelles on specific separations.

In Interfaces and Interphases in Analytical Chemistry; Helburn, R., et al.;
ACS Symposium Series; American Chemical Society: Washington, DC, 2011.

This chapter is structured in the following manner:

- We begin the chapter by evaluating some of the pictures that are commonly used to depict micelles. This is important because the images we create influence our interpretation of experimental results.
- We then consider experimental and computational studies in an effort to define the micelle/water interface, which we ultimately take to include the head groups and associated water molecules and counterions, as well as the first few carbon atoms of the aliphatic chain of the surfactants.

In the next chapter, we continue the analysis of the micelle/water and vesicle/water interface and its influence on solute partitioning by considering the following:

- The Kamlet-Taft solvatochromic comparison method is discussed in relation to studies aimed at characterizing the potential strength of intermolecular interactions at the interface of different surfactant micelles.
- An extensive review of linear solvation energy relationships (LSERs) for characterizing solution/micelle and solution/vesicle interfaces to better understand the use of micelles and vesicles in separation science is then provided.
- We close the chapter by considering the extension of these two characterization methods to the study of solution/vesicle interfaces and consider a selectivity triangle scheme for grouping similar systems based on their LSERs.

Micelle Structure and Representations

In this chapter, we focus primarily on common, roughly spherical micelles that are formed with common cationic, anionic, zwitterionic, and non-ionic monomeric surfactants. Examples of such surfactants include sodium dodecylsulfate (SDS), cetyltrimethylammonium bromide (CTAB), and Triton X-100 (polyoxyethylene, where n = 9.5 on average) (Figure 1). These surfactants share two structural features: a long alkyl chain, commonly referred to as the 'tail' and a charged or polar 'head group'. In aqueous solutions, these surfactants self-assemble to form micelles once they exceed a certain concentration. This concentration is known as the critical micelle concentration (CMC). Micellization is governed by several competing forces: 1) hydrophobic repulsion between water and the alkyl chains, 2) ion-dipole or dipole-dipole attractive interactions between water and the head groups, 3) attractive dipole-dipole interactions among head groups in the case of non-ionic surfactants and repulsive ionic interactions between head groups in the case of ionic surfactants, 4) attractive interactions between head groups and associated counterions, and 5) all of the entropic effects that are associated with the formation of micelles. These forces result in spherical or roughly oblate micellar structures for many surfactants at low to moderate concentrations in

In Interfaces and Interphases in Analytical Chemistry; Helburn, R., et al.;
ACS Symposium Series; American Chemical Society: Washington, DC, 2011.

aqueous solutions, with the non-polar alkyl chains clustered together surrounded by the head groups and associated counterions which are in contact with the aqueous phase. The non-polar region is referred to as 'the core' and has generally been shown to have little to no water in it (more on this below), and the region that includes the head group, counterions, and waters of hydration around and within the micelle is referred to as the 'palisade' or 'Stern' layer. The exact structure of the micelles has been a matter of intense study for decades. This topic will be taken up in the sections below.

When considering the interfacial region of micelles, the images we provide of them can strongly and subconsciously influence our understanding and interpretation of data related to these systems. When viewing any static two-dimensional image of a micelle, it is important to remember that real micelles exist in dynamic equilibrium with surfactant monomers according to the equilibrium:

$$nM \leftrightarrow M_n \quad (1)$$

where M represents a monomer. Thus, monomers are constantly entering, leaving, and protruding from and being taken back into the micelles on a time scale of picoseconds to microseconds. Additionally, because of this dynamic nature, monomers are not evenly distributed throughout the micelles. Furthermore, the monomers are not extended straight out in a fully all-trans fashion, but rather interact with each other and develop bends and kinks in the chains as a result. Due to geometric concerns, it is not possible for all of the alkyl chains to terminate in the exact center of the micelle as if they were spokes on a wheel. Finally, for geometric reasons, the head groups and the first several carbon atoms are separated by some distance, allowing for a slightly more open structure in the outer layer than in the core for most types of micelles. Good representations of micelles will capture these aspects of micelles and provide a more accurate way of thinking about micelles.

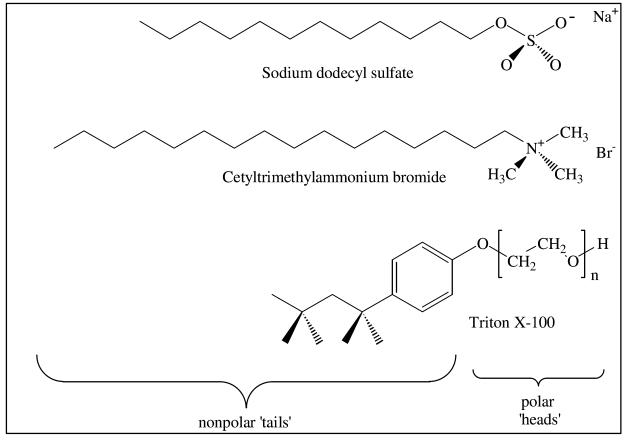

Figure 1. Structure of SDS, CTAB, and Triton X-100.

In Interfaces and Interphases in Analytical Chemistry; Helburn, R., et al.;
ACS Symposium Series; American Chemical Society: Washington, DC, 2011.

All of the above focuses on what a single micelle 'looks like'. It should also be kept in mind that in a micellar solution whose surfactant concentration is above the CMC, not all of the micelles contain exactly the same number of monomers. There is a distribution of aggregation numbers (N_{agg}, the number of monomers in a micelle) and micelle sizes at equilibrium.

Figures 2, 3, 4, 5, 6, and 7 show representations of micelles that have been taken from several sources (*12–17*).

Each of the figures has merits and limitations. Specifically,

- Figure 2, despite being a static picture, captures the dynamic nature of micelles. It is easy to see that the monomers have some freedom of motion and can enter and leave the micelle. It also presents the idea that the micelle is an open structure, in contrast to Figure 4 which looks like an impenetrable sphere.
- Figure 3 loses some of the dynamic nature, but does call attention to the fact that the alkyl chains and head groups are made from individual atoms covalently bonded together. This is not explicitly clear in figure 2. The first two images of Figure 3 suffer, however, from the condition that the terminal methyl groups have been forced to meet in the center of the sphere and all of chains are in all-trans confirmations. This creates a structure that is likely too open. This is corrected in the last image of that figure in which the chains are allowed to have a few kinks in them. Clearly this leads to a more condensed and realistic structure. Credit must be given, though, in that these are literally three-dimensional models. So if one were looking at the actual model, one might get a better sense of micelles from them compared to two-dimensional pictures in the same way that one might get a better sense of the DNA double helix by looking at Watson and Crick's model compared to an image of it. It is also clear that much effort went into hanging all of the monomers to create the micelles.
- Figure 4 perhaps over-regularizes the micelle structure, picturing essentially all of the head groups at essentially the same distance from the geometric center. It also has the head groups directly next to each other having very little open space in which water and/or solutes could reside between or amongst the head groups. However, the dynamic nature of the alkyl chains in the interior of the micelles is suggested as it is in Figure 2.
- Figure 5 nicely depicts what occurs when the conditions of the all-trans alkyl chains with termination in the very center of the micelle are lifted. The degree of 'packing' is obvious, yet the coloring of the oxygen atoms in the head group clearly shows the randomness of the monomers. The image also shows that the surface is not a smooth sphere but rather that there are dips and bumps, some of which are likely arising from monomers partially leaving the micelle, yet the dynamic nature of micelles does not strongly emerge with these images. While water molecules have been excluded for clarity, one can imagine that viewing

a colored image with the water molecules could provide a much clearer and fairly realistic, albeit static, representation of the surface of the micelle.

- Figure 6 acknowledges the monomer/micelle equilibrium and like Figures 2 and 4 captures the dynamic nature of the micelle interior. Furthermore, the explicit representation of water molecules serves to remind the viewer that water does interact with the head groups and potentially with the alkyl chains to some extent. The generic and amorphous nature of the head group and alkyl chains loses the atomic perspective achieved by Figures 2, and 5 and partially by Figure 7.
- Figure 7, like Figure 5, comes from molecular dynamic simulations and captures quite clearly the dynamic nature of monomers fully or partially entering and/ or leaving the micelles. To molecular scientists, the stick figures might still be translated into individual atoms, but perhaps not as readily as the space filling model in Figure 5. The advantage of the stick representation, however, is that it allows the viewer to see 'through' the micelle to get some sense of the interior. Having several simulations presented also suggests that micelles may 'wobble' with time, going into and out of a more or less spherical shape.

Regardless of what model one uses to discuss micelles, it is imperative to remember the warnings of Wennerström and Lindman (*18*) that

> it should always be kept in mind that the micellar aggregate has a highly dynamical molecular structure, that it does not have a well-defined aggregation number, and since it is relatively small, that it is affected by thermal fluctuations.

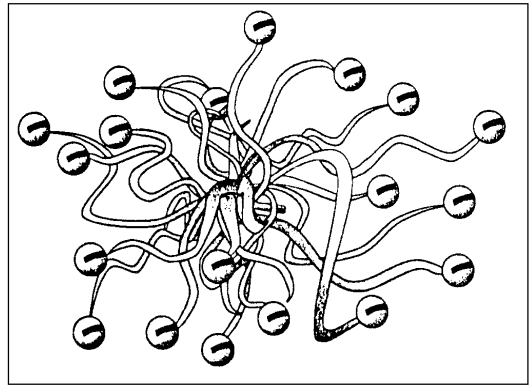

Figure 2. Schematic representation of an anionic micelle (12). © Agilent Technologies, Inc. (2000) Reproduced with permission, Courtesy of Agilent Technologies, Inc.

In Interfaces and Interphases in Analytical Chemistry; Helburn, R., et al.;
ACS Symposium Series; American Chemical Society: Washington, DC, 2011.

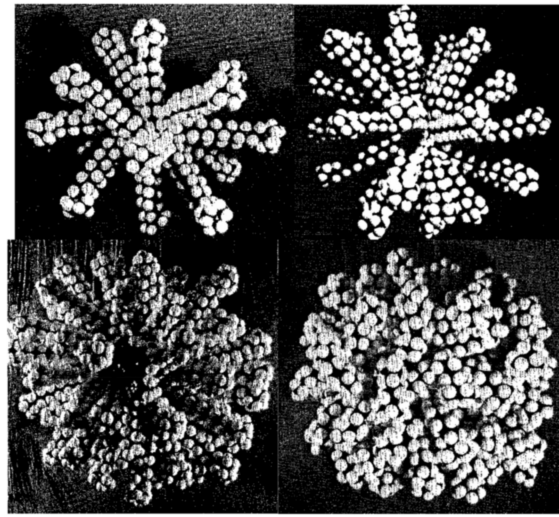

Figure 3. Micelle models made by suspending 3D ball and stick models with threads from a board with 4500 holes spaced 1 cm apart (13). Top left: dodecyltrimethylammonium ion micelle with an aggregation number of 14. Top right: dodecyltrimethyl-ammonium ion micelle with an aggregation number of 30. Bottom left dodecyltrimethylammonium ion micelle with an aggregation number of 58 and all chains fully extended. Bottom right dodecyltrimethylammonium ion micelle with an aggregation number of 58 and chains in mostly a trans conformation but with a few kinks.

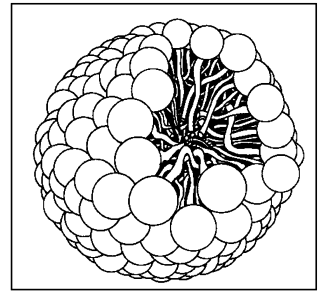

Figure 4. Representation of a spherical micelle. Spheres represent hydrophilic head groups and the stalks represent hydrophobic alkyl chains. Reprinted from reference (14) with permission.

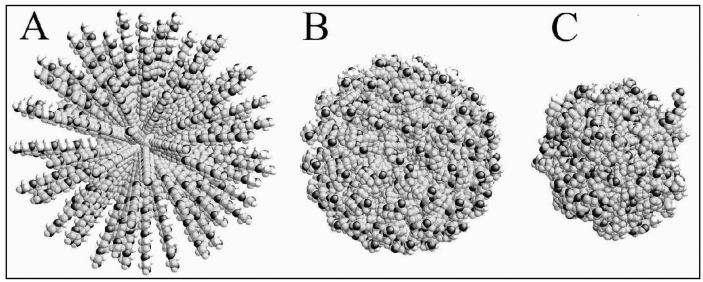

Figure 5. Structures of a micellar aggregate of 80 $CH_3(CH_2)_7$-$(OCH_2CH_2)_5$-OH monomers at different stages in a molecular dynamics (MD) simulation. (a) Initial structure in pre-equilibration run with the all-trans conformation of surfactant molecules, (b) Initial structure in the equilibration run with the nonlinear surfactant conformation. (c) A representative equilibrated micelle structure. The black atoms are oxygens in the hydrophilic head group; the water molecules are not shown for visual clarity. From "Molecular dynamics simulation of C8E5 micelle in explicit water: structure and hydrophobic solvation thermodynamics" Garde, S., Yang, L., Dordick, J.S., Paulaitis, M.E. Molecular Physics, 2002, 100, 2299-2306. Reprinted with permission of the publisher (Taylor & Francis Group, http://www.informaworld.com).

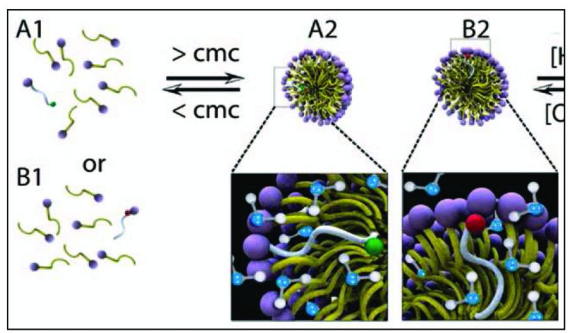

Figure 6. Schematic sketch of two different spin probes – one with a radial at the end of the tail in A1 and one with a radical near the head group in A2 – that incorporate into micelle and vesicle structures above the critical micelle concentration (cmc). The radical is represented as a small sphere on the chain (16). (see color insert)

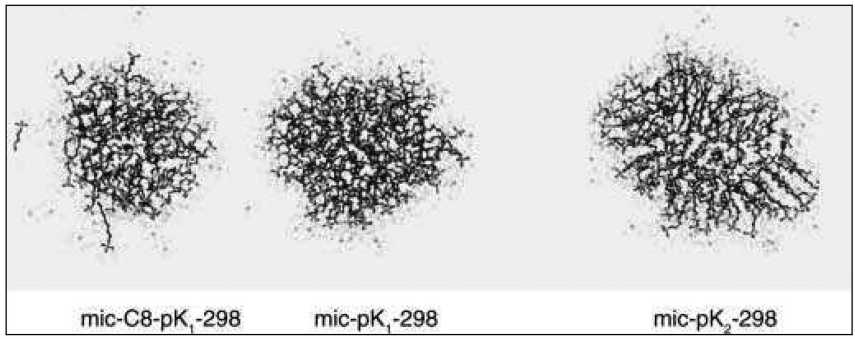

Figure 7. Snapshots from a molecular dynamics simulation of micelles under different conditions. Mic-C8-pK1-298: 90 octylphosphate ions at low pH, 45 Na^+ ions, 6208 water molecules, and 298 K, Mic-pK1-298: 90 dodecylphosphate ions at low pH, 45 Na^+ ions, 6161 water molecules, and 298 K, Mic-pK2-298: 90 dodecylphosphate ions at neutral pH, 135 Na^+ ions, 6071 water molecules, and 298 K. Note the monomers in the left-most figure that appear to be entering or leaving the micelle. Reprinted from reference (17) with kind permission of Springer Science + Business Media.

Similarly, if the images we use come from computational methods, Kuhn, Breitzke, and Rehage (*19*) warn that realistic three-dimensional pictures

> can only be achieved by plotting a hologram or using other types of advanced optical techniques. A picture, projected onto the paper plane gives only a rough impression of the real micellar structure and it is difficult to interpret on grounds of the limited depth of focus. We should also keep in mind that the selected conformations (of monomers) are only snap-shots extracted from a movie showing the real thermal fluctuations of the micelle.

Interfacial Water

One important facet that determines the characteristics of the micelle/water interface is the amount of water associated with the head group region and the 'depth' of its 'penetration' into the alkane-like 'core'. Here, 'depth' and 'penetration' are in quotes as the words themselves seem to rely on an image of the micelle, and more particularly of the 'core', as a largely impermeable structure that the water molecules must pierce or otherwise compromise in order to interact with carbon atoms that are far away from the head groups on the alkyl chain. The issue of water penetration has been the subject of an extraordinarily large number of studies. Space prohibits a full review of all of the studies, but a significant sketch of the terrain and a general proposal about the issue follows.

We begin our analysis with the work of F.M. Menger *et al.* in the late 1970's. In a 1979 review (*20*) of the structure of micelles that considered their shape, viscosity, water penetration, locus of solubilization of benzene inside micelles,

In Interfaces and Interphases in Analytical Chemistry; Helburn, R., et al.;
ACS Symposium Series; American Chemical Society: Washington, DC, 2011.

and aggregation numbers, Menger took issue with the Hartley model of micelles which viewed micelles as an alkane-like droplet surrounded by a polar or ionic shell – the so-called two-state model. They object, saying

> Within the confines of the Hartley model, investigators have been forced to ascribe their probe data either to an aqueous site or to a nonpolar site…this represents a gross oversimplification; solubilized substances are undoubtedly distributed (and rapidly exchanging) among several micellar sites of varied character.

They then, partly through the use of 3-D physical ball and stick models (Figure 3), asserted that the alkyl chains in dodecyltrimethylammonium ionic micelles (with N_{agg} = 58) develop deep grooves with six or more carbon atoms exposed to water, and that for some chains, water could reach well beyond the first six carbons. This is referred to as the 'porous cluster' model of micelles. While these assertions are based on a 3-D ball and stick model, they site experimental support for the deep 'penetration' of water down the length of the alkyl chain (presupposing a model in which the chains are all essentially fully extended). This experimental evidence consists of the solvent-sensitive C-13 NMR chemical shifts of the carbonyl groups in 8-ketohexadecyltrimethylammonium monomers, octanal, 1-naphthaldehyde, and di-n-hexylketone incorporated into the micelles. The probes report polarities similar to that of bulk methanol/water mixtures, 2-propanol, dimethylsulfoxide, and dioxane, respectively. From this, they conclude that a range of polarities, and presumably levels of water penetration, are present inside the micelles. On this basis, they reject the Hartley two-state model. They acknowledge the possibility that the probes themselves are located at unknown positions and other effects such as the 8-ketohexadecyltrimethylammonium chain looping around to orient the keto group near the hydrated head group region. While they acknowledge these possibilities, they generally dismiss them.

Regardless of the soundness of the models or the arguments used to interpret their data, Menger's challenge of the two-state model spurred work in the area of water penetration. This work can be subdivided into studies which used molecular dynamics (MD) simulations to establish where water resides in and around the micelles, and studies based on instrumental techniques in combination with intrinsic or extrinsic probes of varying structures. Efforts along both of these lines are detailed below.

Computational Studies of Water Penetration

In relatively early computational studies, J.P. O'Connell and coworkers used MD methods to investigate micelles structure. In the work considered here, water molecules were not explicitly modeled but rather treated as a continuous field, and an infinite energy spherical wall was used to keep monomers from leaving the micelle (*21*). Furthermore, the heads were attached at the edge of the wall of the micelle with a harmonic potential. Methylene, methyl, and head groups were all treated as soft spheres having 6-9 Lennard-Jones interactions

(head/methylene/methyl interactions) with repulsive interactions between head groups including dipole-like repulsions and excluded volume effects. Their calculations predicted a finite probability of finding the methyl tail segment throughout the micelle, and notably a small but finite probability of finding it at the micelle surface, in agreement with many of the experimental studies discussed below. They also found that while the head groups were predominantly located in the palisade layer, some were also found in the micelle core. The authors acknowledge that this surprising result may be an artifact of constraints placed on the system. On average, tail groups were found further from the micelle center of mass than were segments 6, 7, and 8 of their 9-segment chains. This suggests bending and looping of the chains, consistent with other findings that the chain ordering decreases rapidly from the head to the third segment and then levels off for other segments. They also found that 67% of the bonds between the nonpolar segments were in the trans configuration and that the shape of the micelle was slightly non-spherical. In a subsequent study, Karaborni and O'Connell examined the effects of chain length and head group and found largely similar results to those described above (*22*). In neither study, however, were they able to comment explicitly on the hydration of the micelles because the solvent was modeled as a field. Importantly, they note that their simulations produced results comparable to those from studies in which solvent molecules (water) were explicitly modeled.

Sodium Octanoate

In 1991, Shelley, Watanabe, and Klein used MD to study the structure and dynamics of sodium octanoate micelles consisting of 15 monomers in a 400 ps simulation (*23*). They found that there is a "completely dry core region" (Figure 8), however, they did calculate finite hydration numbers for carbon segments near the terminal methyl group.

They also found that the terminal methyl group is more hydrated than the two methylene units preceding it in the chain. This, combined with the spatial distribution of water molecules, suggests that the chains bend and loop such that the tails are periodically at the micelle surface. With regards to the head group region, they found that 60% of the sodium counterions are generally in the first hydration shell, clustered at 2.9 Å from the carboxylate carbon. Another significant fraction is centered at 5.2 Å away from the carboxylate carbon. While the first layer of sodium ions has reduced hydration – four waters of hydration compared to six for bulk – the sodium ions in the second shell are hydrated comparably to those in bulk water. The authors also note periodic shape fluctuations.

Studying the same sodium octanoate micelles consisting of fifteen monomers, Laaksonen and Rosenholm (*24*) state their results in a manner rather differently than Shelley, Watanabe, and Klein. Rather than appealing to a "completely dry core region" they focus on the formation of a "relatively broad wet interface" on the basis of data shown in Figure 9.

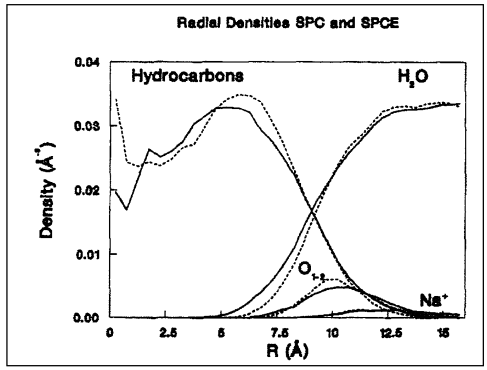

Figure 8. Density profiles of the carbons atoms, sodium ions, head group oxygen atoms, and water molecules with respect to the center of mass of the micelle using two different pair potentials for water (SPC-solid line, SPC/E-dotted line). Reprinted from Electrochimica Acta, vol. 36, "Simulation of sodium octanoate micelles in aqueous solution" Shelley, J.; Watanabe, K.; Klein, M.L. pp. 1729-1734, Copyright 1991 with permission from Elsevier.

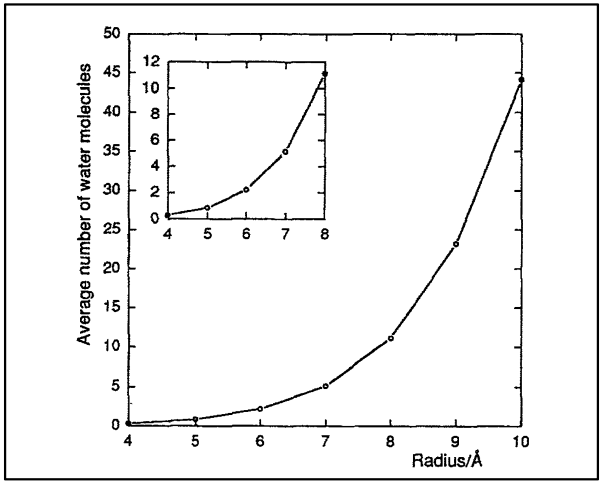

Figure 9. Computed number of water molecules inside a sphere of a given radius from Laaksonen and Rosenholm simulation. Inset: magnified region for a radius of 4-8 Å. Reprinted from Chemical Physics Letters, vol.216 "Molecular dynamics simulations of the water/octanoate interface in the presence of micelles" Laaksonen, L.; Rosenholm, J.B. pp. 429-434, Copyright 1993, with permission from Elsevier.

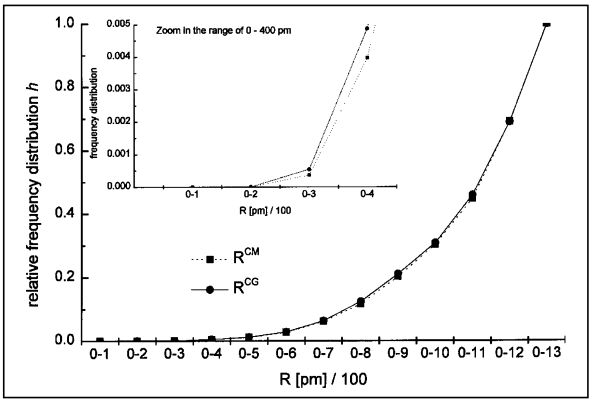

Figure 10. Relative frequency distribution of water molecules as a function of radius for sodium octanoate micelles of 15 monomers. Reprinted with kind permission from Springer Science + Business Media: Colloid Polym. Sci. "The phenomenon of water penetration into sodium octanoate micelles studied by molecular dynamics computer simulation" vol. 276, 1998, pp. 824-832, Kuhn, H.; Breitzke, B.; Rehage, H. Figure 4.

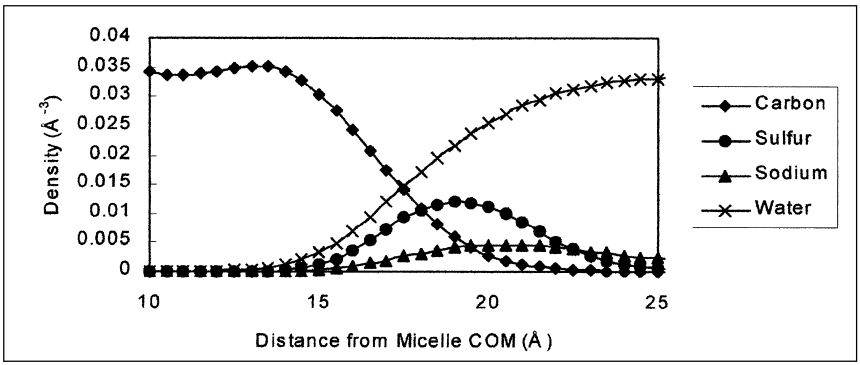

Figure 11. Density of different atoms in the interfacial region between SDS micelles and the aqueous phase as a function of distance from the center of mass from a 5 ns explicit atom simulation (29).

They observed a small possibility of water being within 3-4 Å of the micelle center of mass. They cite both experimental and computational studies that agree with this finding. They also conclude that water around the head groups is highly structured and that the thickness of the ionic hydration sheet is approximately 10 Å, ultimately concluding that the "hydration layer protrudes into the rough surface of the micelle." Importantly, these authors point out that micelles of fifteen monomers allow for relatively open structures which perhaps explains the observation of "deep penetration" of water.

In Interfaces and Interphases in Analytical Chemistry; Helburn, R., et al.;
ACS Symposium Series; American Chemical Society: Washington, DC, 2011.

In the late 1990s, Kuhn, Breitzke, and Rehage also studied sodium octanoate using MD (*25–28*). They conclude from their 400 ps simulation at 300 K that "only a small amount of water molecules was found" in the central region of the micelle (*25*). Specifically, a central sphere with a radius of 0.7 nm contains less than 10% of the water molecules. Nevertheless, according to the authors, this shows that "water penetration is still possible but very rarely observed" (Figure 10) (*25*).

They also studied the distribution of sodium ions and water in the head group region and found three distinct shells of hydration (*26*). In other studies, Kuhn and Rehage found that water molecules near the micelle surface are significantly less mobile than those in the bulk phase, presumably arising from hydrogen bonding with the head group. They also found that the percent trans configurations of the monomer is 77% in the micelle, compared to 60-65% in vacuum, aqueous solution, and octane. They conclude from this that the monomers in the micelle are more elongated and rotate less when in the micelle (*27*).

Sodium Dodecylsulfate

In contrast to the small sodium octanoate micelles discussed above, Berkowitz *et al.* studied a micelle of 60 sodium dodecylsulfate monomers in 7579 water molecules in a 5 ns explicit atom simulation (*29*). They found a 12 Å water-free hydrocarbon core. The existence of the core is illustrated by their excellent plot of the density of various atoms versus distance from the micelle center of mass (Figure 11).

Importantly, in the region between 14 Å and 21 Å, the densities of carbon and water overlap significantly, showing that the hydrophobic chains interact with water, at least to some extent. They also found that sodium ions cluster into three shells of increasing radius and decreasing frequency. Of the sodium ions in the first shell, 72% interact with only one head group, 23% bridge between two head groups, and 5% interact with three head groups. The sodium ions also have decreased diffusion relative to their diffusion in bulk aqueous solution. The water molecules in the first solvation shell have reduced translational diffusion coefficients and have a considerably pronounced retardation of their reorientational mobility, presumably due, at least in part, to hydrogen bonding with the sulfate group. Figure 12 indicates the number of hydrogen bonded water molecules per head group in the hydration shell (defined by a minimum O-H distance and particular maximum bond angle). The authors also found the shape of SDS micelles to have ellipsoidal components.

Based on their extensive study of water molecules, sodium ions, and sulfate head groups, Berkowitz *et al.* estimate that the interface, "defined as the distance between the point where the water reaches 10% of the bulk density and the point where the hydrocarbon diminishes to 10% of its bulk density, is 4.5 Å" (*29*).

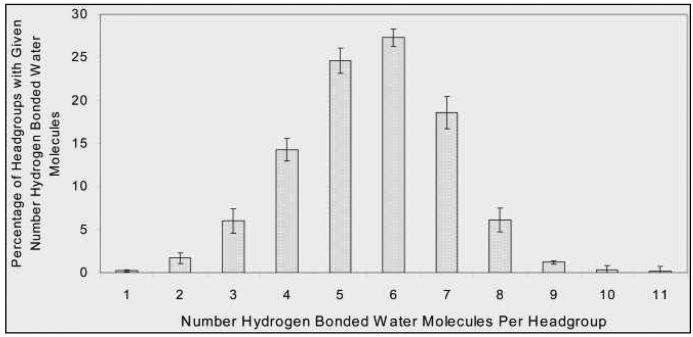

Figure 12. Percentage of head groups with a given number of hydrogen bonded water molecules Number of water molecules hydrogen bonded to a head group in a 60 monomer SDS molecular dynamics simulation (29).

In 2007, Yoshii and Okazaki published MD studies on SDS micelles (*30*). Interestingly, they studied micelles comprised of varying numbers of monomers. Based on free energy calculations, they found that "only one of several ten thousand micelles accommodates a water molecule" in the core (for micelles of 61 and 121 monomers). In another paper they present density profiles of various components relative to the micelle center of mass (Figure 13) (*31*). It is clear that in virtually all cases water remains largely in the same general vicinity as the head group and sodium ions, except in the smaller micelles which have more open structures and allow for more water to interact with more of the hydrophobic groups. Oddly, they found a region near the very center of mass with very low density. They refer to this region as a cavity and offer no explanation as to its origin. In other studies they examine the sodium distribution about the head groups, generally finding them in two shells at r = 3.6 Å and 5.3 Å from the head group sulfur atoms (*32*). They also found most of the sodium ions are located approximately 90° to the main axis of the monomer, but some are located in line with the main axis. By studying nearest neighbor interactions between two surfactant monomers, they found that hydrophobic interactions within the micelles are produced and annihilated repeatedly on a time scale of about 100 ps, breaking and forming about ten times before diffusion breaks the interaction between two specific monomers completely. This serves as a good reminder of the kinetic fluctuations *within* the micelles in addition to the kinetics of monomers that are partially or completely entering and leaving the micelles.

Decyltrimethylammonium Chloride and Bromide

In studies of micelles, the issues of the effects of head groups must be considered. The micelles discussed above are anionic. Here we consider an MD study of cationic decyltrimethylammonium chloride (DeTAC) micelles conducted by Brickmann *et al* (*33*). In the 30-monomer micelle studied, they found a

molecularly sharp interface region and a completely dry interior with a radius of 8 Å (Figures 14 and 15).

Water was found to interact with the head groups but did not penetrate into the region of the chains beyond that. They define an interface thickness of 6 Å, ranging from 10.4 Å to 16.4 Å from the center of mass of the micelle. This corresponds to two to three water layers in the interface region.

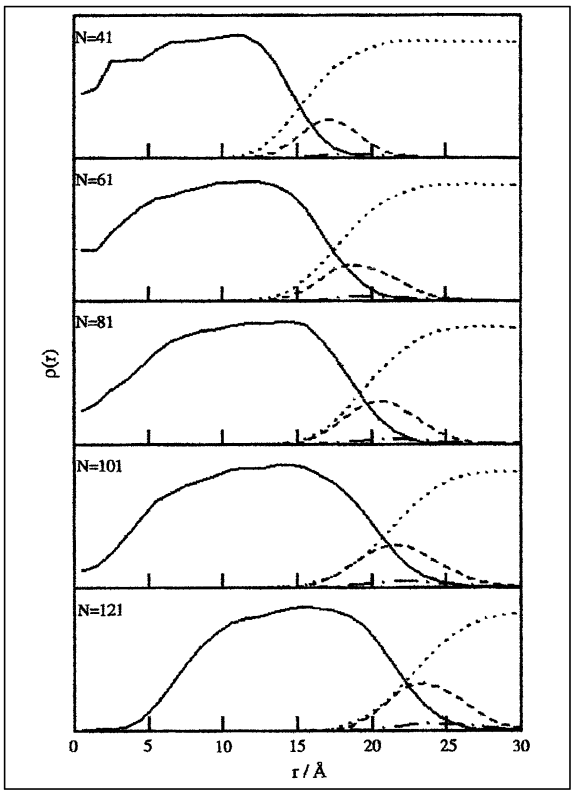

Figure 13. Density profiles from the center of mass of SDS micelles in molecular dynamics simulations of micelles of varying numbers of monomers, N, shown in the upper left of each plot. Solid line: hydrophobic group, dashed line: hydrophilic group, dash-dotted line: sodium ion, dotted line, water. Reprinted from Chemical Physics Letters, 425, Yoshii, N.; Okazaki, S., "A molecular dynamics study of structural stability of spherical SDS micelle as a function of its size" pp. 58-61, Copyright 2006, with permission from Elsevier.

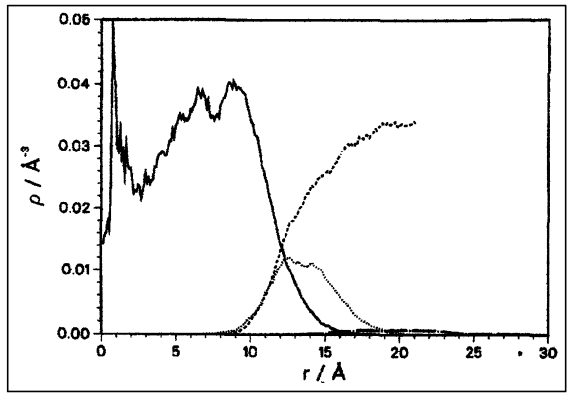

Figure 14. Number density profiles for chain members (C2-C10, solid line), head groups (C1, N, and three methyl groups, dotted line), water molecule oxygen atoms (dashed line), and chloride ions (chain dotted line) as a function of radius with respect to the center of mass for DeTAC micelles from a MD simulation containing 30 amphiphile molecules, 30 chloride ions, and 2166 water molecules (33).

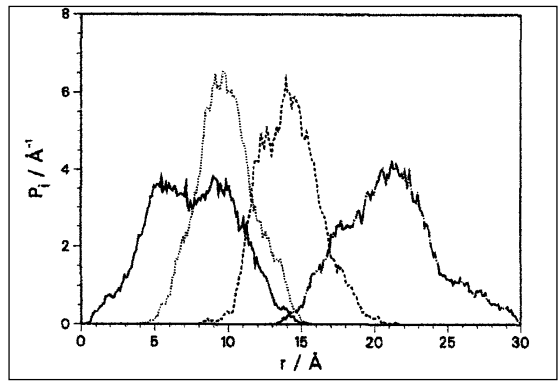

Figure 15. Probability distributions for carbon atoms C10 (solid line), C5 (dotted line), N atoms (dashed line), and chloride ions (chain dotted line) with respect to the center of mass for DeTAC micelles from a MD simulation containing 30 amphiphile molecules, 30 chloride ions, and 2166 water molecules (33).

They also found that the terminal methyl group can reside in the hydrated head group region as has been suggested in numerous other computational and experimental studies. The micelles were found to be slightly ellipsoidal at times and spherical at other times. Interestingly, the trans-gauche ratios starting with the N-C1-C2-C3 dihedral angle were found to be 93%, 69%, 71%, 64%, 72%, 63%, 72%, and 64%, with an average of 73%. This indicates an ordering near the head group region that decreases into a more liquid-like environment near the core. The alternating pattern exhibited is also interesting. Lastly, the authors found that the first shell of chloride ions nearest the head groups 'neutralizes' only 27% of the

In Interfaces and Interphases in Analytical Chemistry; Helburn, R., et al.;
ACS Symposium Series; American Chemical Society: Washington, DC, 2011.

charge on the micelles (i.e., about eight out of thirty counterions are in the direct vicinity of the head group nitrogen atoms). If the second shell is included, 64% of the charge is neutralized, leaving 36% of the chloride ions free in solution.

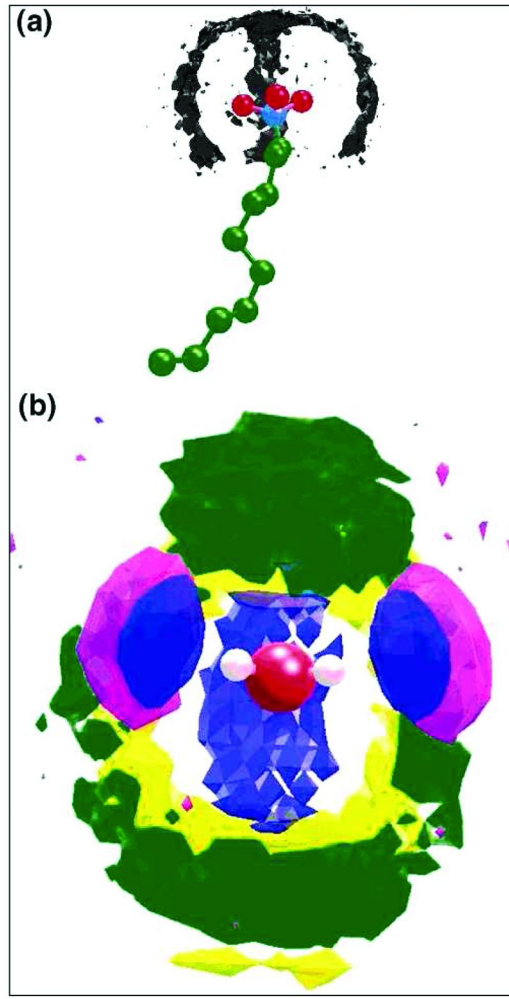

Figure 16. (a) Atomic probability density map of interfacial water molecules around a surfactant head group denoted by the black region. The red spheres represent CH_3 groups, the blue sphere represents the nitrogen atom, and the green spheres represent the CH_2 and CH_3 groups of the surfactant. (b) Environment around an interfacial water molecule (center). Yellow, green, magenta, and blue denote the most probable locations of the methyl group (lightest, generally above and below the water molecule), nitrogen (darkest, above and below the water molecule, bromide ion (light disks on the side of the water molecule), and interfacial water (center of disks and running from top to bottom), respectively, in the DeTAB micellar solution (34). (see color insert)

In Interfaces and Interphases in Analytical Chemistry; Helburn, R., et al.;
ACS Symposium Series; American Chemical Society: Washington, DC, 2011.

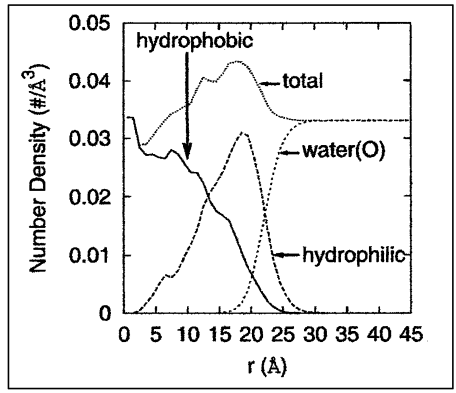

Figure 17. Number densities of heavy atoms in the hydrophobic and hydrophilic parts of C8E5 surfactant molecules and water oxygen atoms as a function of the radial distance from the geometric center of C8E5 micelles from a MD simulation. From "Molecular dynamics simulation of C8E5 micelle in explicit water: structure and hydrophobic solvation thermodynamics" Garde, S., Yang, L., Dordick, J.S., Paulaitis, M.E. Molecular Physics, 2002, 100, 2299-2306. Reprinted with permission of the publisher (Taylor & Francis Group, http://www.informaworld.com).

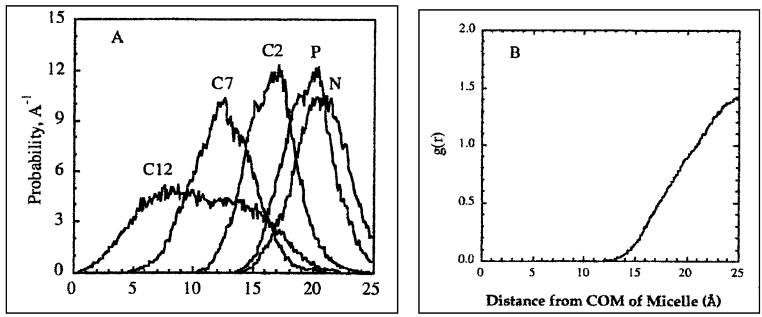

Figure 18. (A) Probability distributions of select atoms on DPC molecules relative to the center of mass of DPC micelles. (B) Radial distribution function of water with respect to the center of mass of DPC micelles. Both based on MD simulations containing 60 DPC monomers and 5294 water molecules. Reprinted from J. Mol. Struct., vol. 485/486, Wymore, T.; Goa, X.F.; Wong, T.C. "Molecular dynamics simulation of the structure and dynamics of a dodecylphosphocholine micelle in aqueous solution" pp. 195-210, Copyright 1999, with permission from Elsevier.

Pal, Balasubramanian, and Bagchi studied decyltrimethylammonium bromide (DeTAB) micelles containing 47 surfactant monomers (*34*). Their results are qualitatively in good agreement with those discussed above but they studied the structure of water around the head groups in even greater detail and developed interesting molecular pictures (Figure 16). They found a different arrangement of

In Interfaces and Interphases in Analytical Chemistry; Helburn, R., et al.;
ACS Symposium Series; American Chemical Society: Washington, DC, 2011.

water molecules around the cationic head group compared to the arrangement in bulk water and around the anionic cesium perfluorooctanoate micelles discussed below. Lastly, they calculated that 57% of the bromide ions reside in the first hydration sphere around the head groups.

Non-Ionic Micelle

Garde *et al.* studied C_8E_5 [CH_3-$(CH_2)_7$-$(O$-$CH_2CH_2)_5$-OH] nonionic micelles comprised of 80 monomers and 9798 explicit TIP3P waters (*15*). As in the studies above for SDS and DeTAB, they found 1) roughly spherical micelles with fluctuations that are significantly non-spherical, 2) no water penetration in the micelle core (Figure 17), 3) considerable exposure of the hydrophobic tails to the water in the interfacial region, and 4) a distribution of C-C-C-C dihedral angles that mirrors that of pure liquid n-octane. Based on a definition of the hydrophobic core as "the distance at which the carbon density equals its value at the center" they calculate the radius of the micelle core to be 17 Å. Based on a similar definition for the water-micelle interface, they estimate an external radius of 22 Å. So the interfacial region is estimated to be about 5 Å, but this does not include non-bulk-like water associated with the head group region.

Zwitterionic Micelle

Wong *et al.* investigated dodecylphosphocholine (DPC) zwitterionic micelles of 60 monomers with 5294 water molecules (*35*). Their findings include 1) slightly prolate micelles, 2) limited penetration of water into the interior of the micelle, and 3) the main interaction of water with the micelle comes from interaction with the head group. Figure 18 shows radial distributions of select atoms that are comparable to distributions from other studies, particular in the fact that the water and the head group phosphorous and nitrogen atoms have low probabilities of being near the micelle center of mass yet the terminal carbon atom on the monomers can be found throughout the micelle, including near the phosphorous and nitrogen atoms in the head group region 15 – 20 A away from the center of mass.

Figure 19 shows hydration numbers as a function of monomer carbon number (integration of the probability distribution function between the carbon atom being considered and the oxygen atoms of water taken to 3.5 Å from the carbon atoms).

There is a clear drop off after the second carbon beyond the phosphate moiety and a definite rise near the terminal methyl group. Based on trans-gauche transition rates, Wong and coworkers state that they "cannot conclude that the fluidity of the DPC micellar interior is significantly different than those of alkanes" and note that this conclusion is in contrast to an earlier SDS simulation that was ten times shorter (1.2 ns vs. 120 ps) (*36*).

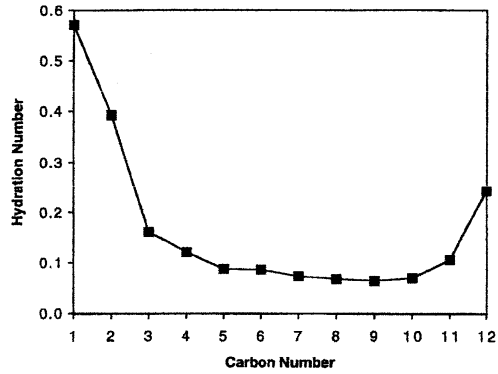

Figure 19. The variation of the hydration number of carbon atoms along the dodecyl chain in DPC micelles. Reprinted from J. Mol. Struct., vol. 485/486, Wymore, T.; Goa, X.F.; Wong, T.C. "Molecular dynamics simulation of the structure and dynamics of a dodecylphosphocholine micelle in aqueous solution" pp. 195-210, Copyright 1999, with permission from Elsevier.

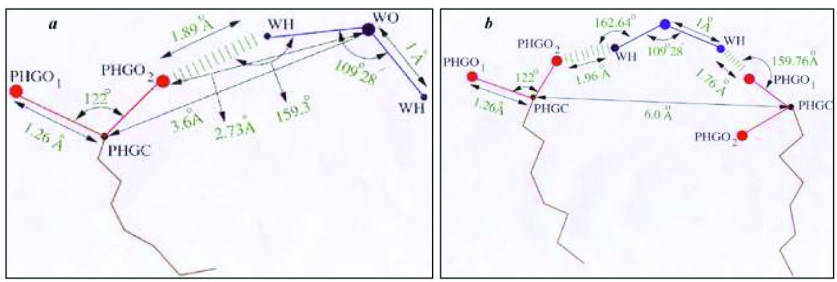

*Figure 20. Schematic description of the environment around bound interfacial waters; **a**, IBW1 (interfacial bound water via one hydrogen bond), and **b**, IBW2 (interfacial bound water via two hydrogen bonds). Numerical values of the geometrical parameters are average values obtained from a MD simulation of cesium perfluorooctanoate. PHGO denotes the oxygen atom of the polar head group of the surfactant, and PHGC denotes the carbon atom in the head group. WO and WH denote the oxygen and hydrogen atoms of the interfacial water respectively. Broken lines between PHGO and WH denote hydrogen bond. Reprinted from reference (41) with permission from Curr. Sci. and the author. (see color insert)*

Interestingly, these researchers report that two lipid monomers were lying on the surface of the micelles, exposing one face of the monomers to water throughout the simulation. They postulate that these lipids could represent monomers that were leaving the micelle (the average N_{agg} of DPC is 56, but the simulated micelle contained 60 lipids).

In Interfaces and Interphases in Analytical Chemistry; Helburn, R., et al.;
ACS Symposium Series; American Chemical Society: Washington, DC, 2011.

Balasubramanian *et al.* studied the structure and kinetics of water in the interfacial region for cesium perfluorooctanoate micelles with 62 monomers and 10,562 water molecules in a number of articles. They found that cesium cations occur predominantly near the micelle/water interface with approximately 0.67 cesium atoms per head group in the first hydration shell (*37*). They also published extensively on the very slow reorientational motion of water molecules near the micelle, finding that the slow component of this reorientation is at least two orders of magnitude slower than in bulk water (*38*). They also found a slow component in the moment-moment time correlation function related to the dielectric relaxation of water molecules (*39*). From this and other findings, they suggest the presence of an extended hydrogen bond network of water molecules at the surface of perfluorooctanoate micelles.

Balasubramanian and Bagchi also extensively characterized the 'types' of water around the head groups and found two types – bound and free – with bound types being either singly or doubly H-bonded to the head groups with a ratio of bound to free of 9:1 (Figure 20) (*40*, *41*). They report that bound "water molecules stay within a 10 Å shell from the head group up to about 350 ps, and not any longer" at a temperature of 350 K (*42*). The radial distributions of all three types of water (bound with one hydrogen bond, bound with two hydrogen bonds, and free) were presented in one of the articles (*40*). Such extensive studies of the particular structures of water and their lifetimes around micelle head groups provide vivid images of the submicroscopic environment of the interface, provided one can imagine the associated kinetics.

Summary of Computational Studies

While it is nearly impossible to give a complete review covering all of the published computational studies of micellar systems, the overview above allows for some generalities to be drawn, which can inform the ways we think about micelles and the pictures we use to capture their essence. The results generally show that

1) Octanoate micelles, with a small aggregation number (N_{agg} = 15), may have a more open structure than micelles with higher aggregation numbers and may therefore allow water to interact with more of the carbon atoms in the surfactant chains.
2) An alkane-like core exists in all large micelles (large arbitrarily being greater than N_{agg} = 15)
3) Shells of hydration exist around the head groups, and the structure of water in those shells is different than bulk water and is generally influenced by the head group.
4) Some water penetration is found in virtually all micelles (i.e., water beyond the head groups, but varying 'depths' are found in each).

Considering the dynamics of the system, it is likely that the α and β carbons at least experience some interaction with water.

5) Monomer chains kink and bend which allows terminal groups to be found in the hydrated head group region.
6) An image of a micelle emerges as a dynamic, fluid structure that is comprised of an alkane-like liquid at its center of mass which transitions into a region with a hydration and polarity gradient, the steepness of which depends on the head group and the counterions. Where the gradient begins is also dependent on the structure, but for most micelles it incorporates the first several (up to three) carbon atoms bonded to the head group and the head group itself.

As a general note about the computational studies discussed above, it is pointed out that the authors were generally very explicit about how they modeled the surfactants and water molecules and generally tried to use realistic aggregation numbers consistent with those found in the experimental literature for the different systems that were examined.

Experimental Studies of Micelles

Just as different computational studies led to different conclusions depending on the types of systems studied and the method employed, experimental techniques for probing the extent of water incorporation have also led to different conclusions.

In 1967, Muller and Birkham studied $CF_3(CH_2)_nCOONa$ micelles with n = 8, 10, and 11 by observing shifts in the CF_3 signal in ^{19}F NMR spectroscopy (*43*). They found the CF_3 signal at a position midway between its position in water and its estimated position in a pure hydrocarbon environment. While they recognize this may be due, in part, to chain looping that allows the terminal CF_3 to be at the micelle surface, they dismiss this as a dominant factor based on anticipated decreases in surface:volume ratios with longer chains surfactants, which had no effect on the position of the CF_3 signals relative to water and a hydrocarbon environment. They conclude that there must be considerable penetration of water into the interior of the micelles with all three chain lengths.

In 1981, Ulmius and Lindman used perfluorinated and partially fluorinated amphiphiles of varying chain length and ^{19}F NMR spectroscopy to probe the issue of water penetration (*44*). Based on their findings, they state that "the picture that emerges for the hydration of fluorocarbon surfactant micelles is one with an appreciable water contact only for the α-CF_2 while we detect no water contact further in…There is certainly no indication of any considerable water penetration deep into the micelles (seven to eight methylene units) as has been suggested in some previous work." The authors acknowledge that fluorocarbon/hydrocarbon demixing as well as the higher hydrophobicity of fluorocarbon chains could restrict their claims to fluorinated micelles, but they cite reasons why these effects would lead to results suggesting an even higher water contact than was observed. They therefore conclude that the water contact must still be relatively small. Importantly,

In Interfaces and Interphases in Analytical Chemistry; Helburn, R., et al.;
ACS Symposium Series; American Chemical Society: Washington, DC, 2011.

they add a footnote about the logic required when comparing their results to other studies that find water in contact with various portions of the hydrophobic chain:

> It may be pointed out as a general comment to studies of extrinsic or intrinsic probes that, if one observes a water contact for a group at some distance from the polar head, this gives no evidence for water penetration deep into the micelle. Thus, the group might reside close to the micellar surface (especially if it is polar), and separate studies are needed to study its location. However, in the converse situation where one obtains no water contact for a group remote from the polar head, one may safely state that there is no water penetration deep into micelles.

Martens and Verhoeven used hydrophobic electron donors and a hydrophilic electron acceptor in combination with UV-absorbance and fluorescence spectroscopy to probe the structure of SDS micelles (*45*). While they do not comment directly on the issue of water penetration, they conclude that their results are in-line with a "channel" model of micelles that would allow water to penetrate into the lipid regions – a model, they note, that is similar to Menger's porous cluster model mentioned at the beginning of this section about water penetration in micelles.

Casal used infrared spectroscopy of 7-oxooctanoate to probe the water penetration into micelles of sodium octanoate and 7-oxooctanoate (*46*). He found that "water penetrates almost everywhere into micelles" with an area completely devoid of water, presumably at the 'core'. In addition he reported that "water penetrates at least up to position 7 of the octanoate chain." On the basis of the findings he postulates the coexistence of at least two micellar regions, one with and the other without water. The author also states that similar experiments conducted on sodium dodecanoate, SDS, and Triton X-100 all yielded similar results.

It may be instructive here to quote Cabane (*47*) who warns:

> For example, one may find that the first four CH_2 groups of the surfactant molecules are hydrated, and conclude that water penetrates the micellar core over a depth of 5 Å. This conclusion would only be correct if the surfactant chains would extend radially from the centre to the surface of the micelle. There is considerable evidence they do not…the disorder of the molecules prevents us from taking information which is related to the molecular frame of reference and expressing it into the micellar frame of reference.

In contrast to Casal's conclusions, Cabane (*47*), Tabony (*48*), and Némethy *et al.* (*49*) reached generally different conclusions about water penetration in three different systems. These studies are presented in Table I. A picture emerges from these studies of an anionic, cationic, and non-ionic micelles that is more in line with the general findings of computational studies, namely, that water does not interact freely with all portions of the surfactant monomer, except perhaps for the

In Interfaces and Interphases in Analytical Chemistry; Helburn, R., et al.;
ACS Symposium Series; American Chemical Society: Washington, DC, 2011.

first one or two carbon atoms beyond the polar/charged head groups. Tabony's findings even limit the interaction of water with the polar head group region.

Fendler *et al.* also studied a variety of micelle systems (*50*). Using UV-visible and NMR spectroscopy of acetophenone and benzophenone, the authors conducted a complex study of the effect of probe concentration and micelle type on the location of the phenones within the micelle and the extent of water penetration. They propose a specific orientation of the phenones inside the micelle (Figure 21) and suggest that the depth of penetration of the probes varies with the type of micelle and the probe concentration.

The implication of their work is that different probes, even structurally related ones, may be located in different regions of micelles and will therefore sense and report different chemical environments. Thus, studies of water penetration that use probes must constantly be aware of and acknowledge this complication.

Das *et al.* used shifts in NMR proton signals of C11 and C12 linear alkyl benzenesulfonates to study water interaction with micelles (*51*). They found that upon micellization, the protons ortho to the sulfonate head group do not shift significantly whereas the meta protons shift in a manner consistent with being in a less polar hydrocarbon environment. These results indicate that water interacts with the head group and part of the aromatic ring, but does not penetrate much further towards the core.

Halle and Carlström studied oxygen-17 relaxation rates to investigate the behavior of water of hydration around ionic micelles as a function of alkyl chain length, head group, and counterion (*52*). While they focus mainly on the dynamics of water reorientation, they do state that based on similarities between the effect of propionate on relaxation rates compared to octanoate that they "can thus infer that the water-hydrocarbon contact in potassium octanoate micelles corresponds to at most two fully exposed methylene groups per amphiphile…the conclusion that the water-hydrocarbon contact corresponds to less than two fully exposed methylene groups holds also for micelles composed of the longer-chain octanoates" (referring to C11, C13, and C15 chains).

Leis *et al.* used NMR spectroscopy to study the location of two nitroso compounds in one anionic and four cationic micellar systems (*53*). They found that "the head group and chain length did not influence the preferential location of the nitroso compounds, the aromatic rings of which were centered in the neighborhood of the β or γ carbons of the hydrocarbon chain." They also conclude that hydration is considerable at the α carbon but minor in the internal regions of alkyltrimethylammonium micelles and that chain looping brings terminal methyl groups into contact with the hydrated region. They also state that

> The Gruen model (*54*, *55*) for micelle structure considers that the hydrocarbon chains are almost as disordered as their bulk liquid state. All segments of the chain spend an appreciable proportion of time near the micelle surface. Thus, even though the core is almost completely devoid of water, each segment of the chain samples a partly hydrophobic environment.

Table I. Findings from several experimental studies regarding water penetration in anionic, cationic, and nonionic micelle systems

Surfactant	*Type*	*Expt'l technique*	*Conclusions*
SDS	Anionic	NMR relaxation rates	The water/surfactant "interface is composed of two regions: a layer which contains the hydrated charges and water, and a layer containing hydrated CH_2 groups…the thickness of the layer containing hydrated CH_2 groups is comparable to the length per CH_2 group in a chain."
Tetradecyltrimethyl ammonium bromide	Cationic	Neutron small angle scattering	"There is almost no water penetration in this layer (a 2.0 Å layer containing the head groups) nor in the paraffin core."
Triton X-100, 102, and 305	Non-ionic	NMR proton chemical shifts and spin-lattice relaxation times	"The interior of the micelle is liquid-like and is not penetrated by solvent to any great extent…Contact with solvent seems to begin in the region after the first ethoxy group following the phenyl group and gradually increases toward the end of the chain."

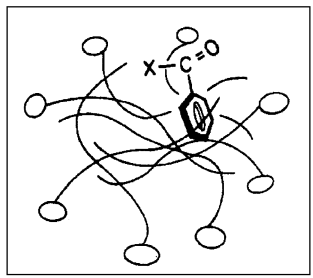

Figure 21. Schematic representation of the general solubilization sites of acetophenone and benzophenone in aqueous micellar solutions proposed by Fendler et al. (50).

In a recent study, Han *et al.* used dynamic nuclear polarization and the interaction between water and stable nitroxide radicals covalently attached to two different positions of the hydrophobic tails of stearic acid molecules to probe the penetration of water in oleate and Triton X-100 micelles (*56*). They found "significant penetration of water inside oleate micelles with a higher average local water viscosity (~ 1.8 cP) than in bulk water, and Triton X-100 micelles…mostly exclude water while allowing considerable surfactant chain motion and measurable water permeation through the soft structure." The interpretation of water penetration relies on the assumption that the chains are fully extended radially from the core of the micelle and that the polar nitroxide that is covalently attached to the chain does not alter this conformation. It is again

In Interfaces and Interphases in Analytical Chemistry; Helburn, R., et al.;
ACS Symposium Series; American Chemical Society: Washington, DC, 2011.

instructive to call to mind the earlier quote from Cabane warning about projecting a molecular frame of reference onto a micellar frame of reference.

In the same manner that Fendler *et al.* postulated different loci of solubilization of UV-visible probes, Huang and Bright reached the same conclusion regarding two fluorescent probes: 2-anilinonaphthalene-6-sulfonic acid (2,6-ANS) and N-phenyl-naphthylamine (1-AN) in SDS micelles (*57*). Based on fluorescent decay kinetics, the researchers conclude that 2,6-ANS is located in the interfacial region and experiences a water gradient, whereas 1-AN resides in the core and experiences a homogeneous environment. The authors also study the effects of electrolytes, n-alcohols, and temperature on the viscosity and extent of water penetration in the micelle.

Mukerjee and Cardinal studied the location of benzene, alkyl derivatives of benzene, and naphthalene in SDS and cetyltrimethylammonium chloride (*58*). They found that the microenvironment of benzene in both is polar, indicating that it resides near the head group interfacial region. As the size of the alkyl derivative increases, the polarity of the microenvironment that the probe senses decreases. Based on this, they propose a 'two-state' model with one state being 'absorbed', or located in the micellar core, and the other being an 'adsorbed' state with the probe located at the micelle/water interface. Different probes, then, could experience these two states to different extents and report a range of polarities. Another possibility, however, is that a polarity gradient exists in the micelles, and that the probes sense that gradient, the exact portion of the gradient experienced being dependent on the size of the alkyl derivatization. They note that because of the small dimensions of the micellar core "the purely 'dissolved' state may be difficult to obtain in practice for any solute." They state further that "any solubilized species is likely to be exposed to water at the interface to some extent on a statistical basis, unless it is actually repelled from the surface."

Mukerjee and Cardinal then go on to consider their results in light of other studies that had suggested benzene was found in the micellar core. Their resolution to the conflicting findings is largely based on the relative concentrations of benzene and micelles. They note that in their study, they kept the concentration of benzene low relative to that of the micelles, and that their results are consistent with other studies conducted under similar relative concentration conditions. Higher concentrations of benzene are likely to modify the micelles themselves and also change the distribution of benzene within the micelles. Therefore, when using probes to study the polarity of, or water penetration into micelles, not only the nature of the probe but also its concentration must be carefully considered when interpreting data.

A broader review of many types of 'water penetration probes' was published by Ganesh, Mitra, and Balasubramanian (*59*). They conclude that because the probes invariably contain polar and aromatic groups that they are inherently interfacially active and thus likely to reside in the head group region of the micelle, and therefore only sense and report on the polarity and water content of the interfacial region, not in core. The authors study three classes of probes: aromatic, ketone, and intrinsic probes, using multiple examples of each that were reported in the literature. In all cases, they reach the conclusion that the probes

generally reside in the head group region, perhaps sensing up to the γ-carbon, but none truly probe solely the micellar core.

Another review of solute location in micelles was presented by Sepulveda, Lissi, and Quina (*60*). They discuss the model dependence on the interpretation of results and caution that probes themselves may primarily report probe-induced perturbations to the micelles rather than information about micelle behavior in the absence of the probe. Their study goes beyond that of Balasubramanian *et al.* mentioned above in that thermodynamic methods for determining the locus of solubilization of solutes are also reviewed. Under a section titled "general trends" the authors discuss the fact that there is no direct evidence to support the 'prejudice' that hydrocarbons such as n-hexane and cyclohexane become solubilized in the micelle core and even suggest that available data contradicts it. Likewise, the authors thoroughly consider the various studies of the location of benzene and state that 1) "the bulk of the data are compatible with an initial 'adsorption' of benzene, at least in CTA (cetyltrimethylammonium micelles)" and 2) "conflicting interpretations appear to arise from studies in which relatively high benzene concentrations were used and also those studies based on thermodynamic measurements." This is consistent with the general conclusions drawn by Mukerjee and Cardinal discussed above. The authors also agree with the intuition that highly polar molecules will be 'adsorbed' at the micelle-water interface. Both reviews are worth examining in detail as they outline the general arguments regarding the topic of solute location in ways that space does not permit here, although we have tried to suggest the major issues via the publications on which we have focused. Even though these reviews were published in the mid 1980s, it seems reasonable to carry their general conclusions forward to today given there has been little change in the intervening time in the nature of the probes and the fundamental experimental techniques used to study water penetration.

Summary of Experimental Results

Given the variability of the experimental techniques, probes, and conditions under which experiments are conducted, it is perhaps a bit more difficult to draw general conclusions from the literature regarding water penetration based on experimental results compared to computational studies. Nonetheless, some trends and important caveats do emerge from such a consideration. Some of these include

1) virtually all probes find some degree of hydration inside the micelle – some reports asserting it extends virtually throughout the micelles, others restricting it more to the immediate head group region and the first few CH_2 groups attached to the head groups.
2) a few researchers have proposed a 'two-state' model, explaining intermediate results as a weighted combination of the probe in each of the two states, while others invoke a gradient of polarity and hydration to explain experimental data.

In Interfaces and Interphases in Analytical Chemistry; Helburn, R., et al.;
ACS Symposium Series; American Chemical Society: Washington, DC, 2011.

3) the microenvironment examined by the probe appears to be heavily influenced by the structure of the probe itself and its concentration relative to that of the micelles.
4) some studies have concluded that water is found in the micellar core, but these assertions are sometimes linked to the use of an intrinsic probe in which a polarity sensing moiety is covalently bonded to some portion of the surfactant alkyl tail. Interpretation of these results relies on a model in which the alkyl tail, despite it's derivatization with a polar functional group, remains in the micellar core.
5) while studies disagree on the presence or absence of water in the core, there is little controversy over the assertion that water does solvate the head group region and perhaps the first several CH_2 groups attached to it, the extent of the penetration being perhaps somewhat dependent on the nature of the head group (i.e. cationic, anionic, non-ionic, or zwitterionic).

Linking these conclusions back to the images presented at the start of the chapter suggests that a mental morphing or composite of Figures 2, 3, 4, 5C, and 7 would produce an image of a micelle that would be most consistent with the computational and experimental results presented here. Such an image would include elements of the dynamic nature of the monomers, the 'rough' surface of micelles created by those dynamics, the presence of space between the head groups in which water and solutes reside, and the existence of a liquid-like interior of the micelle with alkyl chains that kink, bend, and periodically loop back towards the surface. Of course, one needs to keep in mind the earlier warnings that any static image will always be a snapshot of a single moment in the life of the micelle and that a holographic image or physical model is necessary to fully capture their the 3-D nature of micelles. Clearly, a 3-D image that with a fourth dimension, time, would yield closer approximations than any single static, 2-D picture.

Conclusion

Based on the above consideration of computational and experimental examinations of micelles, it seems reasonable to suggest that *the aqueous phase/micelle interface includes the two or three carbon atoms of the aliphatic chain nearest the head groups, the head groups themselves, and the counterions and water molecules associated with the head groups*. Such a definition also includes any terminal methyl groups that may loop back and interact with this region of the micelle. We carry this definition with us to the next chapter in which we consider two specific methods for characterizing the polarity and hydrogen bonding abilities of micelles and the influence these properties have on solute partitioning into micelles.

Acknowledgments

Many thanks go to Professor Christopher Dunlap and Professor Morteza Khaledi for their helpful suggestions in the preparation of this chapter. Acknowledgment is made to the Donors of the American Chemical Society Petroleum Research Fund for their support of this project.

References

1. Cline Love, L. J.; Habarta, J. G.; Dorsey, J. G. *Anal. Chem.* **1984**, *56*, 1132A–1148A.
2. Hinze, W. L. In *Solution Chemistry of Surfactants*; Mittal, K. L., Ed.; Plenum Press: New York, 1979; Vol. 1.
3. McIntire, G. L. *Crit. Rev. Anal. Chem.* **1990**, *21*, 257–278.
4. Pramauro, E.; Pelizzetti, E. In *Comprehensive Analytical Chemistry: Surfactants in Analytical Chemistry*; Weber, S. G., Ed.; Elsevier: Amsterdam, 1996; Vol. XXXI.
5. Pelizzetti, E.; Pramauro, E. *Anal. Chim. Acta* **1985**, *169*, 1–29.
6. *Chromatographic Science: Micellar Liquid Chromatography*; Berthod, A., Garcia-Alvarez-Coque, C., Eds.; Marcel Dekker, Inc.: New York, 2000; Vol. 83.
7. Pramauro, E.; Pelizzetti, E. In *Comprehensive Analytical Chemistry: Surfactants in Analytical Chemistry*; Weber, S. G., Ed.; Elsevier: Amsterdam, 1996; Vol. XXXI.
8. Khaledi, M. G.; Strasters, J. K.; Rogers, A. H.; Broyer, E. D. *Anal. Chem.* **1990**, *62*, 130–136.
9. Marina, M. L.; Jimenez, O.; Garcia, M. A.; Vera, S. *Microchem. J.* **1996**, *53*, 215–244.
10. McIntire, G. L. *Crit. Rev. Anal. Chem.* **1990**, *21*, 257–278.
11. Terabe, S.; Otsuka, K.; Ichikawa, K.; Tsuchiya, A; Ando, T. *Anal. Chem.* **1984**, *56*, 111–113.
12. Heiger, D. N. *High Performance Capillary Electrophoresis: An Introduction*; Publication No. 5968-9963E; Hewlett-Packard: Germany, 2000.
13. Menger, F. M. *Acc. Chem. Res.* **1979**, *12*, 111–117.
14. Atkins, P. W. *Physical Chemistry*, 4th ed.; W.H. Freeman and Company: New York, 1990; p 708.
15. Garde, S.; Yang, L.; Dordick, J. S.; Paulaitis, M. E. *Mol. Phys.* **2002**, *100*, 2299–2306.
16. McCarney, E. R.; Armstrong, B. D.; Kausik, R.; Han, S. *Langmuir* **2008**, *24*, 10062–10072.
17. Schuler, L. D.; Walde, P.; Luisi, P. L.; Van Gunsteren, W. F. *Eur. Biophys. J.* **2001**, *30*, 330–343.
18. Wennerström, H.; Lindman, B. *J. Phys. Chem.* **1979**, *83*, 2931–2932.
19. Kuhn, H.; Breitzke, B; Rehage, H. *Colloid Polym. Sci.* **1998**, *276*, 824–832.
20. Menger, F. M. *Acc. Chem. Res.* **1979**, *12*, 111–117.
21. Karaborni, S.; O'Connell, J. P. *Langmuir* **1990**, *6*, 905–911.
22. Karaborni, S.; O'Connell, J. P. *J. Phys. Chem.* **1990**, *94*, 2624–2631.

23. Shelley, J.; Watanabe, K.; Klein, M. L. *Electrochim. Acta* **1991**, *36*, 1729–1734.
24. Laaksonen, L.; Rosenholm, J. B. *Chem. Phys. Letters* **1993**, *216*, 429–434.
25. Kuhn, H.; Breitzke, B.; Rehage, H. *Colloid Polym. Sci.* **1998**, *276*, 824–832.
26. Kuhn, H.; Breitzke, B. *Prog. Colloid Polym. Sci.* **1998**, *111*, 158–161.
27. Kuhn, H.; Breitzke, B. *Ber. Bunsen-Ges. Phys. Chem.* **1997**, *101*, 1485–1492.
28. Kuhn, H.; Breitzke, B. *Ber. Bunsen-Ges. Phys. Chem.* **1997**, *101*, 1493–1500.
29. Bruce, C. D.; Senapati, S.; Berkowitz, M. L.; Perera, L.; Forbes, M. D. E. *J. Phys. Chem.* **2002**, *106*, 10902–10907.
30. Yoshii, N.; Okazaki, S. *J. Chem. Phys.* **2007**, *126*, 096101/1–096101/3.
31. Yoshii, N.; Okazaki, S. *Chem. Phys. Lett.* **2006**, *425*, 58–61.
32. Yoshii, N.; Okazaki, S. *Chem. Phys. Lett.* **2006**, *426*, 66–70.
33. Böcker, J.; Brickmann, J.; Bopp, P. *J. Phys. Chem.* **1994**, *98*, 712–717.
34. Pal, S.; Balasubramanian, S.; Bagchi, B. *J. Phys. Chem. B* **2005**, *109*, 12879–12890.
35. Wymore, T.; Goa, X. F.; Wong, T. C. *J. Mol. Struct.* **1999**, *485/486*, 195–210.
36. MacKerell, A. D., Jr. *J. Phys. Chem.* **1995**, *99*, 1846–1855.
37. Balasubramanian, S.; Bagchi, B. *J. Phys. Chem. B* **2001**, *105*, 12529–12533.
38. Balasubramanian, S.; Pal, S.; Bagchi, B. *Curr. Sci.* **2002**, *82*, 845–854.
39. Pal, S.; Balasubramanian, S.; Bagchi, B. *J. Chem. Phys.* **2004**, *120*, 1912–1920.
40. Pal, S.; Balasubramanian, S.; Bagchi, B. *J. Phys. Chem. B* **2003**, *107*, 5194–5202.
41. Balasubramanian, S.; Pal, S.; Bagchi, B. *Curr. Sci.* **2003**, *84*, 428–430.
42. Balasubramanian, S.; Bagchi, B. *J. Phys. Chem. B* **2002**, *106*, 3668–3672.
43. Muller, N.; Birkhahn, R. H. *J. Phys. Chem.* **1967**, *71*, 957–962.
44. Ulmlus, J.; Lindman, B. *J. Phys. Chem.* **1981**, *85*, 4131–4135.
45. Martens, F. M.; Verhoeven, J. W. *J. Phys. Chem.* **1981**, *85*, 1773–1777.
46. Casal, H. L. *J. Am. Chem. Soc.* **1988**, *110*, 5203–5205.
47. Cabane, B. *J. Phys.* **1981**, *42*, 847–859.
48. Tabony, J. *Mol. Phys.* **1984**, *51*, 975–989.
49. Podo, F.; Ray, A.; Némethy, G. *J. Am. Chem. Soc.* **1973**, *95*, 6164–6171.
50. Fendler, J. H.; Fendler, E. J.; Infante, G. A.; Shih, P. S.; Patterson, L. K. *J. Am. Chem. Soc.* **1975**, *97*, 89–95.
51. Das, S.; Bhirud, R. G.; Nayyar, N.; Narayan, K. S.; Kumar, V. V. *J. Phys. Chem.* **1992**, 7454–7457.
52. Halle, B.; Carlström, G. *J. Phys. Chem.* **1981**, *85*, 2142–2147.
53. Bravo, C.; García-Río, L.; Leis, J. R.; Peña, M. E.; Iglesias, E. *J. Colloid Interface Sci.* **1994**, *166*, 316–320.
54. Gruen, D. W. R. *J. Phys. Chem.* **1985**, *89*, 146–153.
55. Gruen, D. W. R. *J. Phys. Chem.* **1985**, *89*, 153–163.
56. McCarney, E. R.; Armstrong, B. D.; Kausik, R.; Han, S. *Langmuir* **2008**, *24*, 10062–10072.
57. Huang, J.; Bright, F. V. *Appl. Spectrosc.* **1992**, *46*, 329–339.
58. Mukerjee, P.; Cardinal, J. R. *J. Phys. Chem.* **1978**, *82*, 1620–1627.

59. Ganesh, K. N.; Mitra, P.; Balasubramanian, S. In Proceedings of the 4th International Symposium on Surfactants in Solution, Bordeaux, France, 1984, pp 599−611.
60. Sepulveda, L.; Lissi; Quina, F. *Adv. Colloid Interface Sci.* **1986**, *25*, 1–57.

Chapter 3

Characterizing the Micelle/Water and Vesicle/Water Interface Using Solvatochromism and Linear Solvation Energy Relationships

Mark F. Vitha*

Drake University, Department of Chemistry, Des Moines, Iowa 50311
***Mark.vitha@drake.edu**

In the previous chapter, we reviewed experimental and computational techniques used to study the properties of the micelle/aqueous phase interface. We concluded that the aqueous phase/micelle interface can generally be taken to be the region that includes the two or three carbon atoms of the aliphatic chains nearest the head groups, the head groups themselves, the counterions and water molecules associated with the head groups, and any terminal methyl groups that may loop back and interact with this region of the micelle. Having adopted this definition of the interface, in this chapter we focus on two specific ways to characterize the intermolecular interaction capability of the interfacial micellar region using small molecular probes. First we discuss studies based on the Kamlet-Taft solvatochromic scales and then focus on linear solvation energy relationships (LSERs). We chose to focus on these methods because they are general models that have been used to probe the interactions in numerous separation systems, not just micellar systems. So they have been tested and proven to yield useful information about the intermolecular forces governing a wide variety of partition processes. Additionally, a large number and variety of systems have been studied using these techniques, allowing for interesting comparisons between anionic, cationic, zwitterionic, and neutral surfactant micelles with different chain lengths and counterions.

In Interfaces and Interphases in Analytical Chemistry; Helburn, R., et al.;
ACS Symposium Series; American Chemical Society: Washington, DC, 2011.

Kamlet-Taft Solvatochromic Scales

In the late 1970's, Kamlet, Taft, and Abboud established three empirical scales of solvent strength based on the solvatochromic shifts of small organic molecules in pure solvents (*1–3*). These are the π*, α, and β scales of solvent dipolarity/polarizability, hydrogen bond (HB) donor strength (acidity), and HB acceptor strength (basicity), respectively. They have been used to correlate and explain hundreds of solvent dependent processes, ranging from partitioning in chromatography to the kinetics of organic reactions (*4*).

Solvatochromism is the term used to denote the effect that a molecule's chemical environment has on its spectroscopic properties, including shifts in the position on fluorescence and absorbance bands and the intensities of those bands. It arises from differential strengths of interaction of the ground and excited states of the molecule with it's surroundings. For example, consider a probe molecule that has a ground state with a smaller dipole moment than its excited state such as N,N-dimethyl-4-nitroaniline (Figure 1) (*2*).

In this case, polar solvents stabilize the probe's excited state more than the ground state. Furthermore, this stabilization is greater for more polar solvents compared to less polar solvents, as depicted in Figure 2. In a completely non-polar solvent, the energy of both the ground and excited stated states increases relative to their energies in a moderately polar solvent, with the excited state experiencing a *greater increase* than the ground state. The change in the energy difference, ΔE, leads to a change in the frequency of light absorbed as dictated by Planck's Law:

$$\Delta E = h\upsilon = \frac{hc}{\lambda} \qquad (1)$$

where h is Planck's constant, ν and λ are the frequency and wavelength of electromagnetic radiation, respectively, and c is the speed of light.

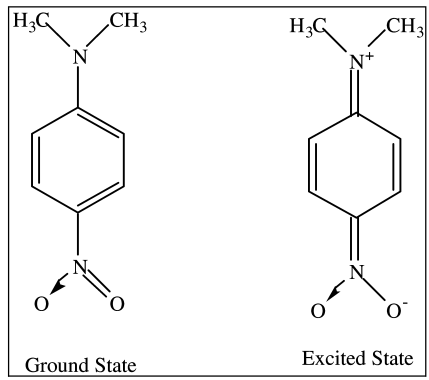

Figure 1. Depiction of the ground and excited states of N,N-dimethyl-4-nitroaniline (2).

In Interfaces and Interphases in Analytical Chemistry; Helburn, R., et al.;
ACS Symposium Series; American Chemical Society: Washington, DC, 2011.

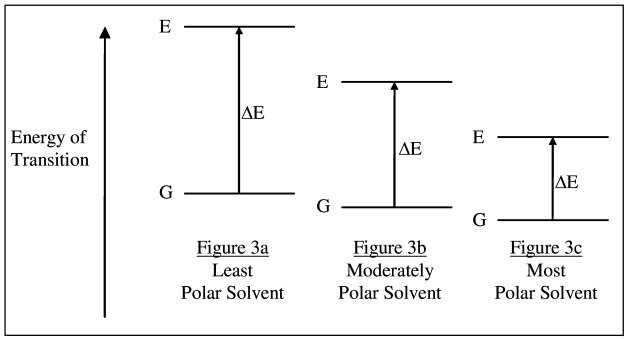

Figure 2. Depiction of the effect of solvent polarity on the ground and excited state energies of a probe with a more polar excited state than ground state such as N,N-dimethyl-4-nitroaniline.

The π* Scale

Working backwards from the discussion above, changes in the measured frequency of maximum absorbance of the probe thus reflect the polarity of the environment in which the probe resides. Kamlet and Taft used this as the basis of their π* scale of solvent polarity/polarizability. They chose cyclohexane and dimethylsulfoxide (DMSO) as solvents that represent extremes in polarity, assigning a π* value of 0.00 to cyclohexane and 1.00 to DMSO. The polarities of other solvents were ranked according to this scale. To determine the π* value of any other solvent, the frequency of maximum absorbance of a probe was measured in the solvent of interest, and the π* of the solvent calculated from the relationship:

$$\pi^* = \frac{\nu_{solvent} - \nu_{cyclohexane}}{\nu_{DMSO} - \nu_{cyclohexane}} \quad (2)$$

Wisely, Kamlet and Taft did not rely on a single probe molecule, as this could introduce probe-specific effects into their scales. Rather, they chose a larger number of probes, primarily nitroaromatic compounds, to establish their π* scale. Furthermore, because they wanted to measure only the dipolarity of the solvents, they selected probes which did not respond to the HB properties of the solvents at all, or only did so to a very small extent. Tabulated π* values for an individual solvent thus reflected the average π* value obtained with multiple probes.

The π* scale can be recast in the form

$$\nu_{i,j} = \nu_{o,j} + s_j \pi_i^* \quad (3)$$

where 'i' represents a solvent and 'j' represents a particular probe. The value of the parameter s_j is specific to each probe and is given by

$$s_j = \frac{\nu_{j,DMSO} - \nu_{j,cyclohexane}}{1.00 - 0.00} \quad (4)$$

In Interfaces and Interphases in Analytical Chemistry; Helburn, R., et al.;
ACS Symposium Series; American Chemical Society: Washington, DC, 2011.

In casting it this way, s_j is seen to be the sensitivity of the spectral shift of the probe to the dipolarity of the solvent. Larger values represent probes with larger solvatochromic shifts and thus are preferable in terms of yielding more easily measured differences in ν_{max} in solvents of different polarity. The parameter $\nu_{o,j}$ serves as an intercept term and can be thought to reflect the probe's ν_{max} in a completely non-interacting solvent (i.e., $\pi^* = 0.00$). Values for common organic solvents are provided in Table I for comparison to values obtained for micellar systems discussed below (*5*). For the common solvents, it is clear that the measured polarities are generally consistent with chemical intuition.

Space does not permit discussion of all of the precautions and careful consideration Kamlet and Taft embedded in the development of their scales, but these are discussed in the original work and elsewhere (*1–4*, *6*). Furthermore, it must be noted that while π^* was intended to be a pure dipolarity term, it was discovered that the probes also responded to polarizability effects, as illustrated by the fact that benzene, while lacking a permanent dipole, has a measured π^* value of 0.59 (*1*, *7*, *8*). A separate parameter, δ, was introduced to account for some of the 'excess' polarizability of aromatic and halogenated compounds and thus make them more consistent with aliphatic compounds. Because we are dealing largely with aliphatic surfactants in this chapter, we do not consider the δ parameter further.

The α and β Scales

Kamlet and Taft also defined scales of solvent HB donor acidity and acceptor basicity based on solvatochromic shifts (*2*, *3*). In order to isolate the portion of the shift due solely to hydrogen bonding, the effect of general dipole-dipole and dispersion interactions had to be subtracted from the total shift. To accomplish this, paired probes were used – one of which was susceptible to HB effects and one which was not. For example, 4-nitroaniline and N,N-diethyl-4-nitroaniline were used to measure solvent HB accepting ability (i.e, basicity). The ν_{max} values of the two probes were first measured in non-HB solvents and correlated with one another as follows;

$$\nu_{max,1} = s\nu_{max,2} + \text{intercept} \tag{5}$$

where s and the intercept are determined by linear regression. Then, to measure the HB accepting ability of solvents, ν_{max} for both probes were measured in the solvent of interest. The ν_{max} value for N,N-diethyl-4-nitroaniline, which only responds to dipolarity/polarizability effects, and the equation above were used to *predict* the ν_{max} value of 4-nitroaniline. This predicted value represents the shift that would arise solely based on dipolarity/polarizability effects. The difference between the theoretical ν_{max} value and that actually obtained in an HB accepting solvent, i.e., $\Delta\Delta\nu = \Delta\nu_{calculated} - \Delta\nu_{measured}$, was attributed to the HB ability of the solvent.

In Interfaces and Interphases in Analytical Chemistry; Helburn, R., et al.;
ACS Symposium Series; American Chemical Society: Washington, DC, 2011.

Table I. π* values of some common organic solvents

Solvent	*π**
diethylether	0.27
carbon tetrachloride	0.28
n-butanol	0.47
tetrahydrofuran	0.58
benzene	0.59
methanol	0.60
hexafluoroisopropanol	0.65
acetone	0.71
ethylbenzoate	0.74
acetonitrile	0.75
dimethylsulfoxide	1.00

As with the π* scale, reference solvents were selected to establish the scale. Hexamethylphosphoramide was chosen as a strong HB acceptor and assigned β = 1.00. All non-HB accepting solvents have β = 0.00. The ΔΔν value for the pair of probes discussed above in hexamethylphosphoramide was -2.80, so β was defined as

$$\beta = \frac{-\Delta\Delta\nu}{2.80} \tag{6}$$

which yields β = 1.00 for hexamethylphosphoramide and a value between 0.00 and 1.00 for most other HB accepting solvents. Again the authors did not rely on just a single pair of probes, but rather used a combination of five different measurements, three of which were based on spectroscopic shifts and two of which were based on thermodynamic measurements of HB complex formation constants.

The α-scale of solvent HB donating ability (i.e., acidity) was established in an analogous manner (i.e., use of paired probes – one sensitive to HB donating effects and one not, correlation of Δν values in non-HB donating solvents, prediction of Δν values for the probe sensitive to HB donating effects, measurement of actual Δν values in HB donor solvents, and calculation of ΔΔν). Methanol was selected as the reference solvent and was assigned an α-value of 1.00. Here again, multiple independent methods for measuring α-values were devised to reduce the potential for any probe-specific bias in the scale. Since their original publication, other methods for measuring α-values have been developed. For example, α can be determined using the probe ET-33 (structurally related to Reichardt's Dye) and the equation:

$$\mathrm{ET}(33) = \frac{28590}{\lambda} = 39.09 + 14.47\pi^* + 14.41\alpha \tag{7}$$

In Interfaces and Interphases in Analytical Chemistry; Helburn, R., et al.;
ACS Symposium Series; American Chemical Society: Washington, DC, 2011.

where λ is the wavelength of maximum absorbance of ET-33 in the solvent of interest and π* of the solvent is measured via the methods discussed above (*9*).

Using these methods, Kamlet, Taft, and Abboud established the four scales of solvent interaction strength. Continuous improvements and refinement took place in the years following their initial publications and hundreds of solvents were eventually characterized using their methods (*5*, *10*). As mentioned earlier, the solvent values have been used to correlate and explain hundreds of solvent-dependent processes ranging from organic reaction rates to solute partitioning between bulk phases (*4*).

Solvatochromic Parameters of Micelles

Two decades elapsed after the first Kamlet-Taft papers were published before their methodology was extended to quantify the interaction ability of common micellar systems. Specifically, Carr *et al.* measured π*, α, and β values for sodium dodecylsulfate (SDS) and dodecyltrimethylammonium bromide (DTAB) (*11–13*). While many other researchers had used general probes to characterize micellar systems, theirs were the first reports of separating polarity from hydrogen bonding effects. Clearly, this is an important distinction in trying to characterize micelles, particularly if the probes are relegated to the hydrated region that is capable of donating and accepting hydrogen bonds. Because all of the probes used by Kamlet and Taft have some polarity and many can form hydrogen bonds, they are certainly likely to reside the interfacial region. Additionally, it has been shown that no single probe can be used to characterize systems in which multiple interactions are possible, so an approach like that of Kamlet and Taft based on multiple probes is required (*14*).

A problem arises, however, in using spectroscopic probes to study micelles if the goal is to characterize the micelle *only*, and not the overall average properties of the micellar system (i.e., the bulk aqueous phase and the micellar microenvironment(s)). The problem is that the small, polar probes used by Kamlet and Taft partition between the micellar and bulk aqueous phases, and each probe partitions differently. Thus, spectra of the micellar solutions reflect an average environment, not the micelle environment *per se*, and the average is weighted by the probe's affinity for the micelles and the ratio of aqueous to micellar volumes. To get just the spectrum of the probe in the micelle itself requires knowledge of the partition coefficient of the probe, which is generally difficult to measure. If that is known, however, and the spectrum of the probe in pure water is known, then it is theoretically possible to subtract the component of the overall spectrum arising from the probe in the aqueous phase from the spectrum obtained in the micellar solution and thereby obtain the spectrum in just the micellar phase, if some approximation of the volume of the micellar phase can be made.

Given the difficulty and typical variability of measuring partition coefficients, Carr *et al.* did not take this approach. Instead, they used chemometrics to obtain the desired spectra of the Kamlet-Taft probes in the micellar phase free from contributions in the aqueous phase. Space does not permit a description of the chemometric approach but it can be found in the literature (*12*). The fact that

In Interfaces and Interphases in Analytical Chemistry; Helburn, R., et al.;
ACS Symposium Series; American Chemical Society: Washington, DC, 2011.

the data were resolved so as to obtain the spectra of the indicators in the micelle free from aqueous phase contributions separates the work from that of many others. In this way, the chemical environment of the probes inside the micelle was characterized. Their results are shown in Table II. Values for common organic solvents for comparison are shown in Table III (*5*). It is also worth mentioning that the curve deconvolution method employed by Carr *et al.* not only produced the spectra of the probe in the micellar environment, but it also provided chemically reasonable estimates of the probe's partition coefficient between the aqueous and micellar phases (*11–13*).

While the results in Table II show some probe dependence, it is clear that the micelles are quite polar, very strong HB donors, and reasonably strong HB acceptors. This is reinforced by comparison to the π^*, α, and β values of common organic solvents like dimethylsulfoxide, methanol, ethylbenzoate, and acetonitrile. While this general impression is important, looking more carefully at some of the results is also illuminating. For example, the average HB donating ability (α) of SDS is 0.87. This is remarkably high considering that SDS monomers have no inherent HB donating sites. Keeping in mind that the contributions from the probe free in solution were subtracted from the spectra, this result must arise from the probes' interactions with water associated with the interfacial region of the micelle. In a related manner, DTAB was found to have significant HB accepting and donating ability ($\alpha = 0.70$ and $\beta = 0.48$). The donating ability may arise from a Lewis acid type interaction with HB basic probes interacting with the ammonium head group, but more likely reflects interactions with associated water molecules. Furthermore, even though DTAB monomers lack recognizable HB accepting sites, the DTAB micelles have a β-value that exceeds that of water measured with the same probe and which is comparable to those of acetone and tetrahydrofuran. It is reasonable to suggest that this result arises from a combination of interactions with water and the bromide ions in the interfacial region.

Fuguet, *et al.* also used the Kamlet-Taft approach to characterize SDS micelles (*15*). They used several of the same or comparable probes as Carr *et al.* to compare the interaction ability of micelles made in water with those made in a pH = 7 phosphate buffer commonly used in micellar electrokinetic capillary chromatography. It is noteworthy that these authors obtained the spectra of the probes in the micelle free from contributions in the aqueous phase by determining the CMC, phase ratio, and partition coefficients of the probes. Despite using dramatically different methods for obtaining the spectra of the probes in the micelle phase only, the π^* and α values obtained by this group agree quite well with those of Carr and coworkers. Specifically, Carr *et al.* obtained $\pi^* = 1.06$ and $\alpha = 0.87$ compared to $\pi^* = 1.02$ and $\alpha = 0.79$ from Fuguet *et al.* The β values were different ($\beta_{Carr} = 0.40$, $\beta_{Fuguet} = 0.62$), but as the authors discuss, this difference likely arises from the use of different methods for calculating β-values. The authors also report that the presence of the phosphate buffer, while fairly dramatically suppressing the CMC, has virtually no effect on the π^*, α, and β values of the micelles, suggesting that the probes in the micelles do not sense or are not affected by the ions in the buffer.

Fuguet *et al.* extended their analysis to other surfactant systems using the same approach (*16*). Their results are shown in Table IV.

In Interfaces and Interphases in Analytical Chemistry; Helburn, R., et al.;
ACS Symposium Series; American Chemical Society: Washington, DC, 2011.

Table II. π*, α, and β values for SDS and DTAB micelles compared to water measured with several indicators

Indicator[a]	π^*_{SDS}	π^*_{DTAB}	π^*_{water}
NNDEA	1.15	1.04	1.34
PENB	1.00	0.99	1.20
PNA	1.04	1.02	1.08
average	1.06	1.02	1.21
	α_{SDS}	α_{SDS}	α_{water}
Et(33)	0.736	0.602	0.947
$Fe(LL)_2(CN)_2$	1.010	0.798	1.099
average	0.873	0.700	1.023
	β_{SDS}	β_{SDS}	β_{water}
PNP	N/A	0.561	0.463
4NA	0.401	0.410	0.113
average	0.401	0.486	0.288

[a] NNDEA = N,N-diethyl-4-nitroaniline, PENB = 4-ethylnitrobenzene, PNA = 4-nitroanisole, Et(33) = 2,6,-dichloro-*p*-(2,4,6,-triphenyl-N-pyridino)phenolate, $Fe(LL)_2(CN)_2$ = bis[α-(2-pyridyl)benzylidine-3,4-dimethylaniline]-bis(cyano)iron(II), PNP = 4-nitrophenol, 4NA = 4-nitroaniline.

The authors note the good agreement between their values for HTAB and those obtained by Carr *et al.* for DTAB discussed above, acknowledging that minor differences can be explained by the different alkyl chain lengths of the two surfactants (*16*). More importantly, by examining a broader range of surfactants, it is clear that different micelles have very different blends of interaction ability. In particular, sodium cholate has a much lower dipolarity/polarizability, somewhat higher HB donating ability, and much higher HB accepting ability relative to the other systems. We caution that α and β are both derived from just one probe for each parameter and may therefore not be entirely representative of average interactions of the micelles with a range of polar solutes, but nonetheless, the results are intriguing.

The results have implications for using micelles and their unique interfacial properties in analytical systems. For example, as discussed below, different interactions will result in different selectivities when the surfactants are used in micellar liquid chromatography or electrokinetic separations. Additionally, it shows that important chemical differences exist that are relevant when trying to use micelles as simple models of lipid bilayers or for predicting octanol/water partition coefficients of relevance to pharmaceutical studies. Studies such as these are critical because they go beyond general 'polarity scales' and try to more finely distinguish the specific intermolecular interaction capabilities that dictate the overall chemical behavior of different systems.

In Interfaces and Interphases in Analytical Chemistry; Helburn, R., et al.;
ACS Symposium Series; American Chemical Society: Washington, DC, 2011.

Table III. π*, α, and β values of SDS and DTAB micelles compared to some common solvents

Solvent	*π**	*α*	*β*
SDS[a]	1.06	0.87	0.40
DTAB[a]	1.02	0.70	0.49
water[a]	1.21	1.02	0.29
methanol	0.60	0.93	0.62
n-butanol	0.47	0.79	0.88
hexafluoroisopropanol	0.65	1.96	0.00
acetone	0.71	0.08	0.48
dimethylsulfoxide	1.00	0.00	0.76
ethylbenzoate	0.74	0.00	0.41
tetrahydrofuran	0.58	0.00	0.55
acetonitrile	0.75	0.19	0.31

[a] Values from previous table.

Table IV. π*, α, and β values of sodium cholate (SC), lithium perfluoro-*n*-octanesulfonate (LiPFOS), *n*-hexadecylammonium bromide (HTAB), and sodium dodecylsulfate (SDS)

	SC	*LiPFOS*	*HTAB*	*SDS*
π*	0.49	1.11	0.96	1.01
α	1.20	1.02	0.62	0.82
β	0.96	0.45	0.47	0.63

These solvatochromic measurements, as well as the linear energy relationships discussed at length below, demonstrate that the chemical environment inside DTAB and SDS micelles is greatly influenced by the water associated with the micelles. To arrive at this conclusion, it is also necessary to assert that all of the probes are located in a highly hydrated region of the micelle. But as discussed above, this is not controversial given the polar nature of the probes. The individual results obtained with each probe suggests that the *exact* location of the probes may differ, but the results suggest loci of solubilization that are generally similar for all of the probes.

Handa, Nakagaki, and Myajima use methylene blue and Reichardt's dye to measure π* and α of sodium tetradecylsulfate (STS) and heptaethylene glycol monododeyl ether (HED) (*17*). Values are shown in Table V.

Table V. π* values of sodium tetradecylsulfate (STS) and heptaethylene glycol monododecyl ether (HED) measured using methylene blue and Reichardt's dye

	STS	*HED*
π*	1.10	0.90
α	0.65	0.56

Table VI. π*, α, and β values of sodium dodecyl sulfate (SDS), cetyltrimethylammonium bromide (CTAB), and TritonX-100 micelles

	SDS	*CTAB*	*Triton X-100*
π*	1.14	0.87	1.06
α	0.52	0.68	0.56
β	0.70	0.53	0.71

The π* value of STS is in good agreement with that for SDS discussed above. The α-value for STS is slightly lower than those for SDS above, but it is in line with the value obtained using Et(33) (α = 0.736), which is structurally related to Reichardt's dye. Compared to STS, HED is slightly less polar and a slightly weaker HB donor. The latter result is interesting given that the ethylene glycol group has explicit HB donor sites on it, whereas SDS does not.

Bagchi *et al.* have used shifts in the wavelength of maximum fluorescence of seven ketocyanine probes to measure π*, α, and β for several micellar systems (*18–20*). As the authors point out (*18*), trends in their values, shown in Table VI, are in general agreement with the results of Carr *et al.* and Fuguet *et al.* discussed above. However, the absolute values are different in some cases. The biggest differences are observed for π* values, with those of Bagchi *et al.* being considerably lower than those reported by the other two groups.

When analyzing shifts in fluorescence wavelength maxima, it must be kept in mind that solvent reorganization around the excited state of the probe can occur prior to the emission of electromagnetic radiation. This reorganization optimizes intermolecular interactions and reduces the overall energy of the system. Thus, the fluorescence emission really reports on the environment of the probe's partially relaxed excited state, rather than the lowest energy configuration of the system reflected in absorbance measurements. Furthermore, the relaxation may occur to different extents in the aqueous phase relative to the micellar phase. It is unclear that the data treatment used to analyze the fluorescence spectra, which naturally include components of the probe in both phases, separates out the potentially different extents of relaxation prior to fluorescence. These effects make fluorescence solvatochromism more difficult to employ than absorbance measurements for determining π*, α, and β values, and in the end, rigorously only allow statements to be made about the probe's relaxed (or partially relaxed)

In Interfaces and Interphases in Analytical Chemistry; Helburn, R., et al.;
ACS Symposium Series; American Chemical Society: Washington, DC, 2011.

excited state environment, which may not directly reflect its environment in the ground state with regards to the strength of intermolecular interactions.

Bagchi *et al.* extended their work to the analysis of SDS micelles modified with poly-N-vinyl pyrrolidin-2-one and found an increase in π* and decreases in α and β upon addition of the polymer (*19*). They have also recently measured π* and α of mixed micelles of SDS and Triton X-100 (*20*). It is worth noting that using the large, non-polar probe pyrene led to π* values of 0.52 and 0.72 for SDS and Triton X-100, respectively, compared to values around 1.00 for SDS reported above by other groups using polar absorption probes. Bagchi *et al.* note that this could result from a different locus of solubilization for pyrene compared to polar molecules, but they also note that the value is consistent with their values obtained with polar fluorescent probes. This suggests that the similarity of results for fluorescence and their discrepancy with those determined from absorbance values relates more to the fundamental measurement (emission compared to excitation) than to the solute location inside the micelle. Regardless of exact agreement or not, it should be noted that even though pyrene is completely nonpolar, it is still reporting a quite polar environment, comparable to that of bulk propanol. This suggests that pyrene is not surrounded by an alkane environment but rather exists predominantly in the interfacial region of the micelles.

Helburn *et al.* synthesized long alkyl chain analogs of N,N-dialkyl-p-nitroaniline π* indicators and compared their behavior to that of the dimethyl and diethyl analogs used by Kamlet and Taft in their original studies (*21*). In the same publication, they reported on their use of these probes to measure π* of SDS and Triton X-114 solutions. They found that increasing the alkyl chain length of the probe from 1-3 carbon atoms slightly decreased the π* values (from approximately 1.27 to 1.15), suggesting that the longer chains help 'pull' the probe into the less polar region of the micelle. However, the spectra were not deconvolved to subtract out contributions arising from the probe in the aqueous phase, so this result may simply reflect the increased partitioning of the longer chain probes into the micelle (i.e., less contribution to the spectra from probe molecules residing in the bulk aqueous phase). Interestingly, they found that for chain lengths of five and six carbon atoms, the spectral shifts more closely resemble that of the probe with only methyl groups. The authors rationalize this by proposing incomplete incorporation of the probe into the micelle with much of it "left hanging outside the micelle" (*21*). Conversely, in the larger Triton X-114 micelles, they find that the analogs with four to six carbons chains exhibit the largest solvatochromic shifts. The authors use spectral shifts and band widths to propose different overall distributions for the probes in the micellar solutions depending on their degree of hydrophobicity.

El Seoud *et al.* used solvatochromic shifts of relatively large polyaromatic probes to investigate the polarities of micelles of general structure $C_{12}H_{15}NR_3Br$ where R = methyl, ethyl, -propyl, and *n* -butyl groups (*22*). They found that polarities of micelles depend on the length of R, the probe structure, and the probe charge. They used NMR to conclude that decreasing polarities associated with increasing R were the result of decreasing hydration rather than increased depth of penetration of the probes into the micelle interiors. Interestingly and importantly, the authors also show that even for the very large and generally hydrophobic probes

employed in the study, partitioning of the probes out of the aqueous phase and into the micellar phase is incomplete at low surfactant concentrations. This means that spectra collected under these conditions will reflect a blend of the probe in the two environments, hence requiring some kind of deconvolution in order to use the probe to study just the micellar environment as discussed above in relation to the work of Carr *et al.* and Fuguet *et al.*

When using pyridium-N-phenolate polarity probes, the work of Reichardt *et al.* must be strongly considered (*23*, *24*). They investigated 127 micellar systems in which the micelles, probes, and nature of the added electrolytes were varied. The authors demonstrate unexpected solvatochromic shifts that result from structural changes in cationic micelles resulting from the addition of organic electrolytes such as n-alkylsulfonate and tosylate salts. Specifically, instead of observing expected red shifts, indicating decreasing polarity of the micelles, blue shifts were observed. These were interpreted as resulting from a dislocation of the probes from the micelle interior towards the outlying areas as the electrolytes induced sphere-to-rod or sphere-to-wormlike transitions in the micellar shapes. While the manuscript details the dependence of these effects on the probe structure and the nature of the electrolytes, it is sufficient here to note simply that their work serves as a caution that the behavior of the observed wavelength of maximum absorbance of a probe is not straightforward and that the nature of the micellar structure under consideration, as well as the probe location within or around the structure, must be carefully considered before correct interpretations can be made.

Related to the notion of probe location, it is similarly important to consider the work of Karukstis *et al.* (*25*) when interpreting spectral data obtained in micellar systems. The authors use multiple Gaussian curves to deconvolve fluorescence spectra of Prodan into various components which presumably relate to the probe in different chemical environments in cationic, anionic, zwitterionic, and non-ionic micelles. In SDS, regardless of concentration from 0-18 mM surfactant, just a single Gaussian curve was needed. In the presence of 0.050 M sodium chloride, however, two Gaussian curves were needed. In cationic C_nTAB (where n = 12, 14, 16, or 18), four Gaussian curves were required to fit the emission curve. Two or three curves were required to deconvolve Prodan spectra in lauryldimethylamine oxide micelles (depending on solution pH), and two Gaussian curves were required for $C_{12}E_8$ and $C_{14}E_8$ systems (where E_8 = $-(OCH_2CH_2)_8-OH$). The authors then associate the peak emission wavelengths of each curve with various locations of the probe within the solution including 1) free in solution, 2) associated with the micelle surface via nonspecific dipolar interactions, 3) associated with the head group through specific cation-quadrupole π interactions, and 4) incorporation into the relatively nonpolar core via dispersion interactions. The area under the Gaussian curve representing the micellar surface component accounted for more than seventy percent of the total area under the emission curve for all but two systems ($C_{18}TAB$, 52%, $C_{16}TAB$, 56%). Thus, on average, Prodan largely reflects the surface/interface properties of the micelles. This illustrates that it is necessary to consider the fact that a probe may be located in different regions in different micelles, and that this needs to be taken

into account when interpreting non-deconvolved spectra, be they emission or absorbance measurements.

Space does not permit a review of the literally hundreds of other studies that use solvatochromic shifts in absorbance and emission spectra to characterize micelles. We have focused on those above because unlike many of the other studies that lead to *general* statements about the overall polarity of the micelle environment or of the micellar solution, these studies have tried to differentiate and *quantify* the *specific* intermolecular interactions (e.g., HB donating, HB accepting, dipole-dipole) that solutes experience in the interfacial region. Furthermore, these studies have used several probes that are well characterized in terms of their response to the interaction ability of their chemical environment. The use of multiple probes is beneficial as it reduces the chance that probe-specific bias is introduced into the data, thereby making extrapolations to other solutes more reasonable. The limitation of the studies above is that they generally used polar solutes. Therefore, the results mainly characterize the interfacial region of the micelle. However, as discussed in the previous sections of this chapter and also in the work involving pyrene as a probe, even nonpolar solutes may reside in the interfacial region. Thus, the information gained using polar probes may also apply to nonpolar solutes interacting with micelles.

Linear Solvation Energy Relationships

Linear solvation energy relationships (LSERs) have been used extensively as a complement to direct solvatochromic measurements to characterize the micelle/aqueous interface. Currently, the most commonly used formulation of the fundamental LSER equation is

$$SP = c + eE + sS + aA + bB + vV \quad (8)$$

where SP is a free energy related term for a particular solute (e.g., solubility or logarithm of a partition coefficient) and the solute descriptors E, S, A, B, and V are measures of the solute's excess molar refraction, dipolarity/polarizability, hydrogen bond (HB) acidity, HB basicity, and McGowan volume, respectively. The coefficients c, e, s, a, b, and v are determined by linear regression after measuring a series of SP values for a wide range of solutes with known descriptors. We will focus on applications of LSERs to solute partitioning between two phases. The coefficients, therefore, represent the sensitivity of SP to the various solutes' abilities to interact through various intermolecular forces. Additionally, they can be viewed as representing *differences in the complementary solvent properties*. For example, B is a measure of solute HB basicity (accepting ability), therefore the coefficient $b = m(A_1\text{-}A_2)$ where A_1 and A_2 are the hydrogen bond acidity (donating ability) of the two solvents and m is a proportionality constant. To be more specific, suppose SP is logk data for a chromatographic separation, where k is the retention factor of solutes based on the equilibrium A_{mob} Û A_{stat} and an LSER is generated by the methodologies described. Further imagine that the b-coefficient is found to be large and negative. This means that solutes with stronger HB accepting ability (larger B values) would have smaller logk

In Interfaces and Interphases in Analytical Chemistry; Helburn, R., et al.;
ACS Symposium Series; American Chemical Society: Washington, DC, 2011.

values and hence be less retained than solutes with weaker HB accepting ability, all else being equal. From this, it can be concluded that the mobile phase must be a stronger hydrogen bond donor than the stationary phase, as is typical for reversed-phase systems where water is a primary component of the mobile phase. *The magnitude of the coefficient indicates just how different the two phases are in this regard*. In this way, by judiciously selecting a range of solutes that span a range in the types and strength of intermolecular interactions in which they participate, quantitative information about the properties and chemical behavior of the *two bulk phases* between which the solutes partition can be obtained.

As another example, consider a situation in which the a-coefficient is found to be very small, or statistically equal to zero. Because this is the coefficient of solute HB acidity, this result would mean that the hydrogen bond basicity of the two solvents are essentially identical. It does not necessarily mean that hydrogen bonds do not occur between the solutes and the solvents, just that it occurs with approximately equal strength in both phases and therefore does not make a net contribution to the overall free energy of the process being explored. Again information is gained about the intermolecular interactions controlling the process and about the two phases relative to one another.

The vV term is included in the LSER to model the energetics of cavity formation. In order for a solute to partition into a phase, a cavity the size of the solute must be created. Solutes will favor partitioning into a phase in which the cavity is more easily created, all else being equal (i.e., assuming equal strength and types of intermolecular interactions). Thus, the vV term represents, at least in part, differences in the cohesivity of the solvents between which the solutes are partitioning.

In this way, LSERs have been used to explore the intermolecular interactions governing reversed phase liquid chromatography, micellar electrokinetic capillary chromatography (MEKC) and micellar liquid chromatography (MLC) (*26*).

Linear Solvation Energy Relationships of Micelle Systems – SDS

Some of the earliest LSERs related to solute partitioning in micellar systems appeared in 1995. Abraham *et al.* reported the following LSER for the partitioning of 132 polar and nonpolar compounds between water and SDS (*27*):

$$\log K = 1.201 + 0.542E - 0.400S - 0.133A - 1.580B + 2.793V \quad (9)$$
$$n = 132 \qquad r = 0.985 \qquad s.d. = 0.17 \qquad F = 817$$

Values of solute partition coefficients, K, were obtained from multiple literature sources. The fact that the LSER describes the behavior of both polar and nonpolar solutes suggests similar loci of solubilization within the micelle. (Note: the original report uses an older solute parameter set and notation, but for ease of comparison, the most recent widely used parameter notation will be used throughout this section of the chapter).

Quina *et al.* also used literature partition coefficients to publish an SDS LSER in 1995 (*28*), and found

$$\log K = -0.62 + 0.32E - 0.57S - 0.08A - 1.84B + 3.25V \quad (10)$$
$$n = 66 \qquad r = 0.989 \qquad s.d. = 0.13 \qquad F = 575$$

Lastly, Khaledi and Yang reported an initial SDS LSER in 1995 based on MEKC retention factors (k) (*29*), which was later updated by Khaledi and Trone (*30*), finding

$$\text{Log } k = -1.86 + 0.24E - 0.30S - 0.18A - 1.85B + 2.98V \quad (11)$$
$$n = 36 \qquad r^2 = 0.987 \qquad s.d. = 0.05$$

Despite some variation in the coefficients, which can likely be ascribed to the use of different solute parameter sets, different solutes, and different methods of measurement, the chemical interpretation of all three LSERs is virtually identical. The large positive magnitude of the v-coefficient indicates that the larger a solute is, the more it partitions out of the aqueous phase and into the micellar phase. This can be seen largely as a manifestation of the hydrophobic effect and is in line with chemical intuition. The energetic cost of creating a cavity large enough to accommodate the solute is smaller in the micellar phase than in the aqueous phase, due partly to the disruption of the hydrogen bond network in the aqueous phase. Larger solutes also tend to be more polarizable, so dipole-induced dipole and London dispersion forces are also embedded in the v-coefficient. The net results show that larger solutes will partition into the micelle phase to a greater extent, all else being equal.

In order to understand the chemical insights about the nature of the micellar environment provided by the other coefficients, it is useful to compare the SDS/water LSERs to the LSER for water-to-hexadecane transfer ($\log K_{C16}$) (*27*):

$$\text{Log } K_{C16} = 0.087 + 0.667E - 1.617S - 3.587A - 4.869B + 4.433V \quad (12)$$

In the SDS LSERs, the magnitude of the b-coefficient (~ 1.6 to 1.8) is much smaller than in the hexadecane LSER (~ 4.9). If the solutes were partitioning into a non-hydrogen bond donating region within the micelle, the LSER coefficients for the water/SDS transfer would be much more similar to those of the water/C16 transfer. Keeping in mind that the coefficients reflect differences in the solvent property that is complementary to the solute property, from the large differences in b-coefficients in the SDS and C16 systems it can be concluded that SDS is more similar to water in its hydrogen bond donating ability than is hexadecane. This is not entirely surprising given that hexadecane and water are considerably different in their hydrogen bond donating ability. However, given that SDS has no inherent HB donating sites, this result suggests that the solutes are still interacting with water to a large extent even when partitioned into the micelle. In other words, the water associated with the micelle interface is playing a critical role in determining the chemical properties of the micelles and how solutes interact with them. This same conclusion was drawn above from the direct solvatochromic measurement of $\alpha = 0.87$ for SDS. So the solvatochromic data and the LSERs are consistent in

In Interfaces and Interphases in Analytical Chemistry; Helburn, R., et al.;
ACS Symposium Series; American Chemical Society: Washington, DC, 2011.

that they measure a considerable ability of SDS micelles to act as HB donors even though SDS monomers *per se* have no explicit hydrogen donating sites.

A comparable situation arises when analyzing the coefficient of solute HB acidity (A). In all of the SDS LSERs, the a-coefficient is very close to zero, indicating that SDS and water are nearly equal in the strength of their hydrogen bond accepting ability. In contrast, the coefficient is -3.59 for water-to-hexadecane solute transfer, suggesting a large difference in the ability of hexadecane to donate hydrogen bonds, completely consistent with what is known about the intermolecular interactions that occur in water and alkanes. The fact that SDS and water are comparable in their HB accepting ability is supported by the direct solvatochromic measurements detailed above, which in one case, even suggests that SDS is a stronger HB acceptor than is water (*11*). Direct measurements of solvent HB accepting strengths are complicated by the fact that they are dependent on the methodology used (*31*). Water, in particular, seems to respond differently than other HB acceptors and thereby complicates interpretations of solvent HB basicity (*32*). Nevertheless, the solvatochromic measurements and the LSER results are in close qualitative agreement that SDS micelles and water are comparable in their HB accepting ability. As with the interpretation of the b-coefficient, this indicates that the solutes are residing in an environment where they are interacting with either water or the sulfate head group, or both. In other words, if one accepts the view presented in the previous chapter that water is present mainly in the head group and near the first few carbon atoms of the alkyl chain, then the micellar interfacial region again seems to dominate the partition process.

As was the case for the a- and b-coefficients, the s-coefficient is much smaller in magnitude for the SDS LSER than for the hexadecane LSER, indicating that SDS micelles are much more similar to water in their interaction with polar/polarizable solutes than is hexadecane. Here again, if the solutes were partitioning into a nonpolar alkane-like environment in the micelles, one would expect the s-coefficients to be comparable in both systems. This is not the case, thus reinforcing the conclusion that solutes are partitioning into a polar environment inside the micelle. The fact that the behavior of polar and nonpolar solutes is described by a single LSER suggests that nonpolar solutes are residing in the same chemical environment as polar solutes inside the micelles. It should be noted, however, that Vitha and Carr found systematic deviations for some solutes in a series of sodium alkyl sulfate systems. Possible explanations for these deviations are discussed in their work (*33*).

The e-coefficient is more difficult to interpret. The solute descriptor, E, was introduced to account for dispersion and dipole-induced dipole interactions arising from very polarizable solutes (e.g., halogenated and aromatic compounds, or more broadly, compounds with π- and n-electron pairs). However, polarizability effects are also embedded in the vV and sS terms, making it difficult to assign specific meaning to the eE term. But from the LSER, it can be generally stated that solutes with larger E values demonstrate increased partitioning into the micellar environment as dictated by the positive sign of the coefficient, comparable to the behavior discussed above for the vV term.

In Interfaces and Interphases in Analytical Chemistry; Helburn, R., et al.;
ACS Symposium Series; American Chemical Society: Washington, DC, 2011.

Poole and Poole gathered literature LSERs for SDS from multiple publications, each determined using MEKC but with different SDS concentrations and different buffer additives and compositions (*34*, *35*). They found no trends as a function of experimental conditions. There were some statistically significant differences between some individual LSERs, but Poole and Poole attribute a significant portion of the variation to poor statistical design of some studies arising from poor solute selection. Despite the few differences, most of the LSERs are generally quite similar, suggesting that the aqueous phase composition does not significantly alter the properties of the micelle or the overall strength and blend of intermolecular interactions governing the energetics of solute partitioning. This is demonstrated by the fact that they are able to combine the data from multiple studies and produce one global SDS LSER by incorporating an 'indicator variable' (either a value of either 1 or 0) for each data set used in the overall regression (*35*). Their global LSER carries the exact same chemical interpretation as presented above with regarding the ability of SDS to interact through various intermolecular forces.

In general, then, LSERs – particularly comparisons between LSERs for different systems – can be used to gain insight into the chemical interactions driving the partitioning of solutes between aqueous and micellar phases. Analytically, this provides important understanding when using micelles to achieve separations using MEKC or MLC. Furthermore, the interpretation of the LSERs supports the direct solvatochromic measurements of the interfacial properties of SDS micelles.

Other Anionic Surfactants

Understanding the interactions that give rise to separations, and hence selectivity, is important as it helps guide selection of pseudostationary phases that will best separate a given set of solutes. The larger the magnitude of a coefficient, the more a small difference in the corresponding solute property could lead to a large difference in log k and hence elution times for two similar solutes. Furthermore, understanding the factors that control retention when using a number of different types of pseudostationary phases (anionic, cationic, and nonionic) can help optimize the selection of particular surfactants for specific separations. It is therefore instructive to look at LSERs of a number of other systems and compare them to each other, and to SDS because it is one of the most commonly used MEKC surfactants. Such comparisons are in the sections that follow, first focusing on additional anionic surfactants, then cationic and nonionic systems.

Sodium Alkyl Sulfate

Vitha and Carr studied the dependence of the LSER coefficients on the alkyl chain length for sodium alkyl sulfate micelles. They found that increasing the length from eight to twelve carbon atoms had very little effect on the coefficients, indicating that increasing the hydrophobic portion of the surfactant does not dramatically change the location of the solutes inside the micelles (*33*).

In Interfaces and Interphases in Analytical Chemistry; Helburn, R., et al.;
ACS Symposium Series; American Chemical Society: Washington, DC, 2011.

Lithium Dodecyl Sulfate (LDS) and Lithium Perfluorooctanesulfonate

Fuguet *et al.* reported on lithium dodecyl sulfate (LDS) and found the following LSER (*36*):

$$\text{Log } k = -1.78 + 0.36E - 0.43S - 0.20A - 1.54B + 2.81V \quad (13)$$
$$n = 40 \qquad r = 0.988 \qquad \text{s.d.} = 0.09 \qquad F = 344$$

These coefficients are quite similar to those for SDS and show that there is little difference between Na^+ and Li^+ in their influence on solute partitioning.

Fuguet *et al.* also studied mixed micelles of LDS and lithium perfluorooctane sulfonate (LPFOS). The normalized LSER coefficients are shown in Figure 3.

The results indicate that the addition of LPFOS to LDS 1) makes it energetically more difficult to create a cavity in the micelles, 2) decreases the interaction with polarizable molecules, and 3) increases the polarity, 4) decreases the HB accepting ability, and 5) increases the HB donating ability of the micelles. Thus, by adjusting the mole ratio of LDS to LPFOS, the system can be tuned to achieve different selectivity as illustrated by the authors in Figure 4.

Yang and Khaledi published an LSER for LPFOS in 1995 (*29*), which was revised in a later publication (*37*). Fuguet *et al.* also published on the same system. The LSERs for both groups are in Table VII. Uncertainties in the coefficients are presented in parentheses.

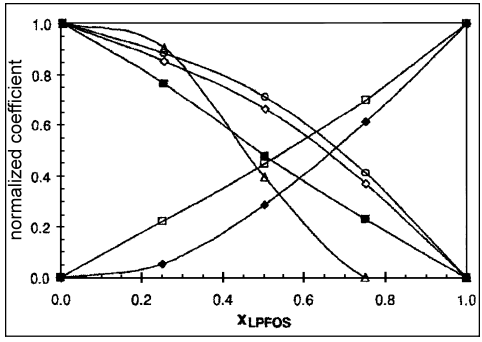

Figure 3. Plot of the normalized LSER coefficients for lithium dodecyl sulfate and lithium perfluorooctanesulfonate (LPFOS) mixed micellar systems as a function of mole fraction. (△) c; (◊) r; (♦) s; (■) a; (□) b; (○) v. Reprinted from J. Chromatogr. A, vol. 907, Fuguet, E., Ràfols, C., Bosch, E., Rosés, M., Abraham, M.H. "Solute-solvent interactions in micellar electrokinetic chromatography: selectivity of lithium dodecylsulfate – lithium perfluorooctanoate mixed micellar buffers" pp. 257-265. Copyright 2001, with permission from Elsevier.

Table VII. LSER coefficients (values of s.d. below in parentheses) for lithium perfluorooctane sulfonate from two literature reports

	c	*e*	*s*	*a*	*b*	*v*	*r*	*n*	*s.d.*	*F*
Yang & Khaledi	-2.05 (0.11)	-0.54 (0.08)	0.48 (0.11)	-0.89 (0.07)	-0.60 (0.12)	2.28 (0.12)	0.979	47	0.10	189
Fuguet *et al.*	-1.90 (0.08)	-0.25 (0.09)	0.00 (0.07)	-0.92 (0.06)	0.00 (0.11)	2.20 (0.08)	0.990	40	0.09	281

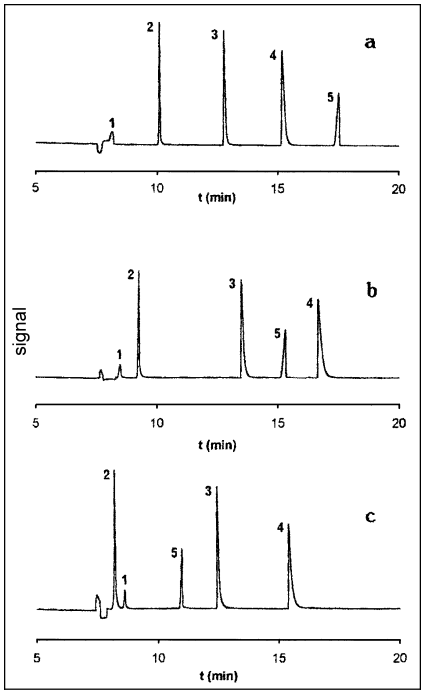

Figure 4. Separation of a test mixture by MEKC in a lithium phosphate buffer, pH 7.00, 25oC, 30 kV, and 80 cm capillary effective length using (a) 40 10-3 mol/L LDS; (b) 20 10-3 mol/L LDS + 20 10-3 mol/L LPFOS; (c) 40 10-3 mol/L LPFOS. Peaks: 1, pyrimidine; 2, phenol; 3, benzonitrile; 4, acetophenone; and 5, toluene. Reprinted from J. Chromatogr. A, vol 907, Fuguet, E., Ràfols, C., Bosch, E., Rosés, M., Abraham, M.H. "Solute-solvent interactions in micellar electrokinetic chromatography: selectivity of lithium dodecylsulfate – lithium perfluorooctanoate mixed micellar buffers" pp. 257-265. Copyright 2001, with permission from Elsevier.

In Interfaces and Interphases in Analytical Chemistry; Helburn, R., et al.;
ACS Symposium Series; American Chemical Society: Washington, DC, 2011.

Table VIII. LSER coefficients for several micellar systems reported by Poole and coworkers

System	*c*	*e*	*s*	*a*	*b*	*v*	*r*	*n*	*s.d.*	*F*
SC[a]	-1.67	0.56	-0.58	0.05	-2.34	2.55	0.985	40	0.10	~285
STC	-2.10	0.60	-0.34	0.00	-2.06	2.43	0.989	40	0.09	377
SDC	-1.69	0.66	-0.47	0.00	-2.47	2.67	0.986	40	0.11	286
STDC	-1.99	0.67	-0.45	0.00	-2.17	2.62	0.991	40	0.09	430

[a] average values for coefficients from five tabulated LSERs are presented here.

There is obvious disagreement in the s- and b-coefficients. Nevertheless, both LSERs show decreased dependence of log k on solute basicity (B) and increased dependence on solute acidity (A) relative to SDS. Specifically, the coefficients show that LPFOS is a stronger hydrogen bond donor than SDS and a weaker HB acceptor. Both s-coefficients, even though in disagreement with each other, suggest that LPFOS micelles are more polar than SDS micelles. These changes indicate that the interactions governing solute partitioning are governed by the specific chemical structure of the surfactant (i.e., counterions, nature of the nonpolar chain, etc.) rather than simply the charge of the head group.

Bile Salts

Poole and coworkers note that "bile salt surfactants are probably the second most widely used group of surfactants in MEKC after SDS (*38*)," so it is certainly worth understanding their behavior and comparing them to SDS. To do so, the authors collected LSERs for sodium cholate (SC), sodium taurocholate(STC), sodium deoxycholate(SDC), and sodium taurodeoxycholate (STDC), which are presented in Table VIII.

The similarity between the bile salt systems is striking. Because they all have similar coefficients they will produce comparable selectivities in MEKC separations. Additionally, none of the systems display a significant a-coefficient meaning that solutes would not be separated on the basis of their HB donating ability. Compared to SDS, the slightly larger magnitudes of the b- and s-coefficients suggest that bile salts will provide increased selectivity for HB acceptors and polar species. SDS, however, will provide greater selectivity for HB donating species. Other than these characteristics, however, the differences between SDS and bile salts are not dramatic in terms of the blend of intermolecular interactions governing elution and separation.

Fuguet *et al.* also studied SC and SDC, finding smaller magnitudes for the b-coefficients, slightly larger magnitudes for the r- and s-coefficients, and comparable values of a and v (*39*). Yang and Khaledi (*29*) produced one of the first LSERs for SC using an older LSER model and parameter set which makes it difficult to compare results. However, updated LSERs from the original data went into the average SC LSER presented in Table VIII.

In a separate article, Poole and Poole report LSERs for SC separations under different buffer conditions (pH, composition, and strength,), SC concentrations, and modifier type (methanol, acetonitrile, tetrahydrofuran, and propan-2-ol) and concentration (*37*). There is surprisingly little variation in the LSER coefficients for all of these systems (except perhaps for a small decrease in the magnitude of many of the coefficients with the addition of organic modifiers) suggesting that the solutes' interactions with the aqueous and micellar phases are generally insensitive to the variables explored, or that any changes in the behavior in one phase are offset by comparable changes in the other. Analytically, this means that in order to change the selectivity of a separation, it is more useful to change to a completely different surfactant than to make adjustments to any of the variables listed above.

It should be noted that in this instance, the LSER coefficients are not consistent with direct solvatochromic measurements for SC. For example, the HB α value for SC was reported to be 1.20, compared to 1.21 for water (Tables III and IV). This means that HB accepting solutes should 'see' no difference between the aqueous and micellar phases, and therefore there should be no dependence of retention on solute β. This is clearly not the case in the LSERs. Furthermore, the HB accepting ability of SC micelles was found to be 0.29 compared to 0.96 for water. In this case, HB donating solutes should prefer the aqueous phase and thus show decreased retention. In the SC LSER, however, the a-coefficient is essentially zero, indicating no dependence of solute retention on HB donating ability. The exact source of these discrepancies is not clear, however, it should be noted that the solvatochromic parameters are based on single probes, whereas LSERs are typically generated using dozens of solutes.

Multiple Anionic Surfactant Head Groups

To complete our coverage of anionic groups and their effect on selectivity, we consider Trone and Khaledi's report of six different anionic surfactants, all with sodium counterions and dodecyl chains. Structures are shown in Figure 5 (*40*).

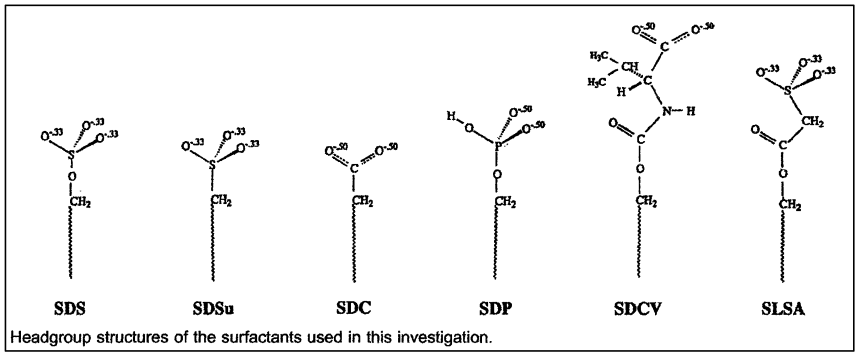

Figure 5. Head groups used in Trone and Khaledi's study (40).

In Interfaces and Interphases in Analytical Chemistry; Helburn, R., et al.;
ACS Symposium Series; American Chemical Society: Washington, DC, 2011.

The volume terms in the LSERs were comparable for all systems. The carbonylvaline (SDCV) and sulfoacetate (SLSA) surfactants were the weakest HB donors. The strongest was SDS. This is interesting in that SDCV, unlike SDS, has a potential HB donating site in the head group. The weakest HB acceptor was to be SDS, and the strongest acceptor was sodium dodecyl carboxylate (SDC). Space does not permit a full discussion of all of the results and their implications for selectivities. The interested reader is directed to the original reference, in which plots and electropherograms are used to show the different selectivities for HB donating and accepting solutes that arise from the different head groups. In these results we see once again the theme of this book in that LSERs provide a means to *characterize* the chemical nature of the micelle/water *interface*. This understanding can then be used to select the surfactant system that will yield the greatest selectivity for a given *analytical application*.

Cationic Surfactants

Alkyltrimethylammonium bromide surfactants are commonly used cationic surfactants. LSERs for tetradecyltrimethyl ammonium bromide (TTAB) and hexadecyltrimethylammonium bromide (HTAB) are presented in Table IX. Uncertainties are shown in parentheses.

While the agreement between some coefficients could be better, the LSERs generally lead to similar qualitative conclusions for the two systems. As in the SDS systems, these surfactants have relatively large positive dependencies on solute volume and large negative dependence on solute hydrogen bond basicity. As with SDS, the b-coefficient is not as large as it is in the water-to-hexadecane transfer LSER, showing that the solute environment inside these cationic micelles is capable of donating hydrogen bonds, presumably due to water associated with the interfacial region or to a Lewis acid/base interaction as postulated in the discussion of the solvatochromic characterization of DTAB presented earlier in this chapter. Similarly, the magnitude of the s-coefficient is also smaller in these systems than in the water/C16 LSER, indicating that the solute environment inside the micelle can interact through dipole-dipole and dipole-induced forces.

The most interesting result, however, is the *positive* dependence on solute hydrogen bond acidity. This result means that solutes with stronger hydrogen bond donating ability will partition into the micelles more than solutes with weaker HB acidity, all else being equal. This implies that the solute environment in the micelles is a stronger hydrogen bond acceptor than is water (or the aqueous phase more generally). This is a puzzling result as a cationic head group would not be thought of as a good HB accepting group. Therefore, this effect must be attributed to the water associated with the interracial region and/or the associated bromide ions. If it arises from water molecules, then they must be behaving in a manner different than those in the bulk phase such that their basicities are enhanced relative to the bulk.

Table IX. LSER coefficients (and values of s.d. in parentheses) for tetradecyltrimethyl ammonium bromide (TTAB) and hexadecyltrimethylammonium bromide (HTAB) micellar systems reported by two groups

System	*c*	*e*	*s*	*a*	*b*	*v*	*r*	*n*	*s.d.*	*F*
TTAB (*39*)	-1.851 (0.051)	0.902 (0.083)	-0.617 (0.051)	0.766 (0.042)	-2.410 (0.059)	2.634 (0.047)	0.994	53	0.089	746
TTAB (*38*)	-2.10 (0.10)	0.36 (0.07)	-0.29 (0.09)	0.90 (0.05)	-2.67 (0.09)	2.82 (0.11)	0.986	59	0.09	380
HTAB (*39*)	-1.833 (0.055)	1.112 (0.089)	-0.755 (0.051)	0.824 (0.040)	-2.437 (0.057)	2.71 (0.049)	0.994	49	0.081	690
HTAB (*38*)	-1.67 (0.11)	0.61 (0.06)	-0.55 (0.07)	0.58 (0.06)	-3.08 (0.10)	3.40 (0.10)	0.993	36	0.08	436

At this point, one could begin to question the veracity of LSERs as leading to chemically incorrect results. However, the LSER results are consistent with and support the same conclusions based on direct solvatochromic measurements by Vitha and Carr for dodecyltrimethylammonium bromide (DTAB) using 4-nitroaniline and 4-nitrophenol as indicators discussed earlier in this chapter – namely that DTAB is a stronger HB donor than is the aqueous phase (*13*). Those measurements, as reported above, were also supported by other literature reports. It therefore seems likely that these results are chemically real and provide interesting, unexpected, and *specific* insights into the chemical nature of the microenvironments that solutes experience upon partitioning into alkyltrimethylammonium bromide micelles.

Comparing SDS to TAB systems, because the b-coefficient in SDS is smaller than it is in TAB systems, it can be concluded that SDS is more similar to water in its ability to donate hydrogen bonds. Furthermore, retention factors in TAB systems are more sensitive to differences in solute HB basicities, suggesting that TAB systems would provide greater selectivity than SDS based on solute HB basicity. In this way, LSERs can begin to shed light on surfactant selection to yield greater selectivities based on the specific properties of the analytes.

Multiple Cationic Surfactants

Schnee and Palmer systematically varied the size of quarternary ammonium head groups and used MEKC to generate LSERs (*41*). They synthesized two series of C-16 surfactants. Structures are shown in Figure 6.

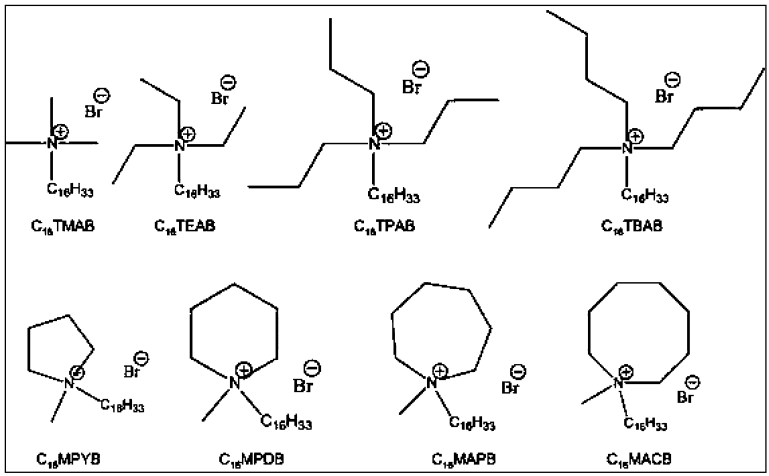

Figure 6. Structures of the cationic surfactants studied by Schnee and Palmer. Schnee, V.P., Palmer, C.P.: Cationic surfactants for micellar electrokinetic chromatography: 1. Characterization of selectivity using the linear solvation energy relationships model. Electrophoresis. 2008. 29. 767-776. Copyright Wiley-VCH Verlag GmbH & Co. KGaA. Reproduced with permission.

One series varied the linear trialkly chains attached to the ammonium nitrogen atom and included the methyl (C_{16}TMAB), ethyl (C_{16}TEAB), propyl(C_{16}TPAB,) and butyl (C_{16}TBAB) derivatives. The other series varied the size of an alkyl ring attached to the ammonium nitrogen, including 1-hexadecyl-1-methylpyrrolidium bromide (C_{16}MPYB – five member head group ring), -methyl piperidine (C_{16}MPdB – six member ring), -methyl-azepanium (C_{16}MAPB – seven member ring), and –methyl-azocan (C_{16}MACB – eight member ring).

The the different magnitudes of LSER coefficients obtained for each system are shown graphically in Figure 7.

With the exception of the v- and s-coefficients for the linear head group surfactants, within a series, all of the surfactants behave essentially identically. The magnitudes of the v- and s- coefficients decrease with increasing head group chain. The decreasing v-coefficient indicates that the cohesivity of the micelles increases as the chain length increases, making it more difficult for solutes to partition into the micelles. The authors suggest this may arise from increased hydrophobic interactions with increasing alkyl chain lengths. They note that only two surfactants, lithium perfluorooctanesulfonate and sodium cholate, have greater cohesivity than C_{16}TBAB. This is important as solute size is one of the dominant factors affecting partitioning into all micellar phases, so changes in the v-coefficient from one system to another can manifest themselves in significant differences in retention and selectivity in MEKC separation, all as a result of the change in the chemical nature of the micelle/aqueous phase interface.

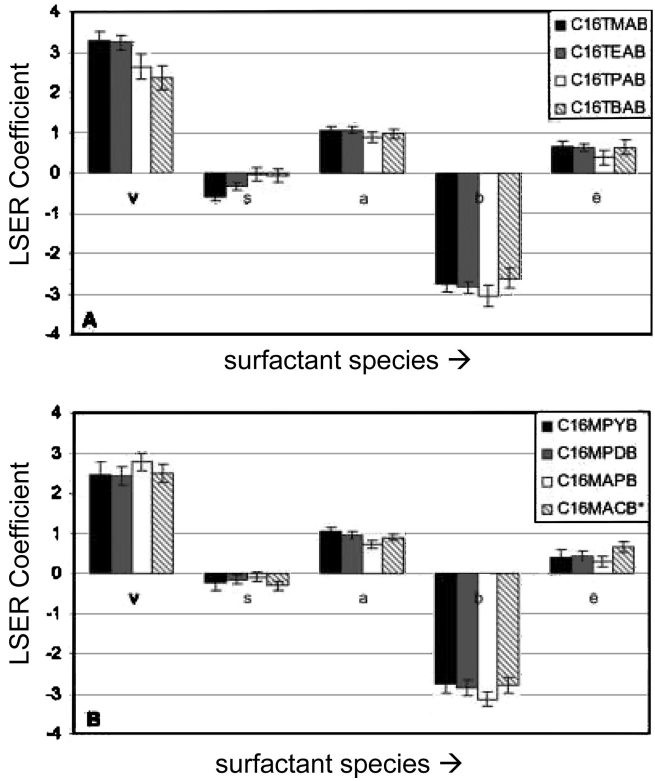

Figure 7. LSER parameter results from Schnee and Palmer (A) Linear head group surfactants and (B) cyclic head group surfactants. Schnee, V.P.; Palmer, C.P. Cationic surfactants for micellar electrokinetic chromatography: 1. Characterization of selectivity using the linear solvation energy relationships model. Electrophoresis, 2008, 29, 767-776. Copyright Wiley-VCH Verlag GmbH & Co. KGaA. Reproduced with permission.

The other trend is the decreasing magnitude of the s-coefficient as the chain length increases for the linear alkylammonium surfactants. This indicates that polar solutes partition into the micelles more as the size of the head group increases. Schnee and Palmer note that the s-coefficients for C_{16}TPAB and C_{16}TBAB are statistically equal to zero, indicating that "the dipole interactions afforded by the two micelles are not significantly different than those afforded by water." They also note that these are the highest polarities reported for common micellar systems. Regarding the trends in cohesivity and polarity, the authors suggest that they may be related "in that polar compounds are not able to enter and be solvated within the hydrophobic core of the micelle, but are solvated at the more polar interface between the micelles and aqueous buffer."

In terms of the coefficients in general, however, the differences between the systems is not staggeringly large, although they will allow for some differences in selectivity. Furthermore, the results for the systems explored by Schnee and Palmer are generally comparable to those obtained for TTAB and HTAB reported

In Interfaces and Interphases in Analytical Chemistry; Helburn, R., et al.;
ACS Symposium Series; American Chemical Society: Washington, DC, 2011.

above. So there seems to be similar behavior for the entire class of alkylammonium bromide micelles, with some subtle variations depending on the exact nature of the head group and its effects on the micelle/water interface.

Hexadecylpyridinium Chloride

Based on literature partition coefficients, Abraham reported an LSER for water –to hexadecylpyridinium chloride micelles (*42*), shown in the equation below:

$$\log K = -0.437 + 0.973E - 0.736S + 0.769A - 2.840B + 3.386V \quad (14)$$
$$n = 46 \qquad r = 0.974 \qquad s.d. = 0.147 \qquad F = 146$$

We note again that since this was an earlier publication, a different set of solute parameters and notations were used in the original report, which has been rewritten here using the newer notation to make comparisons easier. All of the coefficients in this LSER fall within the ranges of the TTAB and HTAB LSERs presented above, indicating that the behavior of this system is not substantially different than those systems. The only exception may be the relatively large magnitude of the v-coefficient in this LSER, which is larger than those reported for HTAB, TTAB, and all of the systems reported by Schnee and Palmer discussed above. It is also noteworthy that the positive dependence of partitioning on solute hydrogen bond acidity in a cationic system is again independently verified.

Nonionic Micelles – Brij-35

Quina *et al.* first published an LSER describing solute partitioning in Brij-35 (polyoxyethylene(23)dodecylether) in 1995 (*43*) and again in 1999 (*44*). The coefficients are summarized in Table X.

While large difference in the coefficients are observed depending on the solute set, both studies show that Brij-35 is a considerably stronger HB acceptor (large positive coefficient of HB acidity), and a considerably weaker HB donor (large negative b-coefficient) compared to the cationic and anionic systems discussed above. These results are consistent with those of Rosés *et al.* who found that the addition of Brij-35 to SDS micelles increased the HB basicity and decreased the HB acidity of the micelles (*45*).

MEKC Retention Indices

Muijselaar, Claessens, and Cramers developed a scale similar to that of the Rohrschneider-McReynolds scale based on retention indices in different surfactant systems (*46–48*). They found that generally, SDS and sodium dodecylsulfonate had higher HB donor strength and lower HB acceptor strength compared to CTAB and DTAB. This is consistent with the LSER results and again demonstrates that the nature of the head group, and hence the properties of the interfacial region, must be considered when using micelles in analytical applications.

In Interfaces and Interphases in Analytical Chemistry; Helburn, R., et al.;
ACS Symposium Series; American Chemical Society: Washington, DC, 2011.

Table X. LSER coefficients for Brij-35 micellar systems published by Quina *et al.*

System	*c*	*e*	*s*	*a*	*b*	*v*	*r*	*n*	*s.d.*	*F*
1995	-1.39	1.63	-0.37	1.62	-3.83	3.65	0.99	19	0.09	159
1999	-0.31	0.88	-0.15	1.06	-3.58	2.83	0.99	27	0.18	163

In their work, they also used LSERs to show that the addition of Brij-35 modified the donating and accepting ability of 50 mM SDS (*46*). Increasing the Brij-35 concentration from 0 to 10 mM changed the a-coefficient from -0.31 to 0.14 and the b-coefficient from -1.56 to -2.77. Both effects are substantial in terms of modifying the selectivity of the system, in particular serving to increase the elution times of hydrogen bond donating species and decrease them for hydrogen bond accepting species. This indicates that Brij-35 increases the HB basicity and decreases the HB acidity of the micellar pseudostationary phase. These results agree with those of Rosés *et al.* (*45*)

Modifiers

Modifiers can be used to alter retention and selectivity in MEKC just as they are used in reversed phase liquid chromatography. Liu *et al.* studied urea, methanol, dioxane, tetrahydrofuran, acetonitrile, and 2-propanol in SDS systems using LSERs (*49*). The cohesivity of the pseudostationary phase was found to decrease relative to the aqueous phase upon increasing modifier concentration for all modifiers, with the most dramatic change being observed for dioxane and tetrahydrofuran (THF) (Figure 8, top left). All of the modifiers increased the polarity of the stationary phase relative to the aqueous phase except for urea (Figure 8, top right). THF displayed the largest effect, although overall the effects were generally minor for all modifiers at the concentrations studied (5 M or less). All of the modifiers except urea decreased the HB acidity of the pseudostationary phase relative to the aqueous phase, with the biggest decrease exhibited by THF (Figure 8, bottom left). Thus, the addition of THF leads to greater selectivity based on solute HB accepting ability. Interestingly, the effects of the modifiers on the b-coefficient were not monotonic with increasing concentration, indicating a complicated blend of modifier effects on the SDS and aqueous phases. Similarly complicated behavior was observed for the effects of dioxane, methanol, and 2-propanol on the LSER coefficients of solute HB acidity whereas monotonic increases in the a-coefficient were observed for THF, acetonitrile, and urea (Figure 8, bottom right). Increasingly positive a-coefficients mean that the pseudostationary phase HB accepting ability (i.e. basicity) increased relative to the aqueous phase buffer, with THF having a far more pronounced effect than acetonitrile and urea.

In Interfaces and Interphases in Analytical Chemistry; Helburn, R., et al.;
ACS Symposium Series; American Chemical Society: Washington, DC, 2011.

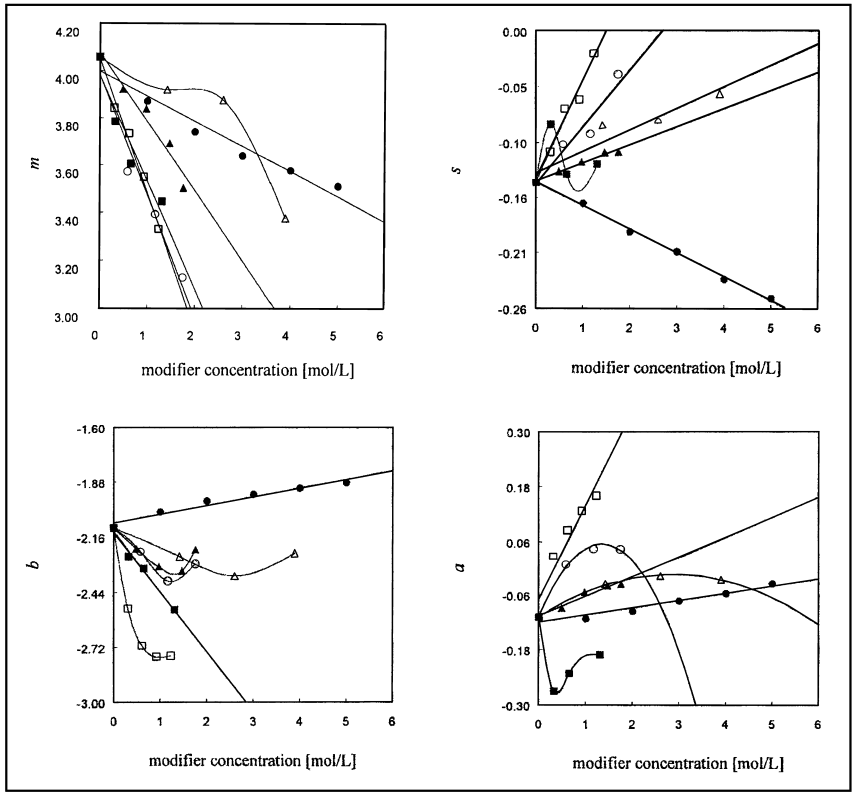

Figure 8. Effect of modifiers on SDS LSER coefficients. Top left: dependence of m-coefficient on modifier concentration. Top right: dependence of s-coefficient on modifier concentration. Bottom left: dependence of b-coefficient on modifier concentration. Bottom right: dependence of a-coefficient on modifier concentration. Symbols: •, urea; △, methanol; ○, dioxane; □, tetrahydrofuran; ▲, acetonitrile; ■, 2-propanol. Reprinted from J. Chromatogr. A, vol. 863, Liu, Z., Zou, H., Ye, M., Ni, J., Zhang, Y., "Effects of organic modifiers on retention mechanism and selectivity in micellar electrokinetic capillary chromatography studied by linear solvation energy relationships" pp. 69-79. Copyright 1999, with permission from Elsevier.

The magnitudes of the changes are not substantial for many of the coefficient, with the exception of the m-coefficient (equivalent to the v-coefficient in the more recent LSER notation). Nevertheless, the study shows that different organic modifiers do influence solute partitioning and can be used to alter retention and selectivity. However, if large changes in selectivity are desired, all of the LSERs discussed in this section indicate that changing the nature of the surfactant (i.e., switching from SDS to CTAB or Brij-35) is more likely to have a significant impact on the intermolecular interactions governing the separation, and hence selectivity, than is changing the aqueous phase buffer composition or adding organic modifiers.

In Interfaces and Interphases in Analytical Chemistry; Helburn, R., et al.;
ACS Symposium Series; American Chemical Society: Washington, DC, 2011.

Micellar Liquid Chromatography

Naturally, micelles are not the only pseudostationary phase being used in electrophoresis, nor is their use restricted to MEKC. LSERs have been used to describe the intermolecular interactions governing micellar liquid chromatography (MLC) (*50–62*). Analyzing these results in terms of the micelle/aqueous phase interface is more complicated than MEKC results, however, because the LSERs include interactions occurring in the stationary phase, the bulk mobile phase, and the micellar pseudostationary phase with the mobile phase. Additionally, modifiers such as propanol are commonly used to increase the efficiency of MLC separations (*63*), further complicating the interpretation of the LSERs if one is seeking to use them to characterize the micelle/water interface. Space does not permit an examination of MLC LSERs and interested readers are directed to references above.

Recent Developments in MEKC LSERs

The discussion above indicates that there has been a lot of work done using LSERs to characterize common MEKC systems. Some systems, such as SDS and the trimethylammonium halide systems, have multiple LSERs reported by several groups. We have not tried to compile all of the LSERs that have been published because extensive compilations already exist (*35*, *38*, *39*, *48*). We have tried, instead, to show how the LSERs reveal differences in the interfacial properties of the systems and to which variables those properties are most sensitive. The selectivity of each system is dictated largely by the nature of the head group, as changes in alkyl chain length were shown to have little effect. This indicates that the intermolecular interactions between the solutes and the micelles are largely governed by the properties of the micelle/water interface. Of particular interest is the fact that cationic surfactants and Brij-35 were found to interact with HB donating solutes better than SDS and even better than the aqueous phase itself. In all systems, solute volume and HB basicity had the largest coefficients, with a positive dependence on volume and negative dependence on basicity. Some tuning of selectivity can perhaps be obtained through the use of additives, changing the surfactant counterion, or by changing the nature of the buffer, but these effects are generally small compared to changes in the LSER coefficients observed with different surfactants.

Given all of the LSER studies cited above and the compilations thereof, it may be useful to consider the direction that future studies in this area could take. Producing more LSERs of standard SDS systems, for example, is unlikely to add significant insight into SDS micelles or into the application of MEKC to achieve separations. Examples of practical applications that exploit what has been learned from LSERs would be interesting. Demonstrating that LSERs can help guide surfactant selection and optimize separations would be of practical importance. Also, including other pseudostationary phases, such as polymeric phases and vesicles, in such studies has already started. It may be in these areas, particularly in studies of biologically relevant lipid bilayers, where CE and LSERs can

continue to prove to be a means of characterizing interfaces that produces new insights about important systems.

Micellar Selectivity Triangle

Towards those ends, Fu and Khaledi have developed a selectivity triangle scheme for classifying the chemical selectivity of micellar systems used in electrokinetic chromatography (*64*). They measured or collected LSERs for seventy-four MEKC pseudophases. The LSER coefficients were manipulated in such a way as to yield a parameter, X_i, where i = s, a, b, or e. These parameters reflect each pseudophase's ability to participate in the intermolecular interactions associated with each of the corresponding LSER coefficients. The key, however, is that the scales are defined such that the sum of all X_i in each system is unity. Three X_i scales were then chosen to be at the apexes of a triangle, and the corresponding X_i values for the seventy-fours systems were plotted within the triangle. Given that there are four scales, four different triangles can be plotted. However, because hydrogen bond acidity is important in determining selectivity, the combination that would exclude hydrogen bond acidity was not considered. Examples of the triangles resulting from the three remaining combinations are shown in Figure 9, with each point in the triangles representing a different micellar system. The authors then looked at the groupings within the plot to define systems that yield similar selectivities (i.e., those have similar X_i values). Such groupings are defined by the solid lines encompassing the different systems. Because the three different triangles generally yielded comparable information, the authors chose to use only the one based on X_b, X_a, and X_s (Figure 9a) to further analyze and understand the LSERs of the seventy-four systems used to create the micellar selectivity triangle (MST).

In Figure 9, group B is mainly comprised on fluorinated micelles. Groups A consists of SDS micelles and its analogs, while group C contains bile salts, microemulsions, and alkyl methacrylate polymeric micelles. Group D is comprised of AGENT-type polymeric micelles and the cationic micelle, tetradecyltrimethylammonium bromide. Based on their position in the triangle, it can be said that the systems in group B are the strongest hydrogen bond donors (highest X_b) and weakest hydrogen bond acceptors (lowest X_a). Furthermore, the systems in group C are weaker HB donors (lower X_b) and slightly stronger HB acceptors (higher X_a) than those in group A, although considerable overlap in HB basicity occurs. Those systems in group D have yet a different blend of interactions.

While these plots contain essentially the same chemical information that the LSER coefficients contain, the advantage of the triangle scheme is that it allows the data to be plotted in a convenient manner that makes for easy visual comparisons between systems. Furthermore, the comparisons can help guide the selection of micellar systems when trying to achieve a separation. For example, if a separation is not working with a pseudophase from group C, changing to another in that group is unlikely to lead to significant changes in selectivity. Thus, one would perhaps try a surfactant from group B or D.

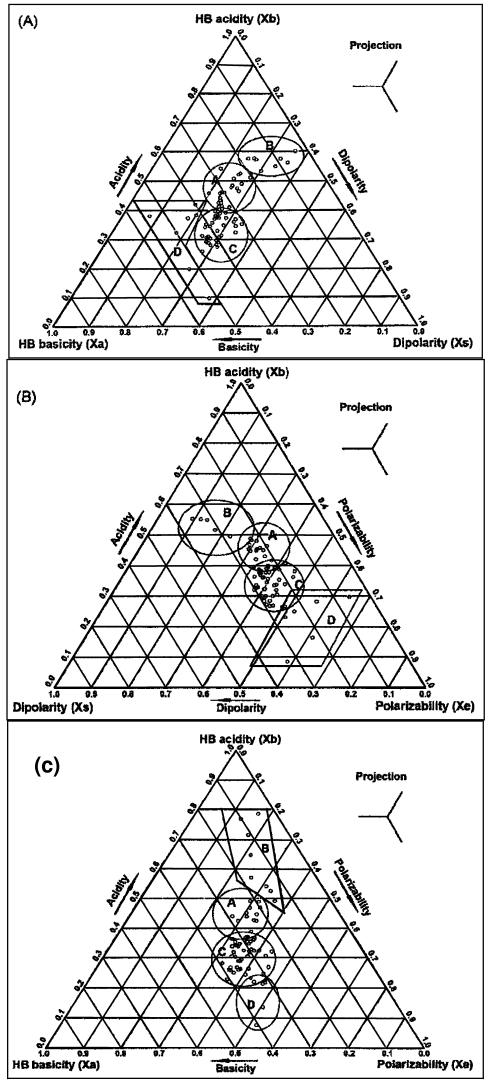

Figure 9. Micelle selectivity triangle schemes of seventy-four micellar systems. Reprinted from J. Chromatogr. A, vol. 1216, Fu,C.; Khaledi, M.G. "Micellar selectivity triangle for classification of chemical selectivity in electrokinetic chromatography", pp. 1891-1900. Copyright 2009, with permission from Elsevier.

The authors note that while the groupings were somewhat subjective, each of the different triangles led to groupings that were in good agreement with each other. It is also reassuring that when the authors applied their scheme to fourteen different literature reports of SDS LSERs, all fourteen clustered together in the triangle despite the fact that the LSERs were obtained by different research groups using different solute sets and slightly different experimental conditions (Figure 10). The

three outliers in the plot were rationalized based on quite different experimental conditions.

Fu and Khaledi have used the MST scheme to characterize pentanol (PeOH) and hexafluoroisopropoanol (HFIP) (*65*). Differences in the selectivities that result from these modifiers are seen in the electropherograms in Figure 11.

Application of the MST to analyze the differences in the nine systems studied yielded Figure 12, which clearly shows that the systems span a range of interaction abilities and will therefore lead to different selectivities.

This is an excellent example of how the MST scheme makes the differences between systems apparent and how it can therefore help guide the selection of pseudostationary phases in electrophoretic separations. More broadly, the MST scheme unites all of the LSER work that has been discussed in this chapter to show how the different interfacial properties of a wide range of micellar systems can be applied to achieve analytical separations.

Extension of Solvatochromic and LSER Studies to Vesicles

Micelles are sometimes said to be simple models of lipid vesicles and cell membranes. Therefore, extending the solvatochromic and LSER studies that have been performed on micelles to vesicles is a natural progression. In this section, we will provide an overview of some studies aimed in this direction.

Lipids, like the surfactants discussed above, have a polar head group and a nonpolar tail (or tails, as many lipids have two long alkyl chains). Lipid vesicles are spherical structures formed from a bilayer of lipids which creates a membrane surrounding an interior aqueous solution (Figure 13). They are different from micelles in that micelles can be thought of as having only one surface, whereas vesicles have two – one on the interior and one on the exterior of the vesicle. Because cell membranes are also formed from lipid bilayers, vesicles are closer mimics of cell membranes than are micellar systems.

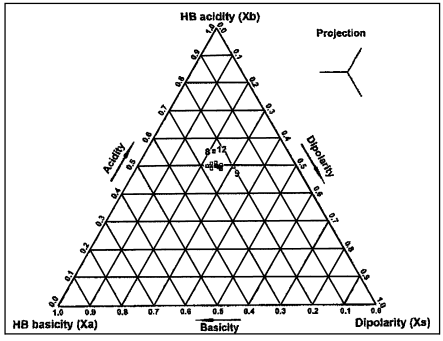

Figure 10. MST for fourteen SDS LSERs. Reprinted from J. Chromatogr. A, vol. 1216, Fu,C.; Khaledi, M.G. "Micellar selectivity triangle for classification of chemical selectivity in electrokinetic chromatography", pp. 1891-1900. Copyright 2009, with permission from Elsevier.

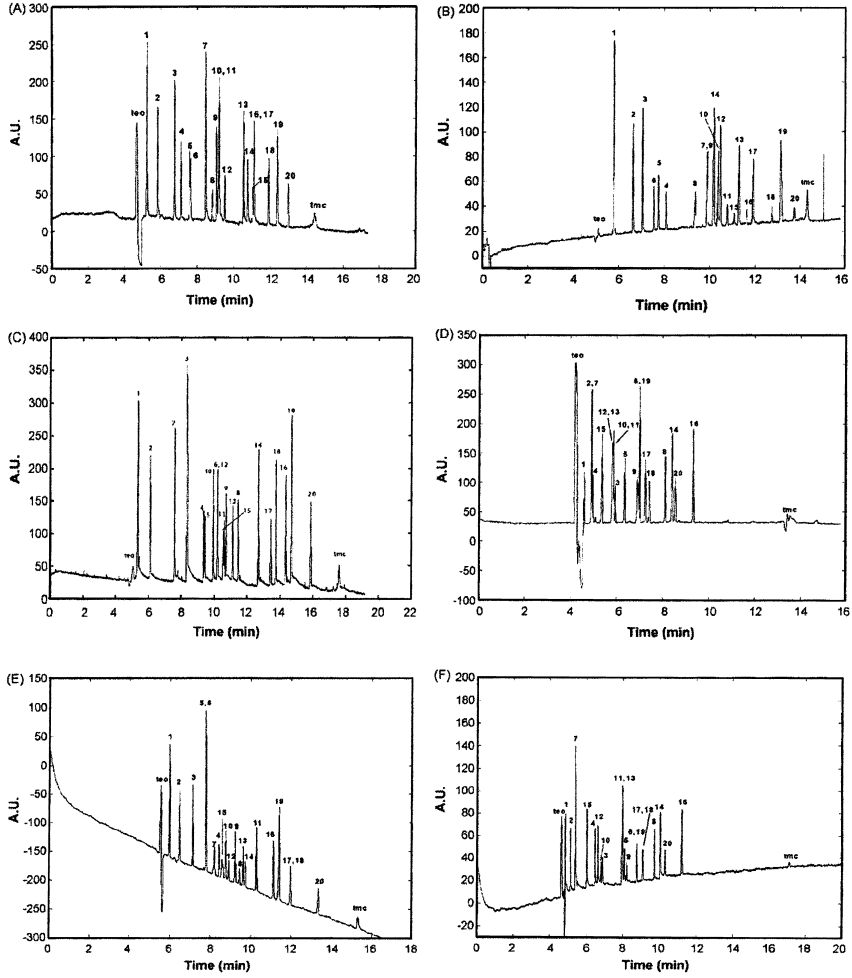

Figure 11. Separation of 20 aromatic solutes composed of hydrogen bond donors: 1 = resorcinol, 2 = phenol, 7 = 3-chlorophenol, 10 = 4-ethylphenol, 12 = 3,5-dimethylphenol, 15 = 4-iodophenol; hydrogen bond acceptors: 3 = phenethyl alcohol, 5 = nitrobenzene, 6 = acetophenone, 8 = methylbenzoate,9 = benzyl chloride, 14 = 3-chloroacetophenone, 16 = methyl-2-methyl benzoate; non-hydrogen bond donors: 4 = benzene, 11 = toluene, 13 = chlorobenzene, 17 = ethylbenzene, 18 = 4-chlorotoluene, 19 = naphthalene, 20 = propylbenzene; micellar phases: (A) 40 mM SDS, (B) 40 mM SDS/400 mM PeOH (4.34 % v/v), (C) 40 mM SDS/400 mM HFIP (4.16% v/v), (D) 40 mM LiPFOS, (E) 40 mM LiPFOS/400 mM PeOH (4.34% v/v), (F) 40 mM LiPFOS/400 mM HFIP (4.16% v/v); a 20 mM sodium phosphate buffer pH 7.0 was used in all SDS micelle systems, running buffer for LiPFOS micelles was 20 mM lithium phosphate buffer at pH 7.0; 20 kV applied on a 70 cm length capillary (effective length 50 cm). Reprinted from J. Chromatogr. A, vol. 1216, Fu,C.; Khaledi, M.G. "Selectivity patterns in micellar electrokinetic chromatography: Characterization of

In Interfaces and Interphases in Analytical Chemistry; Helburn, R., et al.;
ACS Symposium Series; American Chemical Society: Washington, DC, 2011.

fluorinated and aliphatic alcohol modifiers by micellar selectivity triangle", pp. 1901-1907. Copyright 2009, with permission from Elsevier.

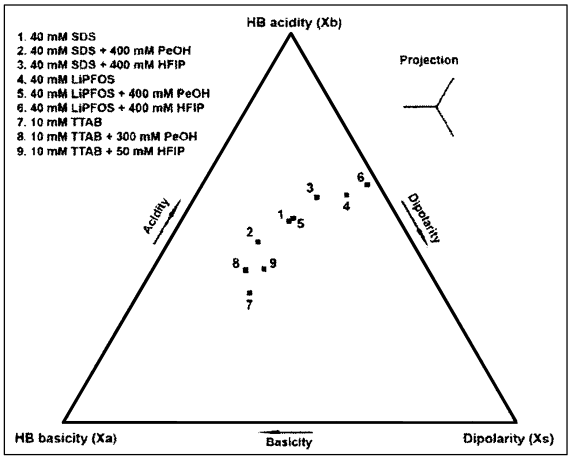

Figure 12. MST for three micelles and six modified micellar systems. Reprinted from J. Chromatogr. A, vol. 1216, Fu,C.; Khaledi, M.G. "Selectivity patterns in micellar electrokinetic chromatography: Characterization of fluorinated and aliphatic alcohol modifiers by micellar selectivity triangle", pp. 1901-1907. Copyright 2009, with permission from Elsevier.

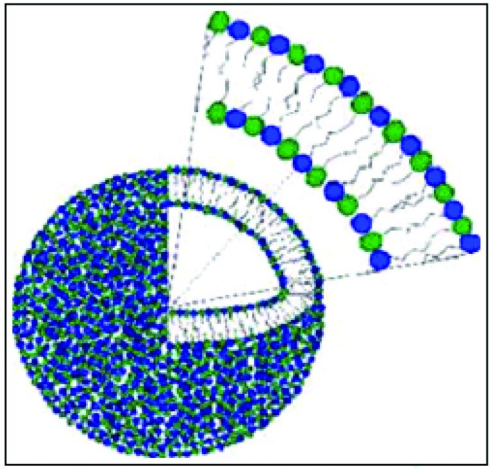

Figure 13. Schematic representation of a lipid vesicle formed from a lipid bilayer. Reproduced with permission from Novera Pharmaceuticals, http://www.noveradrugs.com.

If the vesicle has a single bilayer, it is known as a unilamellar vesicle. Vesicles that incorporate more than one bilayer are called multilamellar vesicles. Depending on their size, vesicles are referred to as small unilamellar vesicles (SUVs, 20 – 100 nm), large unilamellar vesicles (LUVs, > 100 nm), or giant unilamellar vesicles (GUVs, > 1 μm) (*66*). Below we generally restrict our review to SUVs and LUVs.

Solvatochromic Studies of Vesicles

Just as in micellar studies, numerous studies using general polarity indicators have been reported for vesicles. We restrict our considerations in this chapter to studies that parallel the Kamlet-Taft approach and attempt to characterize and quantify *specific* intermolecular forces that occur in vesicles with regards to the strength of dipole-dipole, hydrogen bonding, and dispersion interactions. The most direct report of such was from Khaledi *et al.* who used a homologous set of N,N-dialkyl-4-nitroaniline probes to determine π* values for solutions of small unilamellar vesicles (SUVs) made from mixtures of phosphatidylcholines and cholesterol (*67*, *68*). The alkyl groups on the probe ranged from one to nine carbon atoms in length. The spectra were not deconvoluted to separate contributions from the probe free in solution from that incorporated into the SUVs. They found that the longer chain probes produced π* values of approximately 0.55-0.65 when the probes were incorporated into $PG_{24}PC_{46}Chol_{30}$ liposomes by physical encapsulation via sonication during the SUV preparations (PG = 1,2-dipalmitoyl-*sn*-glycero-3-{phospho-*rac*-(1-glycerol)] (sodium salt), PC = L-α-phosphatidylcholine dipalmitoyl, Chol = cholesterol and the subscripts represent mole fractions of each component) (Figure 14). Values of π* from 0.80 to 1.15 were found for the three shortest chain analogs in SUVs prepared by the same method. The authors note that when the probes are added *after* the SUVs have been prepared, significantly higher π* values are found for the longer chain probes compared to when the probe is included in the vesicle preparation (Figure 15). They suggest that when the probe is added after the SUVs have formed, the bulky, long alkyl chains partially prevent their incorporation into the bilayer, thus making it reside in a more polar environment. The effect is not as significant for the shorter probes and was absent in dihexadecyl phosphate (DHP) vesicles containing 30 mole percent cholesterol (Figure 16). Nevertheless, the shorter chains still reported significantly higher π* values (~1.20) compared to the longest chains (~0.60).

Shin, Schanze, and Whitten used the absorbance bands arising from the nitroaniline and azo chromophores of p-donor-p'-acceptor substituted azobenzene probes to measure π* of three phosphatidylcholine vesicle systems (dimyristoyl: DMPC; dipalmitoyl: DPPC; distearoyl: DSPC) (*69*). The nitroaniline moiety yielded values well below those of the azo moiety. However, the study did not consider effects of hydrogen bonding or probe orientation effects on the spectra, so it is difficult to determine the meaning of these results. Shin and Whitten also measured π* values of the same phosphatidylcholine systems using charge transfer polyenes of varying lengths (*70*). They generally found significantly high π* values (1.0 to 1.74), the exact magnitude of which depended

In Interfaces and Interphases in Analytical Chemistry; Helburn, R., et al.;
ACS Symposium Series; American Chemical Society: Washington, DC, 2011.

on probe, the system, and the method of obtaining the wavelength of maximum absorbance. They obtained lower values (0.5 to 0.6) for all of the vesicles using N,N-dimethyl-4-nitroaniline. Based on their analyses of absorbance and fluorescence spectra, they propose that the probes are oriented within the bilayers such that the amino ends of the probes are embedded in a hydrophobic environment and the nitro ends are located in the hydrophilic interfacial region.

The only study known to the author in which the Kamlet-Taft hydrogen bond acidity was measured for vesicles was published by Handa *et al.* (*71*) They found $\pi^* = 0.88$ and $\alpha = 0.39$ for liposomes of bovine brain phosphatidylserine using Reichardt's dye and methylene blue as probes. For comparison, using the same probes they measured $\pi^* = 1.09$ and $\alpha = 1.13$ for pure water. Thus, the liposome results indicate that the probes are in a significantly polar microenvironment that also has some moderate HB donating ability. These results, like the micellar results, indicate the likelihood that water is likely playing at least contributing in some way to the properties of the vesicles.

Solvatochromic Studies of Vesicles Related to the Kamlet-Taft Parameters

Correa, Silber, and co-workers characterized Prodan's solvatochromism using bulk solvents and the Kamlet-Taft solvent parameters and used it to study large unilamellar vesicles (LUVs) of 1,2-di-oleoyl-*sn*-glycero-3-phosphatidylcholine (DOPC) (*71*). They found that the probe senses two different environments within the bilayer: one comparable in polarity to methanol and the other comparable to tetrahydrofuran. Using two cationic hemicyanine probes, which the authors conclude reside in the interfacial head group region of LUVs made from DOPC, they demonstrated that the region is a "powerful" electron donating environment, but they do not estimate a Kamlet-Taft β-value for this region (*72*).

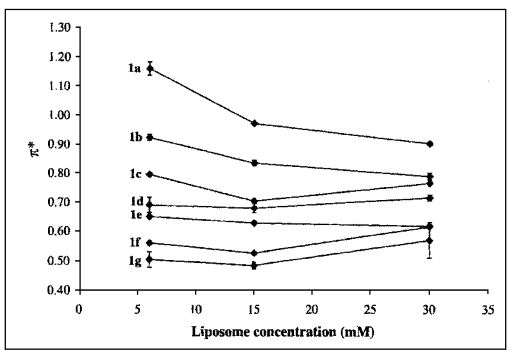

Figure 14. π vs. $PG_{24}PC_{46}Chol_{30}$ concentration for N,N-dialkyl-4-nitroaniline indicators using physical encapsulation via sonication. Indicator alkyl groups are 1a = methyl, 1b = ethyl, 1c = propyl, 1d = butyl, 1e = pentyl, 1f = octyl, and 1g = decyl. Reprinted from J. Biochem. Bioph. Methods, vol. 60, Carrozzino, J.M., Fuguet, E., Helburn, R., Khaledi, M.G. "Characterization of small unilamellar vesicles using solvatochromic π* indicators and particle sizing", pp. 97-115. Copyright 2004, with permission from Elsevier.*

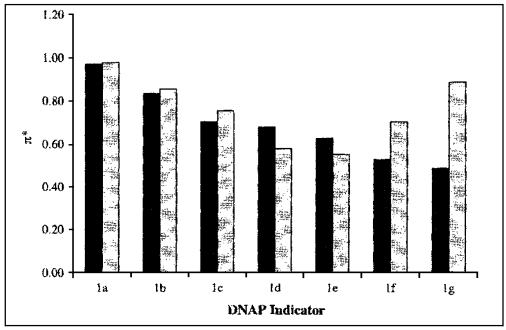

Figure 15. π for N,N-dialkyl-4-nitroaniline (DNAP) indicators in 15 mM $PG_{24}PC_{46}Chol_{30}$ liposomes with different preparation methods. Lighter bars represent dye-liposome dispersions prepared by adding the probe to the preformed SUV dispersion. Black bars represent dye-liposome dispersions prepared by physical encapsulation via sonication. Indicator alkyl groups are 1a = methyl, 1b = ethyl, 1c = propyl, 1d = butyl, 1e = pentyl, 1f = octyl, and 1g = decyl. Reprinted from J. Biochem. Bioph. Methods, vol. 60, Carrozzino, J.M., Fuguet, E., Helburn, R., Khaledi, M.G. "Characterization of small unilamellar vesicles using solvatochromic π* indicators and particle sizing", pp. 97-115. Copyright 2004, with permission from Elsevier.*

Clarke *et al.* used di-8-ANEPPS, which is structurally related to the probes used by Shin and Whitten, to measure the effects of head group structure, cholesterol, and cholesterol derivatives on a polarity-related property known as the dipole potential (*73*). The dipole potential is the voltage drop from the surface of the vesicle to the alkyl interior and arises from the alignment of the polar head groups of the lipids and associated water molecules (*74*). Four of the cholesterol derivatives were found to increase the dipole potential of dimyristoylphosphatidylcholine (DMPC) vesicles and one decreased it, as shown in Figure 17.

These results were rationalized on the basis of the dipoles of the derivatives and their orientation with respect to the vesicle surface. The results indicate that these derivatives influence the interfacial properties of the vesicles and warrant further investigation using probes whose solvatochromic behavior is well characterized in simpler systems.

LeGoff, Vitha, and Clarke also used di-8-ANEPPS to measure the orientational polarizability of phosphatidylcholine (PC) vesicles of varying chain lengths and degrees of unsaturation (*75*). Orientational polarizability is a measure of the ability of a probe's chemical environment to adjust to and resolvate a change in the probe's dipole orientation after excitation but prior to emission. As such, it reflects a blend of polarity and rigidity/fluidity of the probe's environment. The authors found higher orientational polarizabilities for the saturated PC vesicles, which also had higher dipole potentials, compared to the unsaturated PC vesicles, which also had lower dipole potentials (Figure 18).

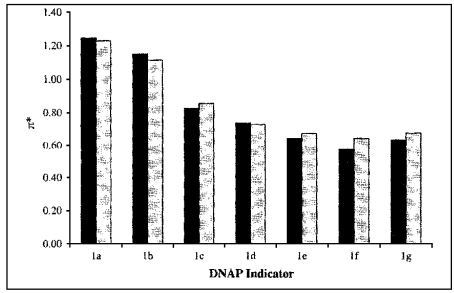

Figure 16. π for N,N-dialkyl-4-nitroaniline (DNAP) indicators in 15 mM $DHP_{70}Chol_{30}$ liposomes with different preparation methods. Lighter bars represent dye-liposome dispersions prepared by adding the probe to the preformed SUV dispersion. Black bars represent dye-liposome dispersions prepared by physical encapsulation via sonication. Indicator alkyl groups are 1a = methyl, 1b = ethyl, 1c = propyl, 1d = butyl, 1e = pentyl, 1f = octyl, and 1g = decyl. Reprinted from J. Biochem. Bioph. Methods, vol. 60, Carrozzino, J.M., Fuguet, E., Helburn, R., Khaledi, M.G. "Characterization of small unilamellar vesicles using solvatochromic π* indicators and particle sizing", pp. 97-115. Copyright 2004, with permission from Elsevier.*

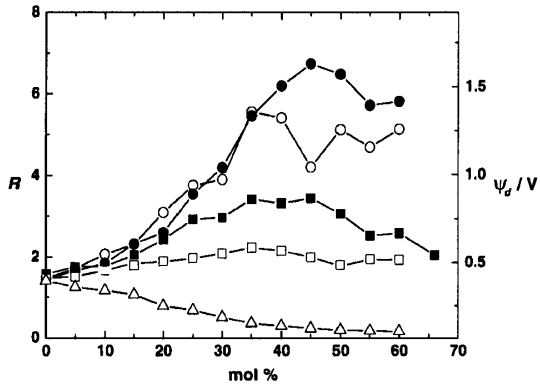

Figure 17. Effect of cholesterol derivative concentration on the dipole potential, ψ_d, measured from the ratio of fluorescence intensity, R, at two specified wavelengths using the probe di-8-ANEPPS. Each point corresponds to a separate vesicle preparation at the given DMPC and cholesterol compositions. Cholesterol derivatives are: (•) 6-ketocholestanol, (○) 4-cholesten-3-one, (■) cholesterol, (□) coprostanol, and (△) cholesten-3β-ol-7-one. Reprinted from Biophys. J., vol. 90, Starke-Peterkovic, T., Turner, N., Vitha, M.F., Waller, M.P., Hibbs, D.E., Clarke, R.J. "Cholesterol effects on the dipole potential of lipid membranes"pp. 4060-4070. Copyright 2006, with permission from Elsevier.

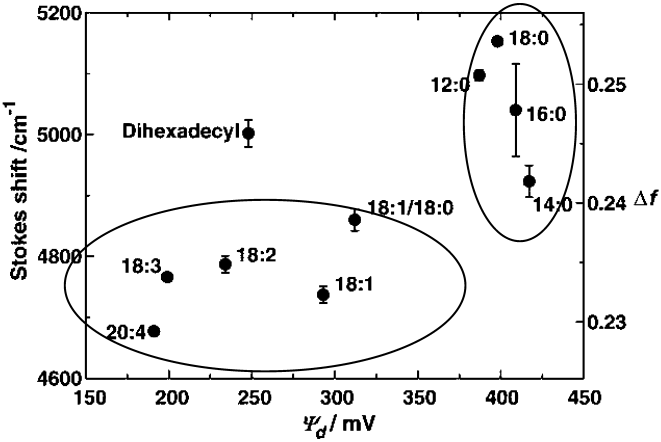

Figure 18. Plot of the Stokes shift of di-8-ANEPPS and the orientational polarizabilities, Δf, of different phosphatidylcholine vesicles versus their corresponding dipole potentials, ψ_d. The bars on each point represent the range of the Stokes shifts measured by exciting 20 nm either side of the wavelength of the absorbance maximum. The first number indicates the alkyl chain length and the second number indicates the number of double bonds in the chains. Reprinted from Biochim. Biophys. Acta – Biomembr., vol. 1768, Le Goff, G., Vitha, M.F., Clarke, R.J. "Orientational polarizability of lipid membrane surfaces" pp. 562-570. Copyright 2007, with permission from Elsevier.

This was attributed to the lower packing density of unsaturated lipids compared to saturated ones. They also studied the effects of cholesterol and some of its derivatives, finding that different derivatives have different effects on the orientational polarizability depending on their effects on packing density and their own dipole moments. Such studies will be important in characterizing lipid membranes and understanding the factors that govern important processes such as transport of ions across membranes and other membrane functions.

Conclusions from Vesicle Solvatochromic Studies

The studies above generally all indicate that liposome head group regions are quite polar, have reasonable hydrogen bond donating ability, and strong hydrogen bond accepting ability. Overall, however, there are relatively few studies on relatively few systems that try to probe for these specific intermolecular interactions. Given their importance as models of cell membranes, there is still a need for systematic studies to fully characterize the wide range of vesicles that can be made, and the effects of biologically relevant additives such as cholesterol on the interfacial properties of those vesicles. Using small organic probes whose solvatochromic response to specific intermolecular interactions is well understood, such as the Kamlet-Taft probes, would facilitate these studies and create a better understanding of the exact nature of the vesicle/water interface. Such studies, however, may require deconvolution to remove contributions from

In Interfaces and Interphases in Analytical Chemistry; Helburn, R., et al.;
ACS Symposium Series; American Chemical Society: Washington, DC, 2011.

the probe free in the aqueous phase. If this is done, however, a more nuanced picture of the bilayer head group region may emerge compared to what is learned from the more general polarity probes that are often used to characterize such systems.

LSERs Applied to Vesicles

Just as the Kamlet-Taft solvatochromic parameters have been used to characterize the water/micelle interface and to some extent the water/lipid vesicle interface, the other characterization technique discussed in this chapter – linear solvation energy relationships – has also been used to study both types of systems. LSER analysis of micelles, mainly based on MEKC measurements, was discussed extensively above, so in this section we turn our attention briefly to LSER vesicle studies in capillary electrophoresis.

As Owen, Stasters, and Breyer note in their extensive review of lipid vesicles in capillary electrophoresis techniques (*76*), "the greatest driving force in utilizing lipid vesicles in CE separations is the assumption that compared to, e.g., SDS micelles, lipid vesicles are more representative of eukaryotic membranes." With that in mind, we will focus on LSER studies of phosphatidylcholine vesicles as these more closely represent the composition of membranes of biological relevance. However, we begin by summarizing the LSERs that have been presented for other vesicle systems.

Khaledi *et al.* presented LSERs for dihexadecyl hydrogen phosphate (DHP) vesicles with and without added cholesterol and compared their behavior to SDS micelles (*77*). In general, the vesicles were less cohesive, considerably weaker HB donors, considerably stronger HB acceptors, and had slightly weaker ability to participate in interactions represented by the S solute parameter (dipolarity/polarizability). Varying amounts of cholesterol had little statistically significant effect on any of the LSER coefficients. It is worth noting that the authors show that the relative strength of interaction represented by the LSERs for the DHP systems more closely mimics the blend found in LSERs for octanol-water partition coefficients (P_{ow}) than in water/SDS partitioning. This is significant in that octanol-water partitioning is often used as a bulk model of partitioning of solutes into membranes. Correlations of $\log k_{DHP}$ versus $\log P_{ow}$ compared to correlations of $\log k_{SDS}$ versus $\log P_{ow}$ show that partitioning from water into DHP vesicles is a better model than water/SDS micelle partitioning for predicting P_{ow} values. The same authors also studied dihexadecyldimethylammonium bromide vesicles and found exceptionally large, positive a-, v-, and e-coefficients, and an exceptionally large negative b-coefficient, relative to coefficients for other vesicle and micelle systems (*78*).

Pascoe and Foley used electrokinetic chromatography to measure LSERs for mixed vesicles of cetyltrimethylammonium bromide and sodium octylsulfate (CTAB/SOS) in the presence of a number of organic modifiers as well as for vesicles of octyltrimethylammonium bromide and sodium dodecylsulfate (OTAB/SDS) (*79*, *80*). LSER coefficients for select systems are shown in Table XI (uncertainties, where available, are shown in parentheses).

In Interfaces and Interphases in Analytical Chemistry; Helburn, R., et al.;
ACS Symposium Series; American Chemical Society: Washington, DC, 2011.

Table XI. LSER coefficients (values of s.d. given below in parentheses) for vesicle systems made with cetyltrimethylammonium bromide and sodium octylsulfate (CTAB/SOS) and octyltrimethylammomium bromide and sodium dodecylsulfate (OTAB/SDS)

System	*c*	*e*	*s*	*a*	*b*	*v*	r^2	*n*
CTAB/SOS	-1.86 (0.19)	0.48 (0.20)	-0.56 (0.18)	0.75 (0.19)	-3.66 (0.32)	3.37 (0.26)	0.96	26
CTAB/SOS w/0.5% v/v 1,3-butanediol	-1.45 (0.19)	0.72 (0.25)	-0.58 (0.20)	0.72 (0.16)	-3.91 (0.29)	3.15 (0.25)	0.97	26
CTAB/SOS w/15% acetonitrile	-1.30 (0.32)	0.52 (0.25)	-0.63 (0.20)	0.44 (0.16)	-2.98 (0.29)	2.48 (0.26)	0.97	26
CTAB/SOS w/0.5% v/v 2-amino-1-butanol	-1.42 (0.24)	1.38 (0.26)	-0.78 (0.18)	0.58 (0.19)	-3.78 (0.32)	2.62 (0.26)	0.96	26
OTAB/SDS	-1.70	0.54	-0.50	0.65	-2.98	3.01	0.97	26

Compared to the standard SDS system used in MEKC, the CTAB/SOS vesicles are generally less cohesive, weaker HB donors, and much stronger HB acceptors. The CTAB/SOS and OTAB/SDS systems show little difference except perhaps in the b-coefficient. Additionally, 1,3-butanediol has little impact on the properties of CTAB/SOS vesicles relative to the aqueous phase, whereas the same percent volume of 2-amino-1-butanol increases the cohesivity and alters the dipole-dipole and HB interactions with solutes. There is also a significant change in how the vesicles interact with solutes that are quite polarizable or have lone electrons (effects incorporated in the eE term). In fact, this result is a bit questionable as it is of significantly larger magnitude than is typical for the e-coefficient. It should be noted that the uncertainties are fairly large. Therefore, actual differences may be considerably smaller than they appear from the coefficients.

Lest we lose focus, it is useful to take a step back and realize that these LSERs show that vesicles govern electrophoretic separations through a different blend of interactions compared to other systems such as SDS. This is supported by the work of Warner and coworkers using vesicles formed from sodium di(undecenyl) tartarate monomer (SDUT), its polymerized form, and SDS (*81*, *82*). Additionally, adding organic modifiers can further tune the selectivities based on particular solute properties. As has been asserted throughout this chapter, these changes are dictated by interactions at the aqueous phase/vesicle or aqueous phase/micelle interface and likely represent differences in the behavior of the water in that region caused by differences in the nature of the head group and/or structure of the vesicles or micelles upon addition of modifiers.

In Interfaces and Interphases in Analytical Chemistry; Helburn, R., et al.;
ACS Symposium Series; American Chemical Society: Washington, DC, 2011.

More interesting in terms of their relevance to biological membranes are vesicles formed from phosphatidylcholines. Khaledi and coworkers used electrophoresis to determine LSER coefficients for two phosphatidylcholine-containing systems (*83–85*). Their LSERs are shown in Table XII.

As with all of the other micelle and vesicle systems presented in this chapter, solute volume and HB basicity play dominant roles in determining solute interactions with the phosphatidylcholine vesicles. Additionally, these systems are much weaker HB donors and much stronger HB acceptors than SDS systems. The positive dependence of partitioning into the vesicles on solute HB donating ability is similar to that found in cationic micelles, suggesting that this dependence arises, at least in part, from the DPPC in these systems. The addition of cholesterol to the membrane, of obvious biological importance, combined with the change in the proportion of the lipids, mainly decreased the HB accepting ability of the vesicles while altering the blend of responses to solute dipolarity/polarizability (S) and excess polarizability (E).

Pascoe and Foley (*79*) determined the following LSER for vesicles made from 80% mole fraction 1-palmitoyl-2-oleyl-*sn*-glycero-3-phosphocholine (POPC) and 20% mole fraction phosphatidyl serine (PS):

$$\log k = -2.04 + 0.70E - 0.54S + 0.02A - 2.90B + 2.68V \qquad (15)$$
$$n = 26 \qquad r^2 = 0.97$$

Relative to the DPPG/DPPC systems above, this system is slightly less capable of accepting hydrogen bonds, is a slightly stronger HB donor, and has a smaller dependence on solute size, perhaps indicating that it is more cohesive than DPPG/DPPC vesicles, although, as has been the case in other comparisons, the uncertainties may be such that these differences are not as significant as they may appear. For example, Pascoe and Foley report an average uncertainty of 0.25 in v-coefficients that they determined for a number of systems. Given this, and the uncertainties in the v-coefficients in the Table XII above, the dependence on solute volume could be nearly the same for all three systems. The same is true for the b-coefficient for which Pascoe and Foley report an average uncertainty of 0.30. Therefore, in general, it can not be said that these systems are dramatically different. It is a little surprising that the a-coefficient is not greater given that both POPC is positively charged and we have seen that many micelles and vesicles that are made from positively charged monomers actually interact more strongly with hydrogen bond donors than does water. In this case, given the value near zero, the implication is that the vesicles interact with HB donors to the same extent that water does.

These are the only publications known to the author that use LSERs to characterize lipid vesicles and their interactions with small molecules. Given the variety of lipids and types of vesicles that can be made, it seems there is opportunity for more exploration in this area, with potential benefit to those trying to model and understand membranes and their functions.

Table XII. LSER coefficients for vesicles formed with dipalmitoyl-L-α-phophatidylcholine (DPPC), dipalmitoyl-L-α-phosphatidylglycerol (DPPG), and cholesterol (Chol). Subscripts indicate the percent molar composition

System	*c*	*e*	*s*	*a*	*b*	*v*	r^2	*s.e.*	*n*
$DPPG_{24}$ $DPPC_{46}$ $Chol_{30}$ (10 mM HEPES)	-2.30 (0.13)	0.54 (0.12)	-0.55 (0.12)	0.32 (0.07)	-3.12 (0.14)	3.01 (0.16)	0.98	0.08	27
$DPPG_{30}$ $DPPC_{70}$ (12 mM HEPES)	-2.21 (0.12)	0.45 (0.10)	-0.44 (0.11)	0.71 (0.06)	-3.23 (0.13)	3.13 (0.14)	0.99	0.07	27

Summary

Not surprisingly, solvatochromic studies and LSERs reveal that micellar and vesicle systems made from different surfactants or lipids have different blends and strengths of interactions with solutes. The dependence of solute partitioning on hydrogen bonding, which in turn is dependent on the nature of the head group, indicates that these differences arise mainly from differences in the water/micelle and water/vesicle interfacial region in the area of the head groups. Thus, in keeping with the theme of this book, the Kamlet-Taft methodology and LSERs provide methods for characterizing the interface between water and micelles and vesicles. Furthermore, the results of LSERs can guide the selection of surfactants and vesicles for electrokinetic and chromatographic separations, so they can also influence the analytical application of these techniques. While many different micellar systems have been examined and the commonly used systems have been thoroughly characterized, there is still considerable room for exploration of relevant biological vesicles using both Kamlet-Taft solvatochromic probes and LSERs. Finally, to 'close the loop,' it is worth considering these results in light of the micelle images presented in the previous chapter. These studies make it clear that the most useful models for helping explain and visualize the partitioning of solutes into micelles are those that 1) capture a dynamic system, 2) have a somewhat uneven surface that can accommodate waters of solvation, counterions, and solutes in a region where all of these entities can interact, and 3) explicitly model head groups, counterions, and water molecules as well as their interactions with solute molecules. Such images will be a long way away from the earliest 'oil droplet' models of micelles. Thanks to all of the computational and experimental work that has occurred in this area, we have arrived at this general image. Similar studies of vesicles and phospholipid membranes are headed in a comparable direction and are yielding a more nuanced understanding of these complex and important systems.

In Interfaces and Interphases in Analytical Chemistry; Helburn, R., et al.;
ACS Symposium Series; American Chemical Society: Washington, DC, 2011.

Acknowledgments

Many thanks go to Professor Christopher Dunlap and Professor Morteza Khaledi for their helpful suggestions in the preparation of this chapter. Thanks also to Professor Ronald Clarke in whose laboratory the phospholipid vesicle solvatochromic data was obtained and to Professor Peter Carr in whose laboratory some of the micellar solvatochromism and LSER results presented in this chapter were obtained. Acknowledgment is made to the Donors of the American Chemical Society Petroleum Research Fund for their support of this project.

References

1. Kamlet, M. J.; Abboud, J. L.; Taft, R. W. *J. Am. Chem. Soc.* **1977**, *99*, 6027–6038.
2. Kamlet, M. J.; Taft, R. W. *J. Am. Chem. Soc.* **1976**, *98*, 377–383.
3. Taft, R. W.; Kamlet, M. J. *J. Am. Chem. Soc.* **1976**, *98*, 2886–2894.
4. Kamlet, M. J.; Taft, R. W. *Acta Chem. Scand., Ser. B* **1985**, *39*, 611–628.
5. Kamlet, M. J.; Abboud, J.-L. M; Abraham, M. H.; Taft, R. W. *J. Org. Chem.* **1983**, *48*, 2877–2887.
6. Carr, P. W. *Microchem. J.* **1993**, *48*, 4–48.
7. Taft, R. W.; Abboud, J. L.; Kamlet, M. J. *J. Am. Chem. Soc.* **1981**, *103*, 1080–1086.
8. Taft, R. W.; Kamlet, M. J. *Inorg. Chem.* **1983**, *22*, 250–254.
9. Park, J. H.; Dallas, A. J.; Chau, P.; Carr, P. W. *J. Phys. Org. Chem.* **1994**, *7*, 757–769.
10. Abboud, J. L. M.; Notario, R. *Pure Appl. Chem.* **1999**, *71*, 645–718.
11. Vitha, M. F.; Weckwerth, J. D.; Odland, K.; Dema, V.; Carr, P. W. *J. Phys. Chem.* **1997**, *100*, 18823–18828.
12. Vitha, M. F.; Weckwerth, J. D.; Odland, K.; Dema, V.; Carr, P. W. *Anal. Chem.* **1997**, *69*, 2268–2274.
13. Vitha, M. F.; Carr, P. W. *J. Phys. Chem. B* **1998**, *102*, 1888–1895.
14. Park, J. H.; Dallas, A. J.; Chau, P.; Carr, P. W. *J. Chromatogr., A* **1994**, *677*, 1–9.
15. Fuguet, E.; Ràfols, C.; Bosch, E.; Rosés, M. *Langmuir* **2003**, *19*, 55–62.
16. Fuguet, E.; Ràfols, C.; Rosés, M. *Langmuir* **2003**, *19*, 6685–6692.
17. Handa, T.; Nakagaki, M.; Miyajima, K. *J. Colloid Interface Sci.* **1990**, *137*, 253–262.
18. Shannigrahi, M.; Bagchi, S. *J. Phys. Chem. B* **2004**, *108*, 17703–17708.
19. Shannigrahi, M.; Bagchi, S. *J. Phys. Chem. B* **2005**, *109*, 14567–14572.
20. Deb, N.; Shannigrahi, M.; Bagchi, S. *J. Phys. Chem. B* **2008**, *112*, 2868–2873.
21. Helburn, R.; Dijiba, Y.; Mansour, G.; Maxka, J. *Langmuir* **1998**, *14*, 7147–7154.
22. Tada, E. B.; Novaki, L. P.; El Seoud, O. A. *Langmuir* **2001**, *17*, 652–658.
23. Mchedlov-Petrossyan, N. O.; Vodolazkaya, N. A.; Kornienko, A. A.; Karyakina, E. L.; Reichardt, C. *Langmuir* **2005**, *21*, 7090–7096.
24. Reichardt, C. *Pure Appl. Chem.* **2004**, *76*, 1903–1919.

25. Karukstis, K. K.; Frazier, A. A.; Loftus, C. T.; Tuan, A. S. *J. Phys. Chem. B* **1998**, *102*, 8163–8169.
26. Vitha, M. F.; Carr, P. W. *J. Chromatogr., A* **2006**, *1126*, 143–194.
27. Abraham, M. H.; Chadha, H. S.; Dixon, J. P.; Rafols, C.; Treiner, C. *J. Chem. Soc., Perkin Trans. 2* **1995**, *5*, 887–894.
28. Quina, F. H.; Alonso, E. O.; Farah, J. P. S. *J. Phys. Chem.* **1995**, *99*, 11708–11714.
29. Yang, S.; Khaledi, M. G. *Anal. Chem.* **1995**, *67*, 499–510.
30. Trone, M. D.; Khaledi, M. G. *J. Chromatogr., A* **2000**, *886*, 245–257.
31. Maria, P.-C.; Gal, J.-F.; De Franceschi, J.; Fargin, E. *J. Am. Chem. Soc.* **1987**, *109*, 483–492.
32. Abraham, M. H. *J. Phys. Org. Chem.* **1993**, *6*, 660–684.
33. Vitha, M. F.; Carr, P. W. *Sep. Sci. Technol.* **1998**, *22*, 2075–2100.
34. Poole, S. K.; Poole, C. F. *J. Chromatogr., A* **1998**, *798*, 207–222.
35. Poole, S. K.; Poole, C. F. *J. Chromatogr., A* **2008**, *1182*, 1–24.
36. Fuguet, E.; Ràfols, C.; Bosch, E.; Rosés, M.; Abraham, M. H. *J. Chromatogr., A* **2001**, *907*, 257–265.
37. Poole, S. K.; Poole, C. F. *Analyst* **1997**, *122*, 267–274.
38. Poole, C. F.; Poole, S. K.; Abraham, M. H. *J. Chromatogr., A* **1998**, *798*, 207–222.
39. Fuguet, E.; Ràfols, C.; Bosch, E.; Abraham, M. H.; Rosés, M. *J. Chromatogr., A* **2002**, *942*, 237–248.
40. Trone, M. D.; Khaledi, M. G. *Anal. Chem.* **1999**, *71*, 1270–1277.
41. Schnee, V. P.; Palmer, C. P. *Electrophoresis* **2008**, *29*, 767–776.
42. Abraham, M. H.; Chadha, H. S.; Dixon, J. P.; Rafols, C.; Treiner, C. *J. Chem. Soc., Perkin Trans. 2* **1997**, 19–24.
43. Quina, F. H.; Alonso, E. O.; Farah, J. P. S. *J. Phys. Chem.* **1995**, *99*, 11708–11714.
44. Rodrigues, M. A.; Alonso, E. O.; Yihwa, C.; Farah, J. P. S.; Quina, F. H. *Langmuir* **1999**, *15*, 6770–6774.
45. Rosés, M.; Ràfols, C.; Bosch, E.; Martínez, A. M.; Abraham, M. H. *J. Chromatogr., A* **1999**, *845*, 217–226.
46. Muijselaar, P. G.; Claessens, H. A.; Cramers, C. A. *Anal. Chem.* **1997**, *69*, 1184–1191.
47. Muijselaar, P. G.; Claessens, H. A.; Cramers, C. A. *Chromatographia* **1997**, *45*, 433–434.
48. Muijselaar, P. G. *J. Chromatogr., A* **1997**, *780*, 117–127.
49. Liu, Z.; Zou, H.; Ye, M.; Ni, J.; Zhang, Y. *J. Chromatogr., A* **1999**, *863*, 69–79.
50. Yang, S.; Khaledi, M. G. *J. Chromatogr., A* **1995**, *692*, 301–310.
51. García-Alvarez-Coque, M. C.; Torres-Lapasió, J. R.; Baeza-Baeza, J. J. *J. Chromatogr., A* **1997**, *780*, 129–148.
52. Guermouche, M. H.; Habel, D.; Guermouche, S. *Fluid Phase Equilib.* **1998**, *147*, 301–307.
53. García, M. A.; Vitha, M. F.; Marina, M. L. *J. Liq. Chromatogr. Relat. Technol.* **2000**, *23*, 873–895.

54. García, M. A.; Vitha, M. F.; Sandquist, J.; Mulville, K.; Marina, M. L. *J. Chromatogr., A* **2001**, *918*, 1–11.
55. Jiskra, J.; Claessens, H. A.; Cramers, C. A.; Kaliszan, R. *J. Chromatogr., A* **2002**, *977*, 193–206.
56. Mutelet, F.; Rogalski, M.; Guermouche, M. H. *Chromatographia* **2003**, *57*, 605–610.
57. Escuder-Gilbert, L.; Sagrado, S.; Villanueva-Camañas, R. M.; Medina-Hernández, M. J. *Biomed. Chromatogr.* **2005**, *19*, 155–168.
58. Hadjmohammadi, M. R.; Rezaie, M. *Iran J. Chem. Chem. Eng.* **2006**, *25*, 13–18.
59. Gil-Agustí, M.; Esteve-Romero, J.; Abraham, M. H. *J. Chromatogr.* **2006**, *1117*, 47–55.
60. Liu, J.; Sun, J.; Wang, Y.; Liu, X.; Sun, Y.; Xu, H.; He, Z. *J. Chromatogr., A* **2007**, *1164*, 128–138.
61. Torres-Lapasió, J. R.; Ruiz-Ángel, M. J.; García-Álvarez-Coque, M. C.; Abraham, M. H. *J. Chromatogr., A* **2008**, *1182*, 176–196.
62. Tian, M.; Kyung, H. R. *Bull. Korean Chem. Soc.* **2008**, *29*, 979–984.
63. Dorsey, J. G.; Deechegaray, M. T.; Landy, J. S. *Anal. Chem.* **1983**, *55*, 924–928.
64. Fu, C.; Khaledi, M. G. *J. Chromatogr., A* **2009**, *1216*, 1891–1900.
65. Fu, C.; Khaledi, M. G. *J. Chromatogr., A* **2009**, *1216*, 1901–1907.
66. Crommelin, D. J. A.; Schreier, H. In *Colloidal Drug Delivery Systems*; Kreuter, J., Ed.; Marcek Dekker: New York 1994.
67. Carrozzino, J. M.; Fuguet, E.; Helburn, R.; Khaledi, M. G. *J. Biochem. Biophys. Methods* **2004**, *60*, 97–115.
68. Helburn, R.; Dijiba, Y.; Mansour, G.; Maxka, J. *Langmuir* **1998**, *14*, 7147–7154.
69. Shin, D. M.; Schanze, K. S.; Whitten, D. G. *J. Am. Chem. Soc.* **1989**, *111*, 8494–8501.
70. Shin, D. M.; Whitten, D. G. *J. Phys. Chem.* **1988**, *92*, 2945–2956.
71. Moyano, F.; Biasutti, M. A.; Silber, J. J.; Correa, N. M. *J. Phys. Chem. B* **2006**, *110*, 11838–11846.
72. Moyano, F.; Silber, J. J.; Correa, N. M. *J. Colloid Interface Sci.* **2008**, *317*, 332–345.
73. Starke-Peterkovic, T.; Turner, N.; Vitha, M. F.; Waller, M. P.; Hibbs, D. E.; Clarke, R. J. *Biophys. J.* **2006**, *90*, 4060–4070.
74. Clarke, R. J. *Adv. Colloid Interface Sci.* **2001**, *89-90*, 263–281.
75. LeGoff, G.; Vitha, M. F.; Clarke, R. J. *Biochim. Biophys. Acta, Biomembr.* **2007**, *1768*, 562–570.
76. Owen, R. L.; Strasters, J. K.; Breyer, E. D. *Electrophoresis* **2005**, *26*, 735–751.
77. Agbodjan, A. A.; Bui, H.; Khaledi, M. G. *Langmuir* **2001**, *17*, 2893–2899.
78. Agbodjan, A. A.; Khaledi, M. G. *J. Chromatogr., A* **2003**, *1004*, 145–153.
79. Pascoe, R. J.; Foley, J. P. *Electrophoresis* **2003**, *24*, 4227–4240.
80. Pascoe, R. J.; Foley, J. P. *Electrophoresis* **2002**, *23*, 1618–1627.
81. Akbay, C.; Agbaria, R. A; Warner, I. M. *Electrophoresis* **2005**, *26*, 426–445.

82. Akbay, C.; Gill, N. L.; Powe, A.; Warner, I. M. *Electrophoresis* **2005**, *26*, 415–425.
83. Burns, S. T.; Agbodjan, A. A.; Khaledi, M. G. *J. Chromatogr., A* **2002**, *973*, 167–176.
84. Fuguet, E.; Ràfols, C.; Bosch, E.; Abraham, M. H.; Rosés, M. *Electrophoresis* **2006**, *27*, 1900–1914.
85. Burns, S. T.; Khaledi, M. G. *J. Pharm. Sci.* **2002**, *91*, 1601–1612.

Chapter 4

Supported Lipid Bilayer Electrophoresis for Separation and Analytical Studies of Cell Membrane Biomolecules

Susan Daniel* **and Ling Chao**

Cornell University, School of Chemical and Biomolecular Engineering, Ithaca, New York 14853
***sd386@cornell.edu**

Solid-supported lipid bilayer electrophoresis is a recently-developed technique for separating membrane-bound species within a native-like environment of a membrane. The key features of the supported bilayer that make this technique possible are two-dimensional fluidity of the membrane constituents and the ability to tune the bilayer chemistry and physical properties. Flexibility in tailoring membrane properties allows separations to be fine-tuned while allowing the analyte biomolecule of interest to maintain its native shape and orientation. Safeguarding biomolecule structure during purification is paramount for performing reliable analytical and diagnostic assays of biomolecule function and interaction after separation.

Introduction

A significant portion of the human genome is dedicated to coding for membrane species: nearly 35% of genes are used in the synthesis of membrane proteins (*1*) and about 5% are used to synthesize myriad lipids (*2*). A challenge in the area of membrane proteomics and lipidomics is development of tools to study these biomolecules that minimally impacts their structure because structure is intimately tied to function, and function to disease. New analytical tools must maintain a robust native-like environment of the cell membrane that preserves the shape, structure, and function of the membrane-associated biomolecule and ideally integrates purification and functional assay in one platform.

In Interfaces and Interphases in Analytical Chemistry; Helburn, R., et al.;
ACS Symposium Series; American Chemical Society: Washington, DC, 2011.

In this chapter, we will review the current state-of-the-art in membrane biomolecule separation and assay. The main focus will be to describe supported lipid bilayer electrophoresis, a technique that can be used to separate membrane biomolecules in a membrane environment that is similar to their native environment in the cell. We will start with an overview of the importance of these biomolecules in nature. Because membrane proteins are a primary target, we will discuss the state of the art in handling them with current techniques and highlight what advantaged bilayer electrophoresis could afford for this class of biomolecules. Next, the current status of bilayer electrophoresis for the separation of lipids will be provided. As a step towards extending the technique to transmembrane proteins, we will review the challenges associated with maintaining transmembrane protein mobility in supported lipid bilayers. Maintaining mobility of transmembrane species is probably the most significant challenge in extending this technique to proteins and so we will review the current status of this area. Once the mobility of the proteins can be maintained well, an understanding of the forces that drive biomolecule migration in these platforms and considerations for tuning these forces to maximize separation efficiency and spatial manipulation of these species will be critical. We include a section on the modeling of protein migration through the bilayer during electrophoresis. The chapter will end with some additional hurdles that must be overcome to extend support lipid bilayer electrophoresis to the manipulation and analysis of transmembrane proteins and strategies for overcoming those obstacles.

Studying the Roles of Membrane Species in Biological Function and Disease

Many proteins, lipids, and other biomolecules important in cellular communication and function are confined to the cell membrane. The cell membrane is essentially composed of lipids and other small amphiphilic molecules that together form a medium that supports the proper function of the proteins suspended within it. Thus the functions of proteins and the cell membrane are intimately coupled to each other. For example, the membrane properly orients the species in it and maintains their mobility. Proper orientation and mobility are vital for preserving protein structure and ensuring that correct interactions can take place within the membrane to form various constructs like ion channels, gates, and lipid rafts (*3*, *4*) as well as for ensuring proper interactions with soluble species from the extracellular and cytosolic spaces that initiate signaling cascades (Fig. 1). Disease results when interaction and signaling processes are hindered (*5*, *6*). In fact, the intention of more than 70% of drug targets is to interact with membrane species to alter biochemical pathways (*7*).

Since membrane proteins are a primary pharmaceutical target, an understanding of their structure-function relationships is key for disease prevention. However, progress has been slow in understanding their roles in biomolecular processes because there are few *in vitro* tools to study these proteins that preserve their native state and membrane environment. To reveal these roles, it is not enough to obtain the sequence of a target protein. A detailed proteomic

analysis is needed where sequence and structural data are combined with "functional" assays to probe molecular interactions within a native environment. This approach will aid in obtaining the full description of the structure-function relationships of membrane associated biomolecules (*8*).

Preserving the membrane environment in *in vitro* platforms would allow proteins in native conformations to be isolated while retaining their natural function and mobility, features that are vital for forming protein crystals for structure determination and for preserving native chemical activity for binding interactions with external species after separation. Other important aspects of an ideal *in vitro* platform are the ability to retain proteins of low abundance after separation and to interrogate their structural changes and chemical activity due to the presence of other membrane species and the surrounding lipids. Recent studies in the literature highlight that functions of membrane proteins should not be assessed without considering the likely important impact of the surrounding lipids and the protein-lipid interface on protein function (*9–11*). For example, it is has been shown that cholesterol analogs play an important role in maintaining activity in certain G-protein coupled receptors (GPCRs) (*9*).

State-of-the-Art in Protein Purification and Assay

It is difficult to study any kind of protein in vivo because of the complex composition of the cell and sequestration of proteins in various compartments. For example, water-soluble species can be sequestered inside cytosolic vesicles and membrane species are confined to the cell membrane. Therefore, proteins are typically removed from the cell, purified, and then interrogated in artificial assays (*8*). In the case of soluble proteins, finding the right experimental conditions to replicate the natural environment closely enough to preserve the protein's structure and function can be difficult. However, high throughput approaches (*12–15*) have enabled tens of thousands of soluble protein crystal structures to be solved. Additionally, studies of protein-protein interactions (*16*) have become rather routine, for example, via co-immuno precipitation assays, ELISA, and far-western blotting techniques (*17*, *18*).

The situation is more complicated for membrane proteins. To study these species, it is also usual practice to remove them from their native environment, i.e. the cell membrane, to purify them and decouple the functional assay from the chemical complexity of the membrane. Following membrane disruption, procedures for protein purification, handling, and crystallization generally mirror very closely the approaches and strategies used for soluble proteins. However, the rate in obtaining information about membrane proteins is in stark contrast to soluble species. Only about one hundred transmembrane protein crystal structures are known with incomplete pictures of their functions and activity (*7*, *16*, *19*). In fact, of the ~1000 GPCRs identified, less than ten unique structures have been solved to date (*20–26*)! The paucity of information on membrane proteins results from a lack of available approaches that can isolate and interrogate the interactions and functions of these proteins within a tunable platform that preserves their

In Interfaces and Interphases in Analytical Chemistry; Helburn, R., et al.;
ACS Symposium Series; American Chemical Society: Washington, DC, 2011.

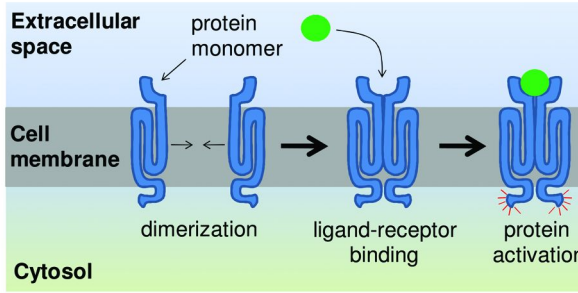

Figure 1. Illustration of some common protein functions in a cell membrane that depend on protein mobility and orientation: inter-membrane protein reactions like dimerization, binding of small molecules (green) from the extracellular space to protein receptors, and protein activation and structural changes to initiate signaling cascades inside the cell. Adapted from Alberts et al. (3). (see color insert)

membrane environment (*27*). Preserving a membrane environment is crucial for at least three reasons:

1) Membrane proteins outside their native environment are extremely unstable and either form unnatural conformations to mask their hydrophobic cores, or simply denature.
2) When the native conformation is lost, binding pockets can be altered or concealed, thus preventing homologous interactions for crystal formation and/or interactions with other species. This increases the unreliability of results obtained from interaction assays.
3) To ascertain the role of membrane lipids in protein interactions and conformation, it is reasonable that the protein should be preserved in "as close to as possible" conditions that mimic the membrane where two-dimensional fluidity, orientation of the active group, and lipid interactions are maintained.

The Gold-Standard in Proteomics: Blotting Techniques

Assaying protein-protein interactions is often carried out by western blot (*28*). The protein of interest is expressed in a host cell, which is then lysed using detergents and sonication to extract the protein from it. Denatured protein is separated into distinct pure bands by gel electrophoresis. To blot, a thin film is placed on the gel to extract the purified protein out of the gel onto the film. Non-specific adsorption is minimized by absorbing sacrificial protein between protein stripes. Finally, "bait" protein is added to assess interactions, usually detected by fluorescence (Fig. 2, top).

While blotting techniques seem to work sufficiently well for some detection purposes there are several downfalls for obtaining quantitative analytical information, especially for membrane species (*28*), listed below:

1) Complete protein transfer is rarely achieved and makes quantitative analysis difficult and impossible for low abundance proteins.
2) Proteins blotted onto the film are immobilized, probably denatured and oriented improperly, and consequently inactive. Unnatural conformations or exposed sites can give false positives, while active sites oriented against the film and shielded from interacting can give false negatives.
3) Many proteins carry out their "functions" after activation with a soluble molecule that causes monomers of protein in the membrane to form multimers. Formation of multimers can only occur if the protein is suspended in a mobile environment where other activated monomers are located and rotation and translation can occur to form proper constructs.
4) Protein function can be intimately tied to surrounding membrane environment (e.g. composition or fluidity) and these subtleties cannot be assessed in the absence of a membrane.
5) Blotting times range from 2 – 16 hours. Such a long transfer time puts a limit on this technique's ability to do rapid screening and analysis.

Many of these downfalls could be overcome by creating a platform that includes a membrane mimic, such as solid-supported bilayer electrophoresis (Fig. 2, bottom), where both separation and interaction assay could be carried out serially without requiring a blotting step.

Other Biophysical Approaches to Assaying Protein Behavior

In addition to blotting assays, other biophysical approaches can be used to obtain information about protein interactions and function. These assays often interrogate protein behavior downstream from the purification process. For example binding kinetics and structural changes can be assessed using surface plasmon resonance (SPR) (*29–34*). Infrared spectroscopy (FTIR) and circular dichroism (CD) can be used to obtain orientational information about proteins and basic structural features such as alpha helix content (*35*). Solid state NMR is also another prevalent technique used to assess protein and membrane structure. In most of these techniques, membrane mimics can be included to house proteins. Protein behavior before and after exposure to other proteins and/or chemicals can be assessed. A good review of other various biophysical techniques, recent advances, and outstanding issues in applying them to transmembrane proteins species can be found in reference (*36*), and articles therein. Integrating these techniques, where possible, with a separation strategy such as supported lipid bilayer electrophoresis would result in an all-in-one platform that purifies, interrogates interactions, and assesses structural information of both the protein and membrane.

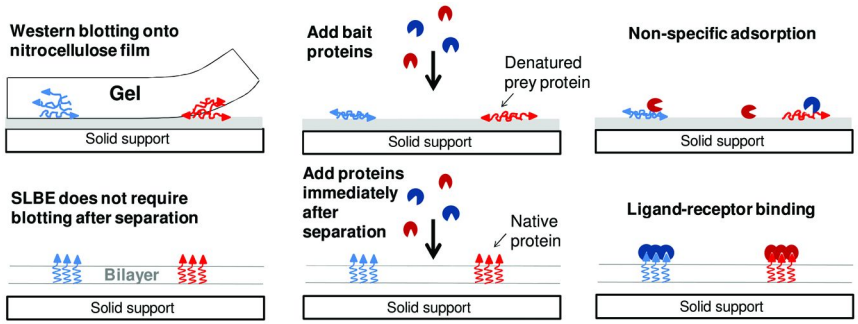

Figure 2. (Top) Blotting of purified protein bands after separation by gel electrophoresis and transfer onto a nitrocellulose film (gray). (Bottom) Separation of proteins by supported lipid bilayer electrophoresis (SLBE) followed by binding with bait proteins. (see color insert)

Supported Lipid Bilayer Electrophoresis

Solid supported lipid bilayer electrophoresis (SLBE) is an *in vitro* method of biomolecule separation that uses a membrane mimic as the separation medium where easy tuning and tight control of the composition of the membrane and its surrounding environment is possible. Recently it has been shown that SLBE can be used to separate lipids and detect subtle differences between isoforms within the native environment of a lipid bilayer (*37*). The ability to separate and identify nearly identical chemical species should afford an unprecedented opportunity to purify membrane-bound species, identify them, and determine their interacting partners through subsequent analytical assays. The separation technique is analogous to gel electrophoresis, except the gel is replaced by a supported bilayer. Membrane species separated in the bilayer medium do not have to be subjected to the harsh, denaturing conditions of typical gel electrophoresis preparations; therefore they should retain their native structure, functionality, and proper orientation for subsequent experiments. Furthermore, since the separation is carried out in the membrane platform, the interaction assay can be carried out immediately following the separation. These features make for an attractive alternative to current blotting techniques to assay protein-protein interactions. Additionally, several other applications of gel electrophoresis should extend to bilayer electrophoresis as well, such as isoelectric focusing for charge determination and detecting proteins for disease diagnosis. Moreover, bilayer electrophoresis could enable additional applications that cannot be achieved with gel electrophoresis, like 2D crystal formation, analysis of lipid-protein interactions, and spatial addressing for applications such as protein sensor arrays. Finally, coupling this separation technique with other "downstream" biophysical techniques could create other all-in-one platforms for interrogating these species in a way that does not currently exist.

Previous Work Combining Electrophoresis and Membranes

Early discussions of electrophoresis to redistribute components in cell membranes were reported in a series of two papers in *Nature* by Jaffe (*38*) and Poo and Robinson (*39*) in 1977. Jaffe's paper focuses on the theory of redistribution of components in an electric field, while Poo and Robinson's paper provides data on the rearrangement of concavalin A receptors in muscle cells. Following these publications were several from Poo and coworkers (*40*, *41*) on electrophoresis and diffusion in the plane of the cell membrane and the role of electroosmosis on macromolecular redistribution in cell surfaces. Stelzle and coworkers (*42*) were the first to report using supported lipid bilayers to study electrophoresis. In their studies, they examined the separation of two oppositely-charged species by electric field. Since then several papers have been published on the electrical manipulation of fluorescently-labeled lipids (*37*, *43–47*), GPI-linked proteins (*48*), molecular separation of species differing by a single charge using microfabricated labyrinths of diffusion barriers (*49*), and vesicles tethered to the bilayer using DNA hybridization (*50*, *51*). More recently, electrophoresis was used to study the frictional drag of recombinant proteins attached by His-tags to Ni-NTA lipids in a monolayer supported on a tethered polymer cushion (*52*). Most recently, supported lipid bilayer electrophoresis (SLBE) was used to determine the charge of streptavidin, a surface-associated protein, that was conjugated to the bilayer with a biotinylated-lipid headgroup (*53*). Finally, a demonstration of one possible scale-up strategy for the electrophoretic separation of charged biomolecules supports bilayers on silica particles to increase the surface area (*54*).

Supported Lipid Bilayers as an Assay Platform

Preparation and Properties

A supported bilayer is essentially a thin, continuous, planar fluid film of lipids that is adsorbed to a hydrophilic surface, typically glass. The bilayer is formed when small unilamellar vesicles fuse to the surface through a balance of van der Waals, electrostatic, hydrophobic, steric, and hydration forces (*55–57*). The balance of these forces leads to the formation of a thin layer of water between the bilayer and the underlying solid support. This water layer helps to maintain the lateral mobility of lipids in both leaflets of the bilayer (*58*), preserving this important biophysical property of biological membranes (Fig 3). Lateral fluidity is key in protein interactions within the membrane, such as protein dimerization (*59*) and multivalent ligand-receptor recognition events with bulk species (*60*). Without mobility, these and many more processes cannot be carried out as they are *in vivo*.

The planar geometry of the supported bilayer makes it compatible with a number of surface analytical tools or techniques such as: total internal reflection fluorescence microscopy (TIRF), fluorescence recovery after photobleaching (FRAP), Fluorescence correlation spectroscopy (FCS), surface plasmon resonance (SPR), atomic force microscopy (AFM), and x-ray reflectivity. Diffusion and mobility can be easily measured using FRAP (*61*, *62*) or FCS (*63*). SPR is used

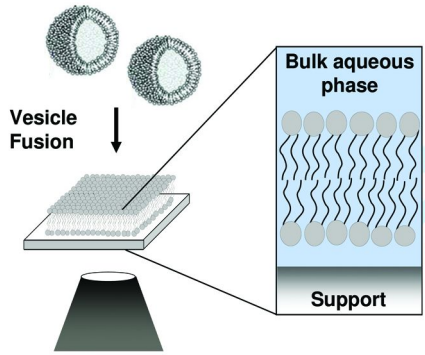

Figure 3. Formation of a supported lipid bilayer by self-assembly from small unilamellar vesicles. Supported bilayers are amenable to many kinds of microscopy and spectroscopy because of their planar geometry. (Inset) Bilayers form with a thin water layer between the bottom leaflet and the support. Individual lipids in both leaflets are mobile, and within a leaflet, they exchange places with each other on the order of 100 nanoseconds in a plain phosphocholine bilayer. (see color insert)

to measure binding kinetics of molecules to surfaces and can detect interactions between proteins and lipid membranes as well as protein-protein interactions. AFM is routinely used to study biomolecule structure and dynamics in supported bilayers from lipid raft formation (*64*) to two-dimensional protein crystals (*65*). Recently, x-ray reflectivity studies using SLBs have provided information about protein-lipid behavior (*66*).

Preparation of Supported Lipid Bilayers for Electrophoresis Experiments

Here, we illustrate how to prepare and implement the supported lipid bilayer electrophoresis technique to separate charged lipid molecules (Fig. 4). In panel 1, a separation bilayer (gray) is formed by vesicle fusion to the glass support. In panel 2, a thin section is removed from the supported bilayer by stamping with the edge of a polydimethylsiloxane-coated (PDMS-coated) coverslip glass slide (*47*). This thin section is removed so that vesicles containing the species to be separated, in this case fluorescently-labeled lipids denoted by the red, pink, and green colors, can be fused into the open space and healed with the surrounding bilayer, as shown in panel 3. This process of "loading" the membrane is analogous to forming wells in a gel using a "comb" and then injecting a protein mixture into the wells. In panel 4, after a voltage potential is applied laterally for a period of time, the charged molecules have migrated towards the opposite pole, and separated into the three distinct colored bands.

The same theme could be applied to other membrane species such as membrane proteins, as long as protein mobility can be maintained. Strategies for maintaining protein mobility in these platforms will be discussed in later sections of this chapter.

In Interfaces and Interphases in Analytical Chemistry; Helburn, R., et al.;
ACS Symposium Series; American Chemical Society: Washington, DC, 2011.

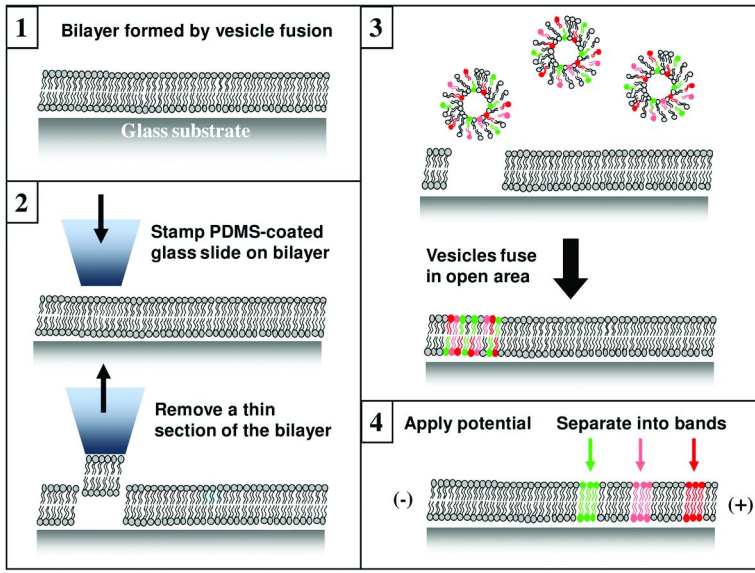

Figure 4. Sample preparation and implementation of solid-supported bilayer electrophoresis. (see color insert)

Experimental Results for Separation of Lipid Isomers by SLBE

SLBE can be used to separate fluorescent lipid isomers (Fig. 5). Two experiments using two different separation bilayer formulations illustrate the sensitivity of the separation of fluorescently-labeled lipid isomers to the composition of the surrounding bilayer medium. In Fig. 6, on the far left-hand side of the bilayer liposomes containing charged isomers of a fluorescently-labeled lipid (Texas red 1,2-dihexadecanoyl-*sn*-glycero-3-phosphoethanolamine, triethyl ammonium salt (TR-DHPE) were fused next to separation bilayers composed of zwitterionic lipids. An electric field (100 V/cm) was applied parallel to the solid-supported membrane for about 30 minutes in both experiments. The electric field induced electroosmotic flow in the aqueous solution above the bilayer as well as an electrophoretic force on the charged species. These forces caused the fluorescently-labeled isomers to migrate with varying velocities based on their size, orientation, and interactions with the surrounding zwitterionic bilayer medium and aqueous medium bathing the bilayer. To achieve separation, it was found that the composition of the zwitterionic bilayer medium was critically important. Separation bilayers made exclusively of 1-palmitoyl-2-oleoyl-*sn*-glycero-3-phosphocholine (POPC) lipids did not separate the Texas red-conjugated lipid isomers well (Fig. 6, left) because lipids remixed rapidly by Brownian diffusion. However, reducing the diffusion of the bilayer by adding cholesterol to it minimized band-broadening and achieved the much better separation as shown in Fig. 6, right.

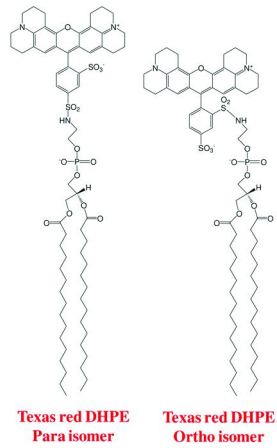

Figure 5. Isomers of Texas red 1,2-dihexadecanoyl-sn-glycero-3-phosphoethanolamine, triethyl ammonium salt (TR-DHPE).

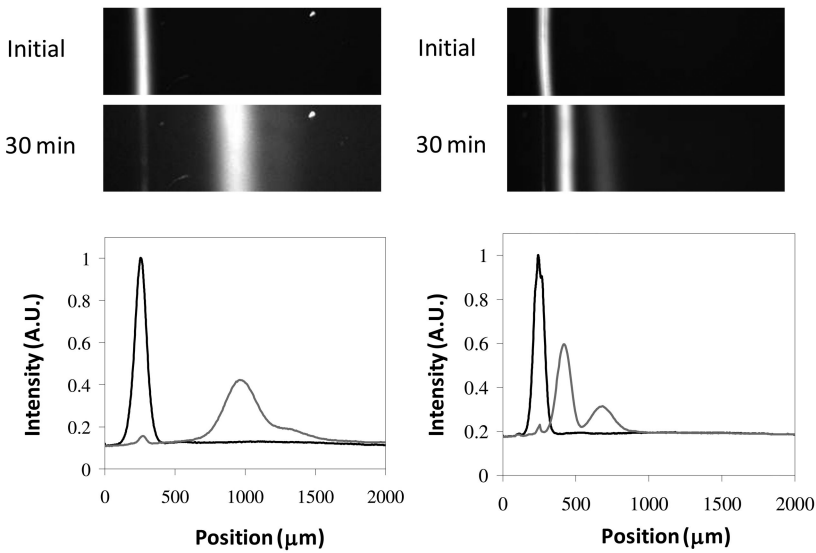

Figure 6. (Left) Electrophoresis of Texas red isomers in a plain POPC bilayer, initially and after 30 min, of applied potential (100V/cm). Linescans below images quantify fluorescence level, which roughly converts to concentration. (Right) Electrophoresis of the same isomer mixture, in a separation bilayer containing POPC and 25 mol% cholesterol. Separation is complete after 30 minutes, with tighter, more concentrated bands.

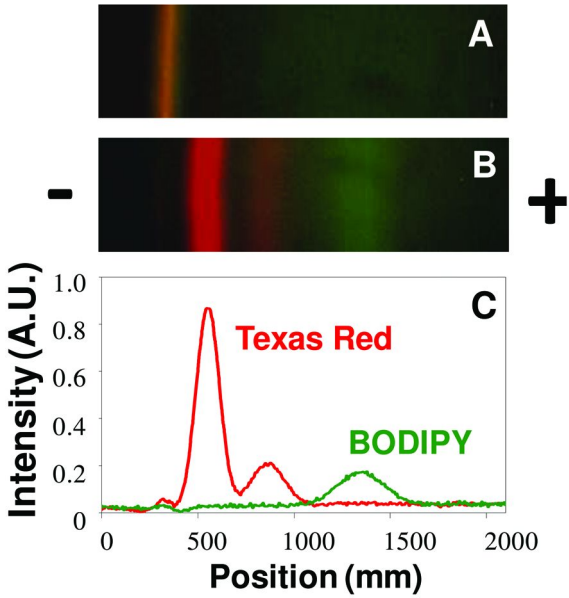

Figure 7. Separation of fluorescent lipids of identical charge. Image (A) is the initial position of the mixture, image (B) is after 30 min of applied potential (100 V/cm), and (C) is a linescan of the fluorescence intensity across image (B). (see color insert)

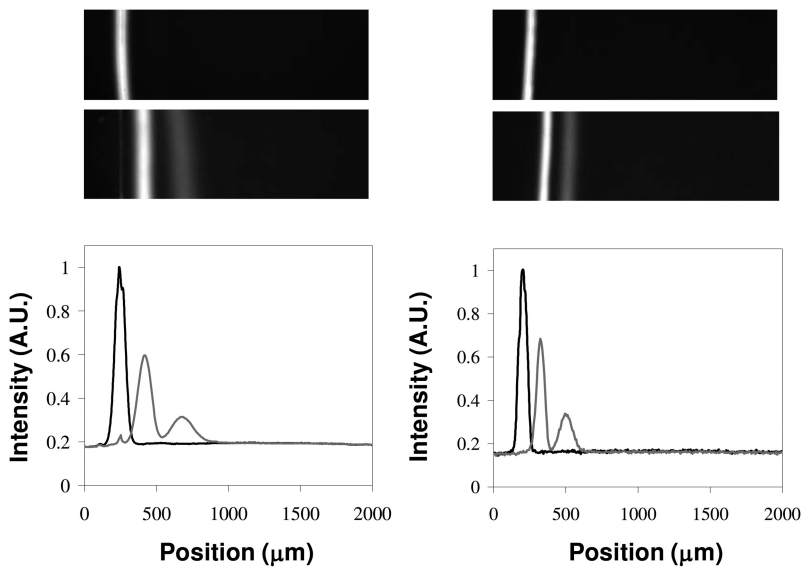

Figure 8. Separation of Texas red isomers in POPC + 25 mol% cholesterol (left) and DLPC + 25 mol% cholesterol (right) after 40 minutes of 100 V/cm applied potential.

Three different fluorescently-labeled lipids of identical charge (two isomers of Texas red 1,2-dihexadecanoyl-*sn*-glycero-3-phosphoethanolamine, triethyl ammonium salt (TR-DHPE) and a green-labeled lipid, N-(4,4-difluoro-5,7-dimethyl-4-bora-3a,4a-diaza-*s*-indacene-3-propionyl)-1,2- dihexadecanoyl-*sn*-glycero-3-phosphoethanolamine, triethyl ammonium salt (BODIPY-DHPE)) were separated using a POPC bilayer containing 25 mol% cholesterol, as shown in Fig 7. 25 mol% cholesterol was used in this experiment because it worked well for the TR DHPE separation and the aim was to simply demonstrate that multiple species could be separated using this method. Thus, the composition of the separation bilayer was not optimized for separation efficiency here; nonetheless, an excellent separation of these different lipids is apparent since the intensity returns nearly to background between the peaks. This demonstration of using SLBE to separate these lipids suggests that this method could be extendable to separating many more species into distinct bands in one experiment.

Tuning Membrane Composition Aids Separation

Recent experiments using other kinds of lipids in the separation bilayer, such as 1,2-dilauroyl-*sn*-glycero-3-phosphocholine (DLPC) and cholesterol yielded higher resolution of the bands with the same operating time (Fig. 8). Thus, tuning lipid composition and additives can improve the separation of the membrane species of interest. For example, various kinds of cholesterol, charged lipids, lipid raft biomolecules, proteins, and glycolipids, could be included to tune the mobility of species in the bilayer to obtain a desired separation. Diversity of bilayer composition and biophysical properties can be exploited in various ways to enhance separation. For example, preliminary data from our laboratory shows that including heterogeneous domains in separation bilayers, for example, can be used to preferentially partition molecules into regions of the bilayer that reduces their mobility, such that separation from a non-partitioning species is enhanced.

Modeling Electrokinetic Motion of Biomolecules in Membranes

Electrokinetic Forces on Biomolecules in Bilayers

Modeling the drift velocity of a lipid membrane associated molecule, such as a protein, is straightforward (*41*, *50*, *53*). In the following description, the forces acting on the portion of the protein embedded in the membrane and on the parts extending into the external aqueous medium are considered. Fig. 9 shows a molecule with portion *M* embedded in the membrane and with portion *A* extending in the external solution. Three forces are considered to act on this molecule: the electrical force due to an external electric field (F_E), the hydrodynamic force resulting from the aqueous medium (F_{HA}), and the drag force in membrane (F_{DM}). No effect of the support is considered here, although that force would be easy to integrate into this analysis. When an electric field is applied to a charged molecule and steady state is reached, the molecule's drift velocity is constant, indicating the sum of all forces exerting on the molecule is zero. This situation is described by the following equation:

$$F_{HA} + F_{DM} + F_E = 0 \quad (1)$$

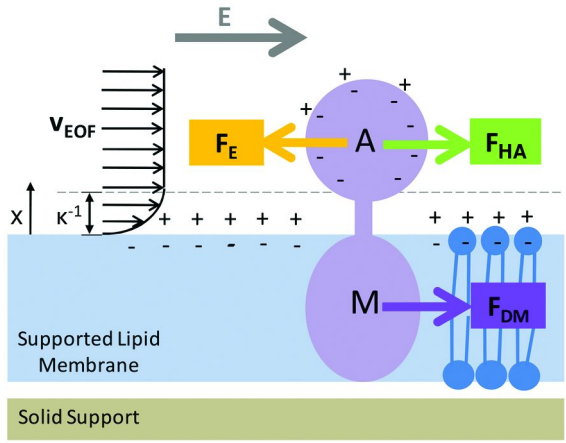

Figure 9. Model of a lipid membrane associated molecule (the purple object) in the electric field (E). The portion A is charged and in the aqueous medium, and the portion M is in the membrane. F_E is the electrical force due to an external electric field, F_{HA} is the hydrodynamic force from the aqueous medium, and F_{DM} is the drag force in membrane. Here, the membrane surface has negative charge and attracts the positive ions in the aqueous medium to accumulate near the membrane, resulting in a diffuse electric double layer adjacent to the surface with a characteristic thickness κ^{-1} (Debye length). The force exerting on the diffuse layer causes an electro-osmotic flow with velocity v_{EOF} in the bulk solution. Diagram adapted from ref (67). (see color insert)

Hydrodynamic Force due to the Aqueous Medium

First, we consider the hydrodynamic force (F_{HA}) on the biomolecule resulting from the flow of the aqueous medium induced by an electro-osmotic flow of ions. Under the condition of low Reynolds number, which is valid for the movement of molecules associated with lipid membranes, the drag force can be calculated by Stokes' law (*68*). The force exerted by the aqueous medium on the molecule is equal to the drag coefficient times the velocity of the flow with respect to the particle. For a sphere, the force based on Stokes' law can be expressed as:

$$F_{HA} = 6\pi\eta_a r_a (v_{EOF} - v) \quad (2)$$

where η_a is the viscosity of the aqueous medium, r_a is the effective radius of the portion *A* of the protein, v is the velocity of the molecule, and v_{EOF} is the velocity of the electro-osmotic flow.

A charged surface attracts counter-ions to accumulate near the surface, forming a diffuse electric double layer. Applying an external electric field creates a force on the diffuse ion layer, which results in an electro-osmotic flow of the

In Interfaces and Interphases in Analytical Chemistry; Helburn, R., et al.;
ACS Symposium Series; American Chemical Society: Washington, DC, 2011.

aqueous medium. The flow velocity profile in the unbound aqueous medium away from the surface can be expressed as (*69*):

$$v_{EOF} = \frac{-\varepsilon_0 \varepsilon_r \zeta_{EOF} E}{\eta_a}(1 - \exp(-\kappa x)) \tag{3}$$

where the velocity is expressed in the direction of electric field, ε_0 is the permittivity of free space, ε_r is the dielectric constant of the medium, κ is the reciprocal of the Debye length (expressed in Equation 4), x is the distance away from the membrane surface, and ζ_{EOF} is the zeta potential of the membrane surface. The zeta potential is the electric potential at the hydrodynamic plane of shear, which can be measured experimentally or can be estimated by the Gouy-Chapman model if the surface charge density and the location of the shear plane are known (*50*, *53*, *70*). The Debye length is the characteristic thickness of the diffuse electric double layer and can be expressed as:

$$\kappa^{-1} = \sqrt{\frac{\varepsilon_0 \varepsilon_r k_B T}{2 N_A e^2 I}} \tag{4}$$

where k_B is the Boltzmann constant, T is the absolute temperature, N_A is the Avogadro number, e is the elementary charge, and I is the ionic strength of the electrolyte solution. Notice that the Debye length can be varied by changing the solution's ionic strength: 100 mM aqueous solution results in ~1 nm Debye length and 10 mM solution results in ~10 nm Debye length.

In the region where x is much larger than the Debye length ($\kappa x >> 1$), the exponential term goes to zero and velocity is no longer a function of x (*71*). If the portion A of the biomolecule (in Fig. 9) locates in this uniform-velocity region, Equation 2 becomes:

$$F_{HA} = 6\pi\eta_a r_a \left(\left(\frac{-\varepsilon_0 \varepsilon_r \zeta_{EOF} E}{\eta_a} \right) - v \right) \tag{5}$$

However, if the location of the portion A is not much larger than the Debye length, the hydrodynamic force, F_{HA}, needs to be obtained by integrating the force varying with x.

Drag Force on a Protein due to the Membrane

Second, we consider the drag force on the portion of the protein suspended in the membrane (M in Fig. 10). Here, we view the membrane as a 3-D unbound medium and apply Stokes' law to obtain the drag force (*41*, *50*, *53*). The Stokes' drag resulting from the membrane medium for both spherical (*41*, *53*) and cylindrical geometry (*50*) have been used in previous literature to model the portion embedded in the membrane. Cylindrical geometry is probably more

In Interfaces and Interphases in Analytical Chemistry; Helburn, R., et al.;
ACS Symposium Series; American Chemical Society: Washington, DC, 2011.

representative for a transmembrane protein with hydrophobic α-helixes in the membrane. Expressions for spherical or cylindrical geometry are given below:

$$F_{DM} = \begin{cases} -6\pi\eta_m r_m v & \text{for sphere with radius } r_m \quad (6a) \\ -\dfrac{4\pi\eta_m L}{\ln(\dfrac{L}{2r_m}) + 0.84} v & \text{for cylinder with height L and radius } r_m \quad (6b) \end{cases}$$

where η_m is the viscosity of the membrane, r_m is the effective radius of the portion M, L is the height of the portion M if viewed as a cylinder, and v is the velocity of the molecule. Drag coefficient expressions for other geometries can be found in the book by Howard (*72*). In experiments, Gambin et al. (*73*) have shown that the measured mobility of membrane-bound proteins can be well fitted to Stokes' form.

Force due to the Electric Field

The third force to consider is that exerted on the charged portion of the biomolecule by the external electric field. If the charged portion is in the medium with no ion atmosphere, the electrostatic force on the charged portion is the product of charge and electric field strength. However, if we consider that the charged portion is in the aqueous medium, the situation is complicated by the interaction between the charged portion and its ion atmosphere. The external electric field applies force not only to the charge portion of the molecule but also to the surrounding ion atmosphere. The force applied to the counter-ions surrounding the charged portion has an opposite direction to the force applied to the charged portion and is transferred to the charged portion surface by viscous stress, which is known as "electrophoretic retardation" (*71*). In addition, the ion distribution in the ion atmosphere can shield the charge and deform and reduce the electrostatic force, an effect which is known as the "relaxation effect" (*71*).

To consider the combination of all these forces due to the externally applied electric field, we view the charged portion of the biomolecule extending into the aqueous medium as a freely suspended charged particle with the same zeta potential (ζ_a). There are four forces acting on a charged particle: first is the electric force on the charge of the particle (k_1); second is the Stokes' friction (k_2); third is the electrophoretic retardation force (k_3); and the fourth is the force due to the relaxation effect (k_4). When the particle reaches steady state, the net force is zero. Thus, the net force by the electric field (F_E) is equal to the Stokes' friction.

$$F_E = k_1 + k_3 + k_4 = -k_2 = -f_c U \quad (7)$$

where f_c is the friction coefficient, U is the velocity of the freely suspended charged particle.

The generally used Helmholtz-Smoluchowski equation (Equation 8) which describes the electrophoretic mobility of a freely suspended charged particle is

obtained by considering the force balance of k_1, k_2, and k_3 of the particle. The relaxation effect is not considered (k_4 is set to be zero). The k_1 value is equal to the particle charge multiplied by the electric field strength, and the k_3 value is derived by considering the force balance of viscous force and electrostatic force to the ions in the aqueous medium surrounding the particle inside the hydrodynamic shear plane of the particle (*71*).

$$\frac{U}{E} = \frac{\varepsilon_0 \varepsilon_r \zeta_a}{\eta_a} \tag{8}$$

Where U is the particle velocity with respect to the bulk aqueous medium, E is the strength of the electric field, ζ_a is the zeta potential of the charged particle, and η_a is the viscosity of the aqueous medium. The equation is valid when the radius of the particle is much larger than the Debye length ($\kappa r_a >> 1$). For moderate κr_a value, the "relaxation effect" can be significant (*74*) and the corrections are determined numerically (*75*).

If we assume the charged portion is spherical ($f_c = 6\pi\eta_a r_a$) and the Helmholtz-Smoluchowski equation is valid, the net force on the charged particle due to the externally applied electric field is:

$$F_E = 6\pi r_a \varepsilon_0 \varepsilon_r \zeta_a E \tag{9}$$

Now, we can substitute the expressions of F_E, F_{HA}, and F_{DM}, to Equation 1 to obtain a membrane molecule's electrophoretic mobility. Note that these expressions are for a membrane molecule with the charged portion in the aqueous medium. We also assume in the following expressions that the length scale of the portion in the aqueous medium is much larger than the Debye length of membrane surface so that it is exposed to an electro-osmotic flow with uniform velocity.

Equation 10 is the electrophoretic mobility expression when Stokes' law for a sphere is applied to model the drag force of the membranous portion:

$$\frac{v}{E} = \frac{\varepsilon_0 \varepsilon_r r_a (\zeta_a - \zeta_{EOF})}{r_a \eta_a + r_m \eta_m} \tag{10}$$

Equation 11 applies to the situation where the membranous portion is approximated by a cylinder:

$$\frac{v}{E} = \frac{3\varepsilon_0 \varepsilon_r r_a (\zeta_a - \zeta_{EOF})}{3 r_a \eta_a + \dfrac{2\eta_m L}{\ln\left(\dfrac{L}{2r_m}\right) + 0.84}} \tag{11}$$

When the mobilities of two or more species in the membrane are different, separation will occur. The above equations show the dependence of mobility on various parameters that can be varied to improve separations. For example, changing the composition of the membrane to modify its viscosity can be an advantage when one molecule has a bigger interface with the membrane or prefers

In Interfaces and Interphases in Analytical Chemistry; Helburn, R., et al.;
ACS Symposium Series; American Chemical Society: Washington, DC, 2011.

to interact more strongly with a particular additive. This effect is observed in the above sections on lipid separation where separation was enhanced by the inclusion of cholesterol in the membrane.

Challenges Ahead for Transmembrane Protein SLBE

Mobility of Transmembrane Proteins in Supported Lipid Bilayers to Date

A major drawback of conventional SLB platforms has been the inability to maintain extensive mobility of transmembrane proteins. To overcome this difficulty, the interaction between the lipids, proteins, and other constituents with the bare solid surface must be minimized. However, bilayers that are directly supported on a surface such as borosilicate glass are only separated from the support by a thin (~1 nm) layer of water (*76*–*78*). This water layer does not provide sufficient spacing between the membrane and the support to prevent the exposed extracellular domains of an integral membrane protein from interacting directly with the solid support (*79*). Therefore, challenges still exist to prevent transmembrane proteins from losing lateral mobility and function in standard SLB platforms.

The logical strategy to overcome this problem is to create a space between the support and membrane large enough to house the extracellular part of the protein to reduce the frictional coupling between incorporated proteins and the solid support (*80*–*83*). The most successful implementations of this strategy places a soft polymeric material, of thicknesses typically less than 100 nm, between the phospholipid membrane and the bare substrate. The polymer acts as a porous support, similar to the cytoskeleton found in actual mammalian cell membranes. Prominent methods for the preparation of polymer supports include: a) the chemical grafting of a soft polymer to the solid support (*83*), b) the reconstitution of lipopolymers into vesicles that automatically provide spacers between themselves and the support upon adsorption and fusion of the vesicle to form a bilayer (*84*), and c) the deposition of soft hydrophilic multilayers of molecules with alkyl side chains (*85*).

While there is a plethora of spacing strategies to choose from, fewer reports are available describing the use of supported systems to study the lateral mobility of transmembrane proteins (*81*, *82*, *86*). One of the best results to date, by Tamm and coworkers (*82*), uses a polyethylene glycol-phospholipid conjugate covalently bound to the silicate substrate. Lateral diffusion of cytochrome b5 and annexin V were measured by fluorescence recovery after photobleaching (FRAP) (*61*, *62*). Although lateral diffusion coefficients were obtained, only ~ 25% of the proteins diffused with diffusion constants that were of the same order of magnitude as the lipids (~3 x 10^{-8} cm^2/s). The rest of the protein molecules diffused extremely slowly or not at all. Another protein mobility study was performed by Tanaka, Sackmann, and coworkers (*81*). In this case, human platelet integrin αIIbβ3 was investigated in an SLB that rested on a cellulose cushion. Again, only about one quarter of the proteins were mobile in the presence of the cushion and none were mobile without it. In a third example, Smith, Wirth, and coworkers studied the mobility of the human delta-opioid receptor on acrylamide

In Interfaces and Interphases in Analytical Chemistry; Helburn, R., et al.;
ACS Symposium Series; American Chemical Society: Washington, DC, 2011.

cushions of various thicknesses (*86*). In this case, however, only data for an individually mobile protein molecule was reported rather than the mobile fraction for a population of membrane embedded proteins. Finally, Davis and coworkers (*87*) used nanoporous microbeads rather than a polymer cushion to support lipid membranes with bacteriorhodopsin. High protein mobile fractions were obtained (~78%) with D = 3.8 x 10^{-10} cm^2/sec for proteins in the pores of the beads. Note that these are some of the best results published in the literature to date and other cushions met with lesser degrees of success.

Double Cushions Bolster Transmembrane Protein Mobility in SLBs

A novel strategy to overcome transmembrane immobility in SLBs uses a lipid bilayer supported on a *double cushion*, to not only create a large space to accommodate the transmembrane portion of the macromolecule, but to also passivate the underlying support to reduce non-specific protein-support interactions (*88*) (Fig. 10). Passivation of the support is essential because inevitably, due to the natural undulations of the flexible bilayer (which grow as the distance between the membrane and the support increases), transmembrane species still occasionally contact the underlying support. However, this interaction can be minimized by a coating of sacrificial protein on the glass surface, so that if the transmembrane portion of the protein does come into contact with the support it can "bounce" back rather than getting stuck permanently. The thickness of the confined water layer between the passivation layer and a bilayer can be tuned by fusing vesicles containing polyethylene glycol (PEG)-conjugated lipids of various molecular weights (*84*, *88–90*).

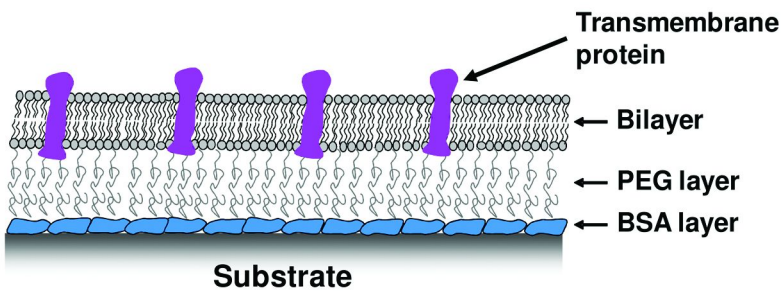

Figure 10. Illustration of the double cushion strategy for achieving transmembrane mobility in planar supported bilayers. The sacrificial layer is a thin coating of bovine serum albumin (BSA). The spacer is a layer of polyethylene glycol (PEG) upon which the bilayer rests. Within the plane of the bilayer, membrane proteins and lipids can translate and rotate. (see color insert)

In these experiments, two-dimensional fluidity of lipids and annexin V (a transmembrane protein channel) were characterized by FRAP. Uniform and mobile phospholipid bilayers with lipid diffusion coefficients around 3×10^{-8} cm^2/sec and percent mobile fractions over 95 % were obtained. Annexin V diffusion constants were around 3×10^{-8} cm^2/sec with mobile fractions up to 75%. These values are a significant improvement over results obtained in bilayers fabricated directly on glass or using single cushion strategies described above. This cushioning strategy should yield mobile transmembrane proteins so that electrophoretic motion of these species through supported bilayers is minimally impeded by the underlying support.

Looking Ahead

The challenges ahead for extending solid-supported bilayer electrophoresis to transmembrane proteins are not negligible; however, the impact of progress here can have far-reaching possibilities, from creating better pharmaceutical screening tools to protein crystallization platforms, which would lead to significant advances in understanding this important class of biomolecules. The main problems to tackle are: 1) extracting protein from a cell membrane and getting it into the platform without compromising its integrity, 2) maintaining a high level of mobility of the proteins with an appropriate cushioning strategy, 3) optimizing the bilayer composition to maximize separation efficiency, 4) managing Joule-heating issues that arise from high salt content of buffer solutions required for proteins, and 5) scale up of this technique to yield higher throughput assay. Just as microfluidic approaches enabled high-throughput experimentation to significantly advance our understanding of soluble proteins, it is possible that the integration of microfluidics with supported lipid bilayer electrophoresis could enhance our ability to rapidly collect and synthesize data on this important class of biomolecules. Microfluidics will also help with Joule heating control because of the small size and the ease of coupling them to cooling stages. These devices are compatible with many cushion strategies and bilayer formation as well. Thus, extension to membrane proteins will eventually be realized.

Acknowledgments

The National Science Foundation (Grant # EEC 0824381) supported some of the work presented in this chapter.

References

1. Loll, P. J. *J. Struct. Biol.* **2003**, *142*, 144–153.
2. van Meer, G.; Voelker, D. R.; Feigenson, G. W. *Nat. Rev. Mol. Cell Biol.* **2008**, *9*, 112–124.
3. Alberts, B.; Johnson, A.; Lewis, J.; Raff, M.; Roberts, K.; Walter, P. *Molecular Biology of the Cell*, 4th ed.; Garland Science: New York, 2002.

4. Horejsi, V.; Drbal, K.; Cebecauer, M.; Cerny, J.; Brdicka, T.; Angelisova, P.; Stockinger, H. *Immunol. Today* **1999**, *20*, 356–361.
5. Barnett, R. E.; Furcht, L. T.; Scott, R. E. *Proc. Natl. Acad. Sci. U.S.A* **1974**, *71*, 1992–1994.
6. Erb, E.-M.; Tangemann, K.; Bohrmann, B.; Muller, B.; Engle, J. *Biochemistry* **1997**, *36*, 7395–7402.
7. Lundstrom, K. *Comb. Chem. High Throughput Screening* **2004**, *7*, 431–439.
8. Nolting, B. *Methods in Modern Biophysics*, 2nd ed.; Springer-Verlag: Berlin, 2006.
9. O'Malley, M. A.; Lazarova, T.; Britton, Z. T.; Robinson, A. S. *J. Struct. Biol.* **2007**, *159*, 166–178.
10. Maynard, J. A.; Lindquist, N. C.; Sutherland, J. N.; Lesuffleur, A.; Warrington, A. E.; Rodriguez, M.; Oh, S.-H. *Biotechnol. J.* **2009**, *4*, 1542–1558.
11. Joshi, M. K.; Dracheva, S.; Mukhopadhyay, A. K.; Bose, S.; Hendler, R. W. *Biochemistry* **1998**, *37*, 14463–14470.
12. Stevens, R. C. *Curr. Opin. Struct. Biol.* **2000**, *10*, 558–563.
13. Zheng, B.; Gerdts, C. J.; Ismagilov, R. F. *Curr. Opin. Struct. Biol.* **2005**, *15*, 548–555.
14. Talreja, S.; Kim, D. Y.; Mirarefi, A. Y.; Zukoski, C. F.; Kenis, P. J. A. *J. Appl. Crystallogr.* **2005**, *38*, 988–995.
15. Li, L.; Mustaff, D.; Fu, Q.; Tereshko, V.; Chen, D. L.; Tice, J. D.; Ismagilov, R. F. *Proc. Natl. Acad. Sci. U.S.A* **2006**, *103*, 19243–19248.
16. Wiener, M. C. *Methods* **2004**, *34*, 364–372.
17. Strom, A.; Diecke, S.; Hunsmann, G.; Stuke, A. W. *Proteomics* **2006**, *6*, 26–34.
18. Su, Y.; Ding, Y.; Jiang, M.; Jiang, W.; Hu, X.; Zhang, Z. *Mol. Cell. Biochem.* **2006**, *289*, 159–166.
19. Caffrey, M. *J. Struct. Biol.* **2003**, *142*, 108–132.
20. Unwin, P. N.; Henderson, R. *J. Mol. Biol.* **1975**, *94*, 425–440.
21. Palczewski, K.; Kumasaka, T.; Hori, T.; Behnke, C. A.; Motoshima, H.; Fox, B. A.; Le Trong, I.; Teller, D. C.; Okada, T.; Stenkamp, R. E.; Yamamoto, M.; Miyano, M. *Science* **2000**, *289*, 739–745.
22. Sprang, S. *Nature* **2007**, *450*, 355–356.
23. Cherezov, V.; Rosenbaum, D. M.; Hanson, M. A.; Rasmussen, S. G. F.; Thian, F. S.; Kobilka, T. S.; Choi, H.-J.; Kuhn, P.; Weis, W. I.; Kobilka, B. K.; Stevens, R. C. *Science* **2007**, *318*, 1258–1265.
24. Rasmussen, S. G. F.; Choi, H.-J.; Rosenbaum, D. M.; Kobilka, T. S.; Thian, F. S.; Edwards, P. C.; Burghammer, M.; Ratnala, V. R. P.; Sanishvili, R.; Fischetti, R. F.; Schertler, G. F. X.; Weis, W. I.; Kobilka, B. K. *Nature* **2007**, *450*, 383–388.
25. Rosenbaum, D. M.; Cherezov, V.; Hanson, M. A.; Rasmussen, S. G. F.; Thian, F. S.; Kobilka, T. S.; Choi, H.-J.; Yao, X.-J.; Weis, W. I.; Stevens, R. C.; Kobilka, B. K. *Science* **2007**, *318*, 1266–1273.
26. Henderson, R.; Unwin, P. N. *Nature* **1975**, *257*, 28–32.
27. Zheng, H.; Zhao, J.; Sheng, W.; Xie, X.-Q. *Biopolymers* **2006**, *83*, 46–61.
28. Phizicky, E. M.; Fields, S. *Microbiol. Rev.* **1995**, *59*, 94–123.

29. Salamon, Z.; Wnag, Y.; Soulages, J. L.; Brown, M. F.; Tollin, G. *Biophys. J.* **1996**, *71*, 283–294.
30. Smith, E. A.; Corn, R. M. *Appl. Spectrosc.* **2003**, *57*, 320A–332A.
31. Plant, A. L.; Brigham-Burke, M.; Petrella, E. C.; O'Shannessy, D. J. *Anal. Biochem.* **1995**, *226*, 342–348.
32. Plant, A. L. *Langmuir* **1999**, *15*, 5128–5135.
33. Silin, V. I.; Karlik, E. A.; Ridge, K. D.; Vanderah, D. J. *Anal/ Biochem.* **2006**, *349*, 247–253.
34. Rossi, C.; Homand, J.; Bauche, C.; Hamdi, H.; Ladant, D.; Chopineau, J. *Biochemistry* **2003**, *42*, 15273–15283.
35. Merzlyakov, M.; Li, E.; Hristova, K. *Langmuir* **2006**, *22*, 1247–1253.
36. Palmer, A. G.; Read, R. J. *Curr. Opin. Struct. Biol.* **2006**, *16*, 608–610.
37. Daniel, S.; Diaz, A. J.; Martinez, K. M.; Bench, B. J.; Albertorio, F.; Cremer, P. S. *J. Am. Chem. Soc.* **2007**, *129*, 8072–8073.
38. Jaffe, L. F. *Nature* **1977**, *265*, 600–602.
39. Poo, M.-m.; Robinson, K. R. *Nature* **1977**, *265*, 602–605.
40. Poo, M.-m.; Lam, J. W.; Orida, N.; Chao, A. W. *Biophys. J.* **1979**, *26*, 1–22.
41. McLaughlin, S.; Poo, M.-m. *Biophys. J.* **1981**, *34*, 85–93.
42. Stelzle, M.; Miehlich, R.; Sackmann, E. *Biophys. J.* **1992**, *63*, 1346–1354.
43. Groves, J. T.; Boxer, S. G. *Biophys. J.* **1995**, *69*, 1972–1975.
44. Groves, J. T.; Boxer, S. G.; McConnell, H. M. *Proc. Natl. Acad. Sci. U.S.A* **1997**, *94*, 13390–13395.
45. Cremer, P. S.; Groves, J. T.; Kung, L. A.; Boxer, S. G. *Langmuir* **1999**, *15*, 3893–3896.
46. Hovis, J. S.; Boxer, S. G. *Langmuir* **2001**, *17*, 3400–3405.
47. Hovis, J. S.; Boxer, S. G. *Langmuir* **2000**, *16*, 894–897.
48. Groves, J. T.; Wulfing, C.; Boxer, S. G. *Biophys. J.* **1996**, *71*, 2716–2723.
49. van Oudenaarden, A.; Boxer, S. G. *Science* **1999**, *285*, 1046–1048.
50. Yoshina-Ishii, C.; Boxer, S. G. *Langmuir* **2006**, *22*, 2384–2391.
51. Yoshina-Ishii, C.; Boxer, S. G. *J. Am. Chem. Soc.* **2003**, *125*, 3696–3697.
52. Tanaka, M.; Hermann, J.; Haase, I.; Fischer, M.; Boxer, S. G. *Langmuir* **2007**, *23*, 5638–5644.
53. Han, X.; Cheetham, M. R.; Sheikh, K.; Olmsted, P. D.; Bushby, R. J.; Evans, S. D. *Integr. Biol.* **2009**, *1*, 205–211.
54. Suzuki, K.; Hosokawa, K.; Maeda, M. *J. Am. Chem. Soc.* **2008**, *130*, 1542–1543.
55. Brian, A. A.; McConnell, H. M. *Proc. Natl. Acad. Sci. U.S.A* **1984**, *81*, 6159–6163.
56. Cremer, P. S.; Boxer, S. G. *J. Phys. Chem. B* **1999**, *103*, 2554–2559.
57. Johnson, J. M.; Ha, T.; Chu, S.; Boxer, S. G. *Biophys. J.* **2002**, *83*, 3371–3379.
58. Zhang, L.; Granick, S. *Proc. Natl. Acad. Sci. U.S.A* **2005**, *102*, 9118–9121.
59. Li, E.; Hristova, K. *Langmuir* **2004**, *20*, 9053–9060.
60. Yang, T.; Jung, S.-Y.; Mao, H.; Cremer, P. S. *Anal. Chem.* **2001**, *73*, 165–169.
61. Axelrod, D.; Koppel, D. E.; Schlessinger, J.; Elson, E.; Webb, W. W. *Biophys. J.* **1976**, *16*, 1055–1069.
62. Soumpasis, D. M. *Biophys. J.* **1983**, *41*, 95–97.

63. Fahey, P. F.; Koppel, D. E.; Barak, L. S.; Wolf, D. E.; Elson, E.; Webb, W. W. *Science* **1977**, *195*, 305–306.
64. Lin, W.-C.; Blanchette, C. D.; Ratto, T. V. *Biophys. J.* **2006**, *90*, 228–237.
65. Richter, R. P.; Brisson, A. *Langmuir* **2003**, *19*, 1632–1640.
66. Horton, M. R.; Reich, C.; Gast, A. P.; Radler, J. O.; Nickel, B. *Langmuir* **2007**, *23*, 6263–6269.
67. McLaughlin, S.; Poo, M.-m. *Biophys. J.* **1981**, *34*, 85–93.
68. Bird, B. R.; Stewart, W. E.; Lightfoot, E. N. *Transport Phenomena*; John Wiley & Sons, Inc.: New York, 1960.
69. Deen, W. M. *Analysis of Transport Phenomena*; Oxford University Press: New York, 1998.
70. Eisenberg, M.; Gresalfi, T.; Riccio, T.; McLaughlin, S. *Biochemistry* **1979**, *18*, 5213–5223.
71. Bier, M. *Electrophoresis: Theory, Methods, and Applications*; Academic Press: New York, 1959.
72. Howard, J. *Mechanics of Motor Proteins and the Cytoskeleton*; Sinauer Associates, Inc.: Sunderland, MA, 2001.
73. Gambin, Y.; Lopez-Esparza, R.; Reffay, M.; Sierecki, E.; Gov, N. S.; Genest, M.; Hodges, R. S.; Urbach, W. *Proc. Natl. Acad. Sci. U.S.A* **2006**, *103*, 2098–2102.
74. Booth, F. *Nature* **1948**, 83–86.
75. Wiersema, P. H.; Loeb, A. L.; Overbeek, J. T. G. *J. Colloid Interface Sci.* **1966**, *22*, 78–99.
76. Bayerl, T. M.; Bloom, M. *Biophys. J.* **1990**, *58*, 357–362.
77. Johnson, S. J.; Bayerl, T. M.; McDermott, D. C.; Adam, G. W.; Rennie, A. R.; Thomas, R. K.; Sackmann, E. *Biophys. J.* **1991**, *59*, 289–294.
78. Koenig, B. W.; Krueger, S.; Orts, W. J.; Majkrzak, C. F.; Berk, N. F.; Silverton, J. V.; Gawrisch, K. *Langmuir* **1996**, *12*, 1343–1350.
79. Salafsky, J.; Groves, J. T.; Boxer, S. G. *Biochemistry* **1996**, *35*, 14773–14781.
80. Purrucker, O.; Fortig, A.; Jordan, R.; Sackmann, E.; Tanaka, M. *Phys. Rev. Lett.* **2007**, *98*, 078102-1–0781021-4.
81. Goennenwein, S.; Tanaka, M.; Hu, B.; Moroder, L.; Sackmann, E. *Biophys. J.* **2003**, *85*, 646–655.
82. Wagner, M. L.; Tamm, L. K. *Biophys. J.* **2000**, *79*, 1400–1414.
83. Elender, G.; Kuhner, M.; Sackmann, E. *Biosens. Bioelectron.* **1996**, *11*, 565–577.
84. Albertorio, F.; Diaz, A. J.; Yang, T.; Chapa, V. A.; Kataoka, S.; Castellana, E. T.; Cremer, P. S. *Langmuir* **2005**, *21*, 7476–7482.
85. Hillebrandt, H.; Wiegand, G.; Tanaka, M.; Sackmann, E. *Langmuir* **1999**, *15*, 8451–8459.
86. Smith, E. A.; Coym, J. W.; Cowell, S. M.; Tokimoto, T.; Hruby, V. J.; Yamamura, H. I.; Wirth, M. J. *Langmuir* **2005**, *21*, 9644–9650.
87. Davis, R. W.; Flores, A.; Barrick, T. A.; Cox, J. M.; Brozik, S. M.; Lopez, G. P.; Brozik, J. A. *Langmuir* **2007**, *23*, 3864–3872.
88. Diaz, A. J.; Albertorio, F.; Daniel, S.; Cremer, P. S. *Langmuir* **2008**, *24*, 6820–6826.

89. Albertorio, F.; Daniel, S.; Cremer, P. S. *J. Am. Chem. Soc.* **2006**, *128*, 5516–552.
90. Kunding, A.; Stamou, D. *J. Am. Chem. Soc.* **2006**, *128*, 11328–11329.

Chapter 5

New Approaches to Monolithic Columns

Stefan Vujcic, Ivonne M. Ferrer, José G. Rivera, Li Li, and Luis A. Colón*

Department of Chemistry, University at Buffalo, The State University of New York, Buffalo, NY 14260-3000
***lacolon@buffalo.edu**

Monoliths of organo-silica hybrids as well as metal oxides are useful chromatographic media for liquid chromatography. These types of monoliths can be synthesized via sol-gel processing. The organo-silica hybrids, conveniently prepared from alkoxysilanes, show higher hydrolytic stability than conventional inorganic silica. Silica hybrid monoliths with surface-accessible functional groups allow the grafting of chemical entities at the silica surface, providing for chromatographic selectivity at the interface of the mobile and stationary phases. Herein, organo-silica hybrid monoliths containing surface allyl groups and their modification via hydrosilylation are presented. Hafnium and zirconium oxides offer a pronounced chemical and thermal stability. Monolithic structures of these metal oxides are emerging for chromatographic applications; the structures show unique adsorptive characteristics. The enrichment/ isolation of phosphopeptides by hafnia will be shown herein, as a potential application in the field of proteomics.

Introduction

Monoliths are a new type of chromatographic media which have emerged as an alternative to particle packed columns for liquid chromatography (*1–7*). A monolithic column is formed of a single co-continuous, porous material with higher permeability than conventional particle-packed columns. The characteristic permeability allows for relatively high linear velocities that are conducive to shorter analysis times using conventional pumping devices.

In Interfaces and Interphases in Analytical Chemistry; Helburn, R., et al.;
ACS Symposium Series; American Chemical Society: Washington, DC, 2011.

Monolithic columns also have short diffusion paths, which provide for favorable mass transfer characteristics in the chromatographic interfacial processes. This is advantageous when operating at linear velocities higher than those typically used with particle-packed columns. Separations with high efficiency and fast analysis times are attractive properties of monolithic columns. A recent comprehensive review of monoliths as they apply to LC can be found in the literature (*3*).

Various approaches have been followed to synthesize monolithic columns; most of the produced columns are based on organic polymers or silica, with the silica-based columns being the most popular due to the mechanical stability of silica. The silica-based monoliths are typically prepared using sol gel chemistry (*1*, *3*, *8*, *9*), which allows tunability of the physical properties (e.g., porosity, surface area) of the material. After synthesizing the monolithic silica support matrix, the surface of the silica monolith is functionalized through conventional silane chemistry to anchor the stationary phase of interest (*e.g.*, C-18) by means of a siloxane bond. The groups at the surface are ultimately responsible for differential retention of compounds during chemical analysis, as these groups exist at the interface of the mobile and stationary phases. The conventional approach to silica monoliths is illustrated in Figure 1.

A well-known aspect of this approach is the poor hydrolytic stability of the bonded phase, which limits the usability of the column to an approximate pH range of 2–8 (*10*, *11*). At low pH, the siloxane bond that attaches the stationary phase to the surface of the silica support material is prone to nucleophilic cleavage, rendering the stationary phase hydrolytically unstable as the pH is lowered. At high pH values on the other hand, the silica dissolves due to hydrolysis of the siloxane backbone. The improvements in stability that have been developed for conventional HPLC silica packing materials (e.g., the use of sterically protected linkages, using bidentate ligands, and synthesizing horizontally polymerized stationary phases) (*12–15*) can potentially be implemented in monolithic structures. These approaches however, have not been explored in detail for silica monolithic columns. A more hydrolytically stable bonded phase can be obtained by silica–carbon (Si–C) or silica–nitrogen (Si–NH–C) bond attachment, rather than by surface O–Si–C linkage (*16–18*).

It is evident that new monolithic approaches with improved stability for the chromatographic interfacial process must be investigated. In search for new and/or improved materials for monolithic columns, we explore the fabrication of two different types of monolithic structures; these are organo-silica hybrids and metal oxides. Herein, we provide our synthetic approach, material's characterization, and initial application for one organo-silica hybrid (i.e., allyl-hybrid) and two metal oxide monoliths (i.e., zirconia and hafnia).

Silica Hybrid Monoliths

The traditional sol-gel processing used to synthesize silica monoliths is based on the hydrolysis and condensation of reactions of one alkoxysilane (*19–22*), such as tetramethoxysilane (TMOS) or tetraethoxysilane (TEOS). Organo-silica hybrids are of interest because they exhibit more hydrolytic stability than

In Interfaces and Interphases in Analytical Chemistry; Helburn, R., et al.;
ACS Symposium Series; American Chemical Society: Washington, DC, 2011.

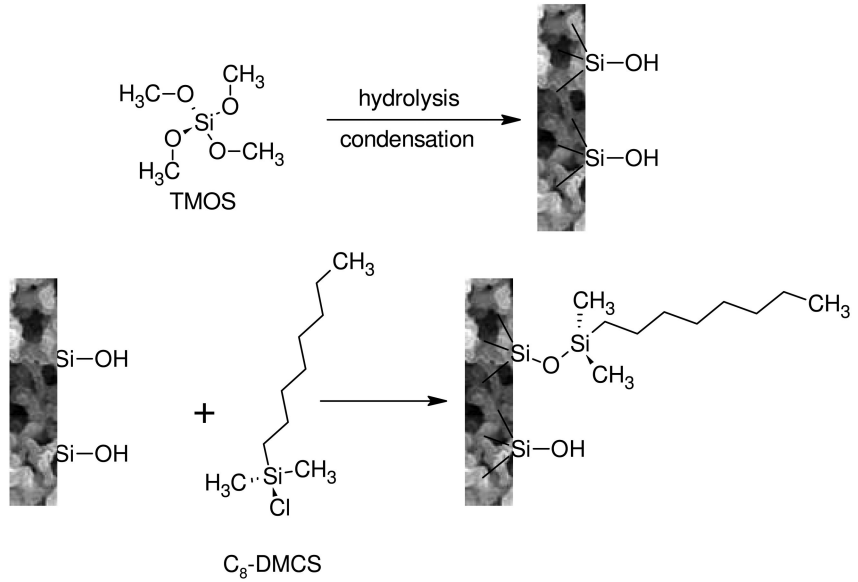

Figure 1. Schematic representation of conventional approach to the silica monolith synthesis and stationary phase attachment (TMOS: tetramethoxysilane, C_8-DMCS: octyldimethylchlorosilane).

conventional silica and can also be prepared via sol-gel chemistry (*4*). To fabricate the hybrid structure, a second silane precursor containing a moiety of interest (e.g., an alkyltrimethoxysilane) is incorporated into the sol-gel reaction, which provides for the inclusion of a functionality of interest during the synthesis of the monolithic structure. Similar to the approach used to produce hybrid coating phases in open tubular columns (*23*, *24*), this moiety can serve as the stationary phase with a given selectivity and is attached through the bulk modification process that provides more hydrolytically stable surface silica-carbon attachment. Such an approach combines the production of the silica matrix with surface funtionalization (i.e., stationary phase attachment) in a single-step, one "pot" reaction. In general, this approach appears to be very attractive for synthesizing monoliths, and various organosilanes have been used to provide monolithic columns with wide-ranging interfacial selectivity (*4*, *25–32*). However, the addition of a second precursor to produce the hybrid silica complicates the hydrolysis and condensation reactions of the system (*30–34*), producing materials with different physical structures every time dissimilar precursors are used, which affects the integrity and final characteristics of the monolith (e.g., porosity and permeability). Therefore, the synthetic conditions for each hybrid-monolithic structure containing different functionalities must be optimized independently. It is indeed very difficult to produce monoliths with optimized structural properties and an optimized stationary phase in one "pot" reactions every time a new phase is desired.

It is more attractive and less time consuming to have a hybrid monolithic platform with a given set of optimized physical properties to which different

In Interfaces and Interphases in Analytical Chemistry; Helburn, R., et al.;
ACS Symposium Series; American Chemical Society: Washington, DC, 2011.

functionalities could be added without the need to optimize the synthetic procedure every time a new surface functional group is preferred. In our approach, the hybrid structure is synthesized containing a derivatizable moiety attached at the surface and then new functionalities are introduced by reaction with the derivatizable moiety. Such an approach decouples the formation of the required structural characteristics of the monolith from the final surface modification to achieve the desired interfacial properties that provide chromatographic selectivity. This can be accomplished by synthesizing a hybrid monolith containing a surface allyl pendant as a derivatizable moiety; although any other appropriate functional group can be utilized.

Allyl-Monolith

Our research group has synthesized a hybrid monolith by reacting allyltrimethoxysilane (Allyl-TrMOS) and tetramethoxysilane (TMOS) producing a monolithic structure with accessible allyl groups (*30*), which is illustrated in Figure 2. A typical preparation of the allyl-silica monolith involves the mixing of acetic acid (1 mL 0.01 M), urea (90 mg), and polyethylene glycol (PEG MW 10,000, 108mg) in an ice cooled bath and then the ally-TrMOS and TMOS are added into the mixture before stirring for one hour at 0°C. The reaction mixture is introduced into a desired length of the column by means of a syringe connected to the column through a piece of Teflon tubing. The column is heated at 50° C for 40 hours after the ends of the capillary columns have been sealed. Afterwards, the column is rinsed with methanol and the monolith is heated from 50° C to 150° C at the rate of 1° C/min, then cooled to ambient temperature, rinsed with ethanol and then washed with mobile phase prior to use under chromatographic conditions.

The mole ratio of allyl-TrMOS:TMOS influences the formation of the structure inside the capillary column, affecting the through pores, the skeleton, and the adherence of the monolith to the column walls. Figure 3 illustrates the effect of the allyl-TrMOS:TMOS mole ratio on the formation of a monolithic structure inside of a 50 μm i.d. capillary column. A mole ratio of 1:4 (allyl-TrMOS:TMOS) produced a stable monolith inside the entire column i.d., attached at the inner surface of the column having through pores of about 2 μm.

The surface area and the mesoporosity of the monolithic structure are controlled by adjusting the amount of PEG added into the reaction mixture, as illustrated in Figure 4 while urea in the reaction provides mesopore uniformity (*35*). The column prepared with the allyl-TrMOS:TMOS mole ratio of 1:4, and 108 mg of PEG showed a surface area of 209 m^2/g with mesopores in the vicinity of 8 nm. Reaction of the surface allyl groups with bromine and performing elemental analysis to determine bromine allows for the determination of surface accessible allyl groups (*30*). About 68% of the allyl groups incorporated into the monolithic structure have been found accessible at the surface (i.e., 1.4 mmol allyl groups/g of material), which corresponds to 6.7 $\mu mol/m^2$ for the monolith having a surface area of 209 m^2/g (*30*).

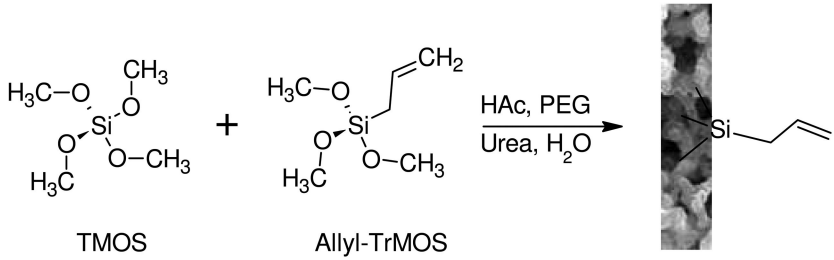

Figure 2. Synthetic approach to allyl-silica hybrid monolithic material (TMOS: tetramethoxysilane, Allyl-TrMOS: allyl-trimethoxysilane).

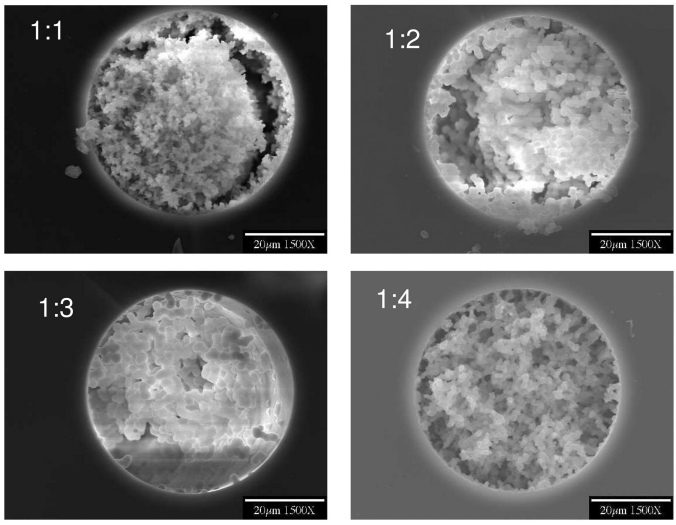

Figure 3. Scanning electron micrographs of allylorgano-silica monoliths inside 50 μm i.d. columns prepared with different mole ratios of allyl-TrMOS:TMOS.

Hydrosilylation

Once the physical properties of the monolith have been established, the allyl moiety at the surface of the monolith can be modified through hydrosilylation. This allows the introduction of other groups at the surface of the monolith that can be used in different interfacial chromatographic processes. Hydrosilylation reactions in which a terminal olefin is reacted with silica particles containing hydride groups at the surface (SiH) has been studied extensively by Pesek and co-workers, showing a very robust approach to the production of stationary phases with improved hydrolytic stability (*18*, *36–38*). The allyl-silica hybrid monolith contains the olefinic group at the surface which can be modified by using an organo-silane hydride. As an example of the modification, the allyl-monolith was reacted with benzyl dimethylsilane (benzyl-DMS) according to the reaction scheme presented in Figure 5. The catalyst for this reaction is chloroplatinic acid. For a typical reaction inside of a capillary column containing the allyl-monolith,

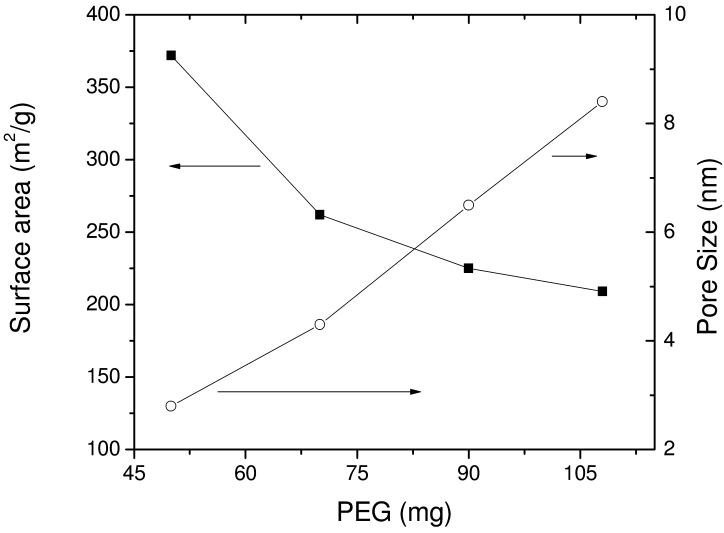

Figure 4. Surface area and pore size as a function of PEG in the reaction mixture on allyl-silica monoliths prepared with allyl-TrMOS:TMOS (1:4).

the catalyst (~1.4 mL of 0.12 mg/mL in isopropanol) is mixed with benzyl-DMS (~50 µL) and introduced into the column. After sealing the ends with rubber septa, the column is heated at 80° C for 24 hours, allowed to come to room temperature, flushed with isopropanol, and conditioned with mobile phase prior to use.

Approximately 29% of the accessible allyl groups on the hybrid monolith reacted with benzyl-MDS. For a monolith with a surface area of 209 m^2/g, this translates to a surface coverage of 1.95 µmol/m^2 of benzyl groups attached to the allyl-monolith. There is evidence that little surface coverage variation occurs from one reaction to another, even if a different functionality is added (*39*). Figure 6 depicts the separation of a mixture containing model compounds separated via capillary electrochromatography (CEC) in an allyl-monolith before (Figure 6A) and after (Figure 6B) hydrosilylation reaction with benzyl-DMS. It can be observed that the allyl column provides retention of the probe compounds under the electrochromatographic conditions used. However, it can be noticed that retention is increased when using the allyl-monolith modified with benzyl-DMS, demonstrating that the hydrosilylation reaction added groups at the surface to further the interactions with the injected solutes. Figure 7 depicts the separation of basic drugs by capillary liquid chromatography (CLC) using the hybrid monolithic columns prepared with benzyl-DMS, illustrating further the viability of this material for separations.

The hydrolytic stability of the hydrosilylated allyl-monolith was tested by exposing a hybrid monolithic column to extreme pH conditions (i.e., pH<2 and pH>11) and monitoring the retention factor as a function of exposure time. The retention factor is then compared to that obtained in silica monolith modified by the conventional approach after exposing to similar pH conditions. Figure 8 illustrates the loss of retention as the monoliths were exposed to column volumes of the mobile phase at the two different pH conditions. After exposing the

In Interfaces and Interphases in Analytical Chemistry; Helburn, R., et al.;
ACS Symposium Series; American Chemical Society: Washington, DC, 2011.

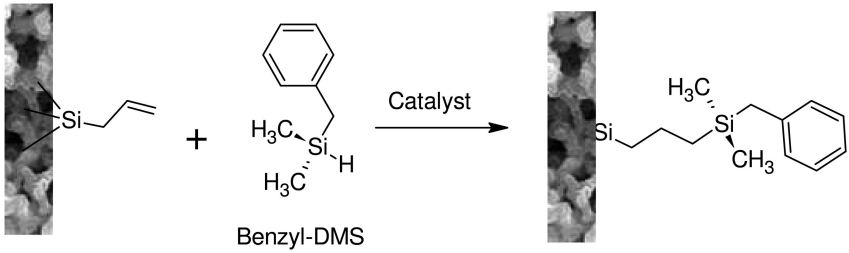

Figure 5. Hydrosilylation scheme to modify the surface of the allyl-monolith.

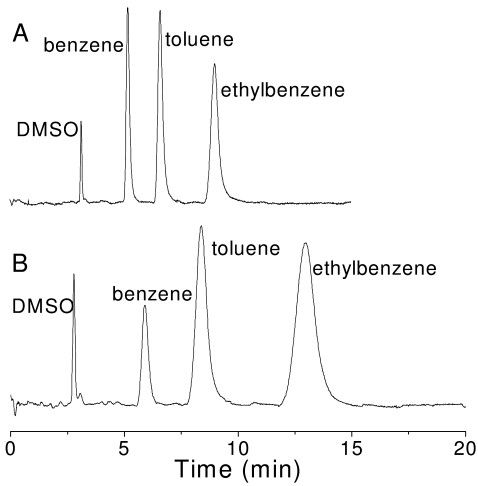

Figure 6. Electrochromatograms for the separation of model compounds using the (A) hybrid allyl-monolithic column before hydrosilylation and (B) after hydrosilylation with the with benzyl-DMS. CEC conditions: separation voltage, 25kV; mobile phase, acetonitrile and 4 mM borate buffer (pH=9.3) (20:80 v/v); column, 20 cm length, 50 µm i.d.; UV detection at 214nm.

hydrosilylated allyl-monolith to acidic or basic conditions, retention of the test analyte remained at or above 85% of the original retention during the time of the experiment. Under the acidic condition (Figure 8A), both columns had a similar loss in retention until about 500 column volumes. Upon further exposure (i.e., 900 column volumes) the hybrid column only lost an additional 5% in retention while the conventionally modified column lost an additional 12%. After 1200 column volumes more than 25% in retention had been lost for the conventional column while the allyl modified monolith did not show further lost in retention during the remaining of the test (up to about 1800 column volumes). Under basic conditions (pH=11.4), the modified allyl-hybrid monolith lost 15% in retention when exposed to about 400 column volumes (~12 hrs) at high pH (Figure 8B). The monolith modified by the conventional approach, on the other hand, lost all retentivity after passing about 20 column volumes (~45 min), which is indicative of stationary phase lost in a very short period of time.

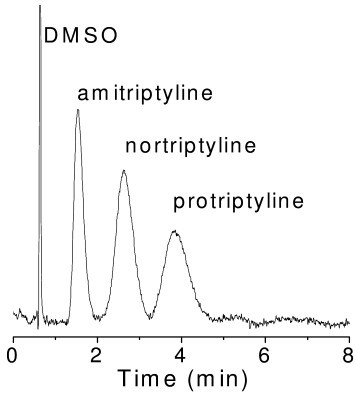

Figure 7. Separation of basic drugs by CLC using a hybrid monolithic column prepared benzyl-DMS. Monolithic column inside a 50 µm i.d. with an effective length of 20 cm; mobile phase consisted of ACN and 4 mM borate buffer (pH = 9.3, 70:30), delivered with at a pressure of 70 psi. (Adapted from ref. (39) with permission. Copyright Wiley-VCH Verlag GmbH Co. & KGaA 2009.)

Hafnia and Zirconia Monoliths

There has been great interest in the use of metal oxide materials as chromatographic support media (*40*). The interest stems from the higher pH and thermal stability of metal oxides, most notably hafnia and zirconia, as compared to silica materials (*41*), despite the limitations associated with the lack of diverse derivatization chemistry of the metal oxides and non-specific adsorption due to a complex surface chemistry (e.g., amphoteric surface and lewis acid sites). Most of the work with metal oxides has concentrated on zirconia particulates, although titania and alumina have also been explored (*40*). The use of metal oxide monoliths in chromatography is a recent development. Our research group reported a synthetic approach to produce monoliths inside capillary columns based on hafnia and zirconia with potential applicability in capillary liquid chromatography (CLC) and capillary electrochromatography (CEC) (*42*). The formation of hafnia and zirconia is based on the hydrolysis and condensation of molecular precursors via sol gel processing; the precursors used were the tetrachloride salt of zirconium and hafnium. Subsequent reports have been published examining on alumina, titania, and zirconia monoliths (*43–48*).

Synthesis

Our approach to hafnia and zirconia monoliths can be represented as follows:

$$MCl_4 + H_2O \longrightarrow MOCl_2 + 2HCl$$

$$MOCl_2 + 2H_2O \xrightarrow{\text{epoxide}} MO(OH)_2 + 2HCl$$

$$\text{Polymerization-condensation} \longrightarrow \text{Monolith}$$

In Interfaces and Interphases in Analytical Chemistry; Helburn, R., et al.;
ACS Symposium Series; American Chemical Society: Washington, DC, 2011.

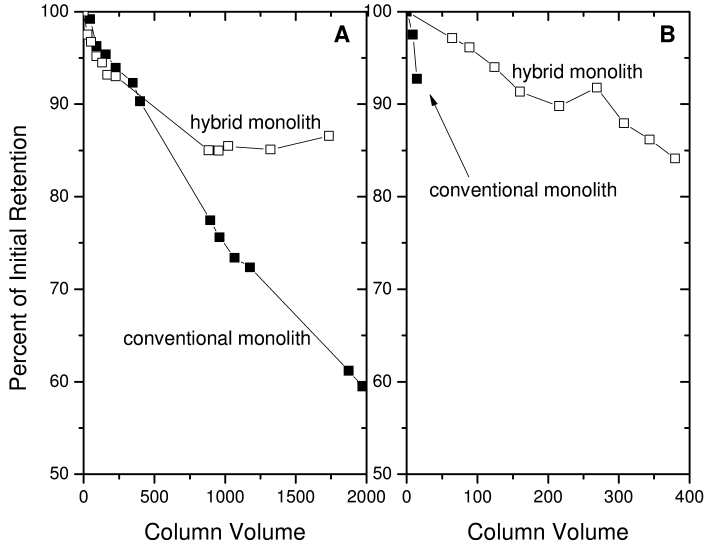

Figure 8. Changes in retention as a function of column volumes at (A) low and (B) high pH conditions for two monoliths. Low pH mobile phase: acetonitrile/ 1% TFA (20:80 v/v) pH=1.4. High pH mobile phase: acetonitrile/20mM triethylamine (20:80 v/v) pH=11.3. Toluene was used as the test solute. Allyl-monolith: allyl-silica hybrid monolith modified with C8-DMS via hydrosilylation. Conventional monolith: silica monolith modified with octyldimethylchlorosilane. (Reproduced from ref. (39) with permission. Copyright Wiley-VCH Verlag GmbH Co. & KGaA 2009.)

where M represents the metal hafnium or zirconium. The procedure starts with an aqueous solution of the metal tetrachloride to which n-methylformamide (NMF) is added. Addition of NMF can provide for a systematic control of both surface area and porosity. Polyethylene oxide (PEO) can also be added to aid phase separation and pore formation (*48*). Solvothermal treatment is used to control mesoporosity. In the process outlined above, gelation is induced by the addition of propylene oxide. The metal oxide monolithic structure is aged following gelation, and then the solvent is removed, increasing the mechanical stability of the material. A heat treatment provides for solvent evaporation and an increased mechanical stability. Typically, the monoliths are heated at 80 °C, 120°C, and 150°C for 4 hrs at each step. Subsequently, monoliths are subjected to further heat treatment at 300°C. This heating treatment results on a structure having a reduction in volume of at least 50% when compared with the original liquid value. The final structure of the monolith is highly affected by the temperature. At elevated temperatures the monoliths undergo considerable shrinkage and pore reshaping due to the influence of capillary forces and syneresis. Treatment at extremely high temperatures (>500°C) produces a high degree of structural alteration, causing changes in the crystal structure of the material (*49*).

Morphology, Surface Area, and Porosity

The morphology of the monolithic metal oxides changes with the amount of NMF present in the original reaction mixture. Two common techniques used to characterize morphology of porous solids are mercury intrusion porosimetry (MIP) and gas (nitrogen) adsorption. Nitrogen adsorption porosimetry, using the Brunauer, Emmett and Teller (BET) theory, provides information about mesopores and surface area, while MIP allows characterization of macropores. In addition, scanning electron microscopy (SEM) can reveal some general information about morphology. SEM images in Figure 9 illustrate the morphological changes of zirconia and hafnia as a function of various NMF concentrations. It is evident that in the absence of NMF, the structure does not contain globular aggregates which lead to macroporosity. The network of macropores facilitates rapid pathways for the movement of solvent through the monolith in a chromatographic experiment. The interconnected skeleton structure does not appear until a considerable amount of NMF is present in the reaction mixture. The SEM images indicate that the through pores of the material increase as the amount of NMF is increased. The morphology of zirconia appears to be affected to a higher degree than that of hafnia.

The concentration of NMF also has an influence on the surface area and porosity of the metal oxide monolithic materials. Figure 10 depicts the surface area and average pore size for hafnia (panel A) and zirconia (panel B) monolithic materials as a function of NMF concentrations (i.e., NMF/metal mol ratio). Figure 10A shows that the largest surface area for zirconia was observed without NMF (i.e., 150 m^2/g). The surface area arises from the microporosity (<1.8 nm) of the material. As the concentration of NMF is increased, a decrease in surface area with a concomitant increase in pore size is observed. The largest pore size is observed when the NMF/Zr molar ratio is about three, producing pores of about 10.5 nm in diameter. Increasing the NMF concentration beyond 3.9 molar equivalents produced a slight decrease in average pore diameter but did not have a major effect on the surface area.

Figure 10B illustrates the effect of NMF on the surface area and average pore diameter on hafnia monolithic structures. Similar to zirconia materials, the largest surface area was observed when no NMF was used (i.e., 95 m^2/g), corresponding to the lowest measurable average mesopore diameter (i.e., ~1.8 nm). The highest concentration of NMF used produced the largest pore diameter (~10 nm), also corresponding to the lowest surface area (10 m^2/g). Similar to the zirconia monolithic structure, it can be noticed that when the NMF/metal molar ratio is changed from about 2 to 3, the most dramatic change in pore size is observed. The through pores, also referred to as macropores, are responsible for the material's permeability. In silica monolithic materials the through pores are typically controlled by incorporating water soluble polymers such as PEO or PEG, which act as porogens (*20*). The amount and molecular weight of PEO has been shown to also have significant influences on the macroporous morphology of titania materials by altering the timing of the onset of the phase separation relative to the sol–gel transition (*50*). PEO has also been utilized to alter the morphology of zirconia monoliths when using metal alkoxides as starting materials (*45*, *48*).

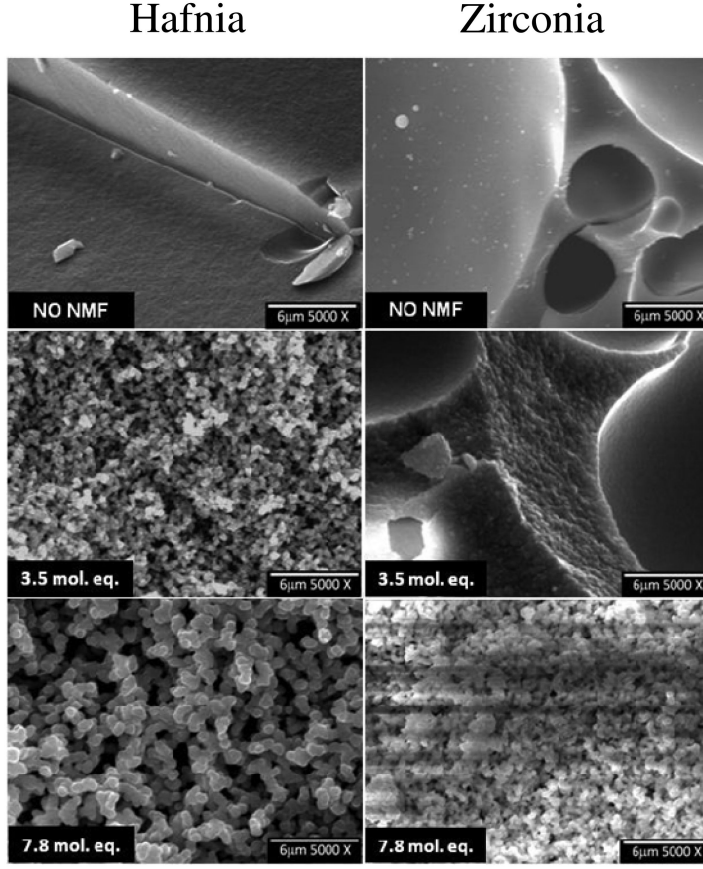

Figure 9. SEM images of hafnia and zirconia monoliths synthesized with different amounts of NMF (mol equivalent relative to metal). 1.28M metal tetrachloride in water with NMF allowed to react for 3 days at room temperature; gelation induced by addition of 7 equiv. of propylene oxide; aging for 3 days at 50 °C; drying by heat at 80 °C, 120°C,150°C (4 hrs at each temperature) and 300°C (12 hrs).

Our monolithic structures are produced from the metal chloride precursors and the through pores can be controlled by the amount of NMF added during the synthesis of the metal oxide. Figure 11 shows plots of pore distribution for both zirconium and hafnium oxide monolithic materials synthesized with different concentrations of NMF, as measured by MIP. MIP measurements confirm the observation from the SEM images presented in Figure 9, showing direct correlation between NMF content and size of the through pores. The highest median pore diameter for zirconia monoliths is 1.1 µm when using 6.5 molar equivalents of NMF. The largest pore median for the hafnia monolith was 0.5 µm at 7.8 molar equivalents of NMF. The concentration of NMF has higher effect on the pore size variation in zirconia than in hafnia monoliths. The synthesis of a

In Interfaces and Interphases in Analytical Chemistry; Helburn, R., et al.;
ACS Symposium Series; American Chemical Society: Washington, DC, 2011.

hafnia monolith with a given pore size requires about twice the amount of NMF needed to produce a zirconia monolith with similar pore size.

Potential Uses

The chromatographic characteristics of monolithic metal oxides are starting to appear in the literature (*42*, *45*). For example, Figure 12 shows a capillary electrochromatographic separation of three compounds using a hafnia monolithic column. The elution order of the compounds followed pK_a values, indicating a ligand exchange type of interaction through the Lewis sites on the hafnia monolith (*42*). Metal oxides of Group IV elements of the Periodic Table, particularly titania and zirconia, have shown adsorptive characteristics due to their unique surface-liquid interfacial ligand exchange capabilities that can be exploited in the isolation/enrichment of phosphorylated compounds (*51–53*). Since hafnium oxide (i.e., hafnia) is another metal oxide from the same group, one would expect it to possess certain similarities. We have studied the potential interfacial adsortive characteristics of hafnia for the isolation/enrichment of phosphorylated peptides using a tryptic digest of bovine β-casein, a model phosphorylated protein (*54*). Bovine β-casein has been reported to have five phosphorylated serine residues, and it is well documented that its tryptic digestion results in both monophosphophorylated and tetraphosphorylated peptides (*55*). The tryptic digest was passed through hafnia material in a format similar to solid phase extraction. The adsorbed compounds are eluted from the hafnia material simply by raising the pH using NH_3OH. These peptides are examined via electrospray ionization-mass spectrometry (ESI-MS). Figures 13 and 14 show MS spectra for a tryptic digest of β-casein. The MS spectrum in Figure 13 is for the tryptic digest without any treatment and Figure 14 is after isolation/enrichment and elution from the hafnia material. The spectrum for the non-enriched β-casein tryptic sample is dominated by non-phosphorylated peptides with the presence of some phosphorylated peptides. Application of HfO_2 prior to ESI-MS analysis results in selective enrichment/isolation of the phosphorylated peptides. This is shown by the increased signals and cleaner MS spectra. Hafnia enriches both the single and tetra phosphopeptides. Monophosphorylated peptides are enriched to a higher degree as compared to tetraphosphosphorylated peptides using hafnia material.

Conclusion

New developments in the area of monolithic columns for HPLC continue to grow, exploring new directions. The organo-silica hybrid monolithic column approach offers improved characteristics over the inorganic silica-based monoliths. Some challenges still remain, particularly in the upscale beyond the capillary format and column to column reproducibility. However, given the success of chromatographic columns packed with organo-silica particles, the potential of organo-silica hybrid monoliths is clear and there appears to be sufficient impetus to continue growth in this direction. The metal oxide monolithic columns are just emerging and much more research needs to be

done. The potential of these metal oxides has been demonstrated here for the enrichment/isolation of phosphorylated compounds. However, our results indicate that hafnia monoliths can also be a useful chromatographic support material for the separation of phosphate-containing species. The growth of monolithic columns in HPLC for chemical analysis will continue. The interfacial properties of the monolithic materials discussed in this chapter contribute to this growth. New applications will appear; only time, however, will indicate how far this technology will go.

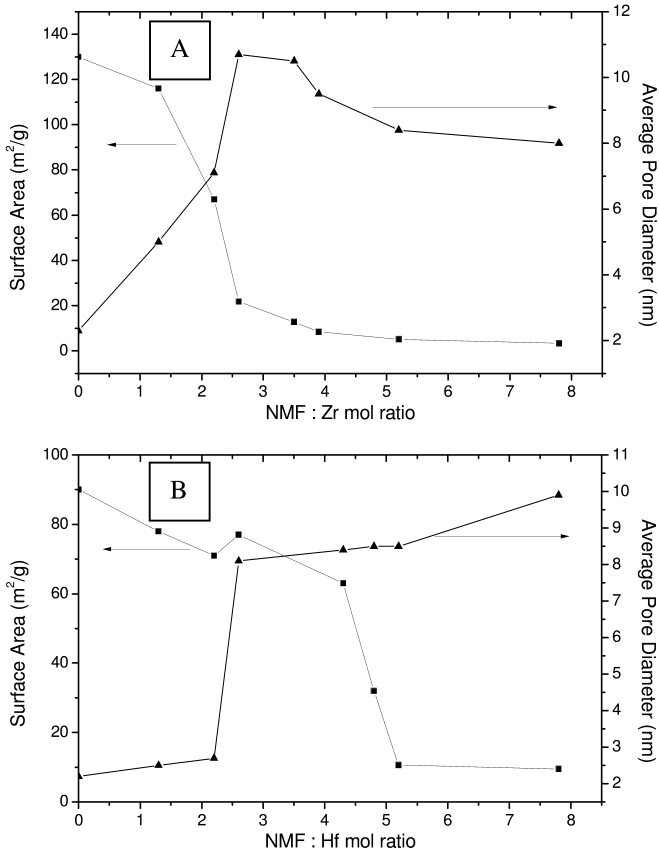

Figure 10. Surface area (■) and average pore size (▲) of (A) zirconia and (B) hafnia monolithic materials as a function of NMF:metal mol ratio. Processing condition as described in Figure 9.

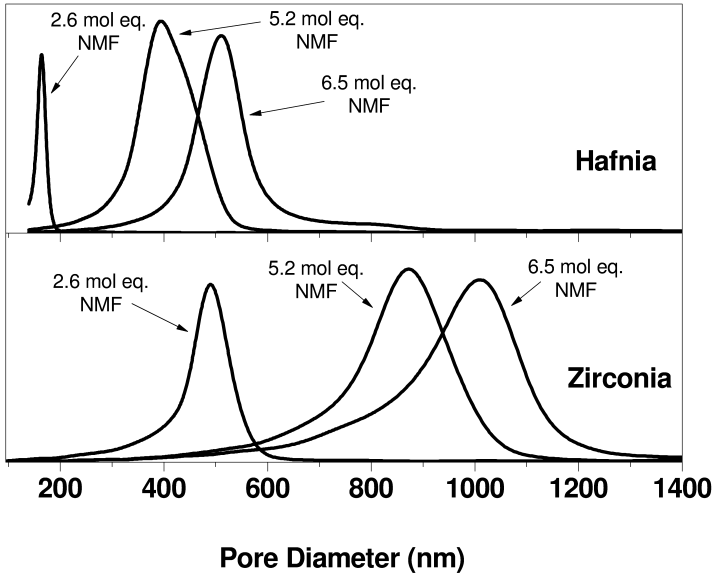

Figure 11. Surface area (■) and average pore size (▲) of (A) zirconia and (B) hafnia monolithic materials as a function of NMF:metal mol ratio. Processing condition as described in Figure 9.

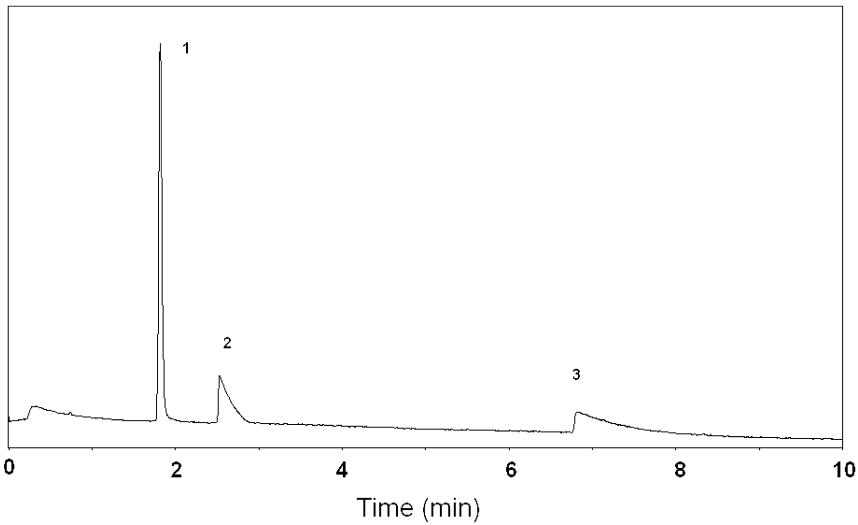

Figure 12. Separation of three components using CEC using a hafnia monolithic capillary column (29 cm length, 50 μm i.d., 21 cm effective length); mobile phase: 5mM phosphate buffer pH 7.1; UV detection at 214 nm; separation voltage of 25 kV; at 25 °C. The separated compounds are (1) pyridine, (2) pyrazole, and (3) imidazole. Adapted from ref. (42) with permission. Copyright Elsevier 2005.)

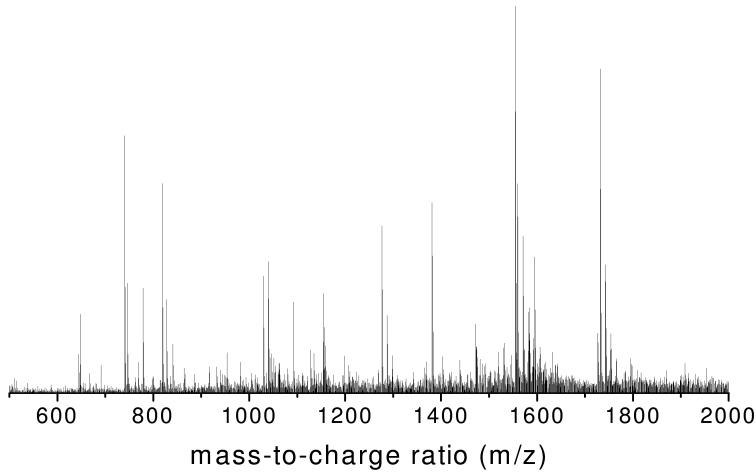

Figure 13. Mass spectrum of bovine β-casein tryptic digest (without HfO_2 enrichment/treatment).

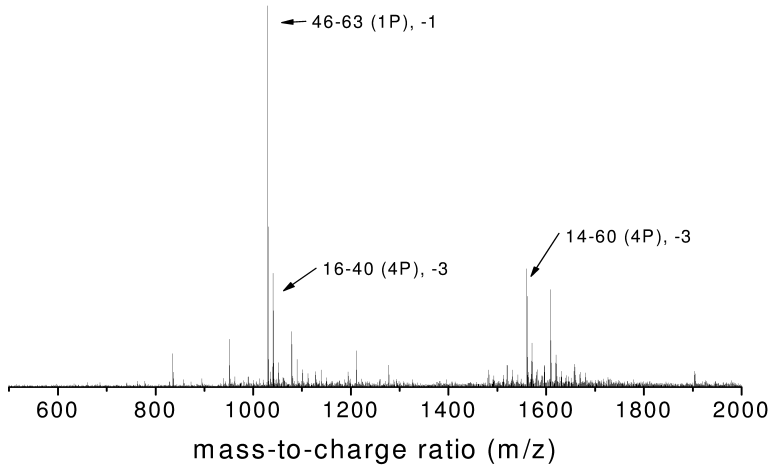

Figure 14. Mass spectrum of bovine β-casein tryptic digest after HfO_2 enrichment/treatment).

Acknowledgments

We acknowledge the financial support provided by The National Science Foundation, USA (CHE-0554677).

References

1. Tanaka, N.; Kobayashi, H.; Nakanishi, K.; Minakuchi, H.; Ishizuka, N. *Anal. Chem.* **2001**, *73*, 420A–429A.
2. *Monolithic Materials: Preparation, Properties and Applications*; Svec, F., Tennikova, T. B., Deyl, Z., Eds.; Elsevier: Amsterdam, 2003.
3. Guiochon, G. *J. Chromatogr., A* **2007**, *1168*, 101–168.
4. Colón, L. A.; Li, L. *Adv. Chromatogr.* **2008**, *46*, 391–421.
5. Svec, F.; Geiser, L. *LCGC North Am.* **2006**, *24*, 22–27.
6. Svec, F.; Huber, C. G. *Anal. Chem.* **2006**, *78*, 2100–2107.
7. Nunez, O.; Nakanishi, K.; Tanaka, N. *J. Chromatogr., A* **2008**, *1191*, 231–252.
8. Miyabe, K.; Guiochon, G. *J. Sep. Sci.* **2004**, *27*, 853–873.
9. Colón, L. A.; Maloney, T. D.; Anspach, J.; Colón, H. *Adv. Chromatogr.* **2003**, *42*, 43–106.
10. Poole, C. F. *The Essence of Chromatography*; Elsevier: New York, 2003; p 285.
11. Majors, R. E. *LCGC North Am.* **2000**, *18*, 1214–1227.
12. Kirkland, J. J.; Glajch, J. L.; Farlee, R. D. *Anal. Chem.* **1989**, *61*, 2–11.
13. Kirkland, J. J.; Adams, J. B., Jr.; Van Straten, M. A.; Claessens, H. A. *Anal. Chem.* **1998**, *70*, 4344–4352.
14. Scholten, A. B.; de Haan, J. W.; Claessens, H. A.; van de Ven, L. J. M.; Cramers, C. A. *J. Chromatogr., A* **1994**, *688*, 25–29.
15. Wirth, M. J.; Fatunmbi, H. O. *Anal. Chem.* **1992**, *64*, 2783–2786.
16. Poole, C. F.; Poole, S. K. *Chromatography Today*; Elsevier: New York, 1991, p 324.
17. Cobb, K. A.; Dolnik, V.; Novotny, M. *Anal. Chem.* **1990**, *62*, 2478–2483.
18. Sandoval, J. E.; Pesek, J. J. *Anal. Chem.* **1991**, *63*, 2634–2641.
19. Brinker, C.; Scherer, G. *Sol-Gel Science: The Physics and Chemistry of Sol-Gel Processing*; Academic Press: New York, 1990.
20. Nakanishi, K.; Komura, H.; Takahashi, R.; Soga, N. *Bull. Chem. Soc. Jap.* **1994**, *67*, 1327–1335.
21. Tanaka, N.; Kobayashi, H.; Nakanishi, K.; Minakuchi, H.; Ishizuka, N. *Anal. Chem.* **2001**, *73*, 420A–429A.
22. Colón, L. A.; Maloney, T. D; Anspach, J. A.; Colón, H. *Adv. Chromatogr.* **2003**, *42*, 43–106.
23. Guo, Y.; Colón, L. A. *Anal. Chem.* **1995**, *67*, 2511–2516.
24. Guo, Y.; Imahori, G. A.; Colón, L. A. *J. Chromatogr., A* **1996**, *744*, 17–29.
25. Hayes, J. D.; Malik, A. *Anal. Chem.* **2000**, *72*, 4090–4099.
26. Yan, L.; Zhang, Q.; Zhang, J.; Zhang, L.; Li, T.; Feng, Y.; Zhang, L.; Zhang, W.; Zhang, Y. *J. Chromatogr., A* **2004**, *1046*, 255–261.
27. Yan, L.; Zhang, Q.; Zhang, W.; Feng, Y.; Zhang, L.; Li, T.; Zhang, Y. *Electrophoresis* **2005**, *26*, 2935–2941.
28. Yan, L.-J.; Zhang, Q.-H.; Feng, Y.-Q.; Zhang, W.-B.; Li, T.; Zhang, L.-H.; Zhang, Y.-K. *J. Chromatogr., A* **2006**, *1121*, 92–98.
29. Xu, L.; Lee, H. K. *J. Chromatogr., A* **2008**, *1195*, 78–84.

30. Colón, H.; Zhang, X.; Murphy, J. K.; Rivera, J. G.; Colón, L. A. *Chem. Commun.* **2005**, 2826–2828.
31. Roux, R.; Jaoude, M. A.; Demesmay, C.; Rocca, J. L. *J. Chromatogr., A* **2008**, *1209*, 120–127.
32. Roux, R.; Puy, G.; Demesmay, C.; Rocca, J. L. *J. Sep. Sci.* **2007**, *30*, 3035–3042.
33. Rodríguez, S. A.; Colón, L. A. *Chem. Mater.* **1999**, *11*, 754–762.
34. Rodríguez, S. A.; Colón, L. A. *Appl. Spectrosc.* **2001**, *55*, 472–480.
35. Nakanishi, K.; Shikata, H.; Ishizuka, N.; Koheiya, N.; Soga, N. *J. High Resolut. Chromatogr.* **2000**, *23*, 106–116.
36. Pesek, J. J.; Matyska, M. T. *J. Sep. Sci.* **2005**, *28*, 1845–1854.
37. Pesek, J. J.; Matyska, M. T.; Sukul, D. *J. Chromatogr., A* **2008**, *1191*, 136–140.
38. Pesek, J. J.; Matyska, M. T. *J. Liq. Chromatogr. Relat. Technol.* **2006**, *29*, 1105–1124.
39. Li, L.; Colón, L. A. *J. Sep. Sci.* **2009**, *32* (32), 2737–2746.
40. Nawrocki, J.; Dunlap, C.; McCormick, A.; Carr, P. W. *J. Chromatogr., A* **2004**, *1028*, 1–30.
41. Dunlap, C. J.; McNeff, C. V.; Stoll, D.; Carr, P. W. *Anal. Chem.* **2001**, *73*, 598A–607A.
42. Hoth, D. C.; Rivera, J. G.; Colón, L. A. *J. Chromatogr., A* **2005**, *1079*, 392–396.
43. Tokudome, Y.; Fujita, K.; Nakanishi, K.; Miura, K.; Hirao, K. *Chem. Mater.* **2007**, *19*, 3393–3398.
44. Backlund, S.; Smatt, J.-H.; Rosenholm, J. B.; Linden, M. *J. Disper. Sci. Technol.* **2007**, *28*, 115–119.
45. Randon, J.; Guerrin, J.-F.; Rocca, J.-L. *J. Chromatogr., A* **2008**, *1214*, 183–186.
46. Konishi, J.; Fujita, K.; Nakanishi, K.; Hirao, K. *Chem. Mater.* **2006**, *18*, 6069–6074.
47. Randon, J.; Huguet, S.; Piram, A.; Puy, G.; Demesmay, C.; Rocca, J.-L. *J. Chromatogr., A* **2006**, *1109*, 19–25.
48. Konishi, J.; Fujita, K.; Oiwa, S.; Nakanishi, K.; Hirao, K. *Chem. Mater.* **2008**, *20*, 2165–2173.
49. Nashima, M.; Kato, T.-A.; Kakihana, M.; Gulgun, M. A.; Matsuo, Y.; Yoshimura, M. *J. Mater. Res.* **1997**, *12* (10), 2575–2583.
50. Konishi, J.; Fujita, K.; Nakanishi, K.; Hirao, K. *Chem. Mater.* **2006**, *18*, 858–864.
51. Pinkse, M. H.; Uitto, P. M.; Hilhorst, M. J.; Ooms, B.; Heck, A. J. R. *Anal. Chem.* **2004**, *76*, 3935–3943.
52. Larsen, M. R.; Thingholm, T. E.; Jensen, O. N.; Roepstorff, P.; et al. *Mol. Cell. Proteomics* **2005**, *4*, 873–886.
53. Kweon, H. K.; Håkansson, K. *Anal. Chem.* **2006**, *78*, 1743–1749.
54. Rivera, J. G.; Choi, Y. S.; Vujcic, S.; Wood, T. D.; Colón, L. A. *The Analyst* **2009**, *134*, 131–133.
55. Dumas, B. R.; Brignon, G.; Grosclaude, F.; Mercier, J.-C. *Eur. J. Biochem.* **1972**, *25*, 505–514.

Chapter 6

Formation, Structure, and Reactivity of Amino-Terminated Organic Films on Silicon Substrates

Joonyeong Kim*

Department of Chemistry, Buffalo State, State University of New York, 1300 Elmwood Avenue, Buffalo, New York 14222
***kimj@buffalostate.edu**

Effects of various preparation conditions on the structure and reactivity of amino-functionalized organic films on silicon substrates were investigated using Fourier transform infrared spectroscopy (FTIR), ellipsometry, contact angle measurement, and fluorescence microscopy. Amino-terminated organic films were prepared on silicon wafers by self-assembling 3-aminopropyltriethoxysilane (APTES) in two different types of solutions (anhydrous toluene and aqueous solution) for varied deposition times, cured at different conditions, and washed by sonication in water. In aqueous solution, structurally comparable APTES films with a thickness of ~10 Å were formed via electrostatic interactions. However, deposition from an anhydrous toluene solution produces APTES films with a wide range of thickness (10 – 144 Å) by either covalent or non-covalent interactions depending upon the deposition time, although thicker films are mechanically unstable in aqueous solutions and proper curing process is required to form physically stable films. Chemical modifications of amino groups on APTES films to three different linkers, *N*-hydroxysuccinimide (NHS) ester, hydrazide, and maleimide ester, are demonstrated.

In Interfaces and Interphases in Analytical Chemistry; Helburn, R., et al.;
ACS Symposium Series; American Chemical Society: Washington, DC, 2011.

Introduction

The formation of organosilane-based thin films provides a simple means to incorporate chemically well-defined functional groups on a silicon surface (*1–5*). Variations in either terminal groups or structures of organosilanes have greatly extended the utility of silicon as a solid substrate in many applications for modern technologies by presenting specific chemical and physical properties. For example, amino-terminated organic thin films on silicon substrates have been popularly prepared since further chemical derivatizations of surface amino groups lead to the introduction of chemical groups such as N-hydroxysuccinimide (NHS) ester, hydrazide, and maleimide ester. Silicon substrates containing these grafted chemical groups have been frequently adopted for site-controlled immobilization of biomolecules during the fabrication of immunoassay-based diagnostic devices (*6–17*).

3-Aminopropyltriethoxysilane (APTES) is one of the most frequently used organosilane agents for the preparation of amino-terminated films on silicon substrates (*1*, *6–17*). A general consensus regarding the APTES film formation is that silanization begins with the hydrolysis of ethoxy groups in APTES, a process catalyzed by water, leading to the formation of silanols. APTES silanols then condense with surface silanols forming a monolayer of APTES via a lateral siloxane network in which amino groups are oriented away from the underlying silicon surface. A host of experimental results, however, have suggested that this is an oversimplified description of the idealized reaction and that the actual process is far more complex and sensitive to reaction conditions (*13*, *17–27*).

The complexity of the APTES silanization reaction mainly stems from the presence of a reactive amino group in APTES and its inherent propensity to enter into competing reactions. The amino groups in adsorbed APTES interact with silanols that are present on the silicon surface and/or in the adjacent hydrolyzed APTES via hydrogen bonding or electrostatic interactions (*18*, *22*, *23*, *28*, *29*). This considerably reduces the number of available silanol groups on both the silicon surface and APTES that could undergo further siloxane condensation. In addition, polymerization and/or physisorption for extended reaction times results in the formation of multiple APTES layers whose structure and reactivity are likely different from those of an APTES monolayer.

Although a major portion of physisorbed APTES could be removed by a sonication-based cleaning process after deposition, our experimental data confirmed that a significant amount remains in the film (*31*, *32*). We proposed that the presence of loosely-bound (physisorbed and/or partially condensed) APTES on the surface is likely to affect the stability of thin films when exposed to aqueous solutions via desorption and/or hydrolysis (*32*, *33*). This is crucial for many applications since immobilization of biomolecules and/or derivatizations of surface amino groups generally proceeds in aqueous solutions (*1*, *6–10*, *15*, *27*, *34*). Therefore, it is of significance to conduct systematic investigations of the structure, stability, and reactivity of APTES thin films on silicon substrates prepared under various experimental conditions.

APTES films on silicon substrates have been characterized by numerous analytical techniques including X-ray photoelectron spectroscopy (XPS) (*21*, *22*,

In Interfaces and Interphases in Analytical Chemistry; Helburn, R., et al.;
ACS Symposium Series; American Chemical Society: Washington, DC, 2011.

35–38), Fourier transform infrared spectroscopy (FTIR) (*39–47*), ellipsometry (*21*, *26*, *48*), scanning probe microscopy (*13*, *21*, *36*, *37*), and contact angle measurement (*22*, *38*, *49*, *50*). In particular, FTIR with various sampling techniques has been popularly used to extract structural information with regard to organic films of various thicknesses on silicon wafers.

Most conventional FTIR data acquisition techniques include transmission (*39*, *40*), external reflection (*41–45*), and internal reflection (*46*, *47*). Both transmission and external reflection methods generally produce infrared spectra with a low signal-to-noise ratio. Hence, these methods generally require a large number of scans (~500 – 1500) and sensitive detection systems (e.g., Mercury Cadmium Telluride (MCT) to produce infrared spectra of good quality. Although the internal reflection method has provided a feasible way to obtain infrared data of organic films with higher signal-to-noise ratio, it requires direct deposition of organic films on infrared-transferable crystals.

Compared to these conventional sampling methods, an exceptional enhancement of absorbance signals in FTIR spectra is achieved when organic layers on silicon substrates are brought into direct contact with high refractive index infrared-transferable crystals (e.g., germanium). This improved sampling technique, a grazing–angle attenuated total reflection (GATR) method, has successfully produced FTIR spectra of monolayers of organic thin films on silicon substrates with enhanced sensitivity (*51–54*).

The thickness of APTES films on silicon substrates prepared under various conditions could be measured by ellipsometry (*21*, *26*, *30*, *31*, *48*). The reactivity and availability of surface amino groups in APTES films have been estimated by fluorescence measurements following the conjugation with amine-reactive fluorophore molecules. Since the quantum yield of conjugated-fluorophores is nearly constant regardless of their conformation on the surface, the measured fluorescence intensity is assumed to be proportional to the amount and reactivity of surface amino groups for a given area as reported previously (*28*, *55*).

In this work, we investigated the effect of experimental conditions such as the reaction solution, deposition time, and curing conditions on the structure and reactivity of APTES films deposited on silicon substrates (*56*). In a first set of experiments, structural characterizations via FTIR, ellipsometry, contact angle measurement, and fluorescence microscopy were conducted for APTES films produced in two different solutions, anhydrous toluene and phosphate buffered saline (PBS), for varied deposition times.

In a second set of experiments, the effect of curing conditions on the structure and stability of APTES films exposed to aqueous solutions was investigated. APTES films were produced in anhydrous toluene solutions, cured under different conditions, and finally sonicated in water. After each procedure, changes in the structure and stability of APTES films were monitored using FTIR-GATR, ellipsometry, and fluorescence microscopy.

Finally, we demonstrate chemical modifications of amino groups on APTES films to three different linkers; N-hydroxysuccinimide (NHS) ester, hydrazide, and maleimide ester. Based on experimental data, the structure, stability, and reactivity of APTES films on silicon substrates are described; the significance of deposition

solvent, reaction time, and curing conditions is discussed, and modifications of surface amino groups are demonstrated.

Experimental Section

A. Chemicals, Materials and Preparation of Waters

Deionized water used for preparation of chemical solutions and in the cleaning of the experimental apparatus was produced by a Millipore Water Purification System with a minimal resistivity of 18.0 MΩ·cm. 3-Aminopropyltriethoxysilane (APTES, 99.0%, Acros), 1,1,1,3,3,3-hexamethyldisilazane (HMDS, 98.0%, Acros), anhydrous toluene (99.8%, extra dry, water < 30 ppm, Acros), ethanolamine (99.0%, Acros), dimethylsulfoxide (DMSO, 99.8% Acros), (1-(3-dimethylaminopropyl)-3-ethylcarbodiimide hydrochloride (EDC, 98%, Acros), *N*-hydroxysuccinimide (NHS, 98%, Sigma-Aldrich), succinic anhydride (SA, 99%, Sigma-Aldrich), 2-(*N*-morpholino)ethanesulfonic acid (MES, 99.5%, Sigma-Aldrich), triethylamine (TEA, 99%, Acros), hydrazine (64%, Arcos), sodium metaperiodate (98.8%, Aldrich), sodium cyanoborohydride (95%, Aldrich), succinimidyl-4-(*N*-maleimidomethyl)cyclohexane-1-carboxylate (SMCC, Pierce Technology), and 5(6)-carboxyfluorescein, *N*-hydroxysuccinimide ester (Marker Gene Technologies, Inc., Eugene, OR) were purchased and used as received without further purification.

P-doped, (100)-oriented silicon wafers (prime grade, 7 – 21 Ω·cm resistivity, ~0.5 mm thickness, 5 inch diameter) were cut into ca. 10 × 10 mm^2 for FTIR and fluorescence measurements and ca. 25 × 25 mm^2 for ellipsometric and contact angle measurements, respectively. Silicon substrates were sonicated in acetone for 10 min, a mixture of acetone (50%) and ethanol (50%) for 10 min, and rinsed with a copious amount of deionized water. After that, silicon wafers were cleaned in freshly prepared Piranha solution (a mixture of 30% H_2O_2 and 70% of H_2SO_4) for at least five hours, rinsed exhaustively with deionized water, and dried in a stream of nitrogen gas before APTES deposition.

B. Preparation of APTES Films

Silicon wafers with APTES films for FTIR, ellipsometry, contact angle measurements, and fluorescence microscopy were prepared simultaneously in the same reaction vessel. All glass reaction vessels were passivated twice by the use of vaporized HMDS at 100 °C before use (*57*, *58*). In a first set of experiments, two types of solvents, anhydrous toluene (water < 30 ppm) and phosphate buffered saline (PBS, pH 7.2 ± 0.1, and ionic strength 10 mM), were used to prepare APTES solutions with a concentration of 2.0% (v/v). APTES films were prepared by incubating clean silicon wafers in APTES solutions for 15 min, 1 h, 4 h, or 24 h. After the controlled deposition, silicon wafers were sonicated twice in APTES-free solvents for 10 min to remove loosely bound APTES. Then, these wafers were dried using a stream of nitrogen gas before data collection.

APTES films for a second set of experiments were prepared by incubating clean and dried silicon wafers in 2.0% APTES anhydrous toluene solutions for 24

In Interfaces and Interphases in Analytical Chemistry; Helburn, R., et al.;
ACS Symposium Series; American Chemical Society: Washington, DC, 2011.

h. After the controlled deposition, silicon wafers were sonicated twice in toluene for 10 min to remove loosely physisorbed APTES, and dried using a stream of nitrogen gas before curing. These APTES films were exposed to two different curing conditions (i) no curing and (ii) curing at 100 °C for 24 h in air.

C. Modification of APTES Films

Chemical modifications of APTES films are outlined in Scheme 1. APTES films for chemical modifications were prepared by incubating clean silicon wafers in 2.0% APTES anhydrous toluene solutions for 24 h as described above. In order to introduce NHS ester and hydrazide groups, amino terminal groups in APTES films were initially converted to carboxyl groups by incubation in 10 mL THF containing 5 mg/ml succinic anhydride (SA) and 5% triethylamine (TEA) for 4 h (a in Scheme 1). After the reaction, silicon wafers were sonicated twice in deionized water for 10 min, and dried using a stream of nitrogen gas before characterization by FTIR and ellipsometry and further chemical derivatizations. For grafting *N*-hydroxysuccinimide (NHS) ester, carboxyl groups on succinylated silicon wafers were reacted with a mixture of (1-(3-dimethylaminopropyl)-3-ethylcarbodiimide hydrochloride (EDC, 50 mg/mL) and NHS (5 mg/mL) in 10 mL 0.5 M MES solution for 3 h (b in Scheme 1) (*59–61*). Silicon wafers were subsequently sonicated two times in deionized water for 10 min and dried before characterization and further experiments.

Hydrazide groups (-$NHNH_2$) were introduced on silicon wafers by reacting NHS ester-functionalized APTES films with 0.1 M hydrazine (NH_2NH_2) solution prepared in pH 7.2 PBS (c in Scheme 1) (*62–64*). After the reaction, residual NHS ester groups in silicon wafers were deactivated by reaction with 0.1 M ethanolamine aqueous solution. Maleimide ester groups were directly introduced on APTES films by the reaction of surface amino groups with succinimidyl-4-(*N*-maleimidomethyl)cyclohexane-1-carboxylate (SMCC, d in Scheme 1) (*65–67*). Silicon wafers with APTES films were incubated in a SMCC solution (5 mg/mL) in THF for 5 h. After the reaction, silicon wafers were sonicated two times in deionized water for 10 min, and dried before further characterization.

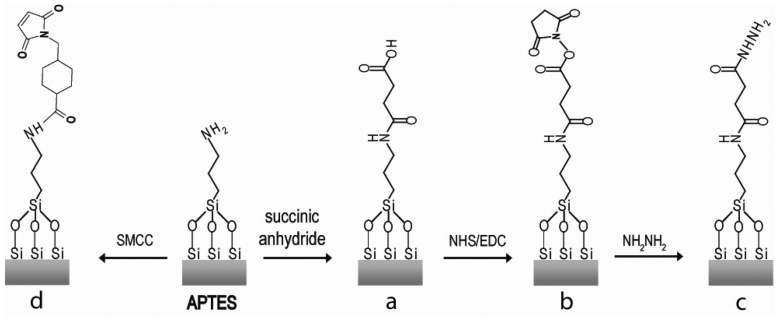

Scheme 1. Amino groups in APTES film on silicon substrates were chemically modified to NHS ester, hydrazide, or maleimide groups.

In Interfaces and Interphases in Analytical Chemistry; Helburn, R., et al.;
ACS Symposium Series; American Chemical Society: Washington, DC, 2011.

D. Characterization of APTES Films

Ellipsometric and infrared spectroscopic characterizations were conducted after the deposition of APTES on silicon wafers under various preparation and curing conditions and after each modification of APTES films. Ellipsometric thickness was measured with a Gaertner L116A automatic ellipsometer equipped with a HeNe laser (632.8 nm). Optical constants of n = 3.865 and k = 0.020 for Si, n = 1.465 and k = 0 for both organic layers and the underlying SiO_2 layer were used (*13*, *68*). The thickness of the silicon oxide layer was measured before APTES film deposition and subtracted from the total thickness after the formation and modification of APTES films as described previously (*13*, *55*, *68*). For each modified film, at least 10 spots from three different silicon wafers were measured to gain the average and standard deviation of the thickness. The thicknesses of two standard silicon wafers having an oxide layer of 100 and 500 Å were measured to be 102 ± 1 and 491 ± 4 Å, respectively, to confirm the proper workability of our ellipsometer before data collection.

FTIR spectra of APTES films on silicon wafers were obtained via a grazing–angle attenuated total reflection method as described elsewhere (*51*, *52*, *54*). A VeeMax™ II sampling stage (Pike Technologies, Madison, WI) equipped with a 60° germanium (Ge) ATR crystal and a high pressure clamp was placed in the sample compartment of a Nicolet Magna 550 FTIR spectrometer. A high pressure swivel clamp 7.8 mm in diameter was used to apply even and constant force (~35 lbs) to the sample during FTIR data acquisition. The angle of incident infrared was set ca. 60° with respect to the surface normal of Ge crystal. Silicon wafers with APTES films were placed (face down) between the Ge crystal and the tip of the high pressure clamp. Each FTIR spectrum represents the average of 200 scans at 4 cm^{-1} resolution. A *p*-polarized infrared beam was used for measurements and the output signal was collected with a deuterated triglycine sulfate (DTGS) detector.

Water contact angle measurements were conducted via the static sessile drop method using a manual goniometer (Ramé-Hart Instrument Co., Model 50-00) as described previously (*38*, *49*, *50*). Measurements were made 10 seconds after dropping 10 µl of deionized water using a microsyringe. For each sample, at least 10 measurements were made to obtain averages and standard deviations reported in this chapter.

The reactivity and stability of APTES films were estimated by fluorescence measurements after carboxyfluorescein ($\lambda_{excitation}$ = 494 nm and $\lambda_{emission}$ = 521 nm) was conjugated to surface amino groups. The conjugation reaction was carried out using 5(6)-carboxyfluorescein, N-hydroxysuccinimide ester (Marker Gene Technologies, Inc., Eugene, OR) at a concentration of 100 µg/mL in a mixture of 0.1 M sodium bicarbonate buffer (pH 8.2) and DMSO (5.0 % v/v) for 3 h. After reactions, silicon wafers with APTES films and conjugated dyes were sonicated twice in deionized water for 10 min and dried with N_2 gas prior to fluorescence measurements.

Fluorescent measurements were conducted using an Olympus BX51 fluorescence microscope and images were recorded with a digital color CCD camera (Diagnostic Instruments model 1.3.0). Recorded images were converted

In Interfaces and Interphases in Analytical Chemistry; Helburn, R., et al.;
ACS Symposium Series; American Chemical Society: Washington, DC, 2011.

into digitized intensities, resolved from a background measurement of an APTES film without dye conjugation, Averages and standard deviations of the background corrected fluorescence intensities from each carboxyfluorescein –conjugated APTES film are reported.

Results

A. Effects of Deposition Solution and Reaction Time

In a first set of experiments, the thickness of APTES films produced in either anhydrous toluene or aqueous solutions for varied deposition times (15 min, 1 h, 4 h, and 24 h) was measured and results are listed in Table I. Ellipsometric data indicate that the thickness of APTES films depends on the reaction time and solution. In both toluene and PBS solutions, thicker APTES films were prepared when deposition was conducted for longer periods of time. While the thickness of APTES films prepared in toluene ranged from 10 to 144 Å, those from PBS were much thinner (8 – 13 Å). An APTES film roughly equivalent in thickness to a monolayer (~7 – 9 Å) was prepared in PBS when reaction time was limited (15 min and 1 h), while multilayers of APTES films were produced in toluene (*29*, *48*).

FTIR spectra of APTES films produced in toluene in the range of 1900 to 1270 cm^{-1} are shown in Figure 1. An FTIR spectrum of an APTES film prepared by spinning-casting on a silicon wafer (thickness ~1300 Å) is included for comparative purpose (see Figure 1e). A vibrational mode around 1655 cm^{-1} is due to the presence of an imine group formed by the oxidation of an amine bicarbonate salt and its intensity is closely related to the film thickness (*20*, *21*, *24*, *25*). There are several vibrational modes with various absorptions between 1610 and 1460 cm^{-1} mainly originating from NH_2 groups in the APTES film. Two weak vibrational modes around 1610 and 1510 cm^{-1} are observed for films with the thickness less than 61 Å (Figure 1a, 1b, and 1c), but they are not clearly observed in spectra of thicker APTES films (Figure 1d and 1e). These modes are assigned to the asymmetric and symmetric deformation modes of NH_2 groups in adsorbed APTES located near the silicon surface (*23–25*). These NH_2 groups are known to associate with silanols present on the silicon surface. A proton transfer from acidic surface silanols to adjacent basic NH_2 groups may give rise to of the formation of $SiO^{-}\bullet\bullet\bullet H\bullet\bullet\bullet NH_2^{+}$ species as was proposed previously (*23–29*).

Two dominant vibrational modes are found around 1575 and 1485 cm^{-1} in Figure 1. It is noticed that the intensity of the modes at 1575 and 1485 cm^{-1} increases as the film thickness increases. However, the intensity of these two modes is comparable for the two films with thicknesses of 144 and 1300 Å (see Figure 1d and 1e). This observation indicates that a major contribution of these vibrational modes at 1575 and 1485 cm^{-1} arises from surface amino groups, rather than those present in the bulk film. It was also observed that the intensity of these modes was attenuated when film deposition was conducted in a N_2 atmosphere (*19*, *20*, *69*). Therefore, the vibrational modes at 1575 and 1485 cm^{-1} arise when surface amino groups form bicarbonate salts in a reaction with atmospheric CO_2, as reported previously (*18*, *25*).

In Interfaces and Interphases in Analytical Chemistry; Helburn, R., et al.;
ACS Symposium Series; American Chemical Society: Washington, DC, 2011.

Table I. The layer thickness (Å) of APTES films prepared in toluene and PBS for 15 min, 1 hr, 4 hr, or 24 hr followed by sonication two times in APTES-free reaction solutions for 10 min

reaction time	*toluene*	*PBS*
15 min	10 ± 1	8 ± 1
1 h	17 ± 1	9 ± 1
4 h	61 ± 2	10 ± 1
24 h	144 ± 3	13 ± 1

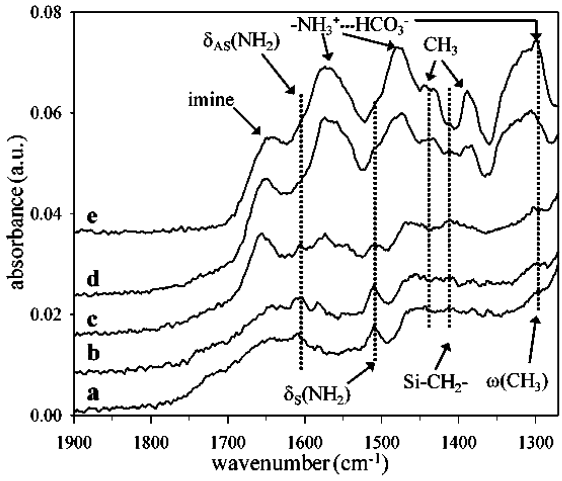

Figure 1. FTIR spectra of APTES films produced in anhydrous toluene solutions with a deposition time of 15 min (a), 1 h (b), 4 h (c), and 24 h (d) followed by sonication twice in toluene for 10 min. The measured thickness of these films was 10, 17, 61, and 144 Å. For comparison, an FTIR spectrum of an APTES film with a thickness ~1300 Å prepared by spinning-cast is also included (e).

In Figures 1c, 1d, and 1e, the asymmetric and symmetric deformation modes of the CH_3 group from ethoxy moieties of APTES are observed around 1440 and 1390 cm^{-1}, respectively (*18*, *25*). The presence of these two modes indicates the existence of ethoxy groups in adsorbed APTES, presumably due to incomplete siloxane condensation or the presence of physically adsorbed unhydrolyzed APTES. The bending mode of the methylene group adjacent to Si in APTES (-Si-CH_2-) is found around 1410 cm^{-1} (*18*, *24*, *25*). The mode near 1330 cm^{-1} is due to the presence of an amine bicarbonate salt (*19*, *20*, *69*). A band at 1300 cm^{-1} is assigned to the CH_2 wagging mode from the APTES backbone (*18*, *25*). Vibrational modes at 1440, 1410, 1390, and 1330 cm^{-1} are not clearly observable in Figure 1a and 1b. This fact suggests that all ethoxy groups in APTES films close to the silicon surface are hydrolyzed leading to siloxane condensation between surface silanols and neighboring surface bound APTES.

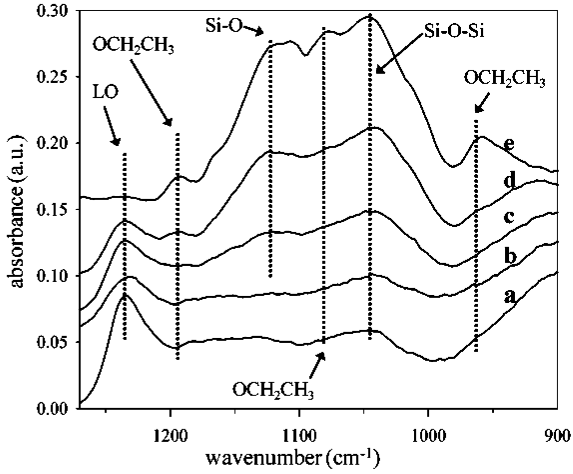

Figure 2. FTIR spectra ranging from 1270 to 900 cm^{-1} for the same APTES films shown in Figure 1. Deposition times were 15 min (a), 1 h (b), 4 h (c), and 24 h (d). An FTIR spectrum of an APTES film with a thickness ~1300 Å was included for comparison (e).

FTIR spectra in the range from 1270 to 900 cm^{-1} for APTES films prepared from toluene solutions are presented in Figure 2. The mode around 1235 cm^{-1} is assigned to the longitudinal optical (LO) mode which is generally observed from a thin reflective silicon oxide film (5 – 100 Å) (*51*, *52*, *70*). The intensity of this LO mode decreases as the APTES layer thickness increases. This LO mode was barely observable when the film thickness is about ~1300 Å (Figure 1e). Vibrational modes around 1195, 1080, and 960 cm^{-1} arise from ethoxy moieties in APTES ($-OCH_2CH_3$) (*18*, *24*, *25*). The presence of these modes, as well as those modes around 1440 and 1390 cm^{-1} in Figures 2d and 2e, indicates incomplete siloxane condensation of adsorbed APTES in films grown for extended periods of time (e.g. 24 h). The peak located around 1125 cm^{-1} is attributed to Si-O moieties of either polymerized or physisorbed APTES. Note that the intensity of this mode is proportional to the APTES layer thickness and increases from 2a to 2d in Figure 2. Comparing with the previously reported FTIR spectra, its position depends on several factors including the presence of ethoxy groups (*18*, *21*, *24*, *25*). The strong mode around 1045 cm^{-1} is attributed to siloxane groups (Si-O-Si) from (i) the silicon substrate, (ii) condensed APTES with the silicon surface, and (iii) polymerized APTES (*18*, *21*, *24*). This mode is also proportional to the APTES layer thickness and increases from 2a to 2d in Figure 2.

FTIR data of the APTES films produced in PBS in the region of 1900 to 1270 cm^{-1} are shown in Figure 3. Compared to spectra from APTES films prepared in toluene solutions (Figure 1), all spectra contain similar vibrational features, intensities, and positions regardless of the reaction time. The presence of the mode at 1510 cm^{-1} along with the absence of observable peaks around 1575 and 1485 cm^{-1} suggests that virtually all of the amino groups in APTES films are associated with surface silanols via noncovalent interactions such as hydrogen boding and

electrostatic interactions. Figure 4 shows FTIR data in the region of 1270 to 900 cm^{-1} from the same APTES films. Again, all spectra are similar to each other with respect to the LO mode and weak shoulders around 1235 and 1125 cm^{-1}. These FTIR spectra indicate that APTES films are structurally comparable to each other regardless of the reaction time when adsorption was conducted in aqueous solutions.

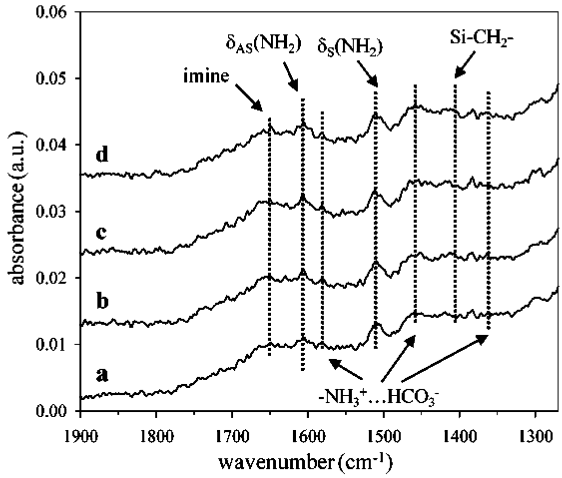

Figure 3. FTIR spectra of APTES films produced in PBS with the deposition time of 15 min (a), 1 h (b), 4 h (c), and 24 h (d) following a 20 min sonication in PBS. Measured thicknesses of these films were about 8, 9, 10, and 13 Å, respectively.

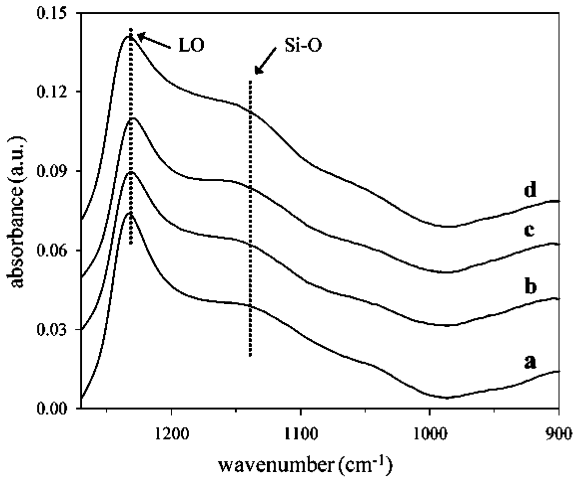

Figure 4. FTIR spectra from same APTES films shown in Figure 3, but in the range 1270 to 900 cm^{-1}.

In Interfaces and Interphases in Analytical Chemistry; Helburn, R., et al.;
ACS Symposium Series; American Chemical Society: Washington, DC, 2011.

Table II. Measured water contact angles (°) for APTES films prepared in toluene and PBS for varied deposition times

reaction time	*toluene*	*PBS*
15 min	50.7 ± 1.6	37.9 ± 2.1
1 h	52.4 ± 1.8	38.2 ± 1.8
4 h	53.0 ± 1.9	41.1 ± 1.8
24 h	54.7 ± 1.6	44.2 ± 0.9

Table III. Fluorescence intensities from carboxyfluorescein conjugated APTES films prepared in toluene and PBS for varied deposition times

reaction time	*toluene*	*PBS*
15 min	17.7 ± 1.7	5.4 ± 0.9
1 h	32.0 ± 4.0	6.5 ± 0.6
4 h	74.3 ± 9.5	6.8 ± 1.1
24 h	90.1 ± 8.5	8.9 ± 1.0

Table II shows static water contact angles measured on APTES films prepared for varied deposition times from two different reaction solutions. Contact angle data indicate that the wettability of APTES primarily depends on the thickness of APTES films. The surface becomes more hydrophobic as the APTES film thickness increases. For APTES films prepared in toluene solutions, water contact angles range from 51 to 55° depending on the film thickness. However, contact angles from APTES films deposited in aqueous solutions are between 38 and 44°.

Table III shows fluorescence intensities of carboxyfluorescein molecules conjugated to APTES films produced in either toluene or aqueous solutions for varied deposition times as described above. It is noted that the fluorescence intensity is proportional to the number of amino groups and their reactivity on the film surface. Fluorescence intensities of APTES films prepared in toluene were greater than those prepared in aqueous solutions for the same deposition time by ca. 3 to 10 times.

B. Effects of Curing Conditions

In a second set of experiments, ellipsometric thicknesses for APTES films deposited for 24 h in toluene before/after curing and after a series of 10 min sonications in water are listed in Table IV. Before curing, the initial thickness of an APTES film deposited for 24 h was measured to be ~167 Å. Without curing, the thickness was significantly reduced to ~61 Å after three cycles of 10 min sonication in water. When cured at 100 °C, the thickness of an APTES film was reduced to ~122 Å after curing. However, a slight increase in the thickness (~3 Å) was observed after subsequent sonication in water.

Table IV. The average thickness and standard deviations (Å) of APTES films on silicon wafers before/after curing and after a series of sonications in water. APTES films were prepared in 2.0% toluene solutions for 24 h, sonicated twice in APTES-free toluene for 10 min, exposed to various curing conditions (no curing or 100 °C for 24 h), sonicated three times in deionized water for 10 min, and dried using a stream of nitrogen before measurements.

curing conditions	*sonication time*	*layer thickness (Å)*
no curing	before sonication	167 ± 15
	10 min	81 ± 7
	20 min	68 ± 5
	30 min	61 ± 5
after curing 100 °C	before sonication	122 ± 27
for 24 h	10 min	124 ± 4
	20 min	125 ± 3
	30 min	125 ± 5

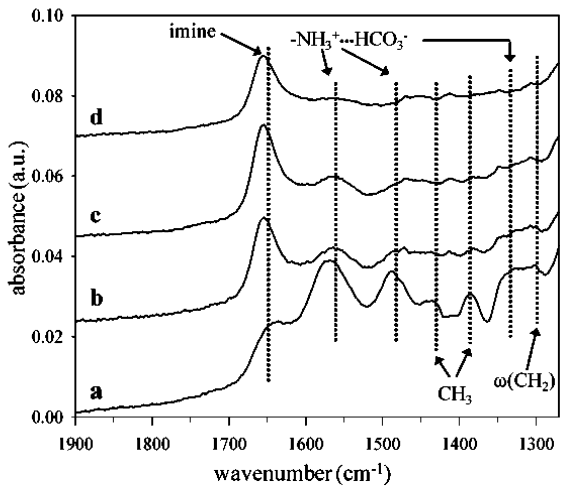

Figure 5. FTIR spectra in the range 1900 to 1270 cm-1 from APTES films produced in dried toluene solutions with the deposition time of 24 h without curing before sonication (a), after sonication in water 10 min (b), 20 min (c), and 30 min (d). The thickness of these films was measured to 167, 81, 68, and 61 Å, respectively.

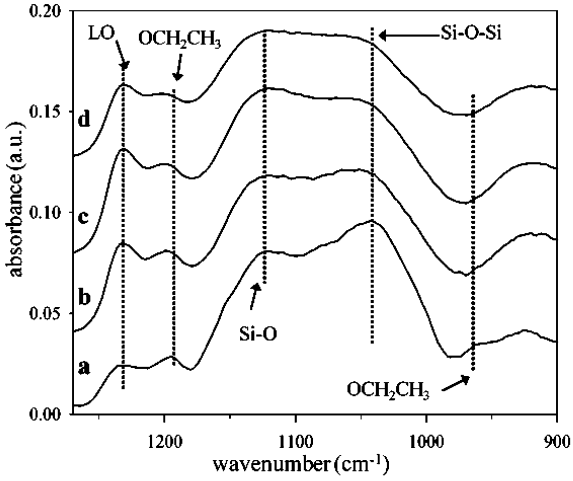

Figure 6. FTIR spectra in the range 1900 to 1270 cm-1 from APTES films produced in dried toluene solutions with the deposition time of 24 h followed by curing at 100 °C for 24 h. Before curing (a), after curing and before sonication (b), after sonication in water 10 min (c), 20 min (d), and 30 min (e). The thickness of these films was measured to ~167, 122, 124, 125, and 125 Å, respectively. After curing, FTIR spectra contain a new vibrational mode around 1550 cm-1.

FTIR spectra were collected for APTES films before/after curing and after subsequent sonication in water. FTIR spectra in the range of 1900 to 1270 cm^{-1} for APTES films deposited for 24 h followed by subsequent sonication in water without curing are shown in Figure 5. Before sonication, several vibrational modes are found in the spectrum mainly originating from NH_2 groups, unhydrolyzed ethoxy groups, and the propyl backbone in the APTES film (Figure 5a). A vibrational mode around 1655 cm^{-1} is responsible for the presence of an imine group formed by the oxidation of an amine bicarbonate salt (*20*, *21*, *24*, *25*). Three vibrational modes around 1575, 1485, and 1330 cm^{-1} arise from bicarbonated surface amino groups in physisorbed and/or partially condensed APTES existing in thicker films (> ~60 Å) as shown in Figure 1 (*19*, *20*, *30*, *31*, *69*). The asymmetric and symmetric deformation modes of the CH_3 group from ethoxy moieties of APTES are observed around 1440 and 1390 cm^{-1}, respectively, presumably due to incomplete siloxane condensation (*18*, *25*).

After sonication in water, the intensity of the vibrational mode around 1655 cm^{-1} increased, while relative intensities of other vibration modes (e.g., 1575, 1485, and 1330 cm^{-1}) decreased in the spectra (see Figure 5b, 5c, and 5d). Changes in FTIR spectra indicate that a substantial amount of loosely bound APTES was removed and surface amino groups were oxidized to imines after sonication in water. It is noted that intensities of these modes were dramatically reduced after the first 10 min sonication, but no further significant reduction was observed after the second and third sonications.

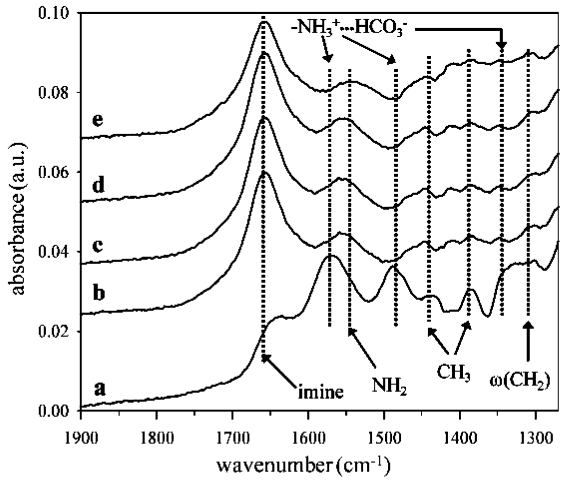

Figure 7. FTIR spectra in the range 1270 to 900 cm-1 from the same APTES films in Figure 5 without curing before sonication (a), after sonication in water 10 min (b), 20 min (c), and 30 min (d). The thickness of these films was measured to 167, 81, 68, and 61 Å, respectively.

FTIR spectra in the range from 1270 to 900 cm^{-1} for same APTES films in Figure 5 (24 h deposition/no curing) are presented in Figure 6. The LO mode around 1235 cm^{-1}, vibrational modes arising from ethoxy ($-OCH_2CH_3$) and Si-O moieties in APTES around 1195 and 960 cm^{-1} are observed (*51*, *52*, *70*). The strong mode around 1045 cm^{-1} is attributed to siloxane groups (Si-O-Si) from (i) the silicon substrate, (ii) APTES condensed with the silicon surface, and (iii) polymerized APTES (*18*, *21*, *24*). The presence of vibrational modes around 1195 and 960 cm^{-1}, as well as those modes around 1440 and 1390 cm^{-1} in Figure 5, indicates incomplete siloxane condensation of adsorbed APTES in films. After sonication in water, the relative intensity of LO increased as the APTES layer thickness accordingly decreased. As in the case of the region between 1900 and 1270 cm^{-1}, general features in FTIR spectra are comparable to each other regardless of the sonication time.

FTIR data from APTES films deposited for 24 h in toluene after curing at 100 °C for 24 h and after sonication in water for 10, 20, and 30 min are shown in Figure 7. An FTIR spectrum of an APTES film before curing is also included for reference (Figure 7a). Conspicuous changes are observed in the spectrum of the APTES film after curing (Figure 7b) compared to the data before curing (Figure 7a). Relative intensities of vibrational modes around 1575 and 1480 cm^{-1} decreased and a new vibrational mode around 1550 cm^{-1} was observed. We suppose that this mode at ~1550 cm^{-1} arises from amino groups existing in polymerized APTES nets which are formed via curing at the elevated temperature. Although a detailed structural description of the amino groups in condensed APTES is not feasible on the basis of these IR spectra, we suppose that the shift to lower frequency indicates tighter association of the amino groups with the APTES network based on measured

APTES film thicknesses which indicate that multilayer APTES films are resistant to dissolution in water after thermal curing.

Figure 8 presents FTIR spectra ranging from 1270 to 900 cm^{-1} for APTES films cured at 100 °C for 24 h followed by a series of sonications in water. For APTES films cured at 100 °C for 24 h, changes in intensities and positions of vibrational modes in FTIR data are found after curing (see Figure 8). After curing, the vibrational mode around 1125 cm^{-1} was shifted to 1140 cm^{-1} presumably due to the polymerization of Si-O moieties in adsorbed APTES (see Figure 8a and 8b). However, the presence of a mode around 1195 cm^{-1} from ethoxy moieties in APTES ($-OCH_2CH_3$) indicates that siloxane condensation is still incomplete (*18*, *21*, *24*, *25*). No further changes in FTIR spectra were found in Figure 8 after a series of sonications in water as was the case for FTIR data in the region between 1900 and 1270 cm^{-1}. The stability of APTES films was estimated by fluorescence measurements.

Table V shows fluorescence intensities from carboxyfluorescein conjugated to APTES films with two curing conditions. It is found that curing conditions significantly affect the fluorescence intensity. For APTES films without curing, fluorescence intensity is measured to be ~10 – 15% compared to that from films with curing.

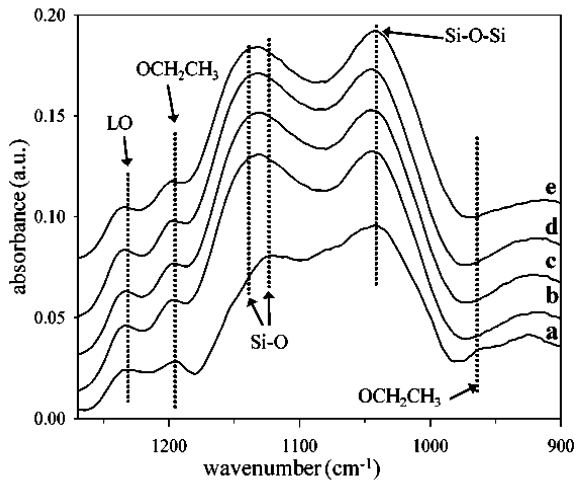

Figure 8. FTIR spectra in the range 1270 to 900 cm^{-1} from the same APTES films in Figure 6 after cured at 100 °C for 24 h. Before curing (a), after curing and before sonication (b), after sonication in water 10 min (c), 20 min (d), and 30 min (e). The thickness of these films was measured to ~167, 122, 124, 125, and 125 Å, respectively.

In Interfaces and Interphases in Analytical Chemistry; Helburn, R., et al.;
ACS Symposium Series; American Chemical Society: Washington, DC, 2011.

Table V. Average and standard deviations (a.u.) of measured fluorescence intensity from carboxyfluorescein-conjugated APTES films on silicon wafers. APTES films were prepared in 2.0% toluene solutions for 24 h, sonicated twice in APTES-free toluene for 10 min, exposed to two curing conditions (no curing or 100 °C for 24 h), sonicated three times in deionized water for 10 min, and dried using a stream of nitrogen.

curing conditions	*sonication time*	*fluorescence intensity*
no curing	before sonication	16.5 ± 2.7
	10 min	16.4 ± 2.0
	20 min	15.5 ± 2.1
	30 min	8.5 ± 1.9
after curing 100 °C	before sonication	131.3 ± 10.6
for 24 h	10 min	125.5 ± 10.5
	20 min	120.7 ± 11.6
	30 min	102.3 ± 10.7

C. Surface Modification of Amino Groups

Changes in ellipsometric thicknesses of APTES films after successive chemical modifications described in Scheme 1 are presented in Table VI. The initial thickness of APTES films before chemical modifications was measured to be ~130 Å. After reaction with succinic anhydride (SA) in THF, the thickness was increased by ~5 Å. Further increase in the thickness by ~5 Å was observed after the introduction of *N*-hydroxysuccinimide (NHS) ester groups on the surface via the reaction of COOH-terminated surfaces with NHS in the presence of EDC. After introduction of hydrazide groups (-$NHNH_2$) by the reaction of NHS ester-functionalized APTES films with hydrazine, the thickness was reduced by ~4 Å, as bulky NHS ester groups were replaced by small-sized hydrazide groups. Grafting maleimide ester groups on a APTES surface using SMCC resulted in an increase in the thickness by ~7 Å.

FTIR spectra in the range of 1900 to 1270 cm^{-1} for APTES films before and after succinylation, after introduction of NHS ester groups, hydrazide groups, and maleimide groups are shown in Figure 9 (*71*). Prior to modification, two dominant vibrational modes are found in the spectrum of the intact APTES film (Figure 9a). A vibrational mode around 1655 cm^{-1} arises from the presence of an imine group formed by the oxidation of an amine bicarbonate salt (*20*, *21*, *24*, *25*, *30*, *31*). The other vibrational mode around 1565 cm^{-1} is attributed to bicarbonated surface amino groups of the APTES film when exposed to air (*19*, *20*, *30*, *31*, *69*).

Table VI. Changes in the APTES film thickness after surface modifications as described in Scheme 1. The thickness of unmodified APTES films was measured to be ~130 (4) Å.

reactions of APTES films with	*changes in measured thickness (Å) after reactions*
succinic anhydride (SA)	5 ± 1
NHS	5 ± 2
succinic anhydride (SA)	5 ± 1
NHS	5 ± 2
hydrazine	-4 ± 1
SMCC	7 ± 1

After reaction of APTES films with SA, the intensity, peak width, and positions of vibrational modes around 1655 and 1565 cm^{-1} were changed and a new mode was observed around 1405 cm^{-1} (see Figure 9b). The full width at the half-maximum (FWHM) of a vibration mode around 1655 cm^{-1} was increased by ~15 cm^{-1} and its position was shifted to around 1650 cm^{-1}. In the case of the vibrational mode around 1565 cm^{-1}, the intensity was dramatically increased and its position was slightly shifted to 1560 cm^{-1}. These two vibrational modes are typical signatures of amide bonds formed by succinylation of amine groups on APTES films as reported previously (*72*, *73*). Succinylation was also confirmed by the existence of a new vibrational mode around 1405 cm^{-1} which arises from terminal carboxyl groups of the modified surface (*74*, *75*). We assume that the presence of these terminal carboxyl groups is partly responsible for the enhancement in vibrational intensity around 1560 cm^{-1} (*76*, *77*).

NHS ester was introduced on the succinylated APTES surface by reaction with NHS and EDC. FTIR data of the surface after reaction reveals several weak features around 1820, 1780, and 1740 cm^{-1} (c in Figure 9). These modes are attributed to the NHS ester groups on the surface (*59*, *78*). The intensity of a vibrational mode for surface carboxyl groups around 1405 cm^{-1} was attenuated after incorporation of NHS ester groups. After the reaction of an NHS-grafted film with hydrazine, hydrazide groups are grafted and vibrational modes around 1820, 1780, and 1740 cm^{-1} were no longer observed in the spectrum (d in Figure 9). A new vibrational mode around 1510 cm^{-1} was found in the presence of hydrazide groups. This mode is due to the symmetric stretch of NH_2 groups in hydrazide moieties (*23–25*).

An FTIR spectrum for an APTES film after reaction with SMCC is presented in Figure 9e. The FTIR spectrum of the APTES surface after reaction with SMCC contains two additional vibrational modes around 1740 and 1705 cm^{-1} compared to the data of unmodified APTES surface shown in Figure 9a. Two different types of amide bonds in grafted maleimide groups give rise to these respective vibrational modes (*66*, *79*). The mode around 1740 cm^{-1} arises from the newly formed amide bond between APTES and SMCC and the other mode around 1705 cm^{-1} is from the amide bond present in maleimide moiety.

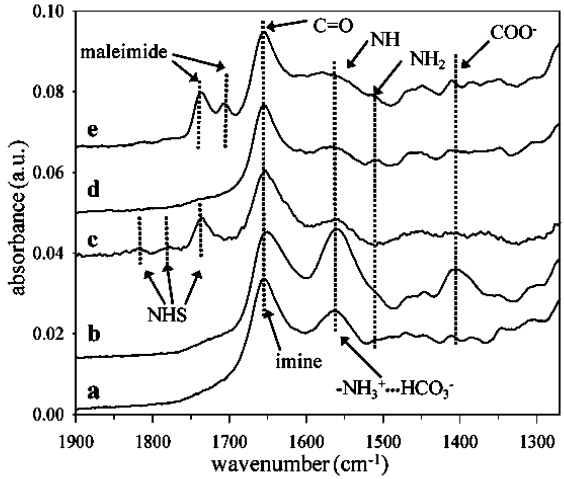

Figure 9. FTIR spectra in the range of 1900 to 1270 cm-1 from APTES films produced in dried toluene solutions with the deposition time of 24 h followed by curing at 25 °C for 24 h (a), after the reaction with succinic anhydride (b), after reaction with NHS/EDC (c), after the reaction with hydrazine (d), and an APTES film after reaction with SMCC (e) as described in Scheme 1.

Discussion

From ellipsometric measurements and FTIR spectra, it was found that APTES films on silicon substrates adopt different structures depending on the reaction solution and deposition time. Such structural differences are attributed to the difference in the APTES adsorption process and film formation mechanism as reported previously (*13*, *17–27*). In an aqueous solution, most ethoxy groups in APTES are readily hydrolyzed to silanols. Since the silicon oxide surface (pK_a < 5) is negatively charged and the amino group in APTES is partially protonated in aqueous solutions at pH ~7.2, APTES likely adsorbs to the silicon surface via electrostatic interactions (*80*). We suppose that a majority of adsorbed APTES adopts a conformation with its amino group directed towards the negatively charged silicon surface while negative (or neutral) silanols point away from the silicon surface as shown in Figure 10a.

The presence of charged APTES and/or APTES with silanol groups directing away from the surface is likely responsible for the formation of the more hydrophilic APTES films in aqueous solutions. In Table II, the measured contact angle from an APTES film produced in aqueous solution for 4 h, 41.1°, is less than that from an APTES film produced in toluene solution for 15 min, 50.7°, despite comparable thicknesses of the two APTES films, ~10 Å. This is also supported by our fluorescence measurements shown in Table III. Fluorescence intensity from APTES films prepared in an aqueous solution for 4 h (thickness ~10 Å) is less by about two times than that from the APTES film of a comparable thickness prepared in toluene for 15 min. This suggests that fewer surface amino

In Interfaces and Interphases in Analytical Chemistry; Helburn, R., et al.;
ACS Symposium Series; American Chemical Society: Washington, DC, 2011.

groups are available on APTES films prepared in aqueous solution presumably due to orientations of amino groups on silicon surfaces (see Figure 10a).

It seems that siloxane condensation between silanol groups of adsorbed APTES and surface silanols is not feasible in aqueous solution. Instead, further deposition of charged APTES in an aqueous solution is expected via electrostatic interactions and/or hydrogen bonding forming multilayers as described in Figure 10b. Unlike those APTES films prepared in toluene, APTES layers formed in water consist of weakly bound APTES via electrostatic interactions/or hydrogen bonding. This may explain our observation that APTES films prepared in aqueous solutions are thinner than those prepared from toluene solutions at equal reaction times after sonication.

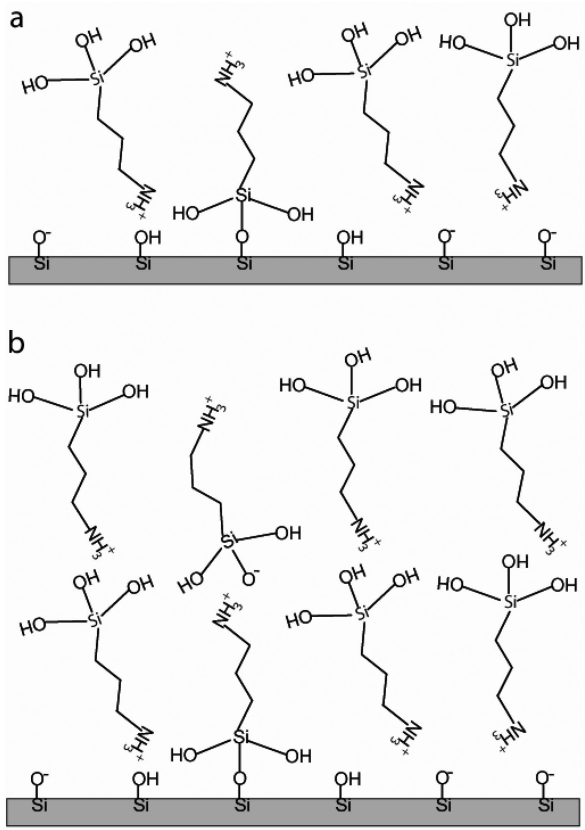

Figure 10. Schematic representation of adsorbed APTES on a silicon wafer in PBS. Initial APTES adsorption is driven via electrostatic interactions between positively charged amino groups and the negatively charges silicon surface in PBS with pH ~7.2. Some of the adsorbed APTES condenses with surface silanols forming siloxane linkages. Further deposition is also expected to proceed by electrostatic interactions and/or hydrogen bonding to form multilayers of APTES (b).

In Interfaces and Interphases in Analytical Chemistry; Helburn, R., et al.;
ACS Symposium Series; American Chemical Society: Washington, DC, 2011.

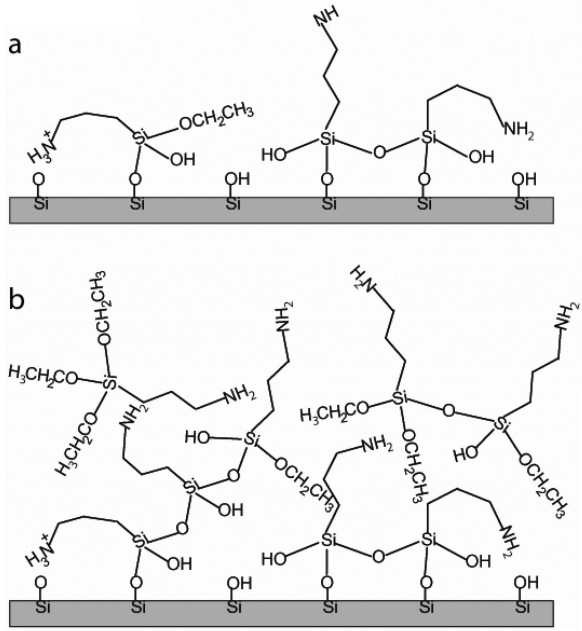

Figure 11. Schematic representation of adsorbed APTES on a silicon wafer in an anhydrous toluene solution. Ethoxy groups of adsorbed APTES are eventually hydrolyzed and form siloxane bonds with surface silanols (a). Further siloxane condensation between surface bound APTES and dissolved APTES and/or noncovalent adsorption of dissolved APTES results in the formation of APTES multilayers on the silicon wafer (b).

In a toluene solution, ethoxy groups in APTES are not completely hydrolyzed. We suppose that hydrogen bonding between the amino group in APTES and surface silanol plays an important role in initial APTES adsorption as indicated by the presence of vibrational features at 1610 and 1510 cm^{-1} in FTIR data. Once near the surface, a fraction of those ethoxy groups in APTES is hydrolyzed by trace amounts of surface bound water and subsequently condenses with surface silanols and other adjacent surface bound APTES giving rise to flat lateral film growth as was proposed previously (see Figure 11a) (*1*).

Unreacted ethoxy (or hydrolyzed silanol) groups of adsorbed APTES may lead to condensation with dissolved APTES giving rise to vertical film growth. However, the condensation is slower due to the absence of water. As the reaction time increases, more APTES accumulates via covalent condensation and/or physisorption leading to thicker films (see Figure 11b). Previous studies by atomic force microscopy (AFM) and scanning electron microscopy (SEM) suggest that thinner APTES films are generally flat and homogeneous, but aggregates are found on thicker films produced for extended reaction times (*13*, *21*, *36*, *37*). These thicker APTES films contain a mixture of condensed (or partially condensed) APTES and physisorbed APTES.

In Interfaces and Interphases in Analytical Chemistry; Helburn, R., et al.;
ACS Symposium Series; American Chemical Society: Washington, DC, 2011.

Although a major portion of physisorbed and/or partially condensed APTES was removed by sonication in toluene, we believe that a significant amount remains in the film. Our experimental results indicate that these loosely-bound APTES located at the outer layer of films generally govern the mechanical stability of the film in aqueous solution. For APTES films without curing, the initial thickness of freshly deposited films was dramatically reduced after just 10 min sonication in water (see Table IV). This indicates that these surface-bound APTES were aggregated via hydrogen-bonding and/or noncovalent interactions making them resistant to dissolution in non-polar solutions like toluene. Two additional cycles of sonication in water further reduced the thickness but by much less compared to the first sonication. FTIR spectra of APTES films after successive sonication show that the intensity of vibrational modes around 1575 and 1480 cm^{-1} was significantly reduced by the first sonication, but was much less attenuated after the second and third sonications in water (see Figure 5). This implies that a major portion of physisorbed APTES was removed after the first sonication in accordance with changes in ellipsometric thicknesses listed in Table IV.

For APTES films cured at 100 °C for 24 h, most structural changes occurred during the curing process via vaporization of aggregated APTES and siloxane condensation between APTES. This is confirmed by decreased infrared signal intensities around 1575 and 1480 cm^{-1} due to APTES desorption and shifts of positions from 1575 and 1125 cm^{-1} to 1560 and 1140 cm^{-1} due to the APTES polymerization in Figure 7. A slight increase in the thickness (~3 Å) of APTES after subsequent sonication in water was presumably caused by conformation changes upon hydration, but no supporting changes in FTIR data were observed. Our results indicate that APTES films cured at 100 °C are physically rigid and thus maintained in water, due to the formation of a chemically stable siloxane net between APTES. Our fluorescence measurements showed that physically durable and chemically reactive APTES films are produced after being cured at 100 °C for 24 h as demonstrated by increased fluorescence intensities as shown in Table V.

Chemical modification of surface amino groups were attempted as described in Scheme 1. For grafting either NHS ester or hydrazide groups, the first step involves converting amino groups in APTES films to carboxyl groups by reaction with SA. Although it was reported that succinylation was previously carried out in a basic aqueous solution (~ pH 11) (*16*, *63*), our FTIR spectra of APTES films after reaction, via reported conditions, reveal no observable vibrational modes expected for succinylated APTES films. Similarly, ellipsometric thickness of these APTES films after the reaction did not show any significant difference.

THF containing ~5% (v/v) TEA was found to be the optimal reaction solution for succinylation. Ellipsometric measurements show that the thickness of these APTES films was increased by ~5 Å after succinylation (see Table VI). Assuming the length of grafted succinylated moiety is ca. 6.3 Å by Corey Pauling Koltun (CKP) model (*81*), the results indicate that surface coverage of succinylated APTES is ca. 80% if there are sufficient succinylation sites are available on the surface. As the surface density of amino groups on an APTES film is reported to be ca. 1.15/nm^2 (*79*), our ellipsometric data suggest that the surface density of grafted succinylated moieties is ca. 0.92/nm^2. The reduced surface density is presumably due to the steric effect of bulky succinylated moieties.

In Interfaces and Interphases in Analytical Chemistry; Helburn, R., et al.;
ACS Symposium Series; American Chemical Society: Washington, DC, 2011.

Although numerous attempts for grafting maleimide groups on APTES films using SMCC were attempted in an aqueous solution as described previously (*82*, *83*), no observable vibrational modes for maleimide groups were found in FTIR data. Instead, DMF was proven to be the best reaction solvent for incorporation of maleimide groups on APTES films, giving rise to two vibrational modes around 1705 and 1740 cm^{-1} in FTIR data (see Figure 9e) (*66*, *79*).

Summary and Conclusions

Ellipsometry, FTIR, contact angle measurements, and fluorescence microscopy show that the structure, thickness, wettability, and reactivity of APTES films are affected by preparation conditions such as the deposition time and the choice of reaction solutions, due to differences in the APTES adsorption process and film growth mechanisms. In aqueous solution, APTES films grow by electrostatic interactions and/or hydrogen bonding. These films are not stable and are easily disrupted by sonication, leaving one or two monolayers of APTES on the silicon surface. However, APTES films grow by both covalent and noncovalent adsorption of APTES in an anhydrous toluene solution. There exist at least three different types of APTES in these films; APTES directly condensed on the silicon surface, APTES condensed with other APTES, and physisorbed APTES. A major portion of the surface amino groups in multilayers of APTES films readily forms bicarbonate salts in a reaction with dissolved CO_2. Without curing, a majority of loosely-bound APTES located at the outer layer of films was removed. Therefore, proper curing at elevated temperature is necessary to produce physically stable and chemically reactive APTES films. It was demonstrated that surface amino groups on APTES films were chemically modified to *N*-hydroxysuccinimide (NHS) ester, hydrazide, or maleimide ester groups for further applications.

Acknowledgments

This work is supported by a startup fund from SUNY Research Foundation and Department of Chemistry, Buffalo State, SUNY. Several parts of Nicolet Magna 550 infrared spectrometer were obtained from Department of Energy via the Used Energy-Related Laboratory Equipment (ERLE) Grant Program.

References

1. Haller, I. *J. Am. Chem. Soc.* **1978**, *100*, 8050–8055.
2. Sagiv, J. *J. Am. Chem. Soc.* **1980**, *102*, 92–98.
3. Netzer, L.; Sagiv, J. *J. Am. Chem. Soc.* **1983**, *105*, 674–676.
4. Ulman, A. *Chem. Rev.* **1996**, *96*, 1533–1554.
5. Onclin, S.; Ravoo, B. J.; Reinhoudt, D. N. *Angew. Chem., Int. Ed.* **2005**, *44*, 6289–6304.
6. MacBeath, G.; Schreiber, S. L. *Science* **2000**, *289*, 1760–1763.

7. Mooney, J. F.; Hunt, A. J.; McIntosh, J. R.; Liberko, C. A.; Walba, D. M.; Rogers, C. T. *Proc. Natl. Acad. Sci. U.S.A.* **1996**, *93*, 12287–12291.
8. Chrisey, L. A.; Lee, G. U.; O'Ferrall, E. *Nucleic Acids Res.* **1996**, *24*, 3031–3039.
9. Saprigin, A. V.; Thomas, C. W.; Dulcey, C. S.; Patterson, Jr, C. H.; Spector, M. S. *Surf. Interface Anal.* **2004**, *36*, 24–32.
10. Hooper, A. E.; Werho, D.; Hopson, T.; Palmer, O. *Surf. Interface Anal.* **2001**, *31*, 809–814.
11. Charles, P. T.; Vora, G. J.; Andreadis, J. D.; Fortney, A. J.; Meador, C. E.; Dulcey, C. S.; Stenger, D. A. *Langmuir* **2003**, *19*, 1586–1591.
12. Flink, S.; Schonherr, H.; Vancso, G. J.; Geurts, F. A. J.; van Leerdam, K. G. C.; van Veggel, F.; Reinhoudt, D. N. *J. Chem. Soc., Perkin Trans. 2* **2000**, 2141–2146.
13. Howarter, J. A.; Youngblood, J. P. *Langmuir* **2006**, *22*, 11142–11147.
14. Pereira, C.; Patrício, S.; Silva, R.; Magalhães, A. L.; Carvalho, P.; Pires, J.; Freire, C. *J. Colloid Interface Sci.* **2007**, *316*, 570–579.
15. Wei, H.; Zhou, L.; Li, J.; Liu, J.; Wang, E. *J. Colloid Interface Sci.* **2008**, *321*, 310–314.
16. Guo, W.; Ruckenstein, E. *J. Membrane Sci.* **2003**, *215*, 141–155.
17. Kovalchuk, T.; Sfihi, H.; Kostenko, L.; Zaitsev, V.; Fraissard, J. *J. Colloid Interface Sci.* **2006**, *302*, 214–229.
18. Chiang, C.-H.; Ishida, H.; Koenig, J. L. *J. Colloid Interface Sci.* **1980**, *74*, 396–404.
19. Culler, S. R.; Naviroj, S.; Ishida, H.; Koenig, J. L. *J. Colloid Interface Sci.* **1983**, *96*, 69–79.
20. Culler, S. R.; Ishida, H.; Koenig, J. L. *J. Colloid Interface Sci.* **1986**, *109*, 1–10.
21. Vandenberg, E. T.; Bertilsson, L.; Liedberg, B.; Uvdal, K.; Erlandsson, R.; Elwing, H.; Lundström, I. *J. Colloid Interface Sci.* **1991**, *147*, 103–118.
22. Herder, P.; Vågberg, L.; Stenius, P. *Colloid Surf.* **1988/1989**, *34*, 117–132.
23. White, L. D.; Tripp, C. P. *J. Colloid Interface Sci.* **2000**, *232*, 400–407.
24. Weigel, C.; Kellner, R. *Fresenius J. Anal. Chem.* **1989**, *335*, 663–668.
25. Peña-Alonso, R.; Rubio, F.; Rubio, J.; Oteo, J. *J. Mater. Sci.* **2007**, *42*, 595–603.
26. Kurth, D. G.; Bein, T. *Langmuir* **1993**, *9*, 2965–2973.
27. Choi, S.-H.; Zhang Newby, B.-M. *Surf. Sci.* **2006**, *600*, 1391–1404.
28. Kamisetty, N. K.; Pack, S. P.; Nonogawa, M.; Devarayapalli, K. C.; Kodaki, T.; Makino, K. *Anal. Bioanal. Chem.* **2006**, *386*, 1649–1655.
29. Chiang, C.-H.; Liu, N.-I.; Koenig, J. L. *J. Colloid Interface Sci.* **1982**, *86*, 26–34.
30. Kim, J.; Seidler, P.; Fill, C.; Wan, L.-S. *Surf. Sci.* **2008**, *602*, 3323–3330.
31. Kim, J.; Seidler, P.; Wan, L.-S.; Fill, C. *J. Colloid Interface Sci.* **2009**, *329*, 114–119.
32. Kozerski, G. E.; Gallavan, R. H.; Ziemelis, M. J. *Anal. Chim. Acta* **2003**, *489*, 103–114.
33. Crampton, N.; Bonass, W. A.; Kirkham, J.; Thomson, N. H. *Langmuir* **2005**, *21*, 7884–7891.

34. Ebner, A.; Hinterdorfer, P.; Gruber, H. J. *Ultramicroscopy* **2007**, *107*, 922–927.
35. Moses, P. R.; Wier, L. M.; Lennox, J. C.; Finklea, H. O.; Lenhard, J. R.; Murray, R. W. *Anal. Chem.* **1976**, *50*, 576–585.
36. Gu, Q.; Cheng, X. *Cur. Appl. Phys.* **2008**, *8*, 583–588.
37. Mo, Y.; Zhu, M.; Bai, M. *Colloids Surf., A* **2008**, *322*, 170–176.
38. Kowalczyk, D.; Slomkowsk, S.; Chehimi, M. M.; Delamar, M. *Int. J. Adhes. Adhes.* **1996**, *16*, 227–232.
39. Maoz, R.; Sagiv, J.; Degenhardt, D.; Möhwald, H.; Quint, M. P. *Supramol. Sci.* **1995**, *2*, 9–24.
40. Tu, H.; Heitzman, C. E.; Braun, P. V. *Langmuir* **2004**, *20*, 8313–8320.
41. Chalmers, J. M.; Everall, N. J.; Ellison, S. *Micron* **1996**, *27*, 315–328.
42. Onclin, S.; Mulder, A.; Huskens, J.; Ravoo, B. J.; Reinhoudt, D. N. *Langmuir* **2004**, *20*, 5460–5466.
43. Brunner, H.; Vallant, T.; Mayer, U.; Hoffmann, H. *Langmuir* **1996**, *12*, 4614–4617.
44. Hoffmann, H.; Mayer, U.; Brunner, H.; Krischanitz, A. *Vib. Spectrosc.* **1995**, *8*, 151–157.
45. Hoffmann, H.; Mayer, U.; Krischanitz, A. *Langmuir* **1995**, *11*, 1304–1312.
46. Vallant, T.; Kattner, J.; Brunner, H.; Mayer, U.; Hoffmann, H. *Langmuir* **1999**, *15*, 5339–5346.
47. Margel, S.; Sivan, O.; Dolitzky, Y. *Langmuir* **1991**, *7*, 2317–2322.
48. Petri, D. F. S.; Wenz, G.; Schunk, P.; Schimmel, T. *Langmuir* **1999**, *15*, 4520–4523.
49. Janssen, D.; De Palma, R.; Verlaak, S.; Heremans, P.; Dehaen, W. *Thin Solid Films* **2006**, *515*, 1433–1438.
50. Krishnan, A.; Liu, Y.-H.; Cha, P.; Woodward, R.; Allara, D.; Vogler, E. A. *Colloids Surf., A* **2005**, *43*, 95–98.
51. Olsen, J. E.; Shimura, F. *Appl. Phys. Lett.* **1988**, *53*, 1934–1936.
52. Rochat, N.; Chabli, A.; Bertin, F.; Olivier, M.; Vergnaud, C.; Mur, P. *J. Appl. Phys.* **2002**, *91*, 5029–5034.
53. Milosevic, M.; Berets, S. L.; Fadeev, A. Y. *Appl. Spectrosc.* **2003**, *57*, 724–727.
54. Lummerstorfer, T.; Kattner, J.; Hoffmann, H. *Anal. Bioanal. Chem.* **2007**, *388*, 55–64.
55. Flink, S.; van Veggel, F. C. J. M.; Reinhoudt, D. N. *J. Phys. Org. Chem.* **2001**, *14*, 407–415.
56. In this paper, curing is the hardening process of APTES self-assembled monolayers (SAMS) on solid substrates via cross-linking by heating.
57. Gun'ko, V. M.; Turov, V. V.; Bogatyrev, V. M.; Charmas, B.; Skubiszewska-Ziba, J.; Leboda, R.; Pakhovchishin, S. V.; Zarko, V. I.; Petrus, L. V.; Stebelska, O. V.; Tsapko, M. D. *Langmuir* **2003**, *19*, 10816–10828.
58. Slavov, S. V.; Sanger, A. R.; Chuang, K. T. *J. Phys. Chem. B* **2000**, *104*, 983–989.
59. Schäferling, M.; Riepl, M.; Pavlickova, P.; Paul, H.; Kambhampati, D.; Liedberg, B. *Microchim. Acta* **2003**, *142*, 193–203.

60. Patel, N.; Davies, M. C.; Hartshorne, M.; Heaton, R. J.; Roberts, C. J.; Tendler, S. J. B.; Williams, P. M. *Langmuir* **1997**, *13*, 6485–6490.
61. Kenseth, J. R.; Harnisch, J. A.; Jones, V. W.; Porter, M. D. *Langmuir* **2001**, *17*, 4105–4112.
62. O'shannessy, D. J.; Wilchek, M. *Anal. Biochem.* **1990**, *191*, 1–8.
63. Soltys, P. J.; Etzel, M. R. *Biomaterials* **2000**, *21*, 37–48.
64. Hirota, J.; Michikawa, T.; Natsume, T.; Furuichi, T.; Mikoshiba, K. *FEBS Lett.* **1999**, *456*, 322–326.
65. MacBeath, G.; Koehler, A. N.; Schreiber, S. L. *J. Am. Chem. Soc.* **1999**, *121*, 7967–7968.
66. Mallik, R.; Wa, C.; Hage, D. S. *Anal. Chem.* **2007**, *79*, 1411–1424.
67. Knight, B. C.; High, S. *Biochem. J.* **1998**, *331*, 161–167.
68. Le Grange, J. D.; Markham, J. L.; Kurkjian, C. R. *Langmuir* **1993**, *9*, 1749–1753.
69. Culler, S. R.; Ishida, H.; Koenig, J. L. *J. Colloid Interface Sci.* **1985**, *106*, 334–346.
70. Hu, S. M. *J. Appl. Phys.* **1980**, *51*, 5945–5948.
71. Kim, J.; Cho, J.; Seidler, P. M.; Kurland, N. E.; Yadavalli, V. K. *Langmuir* **2010**, *26*, 2599–2608.
72. Aoki, N.; Nishikawa, M.; Hattori, K. *Carbohydr. Polym.* **2003**, *52*, 219–223.
73. Li, J.; Li, H.-M. *Eur. Polym. J.* **2005**, *41*, 823–829.
74. Frey, B. L.; Corn, R., M. *Anal. Chem.* **1996**, *68*, 3187–3193.
75. Jordon, C. E.; Frey, B. L.; Kornguth, S.; Corn, R. M. *Langmuir* **1994**, *10*, 3642–3648.
76. Smith, E. L.; Alves, C. A.; Anderegg, J. W.; Porter, M. D.; Siperko, L. M. *Langmuir* **1992**, *8*, 2707–2714.
77. Lu, Y.; Miller, J. D. *J. Colloid Interface Sci.* **2002**, *256*, 41–52.
78. Voicu, R.; Boukherroub, R.; Bartzoka, V.; Ward, T.; Wojtyk, J. T. C.; Wayner, D. D. M. *Langmuir* **2004**, *20*, 11713–11720.
79. Shen, G.; Horgan, A.; Levicky, R. *Colloid Surf. B* **2004**, *35*, 59–65.
80. Iler, R. K. *The Chemistry of Silica*; Wiley: New York, 1979.
81. Corey, R. B.; Pauling, L. *Rev. Sci. Inst.* **1953**, *24*, 621–627.
82. Bieniarz, C.; Husain, M.; Barnes, G.; King, C. A.; Welch, C. J. *Bioconjugate Chem.* **1996**, *7*, 88–95.
83. Kuijpers, W. H. A.; Kaspersen, F. M.; Veeneman, G. H.; Van Boeckel, C. A. A.; Bos, E. S. *Bioconjugate Chem.* **1993**, *4*, 94–102.

Chapter 7

Electrochemical Studies of Self-Organized Porphyrin−Polyoxometalate Films on ITO

Giorgio Bazzan,[1,†] Amit Aggarwal,[1,†] and Charles Michael Drain[*,1,2]

[1]Department of Chemistry and Biochemistry, Hunter College of the City University of New York, 695 Park Avenue, New York, NY 10065 (USA)
[2]The Rockefeller University, 1230 York Avenue, New York, NY 10065 (USA)
[†]G. B. and A. A. contributed equally to this work.
[*]cdrain@hunter.cuny.edu

Sequential dipping of indium-tin oxide electrodes into solutions of tetra cationic porphyrins and tetra anionic polyoxometalates results in the controlled formation of nm thick films. The potential applications of these robust films on electrodes range from catalysts to sensors. This chapter focuses on the electrochemistry of the multilayered films where it is found that the oxidation and reduction potentials of each species remain largely the same as found in solution.

Introduction

Organic-inorganic hybrid materials are of great interest in the field of material chemistry as these materials can exhibit synergetic, electrical, optical, and catalytic properties (*1*). *Polyoxometalates* (POM) are a large class of inorganic oxide clusters with a wide range of chemical and oxidation/reduction properties that are used in both laboratory and commercial materials, as models of oxide surfaces, and as models of inorganic matrixes (*2*). They are used as catalysts, and POMs with defects can bind a plethora of metal ions, which alter their physical chemical properties in precise and predictable ways. Electrodes modified with POM have recently attracted increasing attention because of their good stability, wide ranging chemistry, and catalytic activity (*2*). For example, POM-containing multilayer films can be more efficient in heterogeneous catalysis because they have unique advantages over other chemically modified electrodes, e.g. the

In Interfaces and Interphases in Analytical Chemistry; Helburn, R., et al.;
ACS Symposium Series; American Chemical Society: Washington, DC, 2011.

three-dimensional layered architecture of electrocatalysts and the amount of absorbed electrocatalyst can be precisely controlled (*3–5*).

Typical methods for preparing chemically modified electrodes have been addressed in a review of the electrochemical properties of POMs (*6*). The three main methods commonly used to immobilize POM onto the electrode surface are: (1) adsorption on electrode surface by dip coating (*7*), (2) immobilization of POM as dopant in a conductive polymer matrix (*8*), (3) electrochemical deposition directly on the electrode via application of a potential (*9*). Each of these methods has advantages and disadvantages. Typically, dip coated films are less robust but use the POMs more efficiently because most are exposed to solvent, while the electrodeposited films are more robust but access to the catalytic sites inside the granules may be limited because of higher packing density. The chemistry and characterization on a molecular scale of the hybrid polymer/POM films are difficult, but the performance can be satisfactory.

Layer-by-layer (LBL) deposition involves the sequential dipping of a substrate, such as an electrode, into solutions containing molecules or polymers with complementary intermolecular interactions. Most LBL films are organized electrostatically by sequentially dipping the substrate into solutions containing oppositely charged species – usually polyelectrolytes (*10–12*). Recently, layer-by-layer strategy has been successfully used to modify electrode surfaces based on electrostatic interaction between anionic POM and cationic compounds or polymers (*13–16*).

Porphyrins are robust conjugated tetrapyrrole macrocycles that can complex a wide range of metal ions, and they possess an equally wide range of photophysical properties that arise from the complexed metal ion, exocyclic motifs, and the environment. Many porphyrinoid materials have been investigated over the last decades (*17–25*). The macrocycle and the metallocomplexes also typically have several reversible oxidations and/or reductions (*26*). Thus, porphyrins are used in photonic materials for sensor, catalytic, nonlinear optical, therapeutic and many other applications.

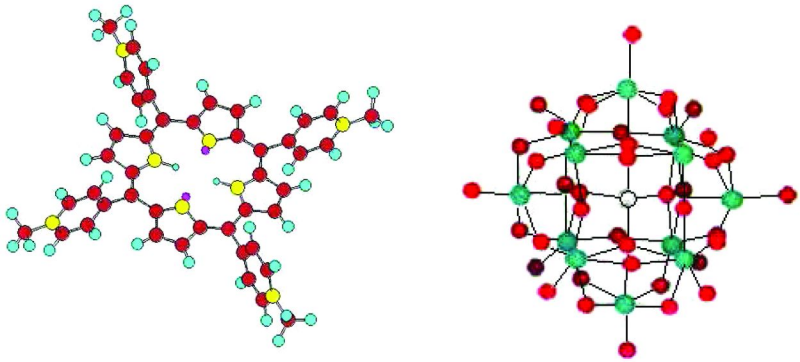

Scheme 1. Left 5,10,15,20-tetrakis(4-methylpyridinium)porphyrin ($TMPyP^{4+}$) is used as the tosylate salt. (H = light blue, N = yellow, C = redbrown), and right: polyoxometalate (POM) $H_4SiW_{12}O_{40}$ (O = red, W = blue, Si = gray) where the counter ions are left out for clarity. (see color insert)

In Interfaces and Interphases in Analytical Chemistry; Helburn, R., et al.;
ACS Symposium Series; American Chemical Society: Washington, DC, 2011.

In terms of catalysts, sensors, and analytical applications, there are a couple of reports on the deposition of cationic porphyrins and anionic POMs on modified glassy carbon electrode (*14*, *27*). These electrodes were found to display electrocatalytic activity for the reduction of O_2 to peroxide and for hydrogen evolution from acidic water, but for their preparation, the glassy carbon electrode needed to be functionalized with 4-aminobenzoic acid, and the material was then deposited by cyclic potential sweeps of the electrode in a solution of the ions to be deposited.

The demonstrated electrocatalytic activity of these porphyrin/POM films, and the formation of other photonic materials with diverse potential applications prompted us to examine the structure and mechanism of electrostatically organized films on a variety of substrates (*20*). We recently demonstrated that porphyrin/POM modified surfaces such as quartz, glass, and indium-tin oxide (ITO) electrodes can be easily prepared by sequentially dipping these supports into solutions containing a tetracationic 5,10,15,20-tetrakis (4-methylpyridinium) porphyrin ($TMPyP^{4+}$) as the tetratosylate salt, and silicotungstic acid hydrate ($SiW_{12}O_{40}^{4-}$) (Scheme1). Notably, sequential dipping of these substrates into solutions of the oppositely charged materials does not require previous preparation of the electrode surface. Since these are lower energy surfaces than those with greater charge density, the amount of either compound deposited on any given deposition is significantly less than a complete (mono)layer (Scheme 2). Several key points from this previous work are germane to the electrochemistry. (1) Estimates of the surface density after one deposition of the porphyrin are ca. 1 per 20 nm^2 and the porphyrin is ca. 1.5 nm^2. Thus, the surface energetics of the substrate dictate how many deposition sequences are needed to completely cover the substrate (about four rounds of dipping for all three substrates) and to form a robust film (ca. eight). (2) There is a linear increase in the porphyrin UV/Vis absorption, e.g. the B (Soret) band, with the number of deposition cycles, which correlates to a linear increase in the amount of material deposited up to about 100 cycles, where we stopped the experiment. (3) After ca. eight layers, the films are stable to sonication in water, 1 M NaCl, and toluene. (4) Patterns of these films can be formed on ITO lithographed with lines of 600 nm wide by 20 nm high polycarbonate, where the film resides only on the bare surface (not on the polymer). We present herein a detailed analysis of the cyclic voltammetric properties of these films, created by sequential dipping, to correlate the structure-function relationships.

Experimental

Materials. All reagents and solvents were of analytical grade and used without further purification. The water was passed through a Barnstead NANOPure Water Purification System. The $TMPyP^{4+}$ and silicotungstic acid hydrate ($SiW_{12}O_{40}^{4-}$) were purchased from Aldrich.

Cyclic voltammetry was performed with a BAS-CV-50W in a conventional three-electrode electrochemical cell, using an ITO (0.6 cm^2) as the working electrode, a platinum wire as the auxiliary electrode, and Ag/AgCl/KCl (3 mol/L)

as the reference electrode. All experiments were performed using the same area of the electrode. NaCl 0.1 M in ultrapure water was used as the supporting electrolyte with two different pH values, pH=3 (adjust by addition of 0.5 M H_2SO_4), and compared to pH=4 acetate buffer (0.1 mol/L). The scan rate was 0.1 V/s. All the solutions were degassed thoroughly with pure nitrogen and kept under a positive pressure of this gas during experimentation. The starting potential and initial direction of scan are indicated by a directional arrow on the individual voltammograms

The ITO substrate was cleaned using a homemade UV/ozone cleaning system, rinsed with ultrapure water, sonicated in ethanol for 10 min., and dried by blowing a steam of nitrogen gas across the surface. Films were prepared at room temperature by soaking the ITO substrate in a 0.5 mM aqueous solution of porphyrin for 1 min, followed by dipping the substrate three times in unbuffered NANOPure water to remove the excess, non-bound porphyrin solution from the substrate. Subsequently, a layer of polyoxometalates was added by soaking the substrate for 1 minute in a 0.5 mM aqueous solution of polyoxometalates, rinsed three times by dipping in NANOPure water. The procedure was repeated until the desired film thickness was obtained. The films on the glass side of the ITO substrates were left in place.

Results and Discussion

Solution Analysis

The electrochemical properties of $TMPyP^{4+}$ have been reported in detail, using both Hg and ITO electrodes (*28*). The reduction chemistry in acidic solution is pH dependent and involves six electrons overall. Between pH=2 and pH=6 two peaks are observed (Figure 1). The first is a quasi reversible reduction (-104 mV) step that involves the reduction of the porphyrin free base to the chlorin free base (Figure 1). The pH dependence is given by the equation below.

$$P(0)H_2 + 2e^- + 2H^+ \Leftrightarrow P(\text{-II})H_4 \qquad \text{pH dependence (60 mV/pH)}$$

At potentials more negative than -0.65 V vs Ag/AgCl a complicated, irreversible four electron reduction occurs (-605 mV) which generates unstable porphyrinogen cations.

The electrochemical response of the $H_4SiW_{12}O_{40}$ in aqueous medium has been extensively studied. Sadakane et al. report that in acid solution using a glassy carbon working electrode the CV shows five reductions waves with an approximate electron ratio of 1:1:2:8:12 (*6*). The first three reductions are reversible while the last two are irreversible and accompanied by chemical reactions of the complex (*6*).

$$SiW_{12}O_{40}^{4-} + e^- \Leftrightarrow SiW_{12}O_{40}^{5-}$$

$$SiW_{12}O_{40}^{5-} + e^- \Leftrightarrow SiW_{12}O_{40}^{6-}$$

$$SiW_{12}O_{40}^{6-} + 2e^- + 2H^+ \Leftrightarrow H_2SiW_{12}O_{40}^{6-}$$

In Interfaces and Interphases in Analytical Chemistry; Helburn, R., et al.;
ACS Symposium Series; American Chemical Society: Washington, DC, 2011.

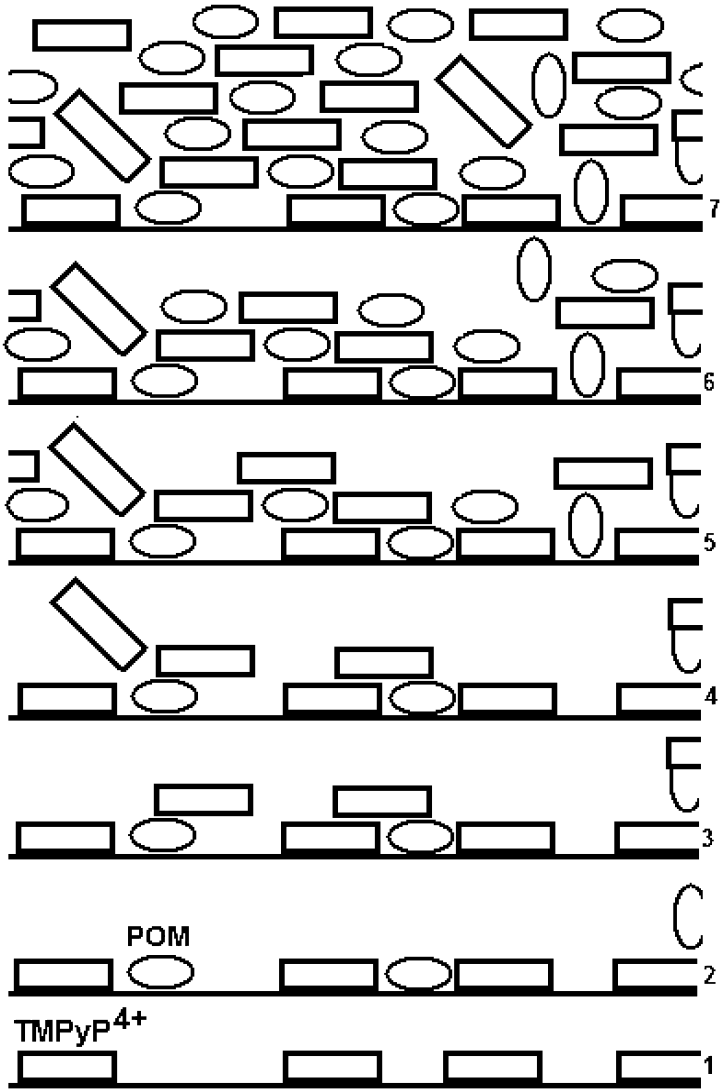

Scheme 2. Sequential dipping of the ITO substrate into solutions of the $TMPyP^{4+}$ and the POM results in formation of thin films. It takes ca. four sequences to form a complete layer, and eight to form a robust film.

In the potential window suitable for the porphyrin (-0.6 V / +0.6 V) there are two reversible reductions for the POM (-215 mV and -490 mV) that are essentially unaltered for $1 < pH < 5$ (Figure 2). Prior to the electrochemical study of the layer-by-layer deposition process, we analyzed the behavior in aqueous solutions (pH=3) of $TMPyP^{4+}$ and $SiW_{12}O_{40}^{4-}$ using ITO as working electrode (Figure 1 and 2). The CV curves at pH=3 confirm the above reductions and indicate that the ITO surface has a small effect on the potential measured. However, the two POM reduction peaks in solution are observed to broaden on the ITO electrode

(*14*). Accordingly, we have set the scan limit of our cyclic voltammetry to -0.55 V vs. Ag/AgCl.

Film Analysis

Cyclic voltammetry can be used to monitor the deposition process and to characterize the electrochemical behavior of the film. Compared to the solution properties, the film exhibits less well resolved redox peaks (Figure 3). There is a broad reduction peak at -325 mV for the porphyrin. The first two POM oxidation peaks almost merge with each other (-270 mV). This is probably due to surface-confined redox processes (*29*). To assure identical and reproducible data, the CV curves shown in Figure 3 are the fifth after a preliminary set of polarization cycles as was done previously (*4*, *14*, *15*). Previous reports do not show the data for the first few CV cycles, and this will be discussed below (Figures 5 and 6).

The CV curves in Figure 3 are recorded with the POM as outermost layer and after eight deposition cycles to assure that complete surface coverage and film robustness have been reached, *vida supra*. Since the currents represent the surface concentration of the POM and porphyrin loaded on the electrode, the currents increase gradually with the number of deposition cycles and indicate that a consistent amount of porphyrin and polyoxometalate are deposited with each deposition cycle. Similar CV curves are obtained when the porphyrin is the outermost layer (Figure 4) but with a slightly different electrochemical behavior and different slopes for plots of current versus number of deposition cycle. (See Figure 7 for the oxidation peak current at -270 mV and Figure 8 for the absolute value of the reduction peak current at -325 mV plotted versus deposition cycle number.)

Figures 5 and 6 show the effect of the first four cycles of potential scans with the POM and porphyrin as the last deposited material, respectively. The cyclic voltammograms are quite different, exhibiting a significant decrease in the currents of both the oxidation peak (e.g. +23 mV porphryin) and the reduction peak (e.g. -325 mV POM) of the films. The current stops diminishing after four potential scan cycle, likely indicating that only the external part of the porphyrinic/POM material present on the film desorbs or decomposes. This difference in the initial scans suggest that POM inhibits desorption of the porphyrin-POM films from the surface, or the interlayer electrostatic interactions between the porphyrin-POM layers is stronger when POM is the last layer. The steeper decrease in the oxidation peak at +23 mV compared to the reduction peak at -325 mV suggests either an irreversible reduction reaction of the porphyrinic material (in spite of the fact that the porphyrin in solution is stable in the potential window examined), or a desorption of some porphyrinic material from the film after the reduction process. UV/Vis absorption measurements of the electrolyte solution after 16 deposition cycles, and consequently many potential scans, indicates a small amount of the porphyrin in solution (Figure A1 inset), moreover the film is stable in high ionic strength solutions, e.g. sonication in 0.1 M NaCl shows that little of the porphyrin comes off of the substrates.

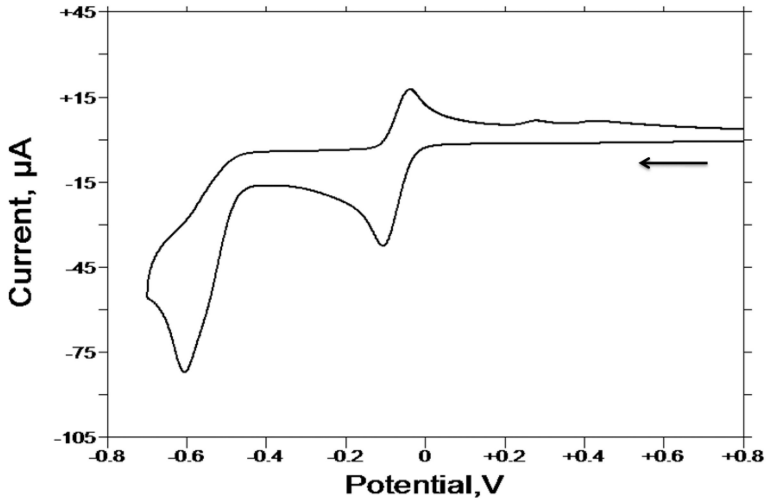

Figure 1. Cyclic voltammogram of a $TMPyP^{4+}$ solution using an ITO working electrode (0.6 cm^2), platinum wire counter electrode and Ag/AgCl/KCl (3 mol/L) reference electrode. Unbuffered NaCl (0.1 mol/L) in ultrapure water, pH=3 (adjusted by addition of 0.5 M H_2SO_4) was used and the scan rate was 0.1 V/s. Reduction peaks:-104 mV, and -605 mV; Oxidation peak: -37 mV vs. Ag/AgCl.

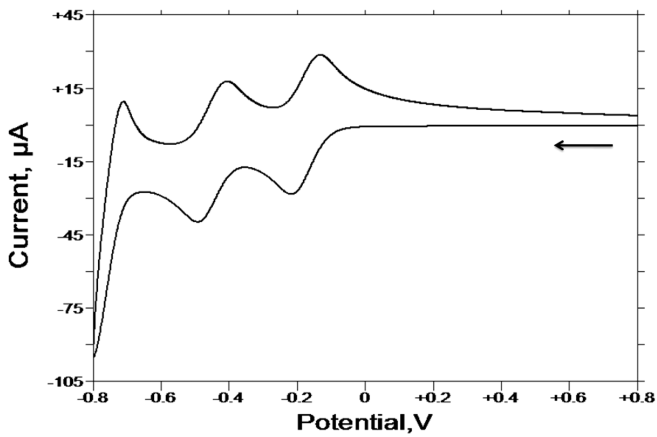

Figure 2. Cyclic voltammogram of a $SiW_{12}O_{40}^{4-}$ solution using an ITO (0.6 cm^2) working electrode, platinum wire counter electrode, and Ag/AgCl/KCl (3 mol/L) reference electrode. Unbuffered NaCl (0.1 mol/L) in ultrapure water, pH=3 (adjusted by addition of 0.5 M H_2SO_4) was used, and the scan rate was 0.1 V/s. Reduction peaks: -215 mV, -490 mV; Oxidation peaks: -710 mV, -408 mV, -135 mV vs. Ag/AgCl.

In Interfaces and Interphases in Analytical Chemistry; Helburn, R., et al.;
ACS Symposium Series; American Chemical Society: Washington, DC, 2011.

However, comparison of the initial UV/Vis spectra of films for 16 porphyrin-POM layers on an ITO substrate to those after the CV experiment shows a small decrease in the absorption maximum in the Soret region (Figure A1 at end of chapter). This indicates either desorption or decomposition of the porphyrinic material. Also, the UV/Vis and fluorescence analysis of the electrolyte solution after the CV experiment shows the presence of trace quantities of the porphyrin in solution, clearly indicating that small amounts of desorption of some material from the ITO surface while the CV analysis was done (Figure A1 and A2 at end of chapter).

Note also that the UV/Vis spectra of both the film and the solution show no evidence of chlorin or other reduced or oxidized porphyrin products. Similar changes are observed when the POM is the last deposited material. Overall, these results suggest that the last deposition sequence, of no matter how many, does not form a complete, stable layer under the CV scanning conditions, perhaps leaving some porphyrin "exposed" even when the POM is the last material deposited. This is consistent with our model of film growth wherein each dipping does not form a layer *per se*, but switches the net surface charge density until an equilibrium is reached (*20*).

Cyclic voltammograms performed after each sequence of deposition (8 through 18 or 21, data from the 5th CV scan) were recorded both when porphyrin and when the POM was deposited last. A plot of the number of deposition sequences versus current (taken from the POM peaks in Figure 3 and 4: oxidation peak current at -270 mV and reduction peak current at -325 mV) reveals that the magnitude of the current is ca. 3-fold less when the porphyrin is added last and the slopes of the lines depends on which compound was deposited last (Figure 7 and 8).

The currents increase because there are more redox active materials on the surface of the electrode, but there may be several explanations for why there is a marked dependence on which of the two molecules is deposited last onto the growing film.

(1) When the POM is the outermost layer, a greater amount of material is deposited each round of dipping.
(2) When the porphyrin is the last material deposited, more porphyrinic material is exposed on the surface and can undergo desorption. This means that the outermost POM prevents the porphyrinic material underneath from desorption.
(3) There may be morphological differences between the surfaces that depend on the last deposited compound such that the POM last films have a greater effective electrode surface, which would result in a greater observed current.
(4) The CV current also depends on the energetics and the electrostatics of the surfaces, and there are differences in the surface properties when the porphyrin is the last deposited material versus the POM. The fact that there is a linear growth of the films with increasing numbers of sequential depositions, indicates that the net surface charges alternate between positive for the $TMPyP^{4+}$ last films, and negative for the POM

In Interfaces and Interphases in Analytical Chemistry; Helburn, R., et al.;
ACS Symposium Series; American Chemical Society: Washington, DC, 2011.

last films, though the surface charge densities may differ. There are also likely differences arising from the hydrophobic porphyrin core versus the hydrophilic POM. Considering that the CVs are performed in acidic solution (pH=3) the net positive charge of the electrode surface when the porphyrin is deposited last may inhibit interfacial proton transport. This is consistent with proton coupled electron transfer with POMs (*9*).

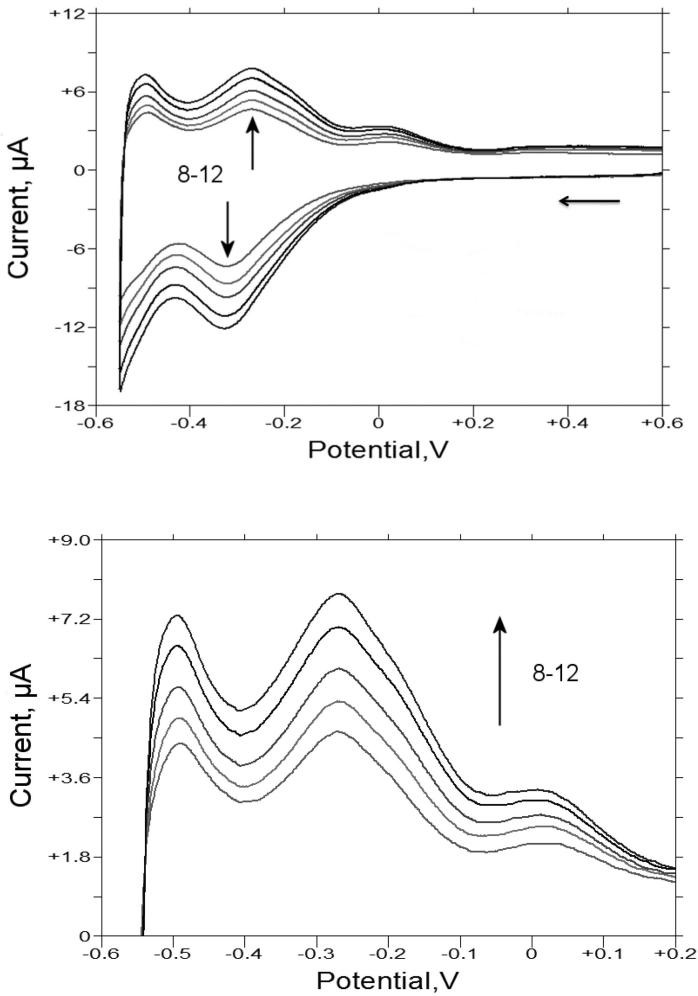

Figure 3. Top: Cyclic voltammogram of the films built on ITO using $TMPyP^{4+}$ and $SiW_{12}O_{40}^{4-}$ with 8 to 12 dipping cycles. Each CV was recorded with the POM as the outermost layer. Bottom: Details of the oxidation peaks. Reduction peak: -325 mV; Oxidation peaks: -495 mV, -270 mV, +23 mV vs. Ag/AgCl. pH=3, for the electrolytic solution.

In Interfaces and Interphases in Analytical Chemistry; Helburn, R., et al.;
ACS Symposium Series; American Chemical Society: Washington, DC, 2011.

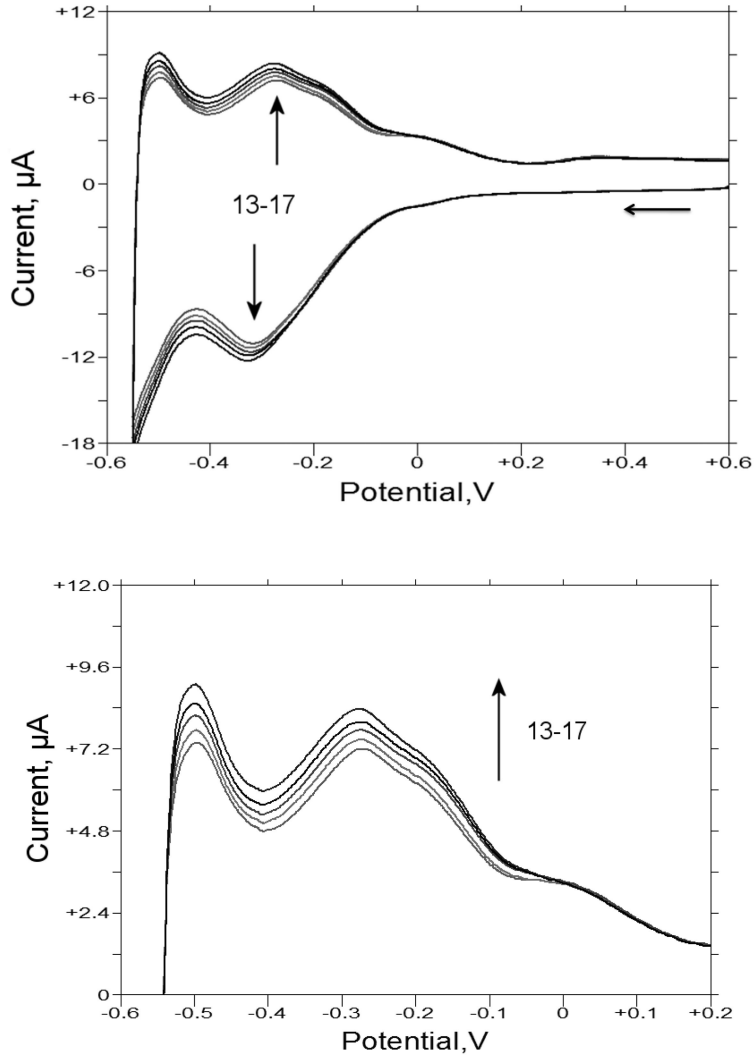

Figure 4. Top: Cyclic voltammogram of the films built on ITO using $TMPyP^{4+}$ and $SiW_{12}O_{40}^{4-}$ with 13 to 17 dipping cycles. Each CV was recorded with the porphyrin as the outermost layer. Bottom: Details of the oxidation peaks. Reduction peak: -325 mV; Oxidation peaks: -495 mV, -270 mV, +23 mV vs. Ag/AgCl. pH=3, for the electrolytic solution.

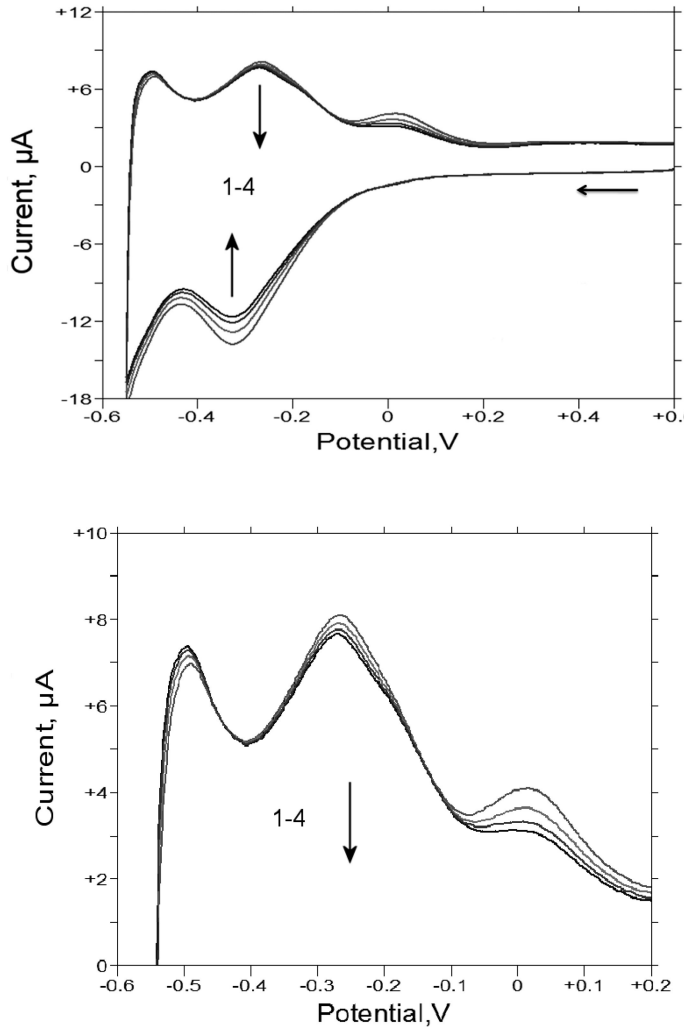

Figure 5. Top: The initial four potential scans of a film built on ITO after 10 deposition sequences with the POM added last shows that the current decreases. The diminishment of the peak currents stop after four CV scans with the fifth scan (see Figure 3) overlapping the fourth. Bottom: Details of the oxidation peaks. Reduction peak: -325 mV; Oxidation peaks: -495 mV, -270 mV, +23 mV vs. Ag/AgCl. pH=3, for the electrolytic solution.

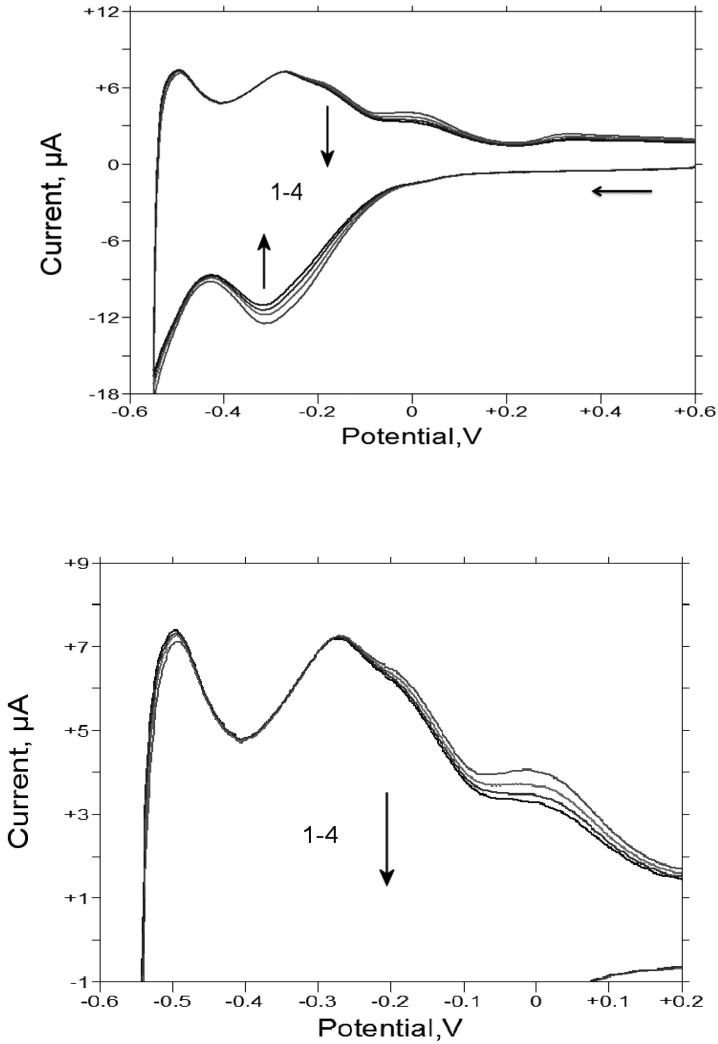

Figure 6. Top: The initial four potential scans on a film built on ITO after 11 deposition sequences with porphyrin added last shows that the current decreases. The diminishment of the peak currents stop after four polarization scans with the fifth scan (see Figure 4) overlapping the fourth. Bottom: Details of the oxidation peaks. Reduction peak: -325 mV; Oxidation peaks: -495 mV, -270 mV, +23 mV vs. Ag/AgCl. pH=3, for the electrolytic solution.

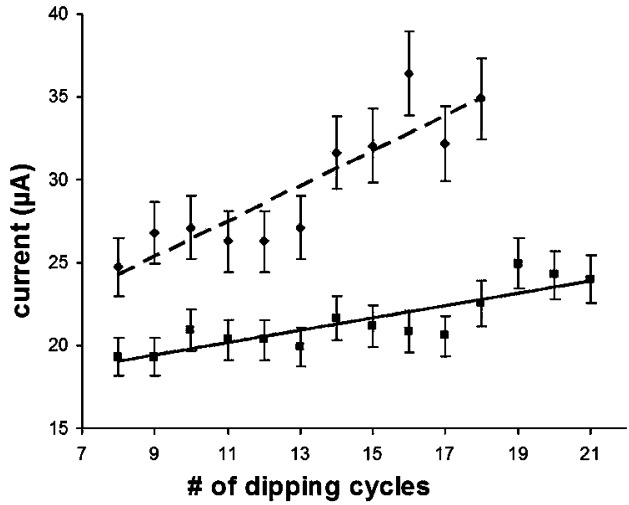

Figure 7. Oxidation peak current at -270 mV when (----) POM is the last material deposited (slope = 1.07), and (—) when the porphyrin is the last material deposited (slope = 0.37). These plots are from CV data similar to what is shown in Figures 3 and 4. Error bars represent the average of four experiments. Data are recorded on the 5th CV scan.

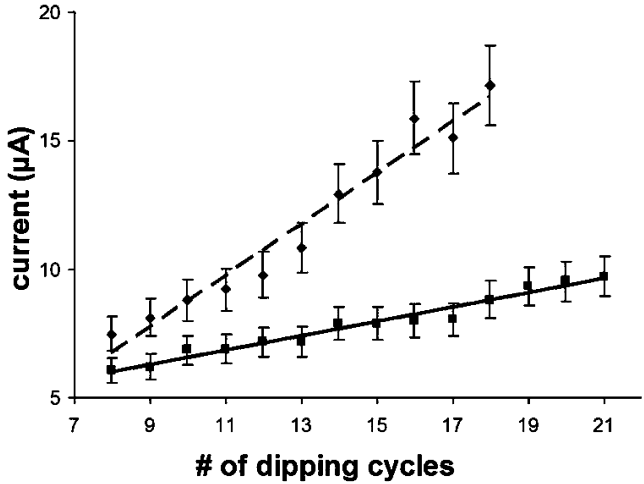

Figure 8. Absolute value of the reduction peak current at -325 mV when (-----) POM is the last material deposited (slope = 0.97), and (—) when the porphyrin is the last material deposited (slope = 0.28). These plots are from CV data similar to what is shown in Figures 3 and 4. Error bars represent the average of four experiments. Data are recorded on the 5th CV scan.

For the solution phase and film CVs in Figures 123456, the electrolyte solutions were adjusted to pH=3. We then performed CV experiments on films where the electrolyte solutions were adjusted to pH=4 and pH=5. The CVs in Figures A3 and A4 demonstrate the narrow pH dependence of these electrode reactions. No resolved peak currents were observed at either of these higher pH values, using a working potential window of -550 mV to +800 mV. At pH=4, two irreversible oxidation peaks start to appear when the POM is added last to the film. (See Figures A3 and A4)

Conclusions

We have avoided the use of the word "layer" to describe the $TMPyP^{4+}$ /POM films because any given dipping of the substrate into either the POM or porphyrin solution does not form a complete layer. The CV peaks for both the porphyrin and the POM indicates that both species have access to the electrode surface. Nonetheless the sequential dipping deposition processes, which are analogous to the layer-by-layer fabrication of films, can be successfully adopted for the formation of chemically modified electrodes, without any previous preparation of the electrode surface and using two electroactive small molecules. There is no *a priori* need for either cyclic potential scans or polymeric materials (e.g. polycationic or polyanionic) to affect the deposition of thin films consisting of porphyrins and POMs.

The electrochemical responses of the film correspond to the sum of the individual components – the porphyrin and the POM. After the first few deposition cycles necessary to reach a complete coverage of the electrode surface, there is no influence of the film thickness on the electrochemical potentials of the components on the modified electrode. Small increases in the currents are observed for each deposition cycle. This indicates that the electron transfer is still possible in the 2-30 nm films. The dielectric properties of the $TMPyP^{4+}$/POM films are markedly different than films containing polyelectrolyte materials because there is a greater charge density. In order for the electron transfer to go from the electrode to the film surface, a possible electron-hopping mechanism may be involved where electron exchange between neighboring redox sites results in "percolation" of electrons through the material under the influence of a chemical potential (*30*). Though the $TMPyP^{4+}$ has an irreversible reduction at -605 mV (versus Ag/AgCl), this is not observed in the porphyrin/POM films, thus the films confer some stability to the macrocycle. Similarly formed porphyrin/POM films have demonstrated catalytic activity (*6*, *24*, *31–33*), and can serve as electrochemical sensors (*12*, *19*, *34*). Small changes in the electrolyte pH (e.g. 2.5 versus 3.0) shift the observed electrochemical oxidation and reduction potentials such that this may be exploited for these applications.

Porphyrins are used as photosensitizers, therefore stimulating catalytic processes by visible light irradiation could change the electrochemical behavior of the film. Catalytic studies on a composite organic/inorganic material formed by association of metalloporphyrins and POMs showed that this material has more efficient catalytic properties than the corresponding metalloporphyrins

alone, and that the POMs contributed to the stabilization of the metalloporphyrin against deactivation during the catalytic cycles (*33*). Hence, the sequential dipping method using porphyrins and polyoxometalates can be a very simple and economic technique to fabricate supported catalysts (with the advantages of heterogeneous catalysis) and sensors.

The $[Fe(III)TMPyP]^{5+}$ also can be used in the above sequential dipping fabrication process as indicated by the linear increase in the UV/Vis absorption of the films with increasing rounds of deposition. Since metalloporphyrins are good catalysts and these films are robust to immersion in organic solvents, perhaps these films can be exploited for a diverse array of organic transformations or for assays of organic species in water, such that the oxidative or reducing equivalents come from the electrode rather than a stoichiometric chemical reagent. Also, the large extinction coefficients of porphyrinoids may facilitate photocatalysis by either the POM or the stabilized porphyrin.

Acknowledgments

CMD acknowledges funding from the National Science Foundation (NSF CHE-0847997). Hunter College Chemistry infrastructure is supported by the NSF, National Institutes of Health, including the RCMI program (G12-RR-03037), and the City University of New York. The authors wish to thank Dr. Jing Jing from the laboratory of Prof. Lynn Francesconi for assistance with the CV experiments.

Appendix

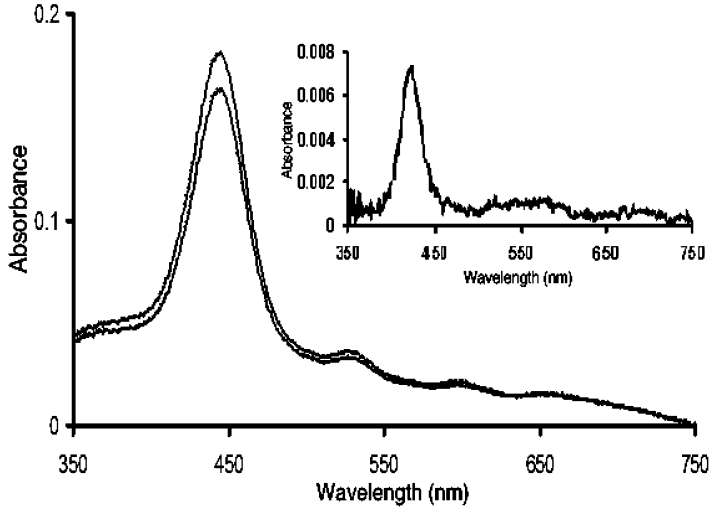

Figure A1. UV-visible studies of films fabricated from 16 porphyrin/POM dipping sequences on ITO before (—) and after (---) CV studies shows that ca. 9% of the porphyrin is removed and no obvious porphyrin decomposition products such as chlorins or dipyrromethanes. Inset : UV-visible spectra of the electrolyte solution (0.1 mol/L NaCl) after 16 CV scans.

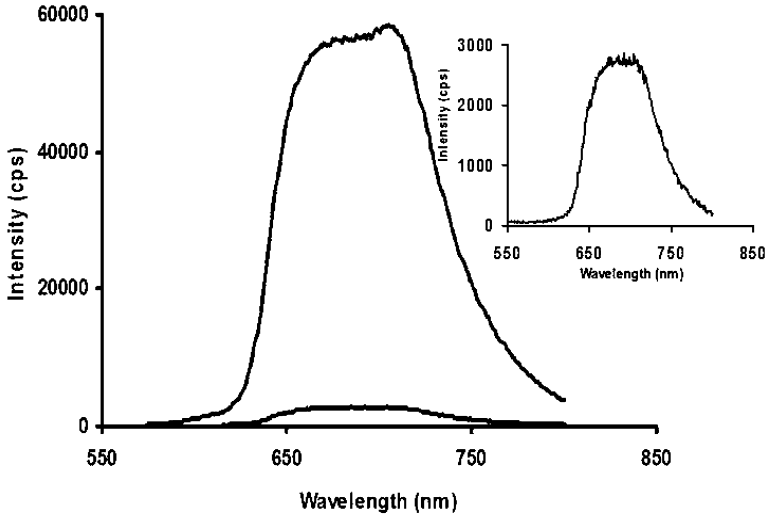

Figure A2. Fluorescence spectra of the ITO surface with 16 alternating depositions of porphyrin and POM and of the electrolyte solution after the CV analysis was done. The large emission peak is for the porphyrin on ITO surface and the small emission peak is for the porphyrin in the electrolyte solution, where the inset is an expanded plot of electrolyte solution emission peak.

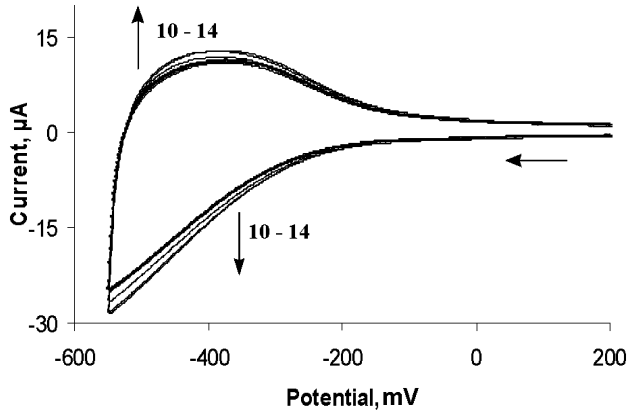

Figure A3. Cyclic Voltammogram of films built on ITO using $TMPyP^{4+}$ and $SiW_{12}O_{40}^{4-}$ with 10-14 dipping cycles. Each CV was recorded with POM as the outermost layer. CV data was recorded when the electrolyte solution has a pH=5, keeping the other experimental parameters same.

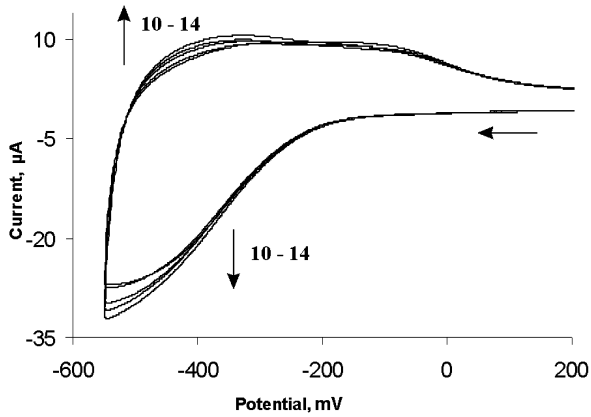

Figure A4. Cyclic Voltammogram of films built on ITO using TMPyP $^{4+}$ and $SiW_{12}O_{40}^{4-}$ with 10-14 dipping cycles. Each CV was recorded with POM as the outermost layer. CV data was recorded when the electrolyte solution has a pH =4, keeping the other experimental parameters same.

References

1. Mitzi, D. B. *Chem. Mater.* **2001**, *13*, 3283–3298.
2. Katsoulis, D. E. *Chem. Rev.* **1998**, *98*, 359–388.
3. Cheng, Z.; Cheng, L.; Gao, Q.; Dong, S.; Yang, X. *J. Mater. Chem.* **2002**, *12*, 1724–1729.
4. Martel, D.; Gross, M. *J. Solid State Electrochem.* **2007**, *11*, 421–429.
5. Moriguchi, I.; Fendler, J. H. *Chem. Mater.* **1998**, *10*, 2205–2211.
6. Sadakane, M.; Steckhan, E. *Chem. Rev.* **1998**, *98*, 219–238.
7. Dong, S.; Wang, B. *Electrochim. Acta* **1992**, *37*, 11–16.
8. Keita, B.; Nadjo, L. *J. Electroanal. Chem.* **1988**, *240*, 325–332.
9. Keita, B.; Nadjo, L. *J. Electroanal. Chem.* **1987**, *217*, 287–304.
10. Ariga, K.; Hill, J. P.; Ji, Q. *Phys. Chem. Chem. Phys.* **2007**, *9*, 2319–2340.
11. Lowman, G. M.; Tokuhisa, H.; Lutkenhaus, J. L.; Hammond, P. T. *Langmuir* **2004**, *20*, 9791–9795.
12. Zhao, W.; Xu, J.-J.; Chen, H.-Y. *Electroanalysis* **2006**, *18*, 1737–1748.
13. Liu, S.; Volkmer, D.; Kurth, D. G. *J. Cluster Sci.* **2003**, *14*, 405–419.
14. Shen, Y.; Liu, J.; Jiang, J.; Liu, B.; Dong, S. *Electroanalysis* **2002**, *14*, 1557–1563.
15. Shen, Y.; Liu, J.; Jiang, J.; Liu, B.; Dong, S. *J. Phys. Chem. B.* **2003**, *107*, 9744–9748.
16. Wang, Y.; Wang, X.; Hu, C. *J. Colloid Interface Sci.* **2002**, *249*, 307–315.
17. Drain, C. M.; Varotto, A.; Radivojevic, I. *Chem. Rev.* **2009**, *109*, 1630–1658.
18. Beletskaya, I.; Tyurin, V. S.; Tsivadze, A. Y.; Guilard, R.; Stern, C. *Chem. Rev.* **2009**, *109*, 1659–1713.
19. Malinski, T. Porphyrin-Based Electrochemical Sensors. In *The Porphyrin Handbook*; Kadish, K. M., Smith, K. M., Guilard, R., Eds.; Academic Press: New York, 2000; Vol. 6, pp 231−255.

In Interfaces and Interphases in Analytical Chemistry; Helburn, R., et al.;
ACS Symposium Series; American Chemical Society: Washington, DC, 2011.

20. Bazzan, G.; Smith, W.; Francesconi, L. C.; Drain, C. M. *Langmuir* **2008**, *24*, 3244–3249.
21. Drain, C. M.; Batteas, J. D.; Flynn, G. W.; Milic, T.; Chi, N.; Yablon, D. G.; Sommers, H. *Proc. Natl. Acad. Sci. U.S.A.* **2002**, *99*, 6498–6502.
22. Drain, C. M.; Bazzan, G.; Milic, T.; Vinodu, M.; Goeltz, J. C. *Israel J. Chem.* **2005**, *45*, 255–269.
23. Drain, C. M.; Chen, X. Self-Assembled Porphyrinic Nanoarchitectures. In *Encyclopedia of Nanoscience and Nanotechnology*; Nalwa, H. S., Ed.; American Scientific Press: New York, 2004; Vol. 9, pp 593−616.
24. Drain, C. M.; Goldberg, I.; Sylvain, I.; Falber, A. *Top. Curr. Chem.* **2005**, *245*, 55–88.
25. Drain, C. M.; Nifiatis, F.; Vasenko, A.; Batteas, J. D. *Angew. Chem., Int. Ed.* **1998**, *37*, 2344–2347.
26. Kadish, K. M.; Caemelbecke, E. V.; Royal, G. Electrochemistry of Metalloporphyrins in Nonaqueous Media. In *The Porphyrin Handbook*; Kadish, K. M., Smith, K. M., Guilard, R., Eds.; Academic Press: New York, 2000; Vol. 8, pp 1−113.
27. Shen, Y.; Liu, J.; Wu, A.; Jiang, J.; Bi, L.; Liu, B.; Li, Z.; Dong, S. *Langmuir* **2003**, *19*, 5397–5401.
28. Neri, B. P.; Wilson, G. S. *Anal. Chem.* **1972**, *44*, 1002–1009.
29. Laviron, E. In *Electroanalytical Chemistry*; Bard, A. J., Ed.; Marcel Dekker: New York, 1982; Vol. 12, pp 53−157.
30. Laurent, D.; Schlenoff, J. B. *Langmuir* **1997**, *13*, 1552–1557.
31. Maldotti, A.; Molinari, A.; Argazzi, R.; Amadelli, R.; Battioni, P.; Mansuy, D. *J. Mol. Catal. A: Chem.* **1996**, *114*, 141–150.
32. Mayer, I.; Nakamura, M.; Toma, H. E.; Araki, K. *Electrochim. Acta* **2006**, *52*, 263–271.
33. Santos, I. C. M. S.; Rebelo, S. L. H.; Balula, M. S. S.; Martins, R. R. L.; Pereira, M. M. M. S.; Simoes, M. M. Q.; Neves, M. G. P. M. S.; Cavaleiro, J. A. S.; Cavaleiro, A. M. V. *J. Mol. Catal. A: Chem.* **2005**, *231*, 35–45.
34. Han, B. H.; Manners, I.; Winnik, M. A. *Chem. Mater.* **2005**, *17*, 3160–3171.

Chapter 8

Temperature Dependent Resistance and Magnetoresistance of Single Wall Carbon Nanotubes Mounted on Silica Fiber Surfaces

Q. Lu,[1] V. Samuilov,[1,2,3] V. Ksenevich,[2] T. Dauzhenka,[2,3] and R. S. Helburn*,[4]

[1]Department of Physics, St. John's University, Jamaica, NY 11439
[2]Department of Physics, Belarus State University, 220030 Minsk, Belarus
[3]CNRS, LNCMI, 31400 Toulouse France & Universite de Toulouse, UPS, INSA, LNCMI, 31077 Toulouse, France
[4]Department of Chemistry & Physics, St. Francis College, Brooklyn Heights, NY 11201
***rhelburn@stfranciscollege.edu**

Single wall carbon nanotubes (SWCNTs) possess multiple analytically useful properties, intrinsic and extrinsic, as well as some that are of potential value. This chapter focuses on the magnetotransport properties of SWCNT coated 0.11mm diameter quartz silica fibers. The fibers were prepared by functionalizing the silica surface with a hydrocarbon layer. SWCNTS (oxidized or un-oxidized) were adsorbed onto the functionalized surface and the entire unit was annealed. Resistance and magnetoresistance in the 1.8–250 K and 1.8 – 8 K ranges, respectively, were examined and modeled to show the existence of two charge transport mechanisms, variable range hopping (VRH) and fluctuation induced tunneling.

Introduction

Carbon nanotubes (CNTS) are rapidly finding their place in analytical chemistry, especially in those methodologies that involve an interface or an interfacial layer. CNTS are a class of graphitic materials that can be organized into two categories, single- and multi- walled carbon nanotubes, *i.e.* SWCNTs and MWCNTs respectively. A SWCNT is a seamlessly rolled up graphene sheet

In Interfaces and Interphases in Analytical Chemistry; Helburn, R., et al.;
ACS Symposium Series; American Chemical Society: Washington, DC, 2011.

(Figures 1a-c) (*1–3*). Likewise, a MWCNT can be envisioned as a rolled up stack of graphene sheets such that the cross section of the MWCNT appears as a set of concentric circles. The surfaces of SWCNTs are hydrophobic due to their π bonding configuration and π -π interactions among the aromatic rings with the result being that individual SWCNTs tend to aggregate into bundles (Figure 1e) (*2*). This aspect of SWCNTs can make them difficult to work with as they do not disperse well in many solvents (*4*, *5*). Accordingly, both SWCNTS and MWCNTs have strong hydrophobic binding capability (*6*, *7*). The abundance of fundamental studies of SWCNTs suggests that they are the most well characterized of the two CNT forms.

SWCNTS: Interfacial Properties and Analytical Applications

The properties of CNTs that make them attractive in the design of sensing probes and chemical separations are those of: 1. a conductor, 2. semiconductor, 3. electrocatalytic surface and 4. an adsorption medium with large surface-to-volume ratio. Mechanical strength and heat tolerance also are valuable attributes (*6–9*). Note, that the extent to which SWCNTs are conducting vs. semiconducting relates to the spatial orientation of individual hexagons in the rolled up graphene sheet (Figure 1a), more specifically the chiral angle (*1*, *10*, *11*), as well as the diameter of the roll (Figure 1c) (*1*). As an example in analytical sensing, the unadulterated SWCNT can be an effective transducer in a gas sensing device (*11*, *12*). Here, SWCNTs behave as an adsorption medium where the SWCNT-analyte surface interaction simultaneously results in a change in the electric properties of the material (*12*), *e.g.* conductance (S), resistance (Ω), current (i). The electric signal is further propagated via SWCNTs' ability to make contact with other conducting materials (*13–16*), thus providing seamless information transfer between the adjacent small molecule and its corresponding concentration based signal.

Greater selectivity and a wider range of analyte interactions on the front end of the sensor are realized when CNT surfaces are chemically modified via covalent processes, or they are inserted into a layered composite. The surfaces of SWCNTs may be directly functionalized, however, harsh and high concentration conditions often are needed to produce polar functional groups on the graphitic surface, moieties that can be further modified through covalent and/or non-covalent processes. Some examples of surface formed reactive groups are -F and -COOH (*17*, *18*). More recently, reactive radicals and an alkyne functionalized SWCNT for use in Click reactions have been achieved (*19*, *20*). To date, combinations of covalent and non specific interactions have been used to tether a variety of species including biomolecules (*e.g.* DNA fragments) and fluorescent probes (*21*).

Some issues to contend with in this respect are that covalent modification can introduce defects that disrupt the CNT sp^2 structure resulting in deterioration of a CNT's intrinsic electronic and mechanical properties (*22*), a phenomenon that is not encountered when SWCNTs are merely added into a layered material. Composites that include CNTs as part of a layered material have been deposited on gold and glassy carbon electrodes (*10*, *23*). In this latter context, the material's electrical conductivity depends on factors such as the intrinsic conductivity of the

SWCNT (or MWCNT), the volume of SWCNT within the composite as well the nature of a contacting polymer or ceramic (*13*).

CNTS and Magnetoresistance

Principles of Magnetoresistance

A relatively new property of CNTs that holds promise towards their use in fundamental aspects of sensing and interfacial signal transfer is magnetoresistance (MR). This electric property refers to the change of resistance in a material when an external magnetic field is applied. It is also a measure of the resistance shift in a material as defined by the following relation.

$$MR = \Delta R/R \qquad \text{Eqn 1}$$

In Equation 1, ΔR is the change of the resistance caused by the applied magnetic field and R is the resistance in the absence of the magnetic field (*24*). This effect was first observed in ferromagnetic thin sheets by Lord Kelvin (*25*). However, only subtle 0.033% increases in electrical resistance were reported in that work. The effect is also prevalent in non-magnetic metals and semiconductors. However, no more than 5% resistance shift is usually observed in pure materials (*26*, *27*).

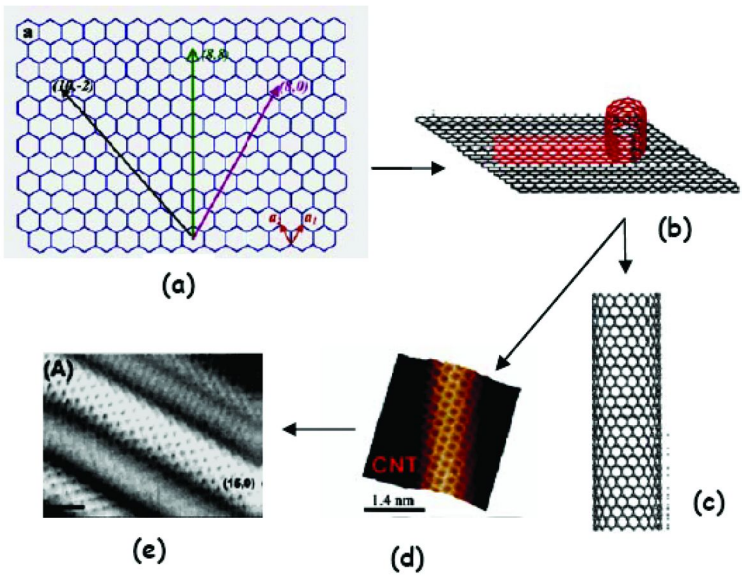

Figure 1. Graphene sheet showing lattice vectors along which the sheet can be rolled (a-b), a zig-zag SWCNT formed by rolling along the 8,0 vector (c); an atomic resolution scanning tunneling microscope (STM) image of a CNT (d), aggregation of SWCNTs via weak interactions and hydrophobic character to form a bundle (e). Adapted and reproduced from References (1–3). (see color insert)

In Interfaces and Interphases in Analytical Chemistry; Helburn, R., et al.;
ACS Symposium Series; American Chemical Society: Washington, DC, 2011.

When a magnetic field is applied perpendicular to an electrical current occuring in a material, the electrons are deflected by the Lorentz force which builds up on one side of the sample surface parallel to the electrical current until a counterbalanced Hall electric field is established (*28*). Under this equilibrium condition, all electrons should follow the same straight paths as if the magnetic field were nonexistent. However, the velocity at which the electrons drift is not always the same as that demanded by their statistical distribution. For those electrons whose drift velocity deviates from the equilibrium condition, *their* paths are twisted by the magnetic field to form cyclotrons (*29*). This impeded travel of the electrons gives rise to MR (*29*).

MR varies for different mechanisms of scattering and valence band structure. The magnetic force causes electrons to move along a circular or helical orbit. The ratio of the magnetic field to resistance depends on how many times electrons go around the cyclotron orbit between successive collisions. This value reflects the ratio of the electronic mean path to the orbit radius, which affects MR as found by Kohler. Kohler also pointed out that the MR depends on the relative orientations of current, magnetic field and the crystalline axes. Thus, MR has long been used as an experimental tool to deduce the Fermi surface and the crystalline structure of solid materials (*30*).

It was not until the discovery of giant magnetoresistance (GMR), with an effect as much as 50%, in thin metallic sandwiches of Fe-Cr-Fe (*31*, *32*) that this century-old phenomenon began to find uses beyond the arena of theoretical physics. As an example, GMR is making its way into the realm of biosensing and biomolecular detection. In this application, a magnetic tag is used in place of a fluorescent label, *e.g.* as a protein biomarker on a microarray substrate. Analyte detection occurs at a selective probe continuous with the surface of a GMR sensor (*33*, *34*). GMR effects are usually observed in layered thin films of two or more ferromagnetic materials separated by very thin non-ferromagnetic spacers. The ferromagnetic alignment realized through thin film layering enables GMR materials to induce a far more pronounced shift in MR than regular (non-magnetic) materials do. The much weaker anisotropic magnetoresistive effect (AMR) is at work in regular materials, and thus only an insignificant magnetoresistive effect is observed (*35*). It is of interest to note that GMR effects up to ≥ 90% have been measured in systems where CNTs comprise the non-ferromagnetic layer and for other Fe-CNT composites (*36*). The MR to be described in this study, which was measured on SWCNTs coated on fused silica fibers, is attributed to an AMR effect.

CNTS and MR: Previous Studies

Magnetotransport properties of SWCNTs have been previously reported but in many cases without a clarified explanation (*i.e.* a mechanistic interpretation) (*37*, *38*). One set of measurements performed on SWCNT bundles and thin films showed negative MR (*39*, *40*) attributed to the weak localization arising from the extrinsic network effect. A more recent study performed on sorted metallic (*i.e.* conducting) SWCNTs revealed positive MR owing to the Aharonov-Bohm (AB) effect, which is thought to be an intrinsic effect of the magnetic field on SWCNTs

In Interfaces and Interphases in Analytical Chemistry; Helburn, R., et al.;
ACS Symposium Series; American Chemical Society: Washington, DC, 2011.

(*41*). In this work we have measured and interpreted the temperature dependent resistance and MR for a series of SWCNT coated 0.11 mm diameter quartz fibers.

Preparation of SWCNT Coated Silica Fibers

The quartz silica fibers were modified with SWCNTs via the following general steps: (1) preparation of the silica surface, (2) creation of a bonded hydrophobic layer on the silica surface via silanization, (3) non-covalent adsorption of SWCNTs (oxidized vs. unmodified) to the hydrocarbon modified surface and (4) annealing at 250-300°C. The silanization reactions that were used are shown below in Figure 2. Figure 3 illustrates a graphic representation of SWCNTs adsorbed onto the covalently attached hydrocarbon layer. Once the hydrocarbon layer was covalently attached, the SWCNTs were added in by physical adsorption. The fiber was then annealed.

Experimental Section

Preparation of Coated Fibers

Reagents and Materials

Octadecyl trimethoxysilane (90%), phenyl trimethoxysilane (97%), phenethyl trimethoxysilane (98%), methyl trimethoxysilane (98%), and SWCNTs produced by carbon vapor deposition (CVD) method of avg. diam x length of 1.1 nm x 0.5-100 *um* (Lot # 12526AE) were purchased from Sigma Aldrich; the lot consisted of $\geq$50% (volume percent) SWCNT and ~40% other nanotubes, amorphous carbon < 5%; ash content reported as Co, Mg, Mo and silicates < 2%. Super purified (SP) research grade SWCNTs manufactured by high pressure CO processing method (HiPco®) were obtained from Carbon Nanotechnologies Inc. CNI–Unidym (Lot # SP0334); lot consisted of $\leq$ 3% TGA (thermal gravimetric analysis) residuals. Purified (P) grade HiPco® SWCNTs with $\leq$25% residual impurities were also obtained from CNI. Acetone (99+%), toluene (pure), cyclohexane (99+%), ethanol (95%, spectroscopic grade), KOH (ACS certified) and NaOH (extra pure) and nitric acid (conc.) were purchased from Acros/Fischer Scientific. Unmodified fused silica fibers, 0.110 mm diameter, were purchased from Supelco.

Method for Preparation of Coated Fibers

Oxidized SWCNTs were prepared using the methods of Zhang et al. (*42*). SWCNTs were sonicated and then refluxed, each for 2 hrs. in an aqueous 10M HNO_3 solution. The resulting material was washed and centrifuged using de-ionized water until the pH of the supernatant was 7.00. A Sorvall RC 5C ultracentrifuge set at 16,000 RPM was used for the SP grade CNI SWCNTs ; a small bench-top centrifuge was sufficient for the Aldrich SWCNTs. SWCNT coated fibers were prepared according to the general scheme in Figure 4. For silanization reactions, we used two types of solvent systems: (1) ethanol spiked

with aqueous NH_3, and (2) cyclohexane with spiked butylamine. Note, in one case we annealed (at ~280-300 C) oxidized SWCNTs *directly* onto an untreated/unsilanized silica fiber.

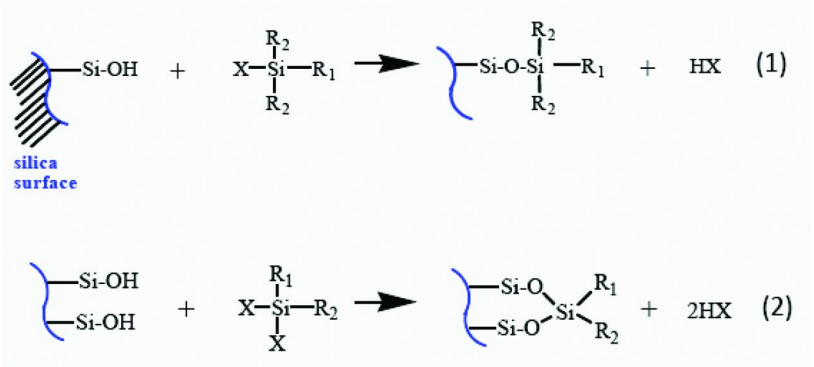

Figure 2. Reactions of surface silanols with substituted silanes; R_1 is a hydrophobic alkyl group; R_2= an alkyl or alkoxy group; X= a leaving group (-OCH_3 or –Cl).

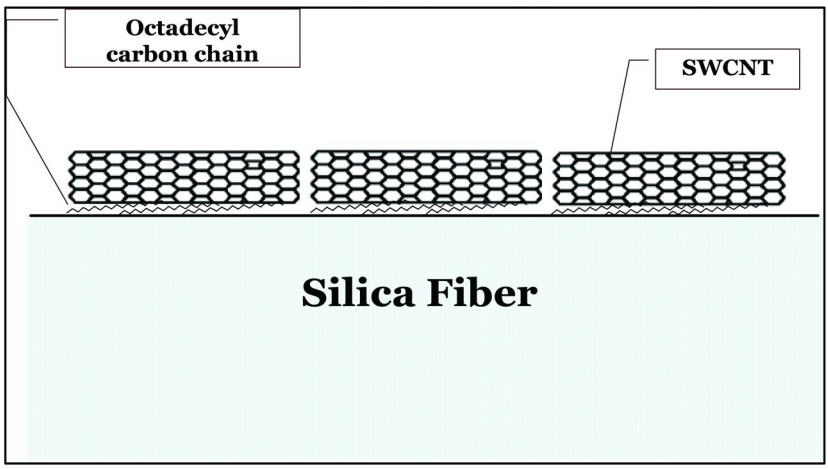

Figure 3. Graphic representation of SWCNT coated silica fiber modified with C_{18} as the covalently bonded hydrophobic layer; not to scale.

Table 1. Substituted silanes used in the covalent modification of the quartz silica fiber surfaces

Silane	*Structure*
octadecyl trimethoxysilane	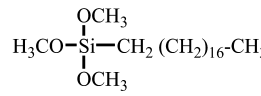
phenyl trimethoxysilane	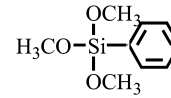
phenethyl trimethoxysilane	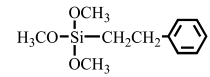
methyl trimethoxysilane	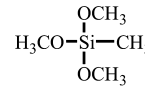

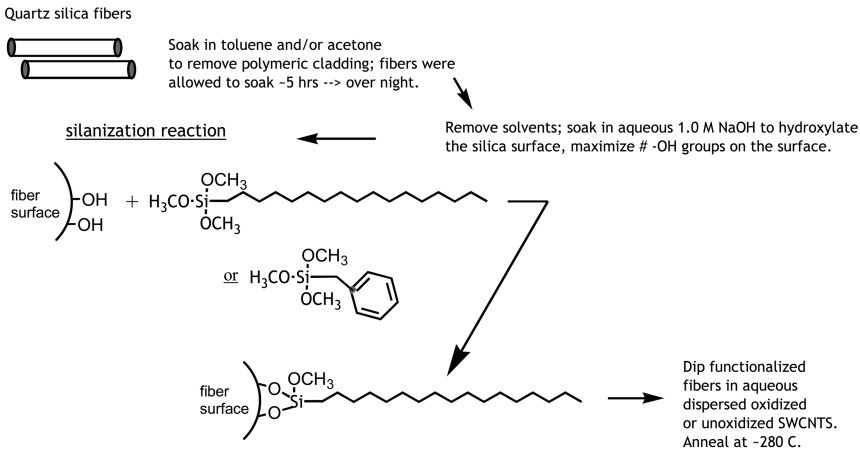

Figure 4. Reaction scheme for preparation of fibers

Characterization of Fibers by Light and SEM Microscopy

Light microscopy was carried out on a PC interfaced *Nikon Optiphot* light and fluorescence microscope at 200X magnification. Images were processed using the *Nikon Optiphot* software. SEM images were obtained on a Leo 1550 SFEG-SEM in the Materials Characterization Laboratory at SUNY-Stonybrook, NY.

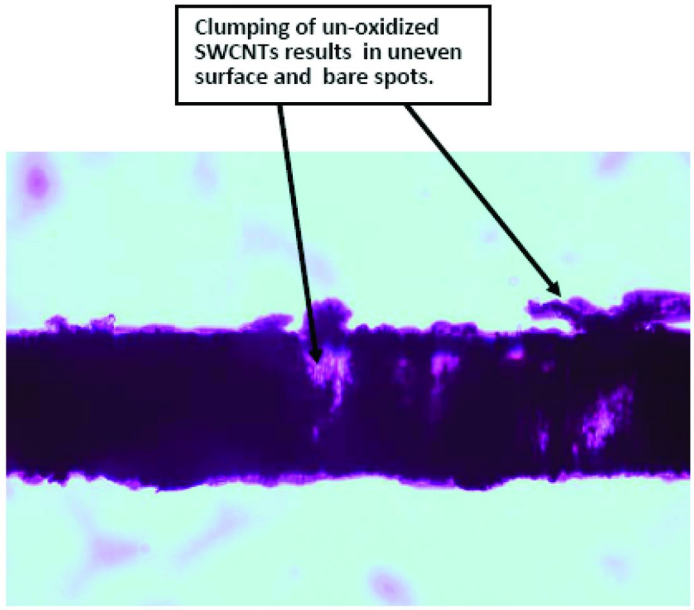

Figure 5. Light micrograph, magnification at 200x ; fiber stripped then silanized using a the phenyl substituted silane; coated with SP grade CNI SWCNTs (un-oxidized) and annealed. (see color insert)

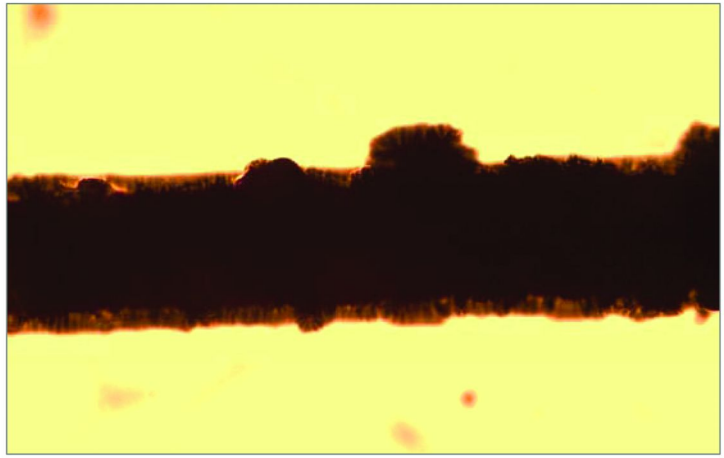

Figure 6. Light micrograph, magnification at 200x, fiber stripped then silanized with the phenyl substituted silane, coated with a mixture of oxidized and un-oxidized SP grade CNI SWCNTs and annealed; addition of oxidized SWCNT to coating appears to provide more uniformity and smoothness to the surface.

Resistance Measurements

Regular 4 point probe contacts in van-der-Pauw and linear geometry were produced on top of the SWNT-fiber system. MR measurements were carried out in pulsed magnetic fields at the Laboratoire National des Champs Magnetiques Pulse/ de Toulouse in the temperature range 1.8-300K, and magnetic field up to 8T.

Results and Discussion

In preparing the individual fibers we experienced uneven results in our ability to achieve stable intact coatings. We attributed this, in part, to lack of a uniform distribution of surface bonded hydrocarbon groups as well as to the differing qualities of the SWCNTs that were employed. We used the methyl trimethoxysilane (see Table 1) as an 'end-capping' step in an effort to minimize polar bare spots on the silica surface. We note one previous report in the literature of MWCNTs coated on the same type of silica fiber (*43*). However the details of that coating process were not revealed (*43*).

The oxidized SWCNTs annealed more readily than un-oxidized ones presumably due to their ability to adhere, initially, to polar portions of the fiber and to the lower temperatures at which they were seen to respond (*i.e.* in the annealing process). At one point, the unsilanized fiber was dipped into the rinsed *oxidized* SWCNTs and annealing was successfully achieved in multiple steps. Light and SEM micrographs illustrating the different observed surface characteristics among fibers coated with oxidized vs. un-oxidized SWCNTs are shown in Figures 5-7.

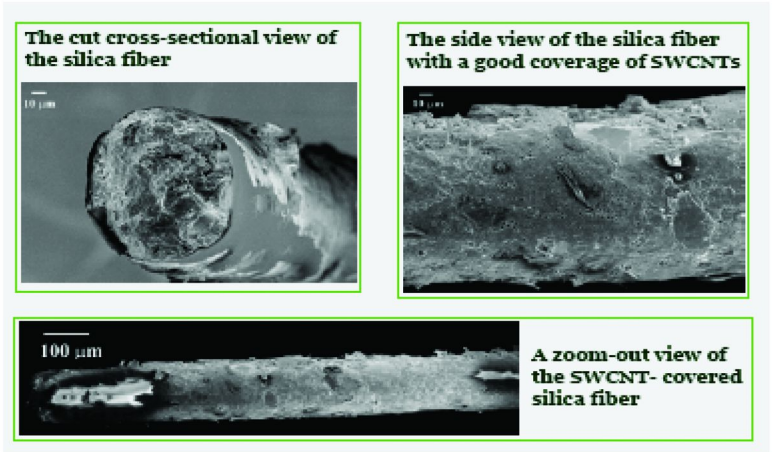

Figure 7. SEM examination showing coverage of SWCNTs on treated silica fibers; P grade CNI SWCNTs (un-oxidized) coated and annealed on a fiber that was stripped and then functionalized using the octadecyl substituted silane.

In Interfaces and Interphases in Analytical Chemistry; Helburn, R., et al.;
ACS Symposium Series; American Chemical Society: Washington, DC, 2011.

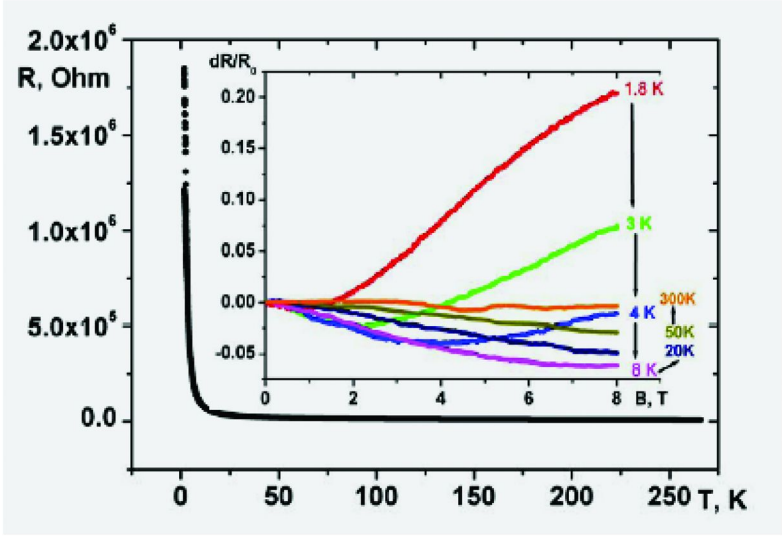

Figure 8. Temperature dependence of the resistance of SWCNT coating on a silica fiber; inset: the normalized MR (dR/R, R is zero field resistance) dependencies on magnetic fields at different temperatures. fiber was stripped and functionalized with a phenyl-substiuted silane and then prepared with a mixture of oxidized and unoxidized SWCNTs. Additional MR data on other prepared fibers are published in Reference (44). (see color insert)

Temperature Dependent Resistance and Magnetoresistance

The extent of oxidation on the SWCNT surfaces did not produce pronounced differences in measured film conductance suggesting that moderate chemical modification of SWCNT surfaces does not significantly alter their MR characteristics. The temperature (T) dependence of the resistance (*R*) of the SWCNT coating on the silica fibers as shown in Figure 8 was found to follow the Mott law for 3D variable range hopping (VRH) conduction in temperature range 2-8 K, and a fluctuation-induced tunneling model in temperature range 8-300 K (*44*). MR data measured at different temperatures are shown in the inset of Figure 8. Mixed positive and negative MR were observed in the temperature range of 1.8-6K. When the temperature exceeded 6 K, only negative MR was observed in the experimental range of magnetic fields. The positive MR in the low temperature range varies with $exp(B^2)$, which is expected for the VRH transport and can be explained by electronic wave function shrinkage in the magnetic field. The negative MR in high temperature range can possibly be explained by the contribution of the weak localization effects in MR (*44*).

Acknowledgments

We thank Dr. Nigel Yarlett and the Haskins Laboratory at Pace University, NY, NY for use of their light and fluorescence microscope.

References

1. Dai, H. *Acc. Chem. Res.* **2002**, *35*, 1035–1044.
2. Ouyang, M.; Huang, J. L.; Lieber, C. *Acc. Chem. Res.* **2002**, *35*, 1018–1025.
3. Avouris, P. *Acc. Chem. Res.* **2002**, *35*, 1026–1034.
4. Zhang, S.; Shao, T; Kose, H. S.; Karanfil, T. *Environ. Sci. Technol.* **2010**, *44* (16), 6377–6383.
5. Lee, K.; Lee, J. W.; Dong, KY.; Ju, DBK. *Sens. Actuators, B* **2008**, *135*, 214–218.
6. Long, R. Q.; Yang, R. *J. Am. Chem. Soc.* **2001**, *123*, 2058–2059.
7. Yang, K.; Zhu, L.; Xing, B. *Environ. Sci Technol.* **2006**, *40*, 1855–1861.
8. Liu, G.; Wang, J.; Zhu, Y.; Zhang, X. *Anal. Lett.* **2004**, *37* (14), 3085–3104.
9. Cao, Q.; Rogers, J. A. *Adv. Mater.* **2009**, *21*, 29–53.
10. Agui, L.; Yanez-Sedeno, P.; Pingarron, J. M. *Anal. Chim. Acta.* **2008**, *622*, 11–47.
11. Brahim, S.; Colbern, S.; Gump, R.; Grigorian *J. Appl. Phys.* **2008**, *104*, 1–9.
12. Sasaki, I.; Minami, N.; Karthigeyan, A.; Lakoubovskii, K. *Analyst* **2009**, *134*, 325–330.
13. Li, C.; Thostenson, E. T.; Chou, T-W. *Compos. Sci. Technol.* **2008**, *68*, 1227–1249.
14. Quinn, B.; Dekker, C.; Lemay, S. G. *J. Am. Chem. Soc.* **2005**, *127*, 6146–6147.
15. Quinn, B.; Lemay, S. G. *Adv. Mater.* **2006**, *18*, 855–859.
16. Kamarchuk, G. V.; Kolobov, I. G.; Khotkevich, A. V.; Yanson, I. K.; Pospelov, A. P.; Levitsky, I. A.; Euler, W. B. *Sens. Actuators, B* **2008**, *134*, 1022–1026.
17. Mickelson, E. T.; Huffman, C. B.; Rinzler, A. G.; Smalley, R. E.; Hauge, R. H.; Margrave, J. L. *Chem. Phys. Lett.* **1998**, *296*, 188–194.
18. Sun, Y.-P.; Fu, K.; Lin, Y.; Huang, W. *Acc. Chem. Res.* **2002**, *35*, 1096–1104.
19. Li, H.; Cheng, F.; Duft, A. M.; Adronov, A. *J. Am. Chem. Soc.* **2005**, *127*, 14518–14524.
20. Campidelli, S.; Ballesteros, B.; Filoramo, A.; Diaz Diaz, D.; de la Torre, G.; Torres, T.; Rahman, G. M.; Ehli, C.; Kiessling, D.; Werner, F.; Sgobba, V.; Guldi, D. M.; Cioffi, C.; Prato, M.; Bourgoin, J.-P. *J. Am. Chem. Soc.* **2008**, *130*, 11503–11509.
21. Fletcher, B.; McKnight, T. E.; Melechko, A. V.; Simpson, M. L.; Doktycz, M. J. *Nanotechnology* **2006**, *17*, 2032–2039.
22. Wu, L.; McIntosh, M.; Zhang, X.; Ju, H. *Talanta* **2007**, *74*, 387–392.
23. Liu, G.; Riechers, S. L.; Mellen, M. C.; Lin, Y. *Electrochem. Commun.* **2005**, *7*, 1163–1169.

24. Rao, C. N. R.; Raveau, B. In *Colossal Magnetoresistance, Charge Ordering, and Related Properties of Manganese Oxides*; World Scientific Publishing Company: Hackensack, NJ, July 1998; p 2.
25. Thomson, W. *Proc. R. Soc. London* **1856**, *8*, 546–550.
26. McGuire, T. R.; Potter, R. I. *IEEE Trans. Magn.* **1975**, *11* (4), 1018–1038.
27. Kittel, C. In *Quantum Theory of Solids*; John Wiley & Sons, Inc.: New York, 1963; p 239.
28. Hook, J. R.; Hall, H. E. *Solid State Physics*, 2nd ed.; John Wiley & Sons: West Sussex, 1991; p 97.
29. Prelas, M. A.; Popovici, G.; Bigelow, L. K. *Handbook of Industrial Diamonds and Diamond Films*, 1st ed.; CRC Press: Boca Raton, FL, 1997; p 396.
30. Feng D.; Jin, G. *Introduction to Condensed Matter Physics*; World Scientific Publishing Company: Hackensack, NJ , 2005; Volume 1, p 212.
31. Baibich, M. N.; Broto, J. M.; Fert, A.; van Dau, F. N.; Petroff, F.; Eitenne, P.; Greuzet, G.; Friederich, A.; Chazelas, J. *Phys. Rev. Lett.* **1988**, *61*, 2472–2475.
32. Binasch, G.; Grünberg, P.; Saurenbach, F.; Zinn, W. *Phys. Rev. B* **1989**, *39*, 4828–4830.
33. Graham, D. L.; Ferreira, H. A.; Frietas, P. P. *Trends Biotechnol.* **2004**, *22* (9), 455–462.
34. Osterfield, S. J.; Yu, H.; Gaster, R. S.; Caramuta, S.; Xu, L.; Han, S-J.; Hall, D. A.; Wilson, R. J.; Sun, S.; White, R. L.; Davis, R. W.; Pourmand, N.; Wang, S. X. *Proc. Natl. Acad. Sci. U. S. A.* **2008**, *109* (52), 20637–20640.
35. Hartmann, U.; van den Berg, H. A. M.; Coehoorn, R.; Gijs, M. A. M.; Grünberg, P.; Rasing, T.; Röll, K. *Magnetic Multilayers and Giant Magnetoresistance: Fundamentals and Industrial Applications*, 1st ed.; Springer: New York, 2000; p 2.
36. Hudziak, S.; Darfeuille, A.; Zhang, R.; Peijis, T.; Mountijoy, G.; Bertoni, G.; Baxendale, M. *Nanotechnology* **2010**, *21* (12), 125505.
37. Vavro, J.; Kikkawa, J. M.; Fischer, J. E. *Phys. Rev. B* **2005**, *71*, 155410.
38. Fedorov, G.; Tselev, A.; Jiménez, D.; Latil, S.; Kalugin, N. G.; Barbara, P.; Smirnov, D.; Roche, S. *Nano Letters* **2007**, *7*, 960–964.
39. Kim, G. T.; Choi, E. S.; Kim, D. C.; Suh, D. S.; Park, Y. W.; Liu, K.; Duesberg, G.; Roth, S. *Phys. Rev. B* **1998**, *58*, 16064.
40. Kim, J.; So, H. M.; Kim, J.; Kim, J. *Phys. Rev. B* **2002**, *66*, 233401.
41. Oshima, Y.; Takenobu, T.; Yanagi, K.; Miyata, Y.; Kataura, H.; Hata, K.; Iwasa, Y.; Nojiri, H. *Phys. Rev. Lett.* **2010**, *104*, 016803.
42. Zhang, X; Sreekumar, T. V.; Liu, T.; Kumar, S. *J. Phys. Chem. B.* **2004**, *108*, 16435–16440.
43. Wang, J. X.; Jiang, D. Q.; Gu, Z. Y.; Yan, X.-P. *J. Chromatogr., A* **2006**, *1137*, 8–14.
44. Ksenevich, V.; Dauzhenka, T.; Seliuta, D.; Kasalynas, I.; Kivaras, T.; Valusis, G.; Galibert, J.; Helburn, R.; Lu, Q.; Samuilov, V *Phys. Status Solidi C* **2009**, *6*, 2798.

Chapter 9

Protein Microarray Substrates with High Interfacial Area Using Silica Colloidal Crystals

Mary J. Wirth,*[,1] Corey M. Smith,[2] Joshua J. Scott,[2] and Michael E. Rice[2]

[1]Purdue University, Department of Chemistry, West Lafayette, IN 47907
[2]bioVidria, Inc., 9040 South Rita Rd., Suite 1100, Tucson, AZ 85721
***mwirth@purdue.edu**

Protein microarrays are growing in use in biomedical research because proteins are more directly representative of physiological processes. There is a need for higher sensitivity because proteins, unlike DNA, cannot be amplified in concentration as simply. A thin layer of silica colloidal crystal provides a combination of high surface area and high optical transparency, promising unprecedented sensitivities for protein microarrays.

Introduction

Microrrays were first introduced in the early 1990's (*1*, *2*), and they have since become an indispensible tool in biomedical research. The most well established microarrays are the DNA microarrays, where tiny spots of oligonucleotides are attached to a surface in a planned pattern to capture their complementary oligonucleotides. By labeling the analyte, typically with a fluorophor, the complementary chain is quantitated by the fluorescence from its position in the microarray. Microarrays containing hundreds of thousands of spots allow the entire human genome to be probed. Spots can be printed by photochemically enabled chain growth, which gives the densest microarrays, by contact printing with tips dispensing nanoliters of solution, or by piezoelectric printing of sub-nL volumes. The most common type of DNA microarray is the gene expression microarray, which is used for the study of how gene expression is affected by diseases and drug treatment (*3*–*8*). More recently, microarrays to probe small interfering RNA have become available to help researchers understand how genes

In Interfaces and Interphases in Analytical Chemistry; Helburn, R., et al.;
ACS Symposium Series; American Chemical Society: Washington, DC, 2011.

are silenced for post-translational regulation of gene expression in cells (*9*, *10*). The technology for printing, exposing, and scanning DNA and RNA microarrays is very well established, and most large institutions have microarray centers with equipment for printing and scanning microarrays.

Protein microarrays have become available much more recently than DNA microarrays (*11–13*). The interest in protein microarrays is strong and growing because proteins are more representative of cellular processes than are gene expression and gene silencing. Protein microarrays come in many varieties, and all of them are designed to assay the concentration of many proteins simultaneously. There are three general types of applications.

- Biomarker discovery
- Profiling of protein concentrations
- Characterizing protein-protein or protein-ligand binding

This chapter is organized into three sections. 1) How protein microarrays work and what the problems and unmet demands are, 2) The principles behind silica colloidal crystals as microarray substrates, and 3) the performance of protein microarrays using silica colloidal crystalline substrates.

How Protein Microarrays Work

A common type of protein microarray is depicted in Figure 1, where a modest number of antibodies are printed onto a small pad of microarray substrate, allowing multiple samples to be assayed on one slide. Each pad has the same microarray pattern printed onto it. A rubber grid is placed over the substrate to make separate wells for each pad, allowing 16 different samples of serum or cell lysate to be analyzed simultaneously. The slide depicted in Figure 1 has spacings corresponding to a 96-well format for compatibility with existing automation equipment. Each different antibody in the array captures a different type of protein in the sample. Aptamers can be printed to spare the expense of antibodies (*14*, *15*). A solution containing a mixture of secondary antibodies for the proteins, all labeled with the same fluorophor, is put in each well to allow binding to the respective proteins to enable sensitive fluorescence detection. A protein is identified by its position on the pad, and its concentration is proportional to the intensity of fluorescence emission from the labeled secondary antibody.

The type of microarray depicted in Figure 1 is tantamount to a multiplexed sandwich immunoassay. In comparison to ELISA (enzyme-linked immunosorptive assay), which is commonly used for sandwich immunoassays in 96-well plates, only one protein per well is used for ELISA. As one example of the use of such a protein microarray, cytokines are a class of protein that are involved in the inflammatory response, and diseases can be characterized by the expression profile of cytokines. In the 16-pad format, there is an array of as many as 8 cytokines, plus controls, on each pad. Multiple slides can be connected together with 96-well geometry to enable the same number of samples to be analyzed as for an ELISA plate, but with each well reporting concentrations for

In Interfaces and Interphases in Analytical Chemistry; Helburn, R., et al.;
ACS Symposium Series; American Chemical Society: Washington, DC, 2011.

all 8 proteins per sample. Slides are available with as few as one pad, allowing as many as 177 cytokines to be analyzed simultaneously for one sample.

Another common type of microarray is the reverse protein array, which is illustrated in Figure 2, next to an antibody array for convenient comparison.

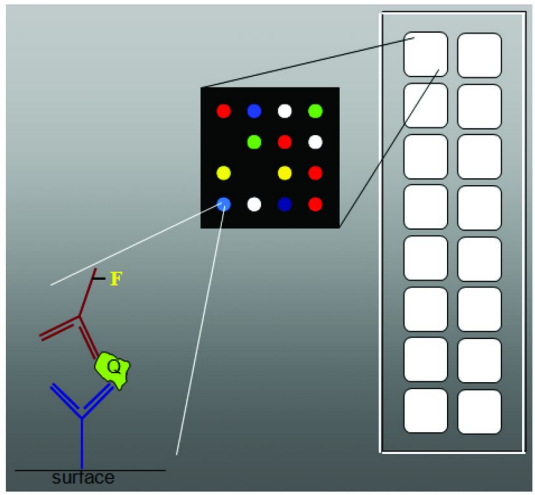

Figure 1. A typical format for a protein microarray, using 16 pads. Q is the protein of interest and F is the fluorescent label. (see color insert)

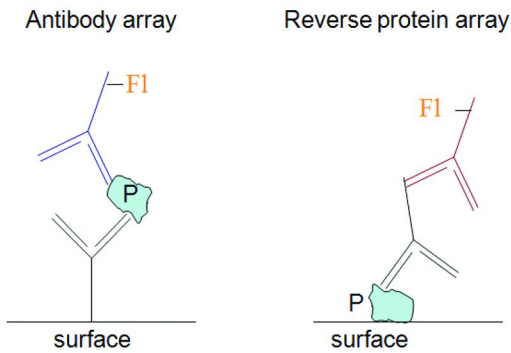

Figure 2. Two types of protein microarrays: assay for antibody array (left) and assay for reverse protein array (right). P is the protein of interest and F1 is the fluorescent label.

For the reverse protein microarray, the assay is simpler; there is only one selective antibody, and this is detected by using anti-IgG, which binds to other antibodies. Labeling the anti-IgG with fluorophor thus enables determination of the concentration of protein. Reverse protein assays tend to be less sensitive, perhaps because microarray surfaces do not bind smaller proteins as well as they bind the larger antibodies.

There are two general uses for reverse protein microarrays. First, imagine if you wanted to see whether a person has an infectious disease. The person would have antibodies to antigenic proteins from the infectious agent. Printing the characteristic antigens for multiple diseases enables the simultaneous testing for many possible diseases by detecting the position in the array where binding occurs. As another example, diseases such as human cancer cause auto-antibodies, which bind to human proteins. The characterization of auto-antibodies can be used in discovering biomarkers for cancer. For this application, there is a microarray available that has over 9,000 human proteins printed on it to enable powerful investigation of biomarkers for diseases in virtually any biological fluid, for example, human cerebral-spinal fluid (*16*).

A second general reason for using reverse protein microarrays is to identify potential biomarkers in protein samples from tissues or fluids of patients with disease. By pre-fractionating the proteins with a prior separation, such as chromatography, each protein fraction can be printed onto a microarray, which can then be characterized by its binding to a secondary agent. One example is a lectin, which is sensitive to glycosylation. Fucosylation is the hallmark of cancer, and fucosylation has been investigated in pancreatic cancer, for example, by binding the appropriate lectin to a reverse protein microarray, made from reverse phase liquid chromatography (RPLC) fractions (*17*, *18*).

The challenges for protein microarrays are mainly in detecting lower concentrations. Proteins of interest are often at trace levels, and unlike DNA, proteins cannot be simply amplified in concentration. Trace analysis of proteins is routinely achieved by a well established competitor to microarrays: the ELISA assay. The sensitivity of ELISA, as well as for antibody microarrays, owes primarily to the strong binding of the antibody: the binding constant of the typical antibody is on the order of 10 nM. Since detection limits can be as low as 100-fold below the binding constant, 0.01 nM detection limits are routinely achievable with ELISA. This corresponds to a concentration of 0.5 ng/mL for a protein having a molecular weight of 50,000 Da. Since the cost of antibodies is on the order of $200/mg, and often much more, for a 96-well plate with 1 μg each of the primary and secondary antibody in every well, the total cost of the antibodies would be $200 per plate. Microarrays offer the same number of samples to be analyzed, but with 8 different protein assays per well, and the only significant cost is the secondary antibody, thus halving the cost of the analysis, while giving an eight-fold higher information content. All of this is advantageous provided that the sensitivity is as high as the ELISA.

A variety of approaches have been devised to increase the signal size in protein microarrays, and there is a recent comprehensive review (*19*). Gold nanoparticles (*20*, *21*), nanowires (*22*), and enzymatic amplification have been used to enhance signal size (*14*). In addition, the signal can be increased by

In Interfaces and Interphases in Analytical Chemistry; Helburn, R., et al.;
ACS Symposium Series; American Chemical Society: Washington, DC, 2011.

increasing the surface area of the microarray slide, as reviewed recently (*23*). High surface area slides are usually made by applying polymer coatings to glass surfaces, with polymers such as polyacrylamide (*24*), polyethyleneglycol (*25*), polyurethane (*26*), and carbohydrates, such as agarose (*27*) and dextran (*28*). These polymers are relatively hydrophilic, enabling proteins to remain hydrated after printing. Protein microarrays rely on the protein remaining functional when it is bound to the surface, keeping the tertiary structure sufficiently intact to allow the selective antibody-protein recognition to occur. Nitrocellulose, which is less hydrophilic, nonetheless gives high sensitivity and maintains protein function. Porous nitrocellulose slides have been shown to be > 10x more sensitive than planar glass slides that use an aldehyde to capture the protein (*29*), and they are the leading slide today for commercial protein microarrays. It is possible that the unique morphology of the nitrocellulose polymer, as shown by the SEM image in Figure 3, enables rapid access to the high surface area by virtue of the large pores, and provides ample room for the sandwich complex to form.

The limit of detection in any assay is defined as the concentration giving a signal corresponding to twice the standard deviation of the background noise. Efforts to increase the signal size are counterproductive if they increase the background noise by the same amount. As an illustration, ELISA uses enzymatic signal amplification, and the limit of detection for this technique is background-limited. This is because the blank has a rather large signal due to nonspecific binding. Further amplification will give little improvement in the detection limit because it is the fluctuations on the background signal that define the detection limit. Fluorescence is extraordinarily sensitive; it is the basis of single-molecule spectroscopy, where it is now routine to resolve one molecule at a time with a high signal-to-noise ratio. Despite the high sensitivity of fluorescence, microarrays scanned by fluorescence readers cannot achieve ultra-low detection limits due to background from nonspecific binding.

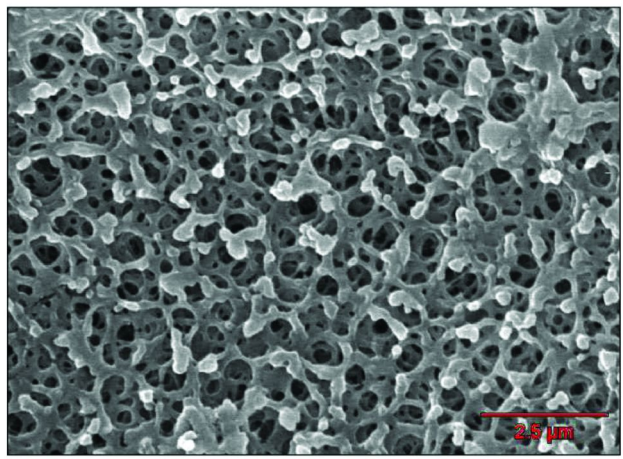

Figure 3. SEM image of a nitrocellulose coating on a commercial protein microarray slide. The scale bar is 2.5 µm. (see color insert)

In Interfaces and Interphases in Analytical Chemistry; Helburn, R., et al.;
ACS Symposium Series; American Chemical Society: Washington, DC, 2011.

Figure 4. Fluorescence image of the edge of a porous nitrocellulose pad , as well as the glass substrate and air, excited at 488 nm . (see color insert)

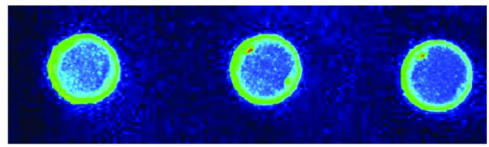

Figure 5. "Coffee ring" spot morphology for a porous nitrocellulose microarray slide printed with a low concentration of protein. (see color insert)

Unlike ELISA plates, the substrate coatings themselves can contribute a large background signal for protein microarrays because polymers are inherently fluorescent. The fluorescence from the slide itself is termed autofluorescence, and this is illustrated in Figure 4 for the case of nitrocellulose. The edge of the nitrocellulose pad is shown to saturate the CCD camera, while on the same sensitivity scale the glass substrate gives barely more signal than air. The fluorescence background from the polymer offsets the high sensitivity of the nitrocellulose. Nitrocellulose is often impregnated with carbon to reduce autofluorescence, but this also reduces optical transparency. Nonporous nitrocellulose films having a 20x lower thickness give an even greater reduction in autofluorescence, but the signal size is also reduced by the thinner coating.

A problem with all microarrays is that the printed spots are sometimes nonuniform. A frequent problem is that the spots can appear as "coffee rings" due to the droplet spreading and evaporating at the edges to give an accumulation of material at the edges. This is especially a problem when lower concentrations of protein are printed, such as in reverse protein microarrays. An example is shown in Figure 5 for a porous nitrocellulose slide printed with a 1 µg/mL protein solution. The coffee ring structure hampers attempts to get a quantitative result. Since spot morphology is not always reliable, microarrays are printed with redundant spots, as many as six replicates, which reduce the potential information content of the microarray. The difficulty that the spot morphology presents is one reason that ELISA remains as the gold standard for sandwich immunoassays.

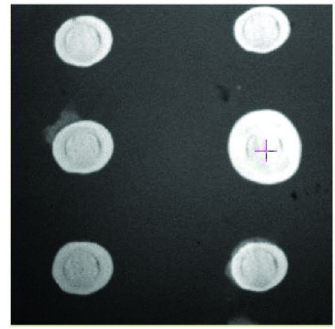

Figure 6. Six replicate spots of labeled BSA printed on porous nitrocellulose.

Spot spreading can also be a problem with porous microarray slides. This problem is illustrated in Figure 6 for a different manufacturer's porous nitrocellulose slide. The pin bites into the material, leaving a dark ring, and the image shows that the protein solution wicks through the material, beyond the bite marks, to spread the spot diameter. This spreading of the spot reduces the printing density. Wicking is caused by capillary forces to give a spreading velocity, v, that decreases with spreading distance, x, depending on the contact angle between the spotting solution and material, θ, the pore size in the material, r, and the solution viscosity, η, as described by Eq. 1 (*30*).

$$v = \frac{r\gamma \cos\theta}{4x\eta} \tag{1}$$

Eq. 1 explains that wicking can be reduced by making the material more hydrophobic, by reducing the amount of surfactant in the spotting solution, and by increasing viscosity of the print buffer, which is often done by adding glycerol. Some porous nitrocellulose slides are sufficiently hydrophobic to avoid significant wicking.

The slides with the lowest fluorescence and no wicking issues are the same slides used for DNA microarrays, which are clear glass having a silane monolayer. These slides are available with a variety of chemical modifications due to the versatility of silane chemistry. Silane coatings would seem quite suitable for protein microarrays. For example, epoxide and aldehyde covalently bind protein, and γ-aminopropylsilane electrostatically binds proteins. Glass slides with silane coatings are less frequently used for protein microarrays, in part because they are not available as porous media to enhance sensitivity.

The uniformity of the microarray slide is a consideration. All applications involve comparing signal sizes from one spot to the next, and any nonuniformity diminishes the information content. The high surface area slide all have to be manufactured in a way that keeps the surface area uniform over all of the usable part of each pad, and the same from pad-to-pad. To our knowledge, there are no published statistical data comparing high surface area protein microarray slides.

A final consideration is the time for analysis. A typical ELISA requires 4 hr for the complete analysis, with 30 min for incubation of the capture antibody.

Microarray analyses require an unspecified amount of time, with manufacturers suggesting incubation times for capture antibodies after printing to be as short as no time at all to as long as 4 days at 4 °C. An overnight incubation is typical.

To summarize, protein microarray slides have compromises among these desired characteristics.

- high protein function
- rapid binding of printed protein
- high capacity
- low autofluorescence
- uniform spot morphology
- uniformity across the slide
- low wicking or spreading

There is no one slide that is adequate in all of these respects; instead, one has to compromise one or more of these features. For example, a clear glass slide with an amino coating gives more rapid binding, lower autofluorescence, higher uniformity and less spreading than porous nitrocellulose, but it has much lower signal. For protein microarrays to achieve their full potential to become a platform that is as reliable, sensitive and relatively fast as ELISA, new substrates that reduce or even avoid these compromises need to be invented.

Silica Colloidal Crystals as Surface Coatings

Silica potentially has advantages over nitrocellulose for the same reason that silica is preferred over polymers in high performance liquid chromatography (HPLC): silica has versatile surface chemistry to minimize nonspecific binding (*31*, *32*). In addition, silica is inherently nonfluorescent, which is why the best fluorescence cuvettes are made of fused silica. Silica particles with uniform, sub-micrometer diameters can easily be made using the Stöber method (*33*). These uniformly sized particles spontaneously pack as face-centered cubic crystals when coated on flat surfaces. A scanning electron microscope image is shown in Figure 7 for a colloidal crystalline film deposited on a silica microscope slide, then snapped in half to reveal the cross-section of the film. The film is shown in this case to be 4 μm thick, comprised of 300 nm silica particles, and the crystalline planes are evident in the image. One can think of this material as the slab version of a chromatographic silica particle of 4 μm in diameter. Chromatographic particles allow fast diffusive transport due to particle diameters of 5 μm or less. Sintering at 900 °C stabilizes the particles to make a rugged coating, which stands up even to sonication, preventing damage in the microarray printing process. Rehydroxylation and chemical modification provide the same variety of surface functional groups for binding proteins that are used for flat glass slides, such as epoxide, aldehyde, and amino groups. The slides can be thought of as the three dimensional version of the conventional glass slides, offering much higher surface area.

In Interfaces and Interphases in Analytical Chemistry; Helburn, R., et al.;
ACS Symposium Series; American Chemical Society: Washington, DC, 2011.

Over the past decade, various methods have been developed to form silica colloidal crystals on glass slides, including evaporation of the meniscus of a colloidal slurry against a slide (*34*), spin-coating (*35*), and coating by capillary action (*36*). A pair of photographs of slides coated with colloidal crystals by spin-coating are shown Figure 8. The film was shaved away at the edges, sintered at 900 °C, and rehydroxylated with base. Three important features are illustrated by the photographs. First, the slides are transparent, which means that fluorescence sensitivity is improved because the excitation light can penetrate the entire film. Second, the material appears blue, despite the fact that silica is colorless. The reason is that Bragg diffraction occurs due to the fact that the particles are on the order of the wavelength of light and evenly spaced (*37*, *38*). The slide is transparent at all wavelengths except for the Bragg wavelength, which is in the blue region of the spectrum in this case. For a 4 μm film, the transmission even at the Bragg wavelength is still much higher than that of a nitrocellulose film of the same thickness. Third, the material is porous: the image on the right in Figure 8 shows that a drop of water readily penetrates the material. The partial index matching makes the blue color disappear to illustrate the porosity.

Silica colloidal crystals were initially investigated as photonic media in the optics and physics communities, where the Bragg diffraction prevents electromagnetic radiation at the Bragg wavelength from entering the material. A variety of applications in chemistry have been developed, including permselective membranes (*39–42*), DNA and protein sieving (*43*, *44*), chromatographic separation (*45*), supports for lipid bilayers (*46*) and live cells (*47*), and for making super-hydrophobic surfaces, (*48*, *49*). We have explored their application as substrates for electrochromatography (*45*, *50*), as well as for HPLC and thin-layer chromatography (TLC), and most relevant to this chapter, for protein microarrays (*51*).

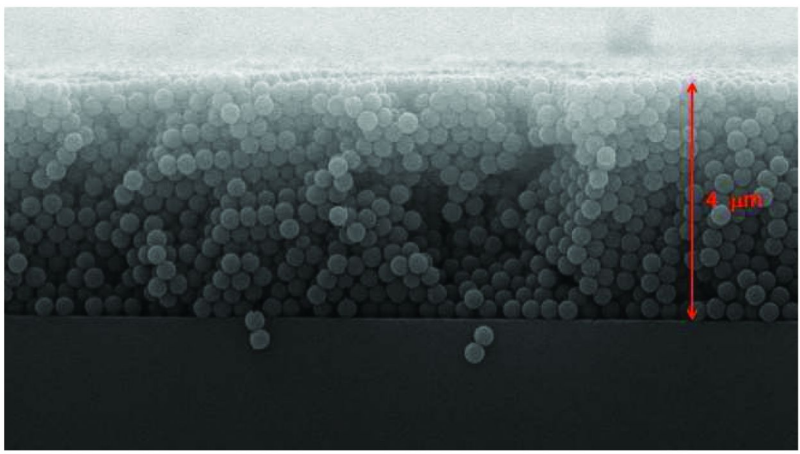

Figure 7. Image of cross-section of a silica colloidal crystalline film on a silica slide using scanning electron microscopy. The image reveals the face-centered cubic arrangement of particles and a 4 μm thickness. (see color insert)

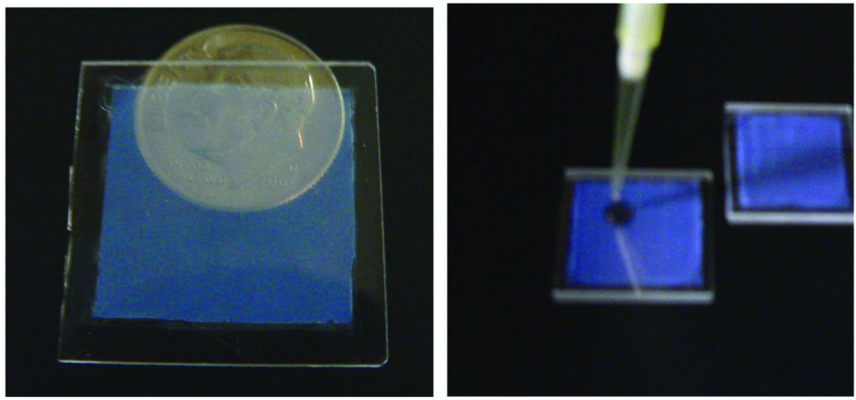

Figure 8. Photographs of silica slides coated with 4 μm films of silica colloidal crystals made of 300 nm particles. (see color insert)

Equilibration of protein solution through silica colloidal crystals is expected to be fast, provided that the pore diameter is much larger than the protein diameter. This is true for particle sizes greater than 300 nm in diameter, since the pore diameter is 15% of the particle diameter. The relation for diffusion inside the material is given in Eq. 2, where D is the diffusion

$$\sigma^2 = 2\gamma Dt \tag{2}$$

coefficient, t is time, σ is the standard deviation of the distance, and γ is the same obstruction term described for chromatography (*30*). For a protein with a diffusion coefficient of 10^{-6} cm^2/s, an obstruction term of 0.1, which is based on diffusion measurements in silica colloidal crystals (*52*), and using σ=4 μm, which is the thickness of the film from Figure 7, the time required for equilibration is calculated to be 0.8 s. This is much faster than a microarray spot dries during the printing process, thus allowing penetration of the spot through the material.

Face-centered cubic crystals are so regular that one can predict the increase in signal size from first principles. The increase in surface area is graphically illustrated in Figure 9. For a given footprint area, l^2, Eq. 3 shows that the surface area is increased by the factor F, which depends on the thickness, t, of the colloidal crystal and the particle diameter, d_p, the penetration depth of the light, δ, and the accessibility of the surface area, Ω, which varies between zero and unity (*51*). The penetration depth is the inverse of the scattering cross-section, k, in Eq. 3. For a penetration depth of 10 μm and a thickness of

$$F = \Omega \frac{4.4}{d_p \cdot k} \left\{1 - \exp\left(-t/\delta\right)\right\} \tag{3}$$

4 μm, the signal can be enhanced by ten-fold relative to that for a flat surface if Ω is no less than 0.6. The question will be whether this enhancement can be obtained without increasing the background noise by a proportional amount, which would preclude an improvement in the detection limit.

In Interfaces and Interphases in Analytical Chemistry; Helburn, R., et al.;
ACS Symposium Series; American Chemical Society: Washington, DC, 2011.

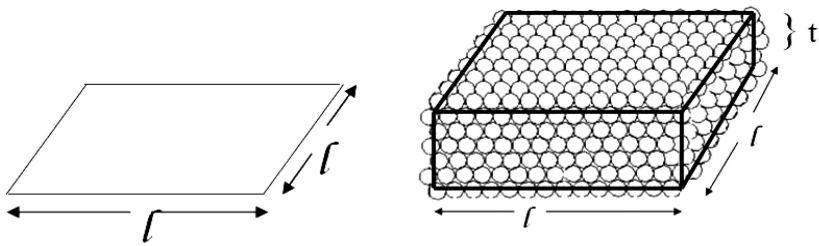

Figure 9. Illustration of the enhancement in the surface area for a footprint of area l^2 by a silica colloidal crystal of thickness, t. Adapted from Zheng et al. (51) with permission.

Performance of Protein Microarrays Coated with Silica Colloidal Crystals

The predicted signal enhancement for a face-centered cubic film was tested experimentally by using 250 nm silica particles and making silica colloidal crystals of varying thickness. The silica was chemically modified with a silane bearing a biotin group to capture fluorescein-labeled streptavidin. The signals for silica colloidal crystals of varying thickness were compared with the signal for a flat silica surface. The results are shown in Figure 10, with the errors measured using different regions of the same slide. A surface enhancement of nearly 40 was achieved for a 4 μm film, and an enhancement as high as 80 was achieved for an 11 μm thick film. The roll-off is from scattering, due to the *1/e* penetration depth of 8.3 μm, which was measured independently by transmission spectroscopy. The solid line in Figure 10 is the best fit to Eq. 3, with Ω as the only fitting parameter, revealing Ω=0.6. This is due to steric hindrance, indicating that larger particles would be advantageous for protein microarrays. A calculation of Ω from first principles predicts Ω=0.6, which means that the solid line agrees with the data without any fitting variables. This illustrates that the adsorption to face-centered cubic crystals can be described well from first principles.

To determine whether the background noise is also increased, background was measured for regions where streptavidin was not deposited. This reveals background signal from the colloidal crystal itself to assess whether scattering is a significant contribution to the overall signal. Figure 11 shows a plot of background signal vs. colloidal crystal thickness. The background is so small that a $\log_{10}$ scale is needed. Based on the slope, the background changes by only 10 units over the thickness range, and the noise on the background is only a fraction of a unit. The background noise due to the colloidal crystal is thus orders of magnitude below the signal size. The small background is due to the fact that silica does not fluoresce. The scattering from Bragg diffraction does not appear to pose a problem.

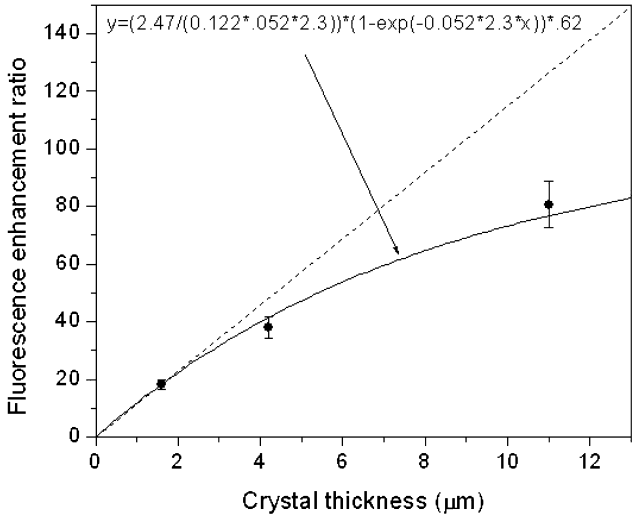

Figure 10. Plot of signal size vs. thickness of silica colloidal crystal for biotin capturing labeled streptavidin. The solid line is the best fit to Eq. 3, and the dotted line illustrates the nonlinear roll-off of the signal. Reprinted from Zheng et al. (51) with permission.

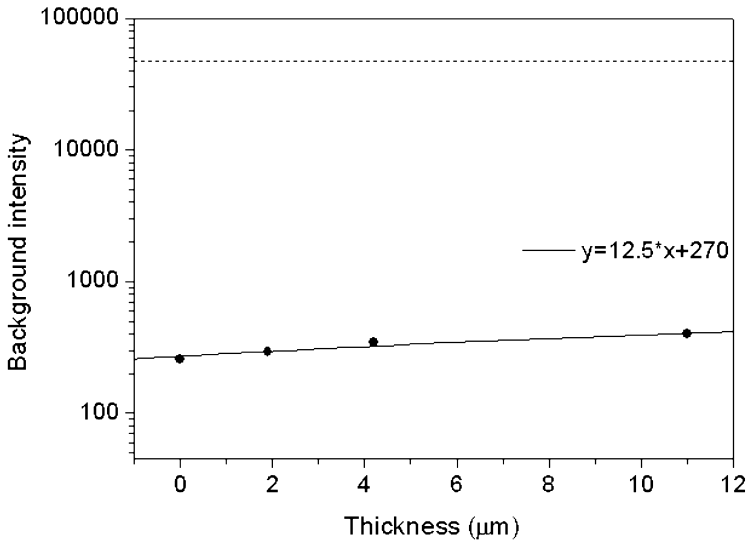

Figure 11. Plot of background (•) vs. thickness for the same silica colloidal crystal as in Figure 10, and linear fit (—). The dotted line is the fluorescence intensity of streptavidin for the 11 μm thick silica colloidal crystal. Reprinted from Zheng et al. (51) with permission.

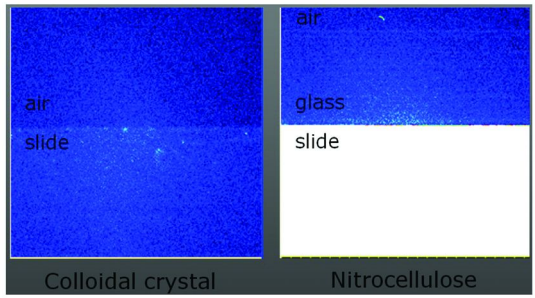

Figure 12. Images of fluorescent backgrounds at fluorescein wavelengths. (see color insert)

Figure 12 shows a comparison of the backgrounds for a 4 μm thick silica colloidal crystal and a microarray slide with an 11 μm film of nitrocellulose using fluorescence excitation and emission filters designed for fluorescein. The two images are shown on the same intensity scale with the same excitation power, using a fluorescein isothiocyanate (FITC) fluorescence cube. The colloidal crystal is shown to contribute little more than bare glass contributes to the background signal, whereas the nitrocellulose saturates the camera. The nitrocellulose was porous and white in this case; carbon black is sometimes added to nitrocellulose to reduce its background fluorescence.

Nonspecific binding of labeled protein contributes even more to the background than does the autofluorescence of the substrate. For example, with a reverse protein microarray, when a protein is spotted onto the microarray slide, its labeled antibody is intended to bind only to that protein. When the antibody binds elsewhere, this is called nonspecific binding. This occurs because the protein microarray is made to be sticky to proteins so that printing works. After printing, a blocking agent is used to tie up the remaining sticky sites, but the problem is that blocking is never 100% efficient. Blocking works fast on silica because protein binding to the silanes is instantaneous.

Reverse protein microarrays are especially fraught with problems from nonspecific binding, presumably because the smaller proteins do not remain bound to the surface as well as the larger antibodies do, thus freeing up space for nonspecific binding. In practice, detection limits are often not even as good as 1 μg/mL of printed protein. To test whether the silane surface retains the printed proteins well, a reverse protein microarray assay was performed for a biomarker protein used to diagnose hepatocellular carcinoma: alpha-fetoprotein (AFP). Commercial proteins were used for this assay: AFP (Meridian A8150H), anti-AFP (Meridian M86641M) and Alexafluor 647-labeled labeled anti-IgG (Abcam ab6563). The colloidal crystal was made of 500 nm silica particles and functionalized with amino groups. The protein was printed on the microarray slide without incubation. The surface was then blocked for 1 hr with Thermo Scientific protein-free blocking buffer (37573), after which the surface was exposed to anti-AFP for 30 min, and finally exposed to labeled anti-IgG for 30 min. The slides were read with a commercial scanner (Genepix 4000b).

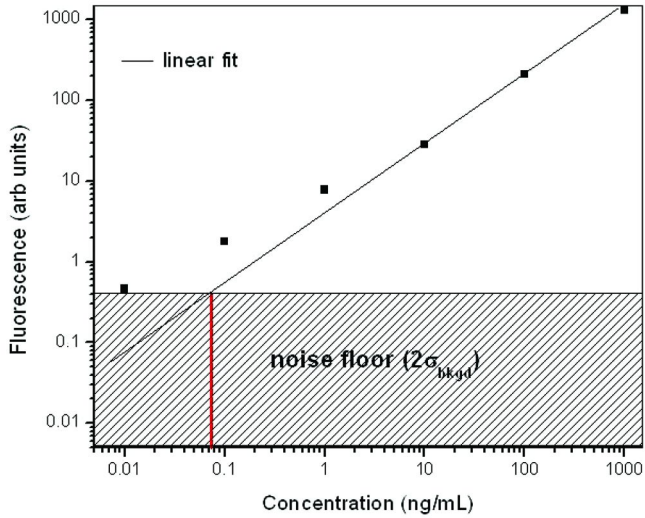

Figure 13. Calibration curve for reverse assay of AFP, using anti-AFP and Alexafluor 647 labeled anti-IgG. The noise floor is 2σ=0.4, and the corresponding detection limit is denoted by the red line to be 80 pg/mL. (see color insert)

The calibration curve for the reverse AFP assay is shown in Figure 13. A level of 1 ng/mL level is easily detectable, as are levels well below. The solid line represents a linear fit through the origin and the highest concentrations on a linear scale. Below the level of 10 ng/mL, the data become nonlinear, and this is not yet understood. Using only the linear data, and combining this with the noise on the background, the detection limit can be calculated. The IUPAC definition of detection limit is twice the standard deviation of the background noise, and the 2σ noise floor is denoted on the graph. The red line points to the concentration corresponding to 2σ, showing a detection limit of 80 pg/mL. This is about 10x better than commercial ELISA kits for detection of AFP. Further, the assay was completed in half the time: 2 hr for the microarrays vs. 4 hr for the ELISA. These results indicate that the silica slides promise to provide higher sensitivity for reverse protein assays to fill the promise of protein microarrays for highly multiplexed protein assays.

Lower detection limits can eventually be achieved with lower background noise. While substrate fluorescence is one contribution mentioned earlier, nonspecific binding of the labeled proteins contributes even more to the background. This phenomenon is illustrated in Figure 14 using images from the same analysis as in Figure 13. The left panel shows the image for an AFP concentration of 10 ng/mL, showing negligible background. The right panel, which is shown with 100x higher sensitivity, reveals the nonspecific binding of the labeled antibody to the substrate. A 16-pad format was used, as was depicted in Figure 1, and the right panel shows the edge of the colloidal crystal pad. Innovations in interfacial chemistry could lead to even lower detection limits.

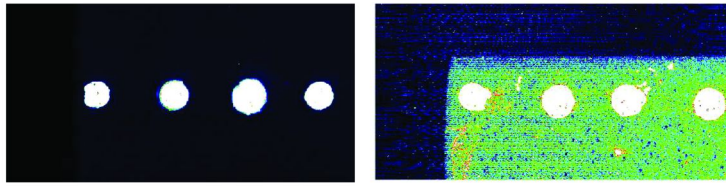

Figure 14. Data illustrating the effect of nonspecific binding. Protein concentrations: 10 ng/mL (left) and 0.1 ng/mL protein (right), with the latter shown on a 100x more sensitive scale. (see color insert)

Conclusion

The research presented here demonstrates the feasibility of using silica colloidal crystals to increase the interfacial area of microarray slides. The absence of fluorescence, and the ability of silanes to rapidly bind both proteins and blocking agent, gives low detection limits. The sensitivity now rivals or even exceeds that of ELISA assays even for reverse protein microarrays. Further improvements are possible with advances in interfacial chemistry

Disclosure

Professor Wirth is a major shareholder in bioVidria, Inc., which has licensed this microarray technology from the University of Arizona.

Acknowledgments

This work was funded by the National Institutes of Health under grants R01GM065980 and R41 GM085938.

References

1. Fodor, S. P.; Rava, R. P.; Huang, X. C.; Pease, A. C.; Holmes, C. P.; Adams, C. L. *Nature (London)* **1993**, *364*, 555–556.
2. Fodor, S. P.; Read, J. L.; Pirrung, M. C.; Stryer, L.; Lu, A. T.; Solas, D. *Science* **1991**, *251*, 767–773.
3. Miller, M. B.; Tang, Y. W. *Clin. Microbiol. Rev.* **2009**, *22*, 611–633.
4. Nygaard, V.; Hovig, E. *Front. Biosci.* **2009**, *14*, 552–569.
5. Coppee, J. Y. *Microbes Infect.* **2008**, *10*, 1067–1071.
6. Thompson, M.; Furtado, L. M. *Analyst* **1999**, *124*, 1133–1136.
7. Duggan, D. J.; Bittner, M.; Chen, Y. D.; Meltzer, P.; Trent, J. M. *Nat. Genet.* **1999**, *21*, 10–14.
8. Schena, M.; Shalon, D.; Davis, R. W.; Brown, P. O. *Science* **1995**, *270*, 467–470.
9. Wang, S. T.; Li, C.; Liu, L. *Curr. Bioinf.* **2009**, *4*, 141–148.
10. Yin, J. Q.; Zhao, R. C.; Morris, K. V. *Trends Biotechnol.* **2008**, *26*, 70–76.

11. Joos, T.; Bachmann, J. *Front. Biosci.* **2009**, *14*, 4376–4385.
12. Kerschgens, J.; Egener-Kuhn, T.; Mermod, N. *Trends Mol. Med.* **2009**, *15*, 352–358.
13. Borrebaeck, C. A. K.; Wingren, C. *J. Proteomics* **2009**, *72*, 928–935.
14. Li, Y.; Lee, H. J.; Corn, R. M. *Anal. Chem.* **2007**, *79*, 1082–1088.
15. Li, Y.; Lee, H. J.; Corn, R. M. *Nucleic Acids Res.* **2006**, *34*, 6416–6424.
16. Roche, S.; Dauvilliers, Y.; Tiers, L.; Couderc, C.; Piva, M. T.; Provansal, M.; Gabelle, A.; Lehmann, S. *J. Immunol. Methods* **2008**, *338*, 75–78.
17. Zhao, J.; Patwa, T. H.; Qiu, W. L.; Shedden, K.; Hinderer, R.; Misek, D. E.; Anderson, M. A.; Simeone, D. M.; Lubman, D. M. *J. Proteome Res.* **2007**, *6*, 1864–1874.
18. Patwa, T. H.; Zhao, J.; Anderson, M. A.; Simeone, D. M.; Lubman, D. M. *Anal. Chem.* **2006**, *78*, 6411–6421.
19. Lee, H. J.; Wark, A. W.; Corn, R. M. *Analyst* **2008**, *133*, 975–983.
20. Park, H. Y.; Lipert, R. J.; Porter, M. D. *Nanosensing: Materials and Devices*; SPIE: Bellingham, WA, 2004; Vol. 5593, pp 464−477.
21. Thaxton, C. S.; Elghanian, R.; Thomas, A. D.; Stoeva, S. I.; Lee, J. S.; Smith, N. D.; Schaeffer, A. J.; Klocker, H.; Horninger, W.; Bartsch, G.; Mirkin, C. A. *Proc. Natl. Acad. Sci. U.S.A.* **2009**, *106*, 18437–18442.
22. Zheng, G. F.; Patolsky, F.; Cui, Y.; Wang, W. U.; Lieber, C. M. *Nat. Biotechnol.* **2005**, *23*, 1294–1301.
23. Rubina, A. Y.; Kolchinsky, A.; Makarov, A. A.; Zasedatelev, A. S. *Proteomics* **2008**, *8*, 817–831.
24. Rubina, A. Y.; Dementieva, E. I.; Stomakhin, A. A.; Darii, E. L.; Pańkov, S. V.; Barsky, V. E.; Ivanov, S. M.; Konovalova, E. V.; Mirzabekov, A. D. *BioTechniques* **2003**, *34*, 1008–1022.
25. Yadavalli, V. K.; Koh, W. G.; Lazur, G. J.; Pishko, M. V. *Sens. Actuators, B* **2004**, *97*, 290–297.
26. Derwinska, K.; Gheber, L. A.; Preininger, C. *Anal. Chim. Acta* **2007**, *592*, 132–138.
27. Mayer, M.; Yang, J.; Gitlin, I.; Gracias, D. H.; Whitesides, G. M. *Proteomics* **2004**, *4*, 2366–2376.
28. Zhou, Y.; Andersson, O.; Lindberg, P.; Liedberg, B. *Microchim. Acta* **2004**, *147*, 21–30.
29. Kukar, T.; Eckenrode, S.; Gu, Y. R.; Lian, W.; Megginson, M.; She, J. X.; Wu, D. H. *Anal. Biochem.* **2002**, *306*, 50–54.
30. Giddings, J. C. *Unified Separation Science*; Wiley: New York, 1991.
31. Huang, X. Y.; Doneski, L. J.; Wirth, M. J. *Anal. Chem.* **1998**, *70*, 4023–4029.
32. Kohler, J.; Kirkland, J. J. *J. Chromatogr.* **1987**, *385*, 125–150.
33. Stober, W.; Fink, A.; Bohn, E. *J. Colloid Interface Sci.* **1968**, *26*, 62–69.
34. Jiang, P.; Bertone, J. F.; Hwang, K. S.; Colvin, V. L. *Chem. Mater.* **1999**, *11*, 2132–2140.
35. Jiang, P.; McFarland, M. J. *J. Am. Chem. Soc.* **2004**, *126*, 13778–13786.
36. Zeng, Y.; Harrison, D. J. *Anal. Chem.* **2007**, *79*, 2289–2295.
37. Mittleman, D. M.; Bertone, J. F.; Jiang, P.; Hwang, K. S.; Colvin, V. L. *J. Chem. Phys.* **1999**, *111*, 345–354.
38. Tarhan, II; Watson, G. H. *Phys. Rev. Lett.* **1996**, *76*, 315–318.

39. Newton, M. R.; Bohaty, A. K.; White, H. S.; Zharov, I. *J. Am. Chem. Soc.* **2005**, *127*, 7268–7269.
40. Smith, J. J.; Zharov, I. *Chem. Mater.* **2009**, *21*, 2013–2019.
41. Schepelina, O.; Zharov, I. *Langmuir* **2008**, *24*, 14188–14194.
42. Smith, J. J.; Zharov, I. *Langmuir* **2008**, *24*, 2650–2654.
43. Zhang, H.; Wirth, M. J. *Anal. Chem.* **2005**, *77*, 1237–1242.
44. Zeng, Y.; Harrison, D. J. *Anal. Chem.* **2007**, *79*, 2289–2295.
45. Zheng, S. P.; Ross, E.; Legg, M. A.; Wirth, M. J. *J. Am. Chem. Soc.* **2006**, *128*, 9016–9017.
46. Ross, E. E.; Wirth, M. J. *Langmuir* **2008**, *24*, 1629–1634.
47. Velarde, T. R. C.; Wirth, M. J. *Appl. Spectrosc.* **2008**, *62*, 611–616.
48. Sun, C.; Gu, Z. Z.; Xu, H. *Langmuir* **2009**, *25*, 12439–12443.
49. Lakshmi, R. V.; Basu, B. J. *J. Colloid Interface Sci.* **2009**, *339*, 454–460.
50. Malkin, D. S.; Wei, B. C.; Fogiel, A. J.; Staats, S. L.; Wirth, M. J. *Anal. Chem.* **2010**, *82*, 2175–2177.
51. Zheng, S.; Zhang, H.; Ross, E.; Le, T. V.; Wirth, M. J. *Anal. Chem.* **2007**, *79*, 3867–3872.
52. Newton, M. R.; Morey, K. A.; Zhang, Y. H.; Snow, R. J.; Diwekar, M.; Shi, J.; White, H. S. *Nano Lett.* **2004**, *4*, 875–880.

Chapter 10

Guanosine Gels for DNA Separations

Linda B. McGown*,[1] and William S. Case[2]

[1]Department of Chemistry and Chemical Biology, Rensselaer Polytechnic Institute, Troy, NY 12180
[2]Department of Chemistry, University of Richmond, Richmond, VA 23220
***mcgowl@rpi.edu**

The use of guanosine gels (G-gels) formed by guanosine 5′-monophosphate (GMP) was investigated for the separation of single-stranded DNA (ssDNA) fragments of equal length based on differences in sequence in capillary gel electrophoresis (CGE). The strands were labeled with the fluorophore 6-carboxyfluorescein (6-FAM) and detected by laser-induced fluorescence (LIF). Baseline resolution was achieved for the separation of a series of homodimers and homopentamers of adenosine, cytidine, and thymidine nucleotides. G-gels provided better resolution than capillary zone electrophoresis (CZE) and a traditional sieving gel in CGE, and this can be traced to analyte-gel interactions. Comparison of migration order among the different techniques suggests that base- or sequence-specific interactions within the buffer-gel system become important in G-gel separations in going from the dimers to the pentamers. G-gels were then applied to the separation of four 76-mers that form part of a highly polymorphic short tandem repeat (STR) sequence used in forensic DNA typing. Resolution of the four strands was achieved using the G-gel in CGE, while no separation was achieved using CZE or CGE with a commercial sieving gel. The separation order of the 76-mers was found to be related to the number of guanosine nucleotides in each strand under conditions of forward polarity (anode as the inlet and cathode as the outlet), with the strand having the most guanosine nucleotides eluting first and the strand having the least eluting last. The results suggest that separation in CGE

In Interfaces and Interphases in Analytical Chemistry; Helburn, R., et al.;
ACS Symposium Series; American Chemical Society: Washington, DC, 2011.

is dependent upon both the number of guanosine nucleotides in each strand and their positions within the strand.

Introduction

Electrophoretic techniques for the separation of biomolecules have led to important advances in many areas (*1–5*). These separations are based upon the different migration rates of analytes in the presence of an applied electric field, with separations typically resulting from differences in the effective charge-to-size ratios of analytes. Capillary electrophoresis (CE) (*6–9*) has become an attractive alternative to more traditional gel electrophoresis for many applications due to the long length and high surface-to-volume ratio of the capillary, which allows use of high field strengths for rapid, high efficiency separations (*10*). CE also requires only minimal sample consumption, on the order of nanoliters, and allows for real time detection of analytes during the separation process.

In the simplest CE technique, capillary zone electrophoresis (CZE), the sample is injected into the capillary filled with a simple buffer. Solutes are separated based on differences in their electrophoretic mobility, which is a function of their mass-to-charge ratio. The separation of DNA molecules cannot be achieved in CZE because DNA that is more than a few nucleotides in length has linear charge density, so that electrophoretic mobility is independent of strand length (*11*, *12*). The successful application of electrophoresis to DNA separations has therefore relied upon the development of media such as sieving gels that provide separations based on differences in strand length or structural conformation.

Early applications of CE to the analysis of DNA involved filling capillaries with polymers commonly used in slab gel applications, resulting in the development of capillary gel electrophoresis (CGE). While these gels afforded excellent resolution, they suffered from breakage, air bubble formation, and hydrolysis within the capillary, resulting in low reproducibility and short capillary lifetimes (*13–15*). Over the years such gels have been replaced by more manageable polymer solutions created from derivatives of common celluloses and alcohols. These gels are stable, easy to prepare and can be replaced between runs.

While sieving gels and polymeric solutions offer high resolution of DNA fragments of different lengths, they are not designed to separate fragments that differ in sequence. To meet this need, techniques have been developed that rely upon the presence of sequence-dependent conformational differences between the DNA strands. These approaches include single stranded length conformational polymorphism (SSCP) (*16–18*), heteroduplex analysis (HA) (*19*, *20*), restriction fragment length polymorphism (RFLP) (*21–23*), and affinity capillary electrophoresis (ACE) (*24–27*). These techniques have been successful in some instances but are limited by the need for sufficient differences in mobilities arising from sequence-based conformational variations among the strands (SSCP, HA, ACE) or the need for specific recognition sites in the DNA (RFLP).

Thus, the ability to resolve ssDNA fragments of equal length based on minor differences in sequence remains a challenge in electrophoresis. The

In Interfaces and Interphases in Analytical Chemistry; Helburn, R., et al.;
ACS Symposium Series; American Chemical Society: Washington, DC, 2011.

ability to perform such separations could lead to great advances in areas such as microbial genomics, forensics, and biomedical analysis that would benefit from the detection of slight differences in DNA sequence among strands of similar length. The present work addresses this challenge through the use of organized media formed by self-association of guanosine 5′-monophosphate (GMP) for sequence-selective DNA separation in CGE.

The formation of gels by guanosine nucleosides and their derivatives has been well documented since the early 1900s (*28–34*). Of the four nucleobases in DNA, gelation is unique to guanosine due to the number and arrangement of hydrogen bond donor and acceptor molecules present within the nucleobase moiety. While guanosine gelation was once primarily considered to be a nuisance that hindered DNA sequencing and synthesis, the phenomenon has received growing attention in recent years for potential applications in nanotechnology (*35*).

G-Gels and G-Gel Formation

The structural basis of G-gels is the G-tetrad that arises from Hoogsten hydrogen bonding between four guanine nucleobases (*31*, *35*). As monomer concentration is increased, discrete G-tetrads begin to stack upon each other to form columnar structures (alternatively, in the case of GMP, the aggregates may be in the form of a continuous, hydrogen bonded helical network (*31*, *36*). The columnar structures are stabilized through the presence of cations that are centrally located between tetrads. As monomer concentration continues to increase, these columnar structures can further organize into cholesteric and hexagonal lyotropic liquid crystalline phases (*37*, *38*). These stages of guanosine aggregation are depicted in Figure 1.

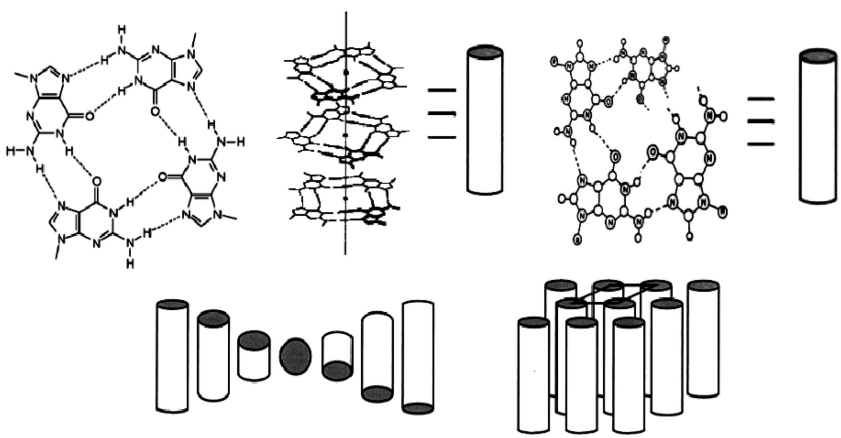

Figure 1. Schematics of a single G-tetrad (top, left), a columnar stack of G-tetrads (top, center), a helical model for GMP (top, right) and more highly ordered cholesteric (bottom, left) and hexagonal phases (bottom, right). Adapted from Reference (35) with permission.

The first use of G-gel phases in CGE (*39*) employed GMP for chiral separations of the enantiomers of propranolol, a drug commonly used for the treatment of angina. The separation was based on the intrinsic chirality of the aggregates of GMP in the gel phase. The use of GMP for DNA separations, in contrast, is based on differential interactions of the GMP organized aggregates with steady state ssDNA as a function of DNA sequence, as illustrated in the work described here and first reported in 2007 (*40*). It is important to recognize that each separation system (presented in this chapter) was individually optimized for a particular set of conditions. The exact nature of the G-gel aggregates under each condition are not known at this time.

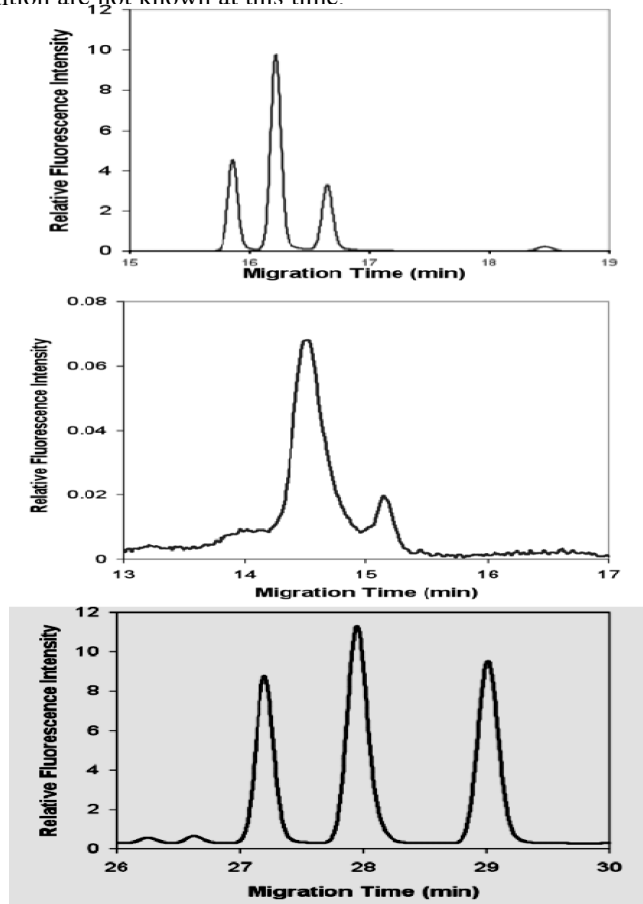

Figure 2. Separation of homodimers (1 µM each). Top: G-gel CGE (0.02 M GMP, 0.02 M KCl in 25 mM potassium phosphate buffer, pH = 7.0, 400 V/cm, 50 µm ID capillary, 25 °C, 5 s hydrodynamic injection). Middle: CZE (0.02 M KCl in 25 mM potassium phosphate buffer, pH 7.0, 400 V/cm, 50 µm ID capillary, 25 °C, 5s hydrodynamic injection). Bottom: sieving gel CGE (89 mM Tris borate EDTA (TBE), pH = 8.0, R-100 commercial sieving gel, 400 V/cm, 100 µm ID capillary, 30 °C, 5 s hydrodynamic injection, as recommended by gel manufacturer).

In Interfaces and Interphases in Analytical Chemistry; Helburn, R., et al.;
ACS Symposium Series; American Chemical Society: Washington, DC, 2011.

Description of Experiment and Results

Separation of Homodimers and Homopentamers

We first investigated the separation of homodimers and homopentamers of A (adenosine), C (cytidine) and T (thymidine). G (guanosine) was not investigated because the guanosine nucleotide at the strand terminus quenches the fluorescence of the FAM (6-carboxyfluorescein) dye used for LIF detection. Results (*e.g.* resolution and elution orders) for CZE were compared with those of CGE using a conventional DNA sieving gel. Figure 2 shows the results for the separation of the homodimers. Baseline resolution was obtained for the homodimers using CGE with both the G-gel and the commercial sieving gel, while only partial separation was achieved using CZE.

The elution order of the homodimers was determined by spiking the samples with each nucleotide component. The order was T,C,A for G-gel CGE, A,C,T for CZE and A,C,T for sieving gel CGE. In order to interpret these orders, it is necessary to consider that G-gel CGE and CZE were performed in forward polarity, with the cathode at the outlet, while sieving gel CGE was performed in reverse polarity, with the anode at the outlet. Additionally, in CZE and G-gel CGE the capillary contents are driven by electroosmotic flow (EOF) in the direction of the cathode, whereas the sieving gels in CGE create a dynamic capillary coating that eliminates EOF and so movement through the capillary is driven strictly by electromigration, which for DNA is in the direction of the anode. Taking these factors into account, G-gel CGE and sieving gel CGE result in the same elution order for the homodimers (T,C,A in forward polarity for CGE and A,C,T in reverse polarity for sieving gel CGE), while the order is reversed in CZE. Since the dinucleotides are too small to assume secondary structure, the similarity between the migration order for the G-gel and the sieving gel suggests that specific interactions with G-gels are not a determining factor in the dinucleotide separations. Rather, for these small homodimers, resolution is attributed to the different nucleotide structures and the disproportionate effects of the fluorescent tag on overall charge density at the GMP concentration and experimental conditions studied here.

It is interesting that the migration order in G-gel CGE is opposite that for CZE since both are performed under forward polarity. In CZE, T_2 (homodimer of thymidine) has the highest electrophoretic mobility towards the positive inlet and therefore appears at the detector last. In G-gel CGE, T_2 appears at the detector first. In G-gel CGE, the electrostatic attraction influences the oligonucleotides and the G-gels all to migrate counter to the EOF and towards the positive inlet, but at different rates that are fastest for the unencumbered DNA strands and slowest for those strands most closely associated with the cumbersome G-gel network. Those oligonucleotides that interact most with the G-gels will therefore have the fastest net forward migration rate and appear at the detector first. It follows that T_2 must have the strongest interaction with the G-gel, in order to slow down its migration toward the positive inlet relative to the other homodimers. This is consistent with the strong interaction of T with the G-gel indicated by anisotropy experiments (*40*).

In order to determine if base-selective interactions play a role in separations of longer oligonucleotides, G-gel CGE separations were performed for the

In Interfaces and Interphases in Analytical Chemistry; Helburn, R., et al.;
ACS Symposium Series; American Chemical Society: Washington, DC, 2011.

homopentamers. Again, quenching of the fluorescent label by interactions with the terminal guanosine nucleotide hindered detection of the guanine pentamer, which was therefore not included in these experiments.

Figure 3 shows the results for the separation of a mixture containing A_5, C_5 and T_5. Baseline resolution was obtained for the mixture using G-gel CGE. Spiking studies determined the elution order for the 5-mers to be the same as for the dinucleotides (T_5, C_5, A_5 in forward polarity). No separation was achieved using CZE, which is consistent with the decreasing influence of the fluorescent tag and oligonucleotide sequence on electrophoretic mobility with increasing oligonucleotide length. Separation in sieving gel CGE achieved resolution of T_5 from co-migrating A_5 and C_5 (confirmed by spiking studies). Since commercial sieving gels are designed to separate oligonucleotides strictly on the basis of size, it is not surprising that similarly sized fragments with little or no secondary structure would not be well resolved. The achievement of baseline resolution in G-gel CGE suggests that sequence specific gel-analyte interactions are important in separating the 5-mers.

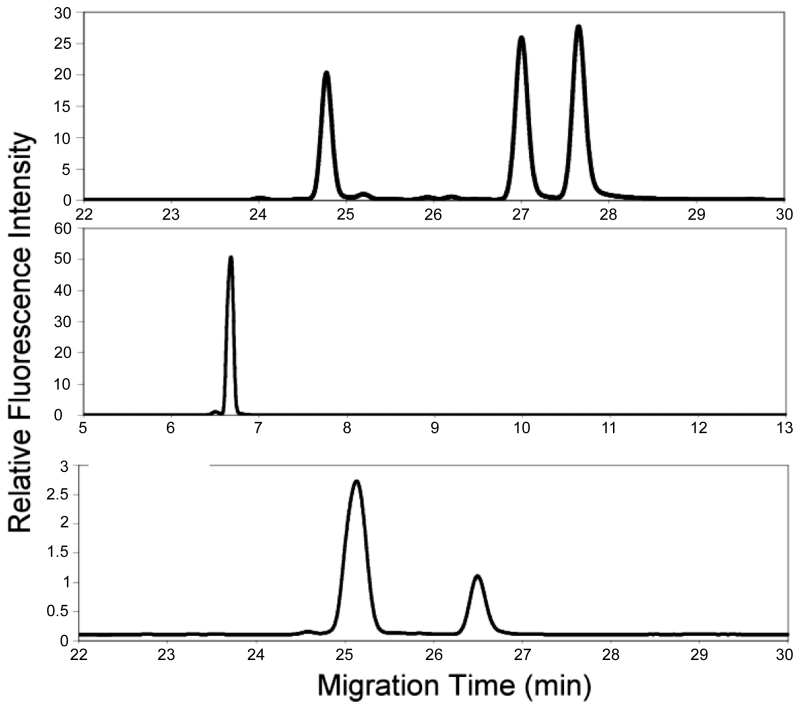

Figure 3. Separation of homopentamers (1 µM each). Top: G-Gel CGE (0.08 M GMP, 0.08 M KCl in 25 mM Tris-HCl, pH 8.0). Middle: CZE (0.08 M KCl in 25 mM Tris-HCl, pH 8.0). Bottom: sieving gel CGE. Separation conditions for G-gel CGE and CZE: 400 V/cm, 50 µm ID capillary, 25 °C, 5 s hydrodynamic injection. Separation conditions for sieving gel CGE: 400 V/cm, 100 µm ID capillary, 30 °C, 5 s hydrodynamic injection (recommended by gel manufacturer). Reproduced from Reference (40) with permission.

Separation of 76-mers

We next investigated separations of a set of four 76-mers, shown in Figure 4, that form part of a short tandem repeat (STR) marker that is commonly used for comprehensive DNA testing in forensic analysis (*41*, *42*). The sequences differ only in the substitution of guanosine nucleotides for adenosine nucleotides. The number and location of the substitutions vary for each sequence, providing a mechanism for exploring G-gel recognition towards adenosine or guanosine nucleotides within each strand. This is of particular interest given the possibility that guanosines in the DNA might interact with the GMP aggregates to form transient G-tetrads as the oligonucleotides migrate through the G-gel. Circular dichroism spectroscopy established the absence of significant conformational differences among the four strands (*40*).

The results for the separations of the 76-mers are shown in Figure 5. At least partial resolution was achieved using G-gel CGE and spiking studies determined the migration order to be Strand 3, Strand 1, Strand 2, Strand 4 (see Figure 4). This is inversely proportional to the number of guanosine nucleotides in each strand (the strand with the most guanosines appears first and the strand with the least guanosines appears last). Since the negatively charged oligonucleotides and G-gel network migrate towards the positively charged inlet, G-rich strands that are more closely associated with the slower moving G-gels will have a faster net velocity towards the negative outlet than the less interactive A-rich strands, therefore reaching the detector first in forward polarity mode. This is analogous to the separations observed for the homodimers and homopentamers and suggests that the interaction of G-gels with guanosine nucleotides present in the 76-mers retards migration towards the positive inlet. Strand 3 is well resolved from the other strands, which is attributed to the presence of more guanosine residues in this strand than the other strands.

Neither CZE nor sieving gel CGE provide significant separation of the 76-mers, which is expected since the oligonucleotides are of the same length and lack significant conformation differences. The ability of G-gel CGE to separate the fragments is therefore attributed to sequence specificity, demonstrating its potential for the separation of polymorphic oligonucleotides of equal length.

1: 5-TCTATCTATCTATCTATCTGTCTGTCTGTCTGTCTGTCTGTCTATCTATCTATCTATCTATCTATCTATCTATCTA-3

2: 5-TCTATCTATCTATCTATCTATCTATCTGTCTGTCTGTCTGTCTGTCTATCTATCTATCTATCTATCTATCTATCTA-3

3: 5-TCTATCTATCTATCTGTCTGTCTGTCTGTCTGTCTGTCTGTCTATCTATCTATCTATCTATCTATCTATCTA-3

4: 5-TCTATCTATCTATCTATCTATCTGTCTGTCTGTCTGTCTATCTATCTATCTATCTATCTATCTATCTATCTATCTA-3

Figure 4. Sequences of DNA 76-mer strands 1, 2, 3 and 4. G-A substitutions are underlined.

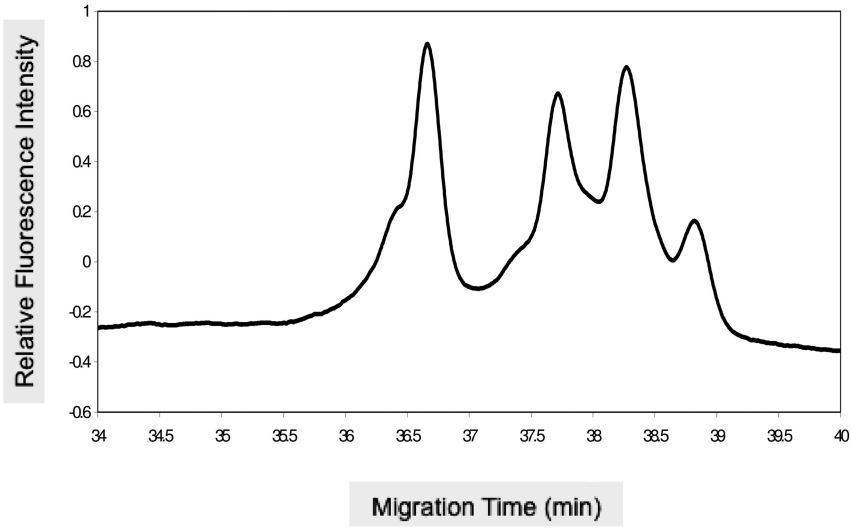

Figure 5. Separation of four DNA 76-mers (1 μM each) using G-gel CGE (0.14 M GMP, 0.04 M KCl in 15 mM Tris-HCl, pH = 7.0, 25 μM ID capillary, 580 V/cm, 55 °C, 5 s hydrodynamic injection.

Conclusions

This work demonstrates the effectiveness of G-gels for the separation of oligonucleotides of identical length based solely on minor differences in sequence. In the CGE separations in forward polarity, the negatively charged G-gels and oligonucleotides electromigrate towards the positive inlet while being driven by EOF to the negative outlet. It is thought that the net velocity in the forward direction would be greatest for those oligonucleotides that are most closely associated with the G-gel network. The G-gels therefore preferentially retard the counter migration of ssDNA that is rich in nucleotides that show the greatest degree of association with the G-gel network (T in the case of A, C and T homodimers and pentamers; G in the case of the 76-mers with A/G polymorphism). Given their low cost, ease of preparation and compatibility with common biological buffers utilized in CE, G-gels offer great promise as a practical approach to the separation of highly similar ssDNA based only on sequence and in the absence of differences in length or conformation.

References

1. Cao, L.; Wang, H.; Ma, M.; Zhang, H. *Electrophoresis* **2006**, *27*, 827.
2. Easley, C. J.; Jin, L. J.; Presto Elgstoen, K. B.; Jellum, E.; Landers, J. P.; Ferrance, J. P. *J. Chromatogr., A* **2003**, *1004*, 29.
3. Liu, C. C.; Huang, J. S.; Tyrrell, D. L.; Dovichi, N. J. *Electrophoresis* **2005**, *26*, 1424.

4. Timerbaev, A. R.; Aleksenko, S. S.; Polec-Pawlak, K.; Ruzik, R.; Semenova, O.; Hartinger, C. G.; Oszwaldowski, S.; Galanski, M.; Jarosz, M.; Keppler, B. K. *Electrophoresis* **2004**, *25*, 1988.
5. Zhang, L.; Yeung, B.; Liu, J. *Am. Lab.* **2006**, *38* (1), 34.
6. Brocke, A.; Freudemann, T.; Bayer, E. *J. Chromatogr., A* **2003**, *991*, 129.
7. Bjorheim, J.; Ekstrom, P. O. *Electrophoresis* **2005**, *26*, 2520.
8. Koumi, P.; Green, H. E.; Hartley, S.; Jordan, D.; Lahec, S.; Livett, R. J.; Tsang, K. W.; Ward, D. M. *Electrophoresis* **2004**, *25*, 2227.
9. Olejiniczak, M.; Kozlowski, P.; Sobczak, K.; Krzyzosiak, W. J. *Electrophoresis* **2005**, *26*, 1.
10. Jorgenson, J. W.; Lukacs, K. D. *Anal. Chem.* **1981**, *53*, 1298–1302.
11. DeDionisio, L. A. *J. Chromatogr., A* **1996**, *735*, 191.
12. Srivatsa, G. S.; Batt, M.; Schuette, J.; Carlson, R. H.; Fitchett, J.; Lee, C.; Cole, D. L. *J. Chromatogr., A* **1994**, *680*, 469.
13. Chiari, M.; Righetti, P. G. *Electrophoresis* **1995**, *16*, 1815.
14. Drossman, H.; Luckey, J. A.; Kostichka, A. J.; D′Cunha, J.; Smith, L. M. *Anal. Chem.* **1990**, *62*, 900.
15. Swerdlow, H.; Gesteland, R. *Nucleic Acids Res.* **1990**, *18*, 1415.
16. Liu, Q.; Scaringe, W. A.; Sommer, S. S. *Nucleic Acids Res.* **2000**, *28*, 940.
17. Orita, M.; Iwahana, H.; Kanazawa, H.; Hayashi, K.; Sekiya, T. *Proc. Natl. Acad. Sci. U.S.A.* **1989**, *86*, 2766.
18. Snyder, T. M.; McGown, L. B. *Appl. Spectrosc.* **2005**, *59*, 335.
19. Nagamine, C. M.; Chan, K. L; Lau, Y. F. *Am. J. Hum. Genet.* **1989**, *45*, 337.
20. Velasco, E.; Infante, M.; Durán, M.; Esteban-Cardeñosa, E.; Lastra, E.; García-Girón, C.; Miner, C. *Electrophoresis* **2005**, *26*, 2539.
21. Ho, H.; Chang, P.; Hung, C.; Chang, H. *J. Clin. Microbiol.* **2004**, *42*, 3525.
22. Pourzand, C.; Cerutti, P. *Mutat. Res.* **1993**, *288*, 113.
23. Schwartz, H. E.; Ulfelder, K.; Sunzeri, F. J.; Busch, M. P.; Brownlee, R. G. *J. Chromatogr., A* **1991**, *559*, 267.
24. Baba, Y.; Sawa, T.; Kishida, A.; Mitsuru, A. *Electrophoresis* **1998**, *19*, 433.
25. Murakami, Y.; Maeda, M. *J. Chromatogr., A* **2006**, *1106*, 118.
26. Muscate, A.; Natt, F.; Paulus, A.; Ehrat, M. *Anal. Chem.* **1998**, *70*, 1419.
27. Sato, K.; Onoguchi, M.; Hosokawa, K.; Maeda, M. *J. Chromatogr., A* **2006**, *1111*, 120.
28. Bang, I. *Biochem. Ztschr.* **1910**, *26*, 293.
29. Chantot, J. F.; Sarocchi, M. T.; Guschlbauer, W. *Biochimie* **1971**, *53*, 347.
30. Chantot, J. F.; Haertle, T.; Guschlbauer, W. *Biochimie* **1974**, *56*, 501.
31. Gellert, M.; Lipsett, M. N.; Davies, D. R. *Proc. Natl. Acad. Sci. U.S.A.* **1962**, *48*, 2013.
32. Pieraccini, S.; Giorgi, T.; Gottarelli, G.; Masiero, S.; Spada, G. P. *Mol. Cryst. Liq. Cryst.* **2003**, *398*, 57.
33. Sasisekharan, V.; Zimmerman, S.; Davies, D. R. *J. Mol. Biol.* **1975**, *92*, 171.
34. Wu, G.; Wong, A. *Chem. Commun.* **2001**, *24*, 2658.
35. Davis, J. T.; Spada, G. P. *Chem. Soc. Rev.* **2007**, *36*, 296.
36. Walmsley, J. A.; Burnett, J. F. *Biochemistry* **1999**, *38*, 14063.
37. Gottarelli, G.; Proni, G.; Spada, G. P. *Liq. Cryst.* **1997**, *22*, 563.

38. Sreenivasacahry, N.; Lehn, J. M. *Proc. Natl. Acad. Sci. U.S.A.* **2005**, *102*, 5938.
39. Dowling, V. A.; Charles, J. A. M.; Nwakpuda, E.; McGown, L. B. *Anal Chem.* **2004**, *76*, 4558.
40. Case, W. S.; Glinert, K. D.; LaBarge, S.; McGown, L. B. *Electrophoresis* **2007**, *28*, 3008.
41. Butler, J. M. *Forensic DNA Typing*; Academic Press: Burlington, MA, 2001.
42. Butler, J. M.; Buel, E.; Crivellente, F.; McCord, B. R. *Electrophoresis* **2004**, *25*, 1397.

Chapter 11

The Interface in Biosensing: Improving Selectivity and Sensitivity

John I. Njagi*,[a] and Stanley M. Kagwanja[b]

[a]Clarkson University, Department of Chemical and Biomolecular Engineering, Potsdam, NY 13699
[b]Chuka University College, P.O Box 109-60400, Chuka, Kenya
***Corresponding Author: njagiji@clarkson.edu**

Application of sensors and biosensors for real time *in vivo* monitoring of clinically-relevant physiologic-based analytes has been restricted to the laboratory or at most the first clinical trial stage. This is primarily because they suffer from poor selectivity and sensitivity when used in complex biological matrices. Other factors that have contributed to poor application (of sensors and biosensors) include: (i) nonbiocompatibility of materials used in their development, (ii) some of those developed on the bench are too large to be implanted; (iii) they often foul after implantation; (iv) there are problems with *in vivo* calibrations due to decreased sensitivity by fouling; (v) long term stability or continuous operation stability is a problem and (vi) selectivity to the analyte of interest is also a concern. At issue is the design and fabrication of the sensor-solution interface and its effect on sensitivity and selectivity. This chapter presents a review of specific approaches for designing modified electrode surfaces of amperometric biosensors intended for clinical application, with an emphasis on how these modifications have impacted a probe's sensitivity and selectivity toward target analytes. We address challenges that need to be overcome, with respect to design and application. We conclude with a look at the future direction of research in the field of designing sensors and biosensors for real time applications.

In Interfaces and Interphases in Analytical Chemistry; Helburn, R., et al.;
ACS Symposium Series; American Chemical Society: Washington, DC, 2011.

1. Introduction

Since the discovery of the first electrode biosensor by Clark in 1965, a wide range of these sensors have been developed. Interest in biosensing has evolved from the breadth of potential applications in fields such as clinical diagnosis, environmental monitoring and food quality control (*1*). Compared to traditional analytical techniques, biosensors have several advantages. These sensors possess a high degree of specificity, are easy to handle and can be miniaturized. They display short response times and detection of the analyte of interest can be accomplished without prior sample separation (*2*).

A chemical sensor is a self contained integrated device that transforms a physical quantity into an analytically useful signal, and which in turn provides chemical information ranging from the concentration of a specific sample component to total composition analysis. Chemical sensors usually contain two basic components, a chemical (molecular) recognition system (receptor) and a physico-chemical transducer (*3*). In a biological sensor or *biosensor*, the chemical recognition system is biologically–based and could be an enzyme or enzymes, an antibody, a membrane component, an organelle, a prokaryotic or eukaryotic cell, microorganisms, or living tissues. An important aspect of this two-component (recognition and transduction) portion is the direct spatial contact between the biological recognition medium (bio-receptor) and the transduction element. The recognition layer engages in an interaction with a target substance and produces a signal. Because the bio-receptor is attached directly onto the surface of the transducer, the produced signal can be immediately transformed into a physical quantity which is further processed and modified, resulting in read-out information (*3*, *4*). We note also that biosensors offer a high degree of selectivity and this can be attributed to the specificity of interaction between surface receptor and target substance.

Detection at the transduction site can be achieved using optical, acoustic, calorimetric, piezoelectric or electrochemical methods. Among these, electrochemical detection techniques, the focus of this chapter, tend to be most prevalent and these can further be sub-divided into amperometric, potentiometric, conductometric or impedance (*5*, *6*). The performance of a biosensor is highly dependent on the technique used for immobilization of the bio-receptor. Several techniques are available for this purpose and they include physical adsorption, covalent linkage, affinity immobilization and entrapment (*7*). Although each of these techniques has its own advantages, the choice of method is generally influenced by the intended application (for the biosensor). Other key factors that affect the performance of a biosensor include the following.

i. *Selectivity* – like any other analytical tool, this is the ability of the sensor or biosensor to preferentially recognize the target molecule from a group of molecules referred to as the analytical environment or sample matrix.
ii. *Sensitivity* – the ability of the sensor to dependably and measurably respond to the changes in analyte concentration.
iii. *Stability* – the ability of a sensor or biosensor to reproduce the same magnitude of signal when repeatedly treated with the same concentration

In Interfaces and Interphases in Analytical Chemistry; Helburn, R., et al.;
ACS Symposium Series; American Chemical Society: Washington, DC, 2011.

of analyte over time (operational stability). It can also be evaluated by monitoring sensor sensitivity intermittently over a certain storage period (storage or long term stability). Other forms of stability recently reported are continuous stability where the biosensor is treated with a known concentration of analyte once and its signal degradation is monitored over time.

iv. *Response time* – how fast the signal is generated once the biosensor comes into contact with analytes (time required for the signal to reach at least 95% steady state).

v. *Others* are resistance to fouling or poisoning of the biosensor membrane by other substances present in the analysis media or from reaction with byproducts generated during the enzyme catalyzed conversion of substrate to products.

While many techniques and methods have been developed to address each of the above concerns, rarely does improvement in any one parameter leave another unaffected. The effect could be either positive or negative. For example, it is very hard to improve selectivity (in a sensor or a biosensor) without compromising sensitivity and response time (*8*). This has severely limited practical applications of biosensors in the real analytical environment, *e.g. in vivo* biological systems. This chapter focuses specifically on approaches for crafting the electrode-solution interface, *i.e.* the modification of the electrode surface, so as to improve the selectivity and sensitivity of amperometric biosensors intended for the probing and monitoring of critical physiologic-based analytes such as glucose, lactate, glutamate, nitric oxide (NO) and cholesterol. We explore how attempts to improve sensitivity and selectivity impact analytical performance. In addition, we look at some problems that are encountered during real time applications of these biosensors. We take a review approach with an emphasis on recent trends.

2. Selectivity

The ability of an amperometric biosensor to distinguish a target analyte from other species in a complex matrix is the key to its successful application in real time monitoring. Although the enzyme based reaction may be selective, the signal transduction process is often hampered by the presence of other undesired substances (interferents) and their impact on on the electron transfer pathway. There has been tremendous improvement in developing biosensors that have a reduced response toward these interferences, and a simultaneous increase in selectivity and sensitivity. In the subsequent paragraphs we review some specific techniques that are used to enhance the overall *selectivity* of biosensors. Note, values of *selectivity* are unitless, and for a sensing device (where reported here) they can be interpreted as the concentration of the target analyte that gives the same signal as that of an interferent.

In Interfaces and Interphases in Analytical Chemistry; Helburn, R., et al.;
ACS Symposium Series; American Chemical Society: Washington, DC, 2011.

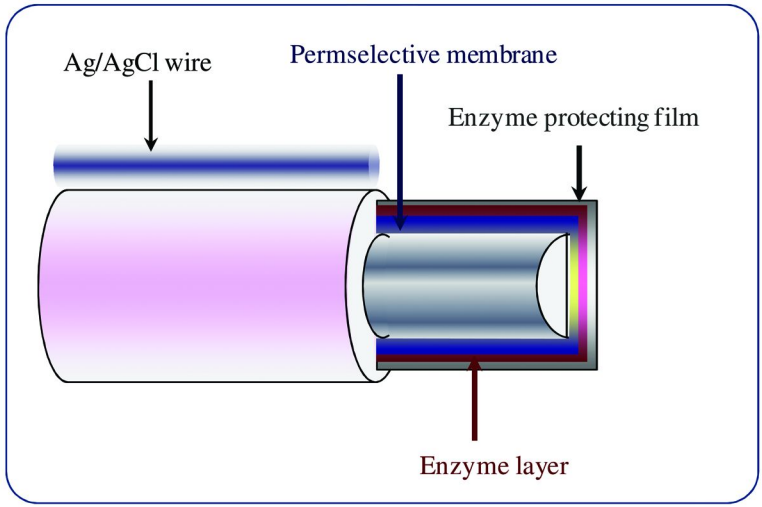

Figure 1. Schematic drawing showing various membranes used in biosensor or sensor fabrication to enhance selectivity. (see color insert)

2.1. Permselective Membranes

Using a permselective membrane is a simple approach that has been widely adopted in designing the front end interface of a biosensor. In principle, different polymers are coated in front or behind the enzyme membrane in layers or multilayers to form a membrane with different transport properties which are then used to distinguish interfering species based on their size, charge or both. Figure 1 is a schematic drawing showing an example of how permselective membranes are incorporated in sensors or biosensors (to enhance selectivity).

2.1.1. Electrostatic Repulsion

Charged interferences can be electrostatically discriminated against by the sensor through introduction, within the sensing matrix, of a membrane that has a charge similar to that of the targeted interferent. Membrane films that function via electrostatic repulsion include Nafion (*9–13*) or 4-vinylpyridine-styrene co-polymer (*14*, *15*). Historically, Nafion, an anionic perfluorinated ionomer, has been effectively used to restrict negatively charged electroactive interferents, such as ascorbate, from accessing the electrode surface. However, the charged sulfonic acid groups on Nafion also concentrate cationic species such as dopamine, serotonin and norepinephrine which are also present in the physiological system and this too can interfere with a measured signal. Another disadvantage with Nafion is that once the electrode tip is inserted in an aqueous medium, it must, at the very least, remain moist. If this membrane is allowed to dry, it will quickly develop cracks that provide an avenue for other chemical interferents to pass

In Interfaces and Interphases in Analytical Chemistry; Helburn, R., et al.;
ACS Symposium Series; American Chemical Society: Washington, DC, 2011.

through. To avoid this, Nafion is commonly used in conjunction with other exclusion layers such those prepared from *o* or *m*-phenylenediamine (*13*).

4-Vinylpyridine-styrene is positively charged membrane film that restricts access of positively charged ions to the sensing surface (*14*). Marcela et. al. developed a bioelectrocatalytic assembly by layering glucose oxidase and different polyelectrolytes via electrostatic layer-by-layer adsorption on a thiolated gold surface (*16*). The multilayer was assembled by sequential deposition of polyethylenimine and Nafion (used as interference barriers) followed by a stabilization of the membrane by polyethylenimine and DNA, and finally co-deposition of glucose oxidase and polyethylenimine as the biocatalytic layer for glucose. The resulting biosensor exhibited excellent analytical performance and fast response time. The authors also demonstrated that electrostatic adsorption by the polyelectrolyte significantly improved selectivity as well as sensitivity of this biosensor.

Volotovsky et al. (*14*) developed a glucose-sensitive ion-selective field-effect transistor biosensor with an additional positively charged membrane which extended the dynamic linear range and also reduced the influence of buffer concentration on the biosensor response. The positively charged functional groups inside the polymeric membrane created a barrier for positively charged ions. By blocking the buffer mediated and facilitated transport of protons out of the enzyme layer, the positively charged polymer membrane increased the sensor response (*14*). Because charged permselective membranes can only discriminate against ions of same charge, overlaid multilayers each with unique properties have often been combined to form a permselective membrane with multiple capabilities. For example, Vaidya and co-workers developed a glucose biosensor using a carbon powder electrode coated with a cellulose membrane and a negatively charged hydrogel layer that was able to remove interferents such as ascorbic acid, bilirubin and l-cystine (*15*). Zhang et al. also combined Nafion and cellulose acetate deposited alternately to eliminate interference by the negatively charged uric acid, ascorbic acid and neutral acetaminophen respectively (*17*).

2.1.2. Size Exclusion

Another commonly used method for eliminating interferents from the biosensing surface is the use of porous permselective membranes that discriminate on the basis of molecular size. Under such arrangement, selectivity is achieved by forming a size exclusive layer that allows smaller molecules such as nitric oxide (NO) and hydrogen peroxide (H_2O_2) to pass through while preventing larger molecules such as ascorbic acid, dopamine, serotonin and 3,4-dihdroxyphenlacetic acid from reaching the recording surface (*8*, *18*, *19*). However, the effect of porous membranes in removing interferents usually depends on the size and uniformity of the membrane pores which in turn is dependent on how the membrane is generated. Generally, electropolymerized films such as poly(phenylenediamine) (*8*, *19–22*), poly(aminophenol) and polyphenol (*17*, *23*) have been demonstrated to be extremely useful in the rejection of interferents based on size exclusion. This is because the electropolymerization process can be controlled to generate

In Interfaces and Interphases in Analytical Chemistry; Helburn, R., et al.;
ACS Symposium Series; American Chemical Society: Washington, DC, 2011.

compact, thin and uniform membranes on large or even extremely small surfaces with complex rugged geometries. While permselective films generated this way often suffer from degradation when used for *in vivo* measurements, they can be reinforced with other additives. For example, Chen et. al. developed an electrochemically generated polyphenol film within a previously electrodeposited glucose oxidase enzyme membrane. The sensor was further coated with a stability enhancing film generated from electrochemically assisted cross-linking of 3-amino-propyl trimethoxysilane (ATS), schematically shown in Figure 2. When this biosensor was coated with the hybrid film it displayed superior selectivity properties towards acetaminophen, ascorbic acid and uric acid. At the same time, sensitivity toward H_2O_2 (the catalytic product of enzymatic glucose oxidation) was compromised, decreasing from 4.75 ± 0.32 nA μM^{-1} (bare Pt) to 0.71 ± 0.04 nA μM^{-1} (Pt/PPH) and finally to 0.58 ± 0.04 nA μM^{-1} (Pt/PPH/ATS) (*23*).

Njagi et. al. have also reported the use of *o*-phenylenediamine in the fabrication of an NO sensor using a platinum microelectrode previously coated with the electron transfer mediator Meldolas blue (*8*). The selectivity of the NO sensor to ascorbic acid, dopamine and serotonin, increased from 0.072(±0.15), 0.016(±0.005) and 2.3(±0.3) to 102(±7.2), 37(±2.6) and 42(±6.5) respectively. But in the absence and presence of *o*-phenylenediamine the *sensitivity* of the microelectrode to NO decreased from 50 to 20 (±2.34) nA μM^{-1} in that order (*8*). Other films that have been used as size exclusion membranes are mercaptosilane (*24*) and cellulose acetate (*25*).

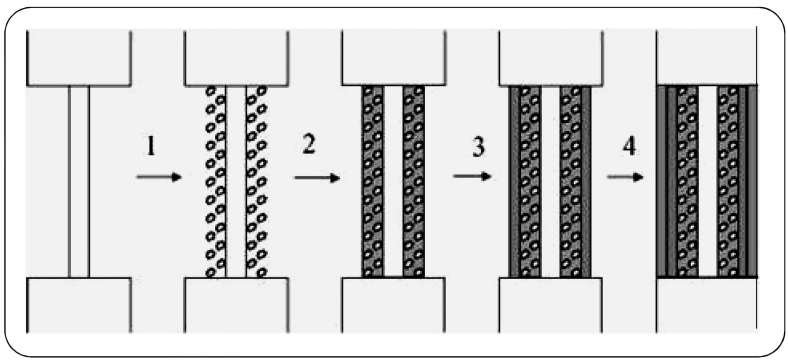

Figure 2. Scheme for the preparation of the glucose oxidase biosensor on a Pt electrode. Step1: electrodeposition of glucose oxidase. Step 2: electropolymerization of phenol. Step 3: electrochemical cross-linking of (3-aminopropyl)trimethoxysilane. Step 4: coating of polyurethane outer membrane. Reproduced with permission from Reference (23).

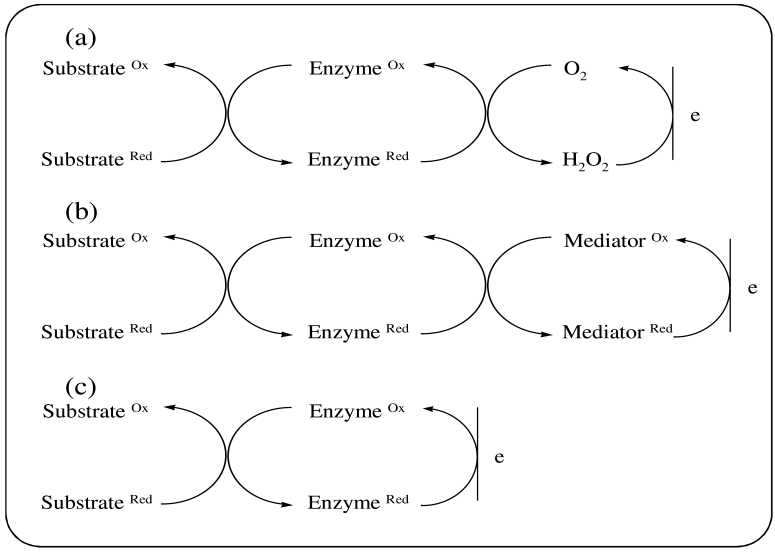

Figure 3. General schematic showing the three configurations of biosensors based on oxidase enzymes. Reproduced with permission from Reference (27).

While the use of permselective membranes in sensors and biosensors has provided researchers with a simple and fast way to block access of interfering species to the electrode surface, several challenges still remain for these membranes to be used *in vivo*. Coating the electrodes with permselective membranes creates a diffusion barrier which increases the response time but reduces the sensitivity of the electrode. Consequently careful optimization is required to determine optimal coating procedures for both exclusion layer and enzyme layer coating (*13*). Modification of the electrodes with Nafion and other non-electropolymerizable permselective membranes is generally achieved through drop coating, spin coating or immersion of the electrode surface to the polymer. In these procedures, membrane pore size and thickness are very difficult to control. In addition, adhesion of the membrane on the electrode surface is very poor. The reproducibility of this deposition process remains a challenge.

2.2. Lowering the Sensor or Biosensor Detection Potential

In the first generation glucose biosensors, such as those designed by Clark and Lyons (*26*), analyte detection was accomplished by monitoring freely diffusing redox-active species, such H_2O_2 and O_2. As an example, Figure 3a shows the surface oxidation of H_2O_2 or reduction of O_2. Specifically, the enzyme integrated prosthetic group (Figure 3a) is regenerated by free diffusion of O_2 while either the decrease in O_2 or increase of the reaction product H_2O_2 is monitored. Because detection is primarily based on the direct reduction of O_2 or oxidation of H_2O_2, high reduction or oxidation potentials respectively are required. Consequently, biosensors in this configuration are not selective because other electrochemically active compounds are also oxidized or reduced at these potentials. Apart from

In Interfaces and Interphases in Analytical Chemistry; Helburn, R., et al.;
ACS Symposium Series; American Chemical Society: Washington, DC, 2011.

use of permselective membranes, other strategies used to address this problem include incorporating in the biosensor an electron transfer mediator that lowers the biosensor operating potential or links the enzyme prosthetic group to the electrode surface to provide direct electrochemical communication as shown in Figures 3(b) and 3(c). Sometimes direct electrochemical communication (1) as well as lowering the potential through use of a mediator (2) are workable options. In this section we look at the methods that are commonly used to improve selectivity in each of these two categories.

2.2.1. Use of Mediators

Figure 3(b) shows the electron transfer mechanism of a mediator-based biosensor system in what is commonly referred to as 'second generation' biosensors. In this set up, an electron transfer mediating compound is incorporated in the biosensor matrix as a redox relay between the enzyme and the electrode surface. These biosensors involve two electrode processes: (1) enzymatic transformation of the substrate to the first redox form the mediator and (2) re-oxidation of the mediator at the electrode surface. In this case, the transduction signal, which is directly proportional to substrate concentration, is determined by the oxidation or reduction current of the mediator. Because second generation biosensors operate at the redox potential of the mediator, the operating potential of these sensors is lowered, hence, eliminating the problem of simultaneous oxidation or reduction of interfering species.

Before a mediator can be used in a biosensor it must satisfy the following criteria (*2*, *28*, *29*):

- provide fast electron transfer between the electrode and the enzyme prosthetic group.
- be stable in its reduced and oxidized states.
- offer the possibility of achieving strong attachment to the biosensor architecture.
- have high value of the second order rate constant for electron transfer to minimize competition with O_2.
- have low solubility in the analysis medium.
- be non-toxic to the enzyme and analysis environment.

Mediators can be classified into the following groups, as discussed below.

2.2.1.1. Metal Complexes

These mediators are primarily transition metal organometallic compounds. Examples include ferrocene derivatives, $K_4[Fe(CN)_6]$ (*30*, *31*), ruthenium or osmium complexes (*32–34*), metal porphyrins (*35*) and cobalt phthalocyanine (*36*). As an example, a "wired" enzyme biosensor for amperometric detection of glucose and lactate was constructed by immobilizing the enzymes in an

In Interfaces and Interphases in Analytical Chemistry; Helburn, R., et al.;
ACS Symposium Series; American Chemical Society: Washington, DC, 2011.

osmium-based three-dimensional hydrogel that electrically connected the enzyme redox centers with the electrode (*37*). The enzyme "wiring" hydrogel was constructed by cross-linking poly(1-vinylimidazole) complexed with Os-(4,4'-dimethylbpy)$_2$Cl and poly-(ethylene glycol) diglycidyl ether. The biosensor exhibited negligible electro-oxidation currents from acetaminophen, ascorbate, urate and L-cysteine.

In other studies a porphyrin-based NO sensor was fabricated by electrodepositing manganese porphyrin / polypyrrole films onto a platinum electrode (*38*). After coating the sensor with a permselective membrane, the resulting probe exhibited reasonable selectivity toward the negatively charged ascorbate, nitrite (NO_2^-) and nitrate (NO_3^-) which coexist with NO in the physiological system.

A glutamate biosensor based on Prussian blue, "artificial peroxidase," as a transducer for H_2O_2 has been reported (*39*). The Prussian blue electrocatalyst was selective toward H_2O_2 reduction in presence of O_2 at 0 V. However, the biosensor was also coated with an electrostatic repulsion layer Nafion to aid in rejection of other interferences. This biosensor was capable of discriminating among D-glutamic acid, D,L-aspartate, acetaminophen and ascorbic acid in the presence of L-glutamate.

2.2.1.2. Organic Dyes

Organic dyes such as methylene blue (*40*, *41*), toluidine blue (*42*), Meldola's blue (*43*, *44*), methylene green (*45*, *46*), methyl viologen (*10*, *47*), azure (*48*), and others are reported mediators that have been used in biosensors to either directly catalyze reduction of H_2O_2 or decrease the redox potential of the co-enzyme nicotinamide adenine dinucleotide (NAD). For example, Vasillescu et al. electropolymerized Meldola's blue onto a screen printed electrode to form versatile glucose biosensors for H_2O_2 and NADH. In its optimized form, the biosensor reduced the catalytic detection of H_2O_2 to -0.1V. The electrocatalytic oxidation of NADH was 0 V (*44*).

Liu et al. developed an H_2O_2 detecting biosensor by co-immobilizing horseradish peroxidase and methylene green onto a zeolite modified glassy carbon electrode. In the presence of glucose, the biosensor exhibited good selectivity toward L-lactate, uric acid, ascorbic acid, galactose, L-cysteine, L-glutamic acid and any other amino acid tested (*46*). Other organic compounds that have been used as mediators include sulphur compounds *e.g.* tetrathiafulvalene (TTF) (*49*) and quinones such tetracyanoquinodimethane (TCNQ) (*50*).

2.2.1.3. Conducting Organic Salts

The conducting organic salt tetrathiafulvalene-tetracyanoquinodimethane (TTF-TCNQ) has been extensively used in biosensors as a mediator (*51–53*). Zhijun and co-workers developed a third generation glucose biosensor by immobilizing horseradish peroxidase on an Au electrode modified with a

nanocomposite film of TTF-TCNQ and multiwalled carbon nanotubes (MWCNTs) (*52*). The TTF-TCNQ / MWCNTs nanocomposite reduced the H_2O_2 reduction potential from 0.6V to 0 V. The biosensor exhibited a linear concentration range of 0.005 – 1.05 mM and a detection limit of 0.5μM for glucose.

Palmisano and Zambonin developed a third generation disposable glucose biosensor by immobilizing glucose oxidase on TTF-TCNQ, synthesized in situ onto an overoxidized polypyrrole film. By direct complete re-oxidation of enzyme on the surface of TTF-TCNQ crystals, the dependence of the biosensor on O_2 was completely eliminated. The overoxidized polypyrrole film served to eliminate the sensor's response to various interferents (*54*). The sensor's response to the most common interferents ascorbate, urate, cysteine and paracetamol at their physiological concentrations was negligible.

Although mediator based biosensors can effectively avoid other coexisting oxidzable interfering species by lowering the electrode potential, their redox potential may still overlap with that of O_2. In addition, O_2 can also compete with mediators thus interrupting the cascade of the redox process occurring at the electrode surface. Moreover, interferents such as ascorbic acid can actually reduce a mediator during the redox cascade, resulting in a compromised biosensor *sensitivity* (*55*). Mediators may also leach from the sensor surface into the adjacent solution and this can cause significant sample contamination, unforeseeable deterioration and instability problems. It therefore remains difficult to use a mediator approach alone to remove most interference due to easily oxidizable species (*27*). A more promising approach, in lieu of redox mediators for the removal of most sources of interference in an enzyme based biosensor, would be to covalently attach an electron relay between the enzyme prosthetic group and electrode, and this gives birth to 'third generation' biosensors as shown in Figure 3(c).

2.2.2. Direct Electron Transfer between Electrode and Enzyme

Direct electrochemical communication between the enzyme prosthetic group and the electrode surface eliminates interferences by providing for direct electron transfer (DET). DET avoids intermediate electron transfer steps arising from self-exchange reactions, which are prone to interference. However, DET is only applicable to those enzymes that are in very close proximity to the electrode surface, preferably the first monolayer and those that do not have the prosthetic group buried deeply within the proteic structure. Thus, DET is possible only for small enzymes whose prosthetic groups are easy to access. The enzyme active site group can also be covalently bound to a redox mediator or to a conducting polymer, generating the so-called "electroenzymes". In this context Willner et. al. developed an electron transfer gold nanoparticle (Au-NP), *i.e.* or an electron relay to improve the enzyme-electrode contact of glucose oxidase (*56*) (Figure 4). The authors used a dithiol linker to attach a carboxylic acid functionalized Au-NP onto the Au electrode. They then covalently attached the aminoethyl-modified flavin adenine dinucleotide (FAD) to the Au-NP and reconstituted the apo-glucose onto the FAD-functionalized Au-NPs as shown in Figure 4. The Au-NP acted

In Interfaces and Interphases in Analytical Chemistry; Helburn, R., et al.;
ACS Symposium Series; American Chemical Society: Washington, DC, 2011.

as a nanoelectrode as well as a relay unit to transport electrons from the FAD center to the Au-electrode, thus activating the bioelectrocatalytic activity of the glucose oxidase. In other studies, DET between glucose oxidase immobilized on boron doped carbon nanotubes on glassy carbon (CNT/GCE) has been reported. In the presence of glucose, the electrode exhibited a sensitivity of 111.57 μA mM^{-1} cm^{-2} and a detection limit of 10 μM, for glucose. The sensor also exhibited good stability and excellent selectivity toward uric acid and ascorbic acid (*57*). Another reagentless glucose oxidase biosensor was constructed based on DET of the enzyme immobilized on CNT/GCE using a chitosan film. The biosensor was very selective toward common blood-based interferences, *e.g.* ascorbic acid, uric acid and acetaminophen (*58*). It should be noted that despite the availability of biosensors that exploit DET in their mode of analyte detection, these biosensors have not, to date, been used for *in vivo* applications.

2.3. Combining Permselective Membranes and Mediators

One of the drawbacks of mediator based biosensors in combating problems with selectivity is that they can actually extend electrocatalytic activity to that of the interferents. To address this problem, mediators are often used together with permselective membranes such as Nafion or polyethylenediamine. As an example, a glutamate biosensor was constructed by cross-linking glutamate oxidase onto a GCE that was chemically modified with Nafion (as the permselective membrane) and methyl-viologen (as the mediator) (*10*). This biosensor turned out to be highly selective toward ascorbic acid, uric acid, acetaminophen and 20 mM of 15 different amino acids (L-isoleucine, L-leucine, L-methionine, L-phenylalanine, L-proline, L-tryptophane, L-valine, L-asparagine, L-glycine, L-serine, L-threonine, L-arginine, L-histidine, L-lysine and L-aspartic acid). While methyl viologen provided electrocatalytic activity to the enzyme reaction product H_2O_2, Nafion served to eliminate the other interferents whose electrocatalytic activity could have been enhanced by methyl viologen with a possible consequence of decreasing biosensor selectivity.

Another common strategy used for improving biosensor selectivity is co-immobilization of horseradish peroxidase (HRP) with other H_2O_2 based enzymes, *e.g.* glucose oxidase (GOx) or glutamate oxidase (GlOx), in the presence of mediators. This technique removes biosensor dependence on O_2. For example a glucose biosensor utilizing HRP and GOx immobilized in a poly (toluidine blue O) film was constructed on a MWCNT modified GCE (*59*). In the presence of O_2, the role of HRP was to detect H_2O_2, while that of HRP+GOx was to detect glucose. In the absence of O_2, glucose oxidation proceeded via electron transfer between GOx mediated by poly(toluidine blue O). This biosensor exhibited excellent selectivity to ascorbic acid, uric acid and acetaminophen. In the presence of O_2, the biosensor exhibited a sensitivity of 113 mA M^{-1} cm^{-2} and a linear concentration range of 0.1 to 1.2 mM. A major drawback of this biosensor is that its linear range is below the normal physiological level of glucose of between 4 mM to 5 mM. If the biosensor was to be used for glucose determination in physiological systems, it would respond as though the glucose level was low because of its short linear range.

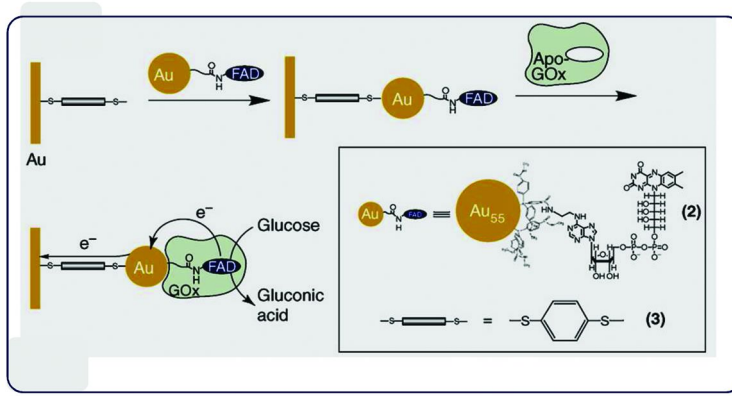

Figure 4. Electrical wiring of glucose oxidase with an electrode by gold nanoparticles. Electrical contacting of glucose oxidase (GOx) by the reconstitution of apo-GOx on FAD-functionalized gold NPs (2) linked to an electrode by dithiol (3) bridges. Reproduced with permission from Reference (56). (see color insert)

In other studies, selectivity *and* sensitivity of glutamate biosensors fabricated either by immobilizing GlOx on Pt, Au, Pd and GCE electrodes coated with permselective membranes poly (*o*-phenylenediamine) (PPD) or HRP redox polymer (Os^{2+}- polyvinylpyridine) (Os^{2+}-PVP/HRP) to ascorbic acid and 4-methylcatechol were compared (*60*). While the electrodes coated with PPD showed high selectivity, their sensitivity to glutamate dropped significantly. On the other hand Os^{2+}-PVP/HRP electrodes displayed greater sensitivity than the PPD modified electrodes except for the Pt electrodes which had similar sensitivity.

2.4. Coating with an Interference Pre-Oxidizing Layer

Another way to eliminate interfering species in a biosensor would be to coat the outer sensing surface with a pre-oxidizing layer that converts the electroactive interferent into an electrochemically inactive form before it reaches the electrode surface. For example, in removing ascorbic acid, a popular approach is to coat the electrode with the enzyme ascorbate oxidase (AsOx) which catalyzes the oxidation of ascorbic acid to dehydroascorbic acid and H_2O as shown in the reaction (Eqn 1) below.

$$\text{L-ascorbic acid} + \tfrac{1}{2}\,O_2 \xrightarrow[\text{Oxidase}]{\text{Ascorbate}} \text{dehydroascorbic acid} + H_2O \qquad \textit{(Eqn. 1)}$$

A layer-by-layer assembly of alternating GOx and AsOx on a platinum electrode was reported as a glucose biosensor with capability of detecting glucose in the presence of ascorbic acid (*61*). The GOx/AsOx enzyme multilayer biosensor was useful for determining the normal level of glucose (5 mM) in the presence of a physiological level of ascorbic acid (0.1 mM) at a potential of 0.6 V. However, the catalytic activity of AsOx was inherently unstable, and hence, the

In Interfaces and Interphases in Analytical Chemistry; Helburn, R., et al.;
ACS Symposium Series; American Chemical Society: Washington, DC, 2011.

biosensor was only stable for about 10 days. Stability problems and limitations in selectivity toward other physiologically present interferences, *e.g.*, NO, uric acid, dopamine and other catecholamines, are the technical challenges that *could* be met with this biosensor, for real time *in vivo* measurements. Although the approach of co-immobilizing AsOx with other enzymes to remove ascorbic acid has been reported for glutamate and glucose biosensors, a similar approach utilizing the enzyme uricase to remove uric acid has not yet been reported.

Another strategy for removing interferents via pre-oxidization has been the use of strong oxidant metal oxides such as MnO_2 and PbO_2 (*62*). For example, a disposable glucose biosensor was fabricated by immobilizing glucose oxidase on a PbO_2 modified nitrocellulose strip (*63*). This biosensor was shown to be practically in-susceptible to acetaminophen, uric acid and ascorbic acid. Choi et. al. utilized PbO_2 to fabricate a glucose biosensor which was highly selective toward physiological concentrations of uric acid, acetaminophen and ascorbic acid (*62*). In their studies they investigated MnO_2, CeO_2 and BaO_2. However, only PbO_2 was found to have superior pre-oxidizing ability, relative to the other metal oxides. In their work, the metal oxide powders were mixed with polymers and the mixture was dispersed over an enzyme membrane to form the 'interference oxidant membrane'. In tests of these systems, MnO_2 was not only found to oxidize the interferents but also the analytes hence diminishing the glucose signal. This was caused by migration of the MnO_2 particles from the outside of the enzyme membrane to the inside where it decomposed the enzymatically generated H_2O_2. In an attempt to improve on this situation, Hu et. al. distributed MnO_2 nanoparticles in a chitosan solution and electrodeposited the composite onto the electrode to form a more stable oxidant membrane (*64*). The MnO_2 containing chitosan was able to effectively remove ascorbic acid while minimally interfering with the glucose signal.

Recently, a cholesterol biosensor was fabricated by immobilizing cholesterol oxidase onto a sol-gel derived nano-structured CeO_2 film which was then deposited onto an indium tin oxide (ITO) glass electrode (*65*). The response of this biosensor to cholesterol was not significantly affected by the presence of glucose, uric acid and ascorbic acid.

Metal oxides have also been combined with permselective membranes such as Nafion and MWCNTS to construct a glucose biosensor with excellent anti-interferent properties toward uric acid and ascorbic acid (*66*). In this proposed biosensor, Baby and Ramaprabhu (*66*) describe core–shell Fe_3O_4 / SiO_2 / MWNT nanoparticles that are prepared by growing silica layers onto a surface of the Fe_3O_4/MWNTs. The Fe_3O_4 / SiO_2 / MWNT nanoparticles are then dispersed in Nafion and coated onto a glassy carbon electrode (GCE). Finally glucose oxidase is deposited onto the Fe_3O_4 / SiO_2 /MWNT / GCE and allowed to dry before testing.

2.5. Working at the Electro-Reduction Potential

For many biosensors whose enzyme transduction molecule is H_2O_2, *e.g.* those for glucose and lactate, a common strategy to ward off interferences is to incorporate into the sensing architecture a material that can aid in detection of

In Interfaces and Interphases in Analytical Chemistry; Helburn, R., et al.;
ACS Symposium Series; American Chemical Society: Washington, DC, 2011.

H_2O_2 at its reduction potential. Such strategies include use of metalized carbon or incorporation of single walled carbon nanotubes (SWCNTs) or MWCNTs in the biosensor configuration. For example, metalized carbon transducers can catalyze reduction of H_2O_2 at a potential of around 0.0 V where many interferences are electrochemically silent. Wang et. al. (*67*) have designed a highly selective amperometric glucose biosensor using rhodium-dispersed carbon paste/glucose oxidase electrodes. The dispersed rhodium particles exhibited efficient and preferential electrocatalytic activity towards H_2O_2 and allowed cathodic detection of the glucose substrate at -0.10 V (*67*). This biosensor was electrochemically inert to physiological levels of ascorbic acid, uric acid, acetaminophen, salicylic acid, tyrosine, urea, galactose, and glutathione. Elsewhere, Pt nanoparticles (Pt-nano) were combined with MWCNTs to fabricate a *sensitivity* enhanced electrochemical lactate biosensor. The Pt-nano / MWCNTs composite was dispersed on a GCE, and L-lactate oxidase was immobilized via adsorption. The biosensor displayed excellent anti-interferent ability (*68*).

2.6. Self Referencing

Self referencing is emerging as a common tool for increasing selectivity in many sensing and biosensing systems. In this scenario, two working electrodes are fabricated in a similar way such that one responds to all possible species including the analyte while the other responds to all interfering species present in the system but *not* the analyte. The difference between the two signals is the signal due to the analyte. As an example in the detection of glutamate, this approach has been applied with a high degree of resulting selectivity. This specific biosensor employed a combination of carbon nanotubes (CNTs) for the interferent-responsive electrode and CNTs with glucose oxidase for the analyte-responsive electrode (*69*).

A classic example of sensors in the self-referencing group is the presently used glucose monitor test strip. Early glucose monitors depended on measuring current from oxidation of H_2O_2 as shown in Equations 2-3 below. These early devices were overwhelmed with problems due to interfering species and to their dependence on O_2 present in the reaction medium.

$$\beta\text{-D-glucose} + \tfrac{1}{2}\,O_2 \xrightarrow[Oxidase]{Glucose} \beta\text{-D-gluconic acid} + H_2O_2 \qquad \textit{(Eqn. 2)}$$

$$H_2O_2 \xrightarrow{0.6\ V} O_2 + 2H^+ + 2e^- \qquad \textit{(Eqn. 3)}$$

To minimize the dependence of sensor response toward O_2, these modified electrodes were initially fitted with mediators so that rather than measuring the oxidation current from produced H_2O_2, the reduction current for the mediator was measured, which would be directly proportional to concentration of reacted mediator which in turn would be proportional to glucose concentration (see Equations 4 and 5 below).

$$\beta\text{-D-glucose} + \text{mediator (Ox)} \xrightarrow[\text{Oxidase}]{\text{Glucose}} \beta\text{-D gluconic acid} + \text{mediator (Red)} + 2H^{+} \quad \textit{(Eqn. 4)}$$

$$\text{mediator (red)} \xrightarrow[\text{working electrode}]{-e^{-}} \text{mediator (ox)} \quad \textit{(Eqn 5)}$$

While this latter approach (Equations 4-5) addressed the problem of sensor dependence on O_2, it did not solve the problem of sensor response to interferents such as ascorbic acid, acetaminophen and uric acid which are also present in the blood stream. To address this, the test strip of the present-day glucose monitor has two working electrodes (electrode 1 and electrode 2) and one Ag/AgCl reference electrode as shown in Figure 5.

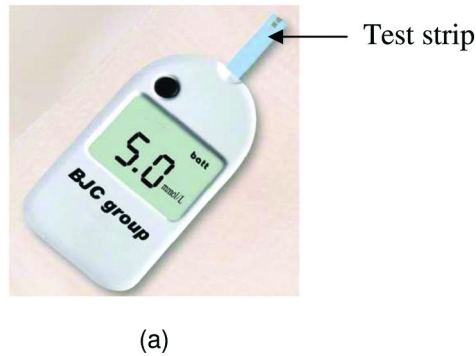

(a)

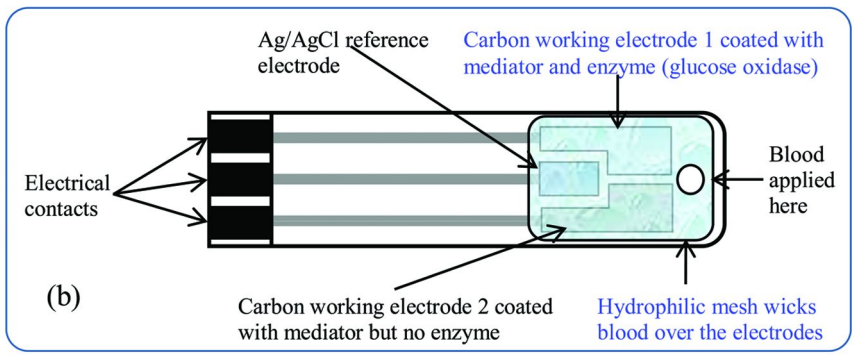

Figure 5. (a) Glucose monitor fitted with a glucose disposable test strip. (b) Details of a disposable glucose test strip to which blood is applied. Reproduced from Reference (70) with permission. (see color insert)

Figure 5 shows that electrode 1 is fitted with glucose oxidase and a mediator while the surface of electrode 2 contains the mediator only. Thus, all the interfering species and glucose are reduced at electrode 1 while only interferents are reduced at electrode 2. Thus, the current due to glucose is the current at electrode 1 minus the current at electrode 2. The main challenge here is to fabricate the test strips in a reproducible manner. Many of these biosensor architectures that involve a self referencing approach work at positive potentials. Consequently, the design presented here (Figure 5) would only be applicable to analytes such as glucose, glutamate and lactate that are electrochemically inert at those positive operation potentials.

In yet another example, a polypyrrole glucose biosensor, free of interferents, was constructed with a four electrode cell consisting of: (1) a polypyrrole film electrode, (2) a polypyrrole-glucose electrode, (3) a counter electrode and (4) a reference electrode (*71*). The catalytic current due to glucose oxidase was obtained from the difference between the response currents of the two polypyrrole working electrodes (*71*).

3. Sensitivity

Sensitivity refers to the ability an analytical system to respond reliably and in a measurable manner to changes in analyte concentration (*70*). In many sensors or biosensors, sensitivity is only useful within the linear range (of the calibration) and is also sometimes given as slope of that plot as described in the Equation 6 below.

$$\textit{Sensitivity} = \frac{\textit{Change in signal (current, potential etc)}}{\textit{Change in analyte concentration}} \qquad \textit{(Eqn. 6)}$$

Increasing a sensor's sensitivity involves improving electron transfer between the target redox substance and the electrode surface. This can be done by incorporating in the sensing or biosensing membrane a material that serves to enhance the rate of electron transfer between the target redox species and the electrode surface. Such incorporation works by limiting diffusional constraints on a redox species and / or the ability of e^- to reach the electrode surface. Response time is also improved. Yet these tactics do not necessarily result in better interference exclusion.

Materials incorporated in the sensor or biosensor membrane for the purpose of enhancing heterogeneous electron transfer can operate by creating electron conduction pathways or electron relays. Several such materials that have been explored include metal nanoparticles (*72–74*), nano-rods, nanofibers (*75*), carbon nanotubes (*76*) and conducting polymers (*77–79*). Sometimes, combinations of two or more of these materials where each plays a different role are used, and when this occurs the film is referred to as nanocomposite (*7*, *80*, *81*). Every so often electron mediators are also employed as electron relays, as shown schematically (Figures 6a-c).

Ren and co-workers developed a simple procedure for fabricating a glucose biosensor with improved sensitivity (*82*). This modified sensor was constructed

by forming a sol-gel of GOx and Ag nanoparticles on a Pt electrode. The film was then coated with polyvinyl butyral (PVB). In the presence of the Ag nanoparticles, the biosensor sensitivity increased 10 times and response time improved dramatically. This was attributed to improved electron transfer between the GOx co-factor FAD and the electrode due to the presence of the Ag nanoparticles (see Figure 6a). Metal nanoparticles may not only improve biosensor sensitivity by simply providing an accelerated electron shuttle to and from the electrode surface but they can also contribute to the catalytic or mediating effect on the analyte. For example CeO_2/TiO_2 nanoparticles were found to catalytically improve the sensitivity of a dopamine biosensor fabricated with tyrosinase (*83*). This dopamine biosensor was used for *in vivo* monitoring of dopamine produced in the striatum of anesthetized male Sprague rats, where it was found to be also highly selective toward ascorbic acid, uric acid, serotonin, norepinephrine, epinephrine and L-3,4-dihydroxy phenylalanine (L-DOPA).

Another example of a glucose biosensor in which a conducting polymer significantly improved sensitivity and response time (see Figure 6b) has been presented by Ramanavicius et. al. (*84*) In their work, glucose oxidase was encapsulated within polypyrrole and the combined matrix then immobilized via adsorption on carbon rod electrodes. As a control, free GOx was immobilized (on carbon rod) by cross-linking with glutaraldehyde. In the presence of polypyrrole the sensitivity of the GOx biosensor, including the apparent Michaelis constant ($K_{M(apparent)}$), both increased 10 fold. This improved performance was attributed to enhanced electron transfer in the presence of the conducting polymer polypyrrole.

Sánchez-Obrero et. al. investigated various combinations of poly(vinyl chloride (PVC), TTF-TCNQ, GOx and Au colloid (Au_{coll}) nanoparticles on the sensitivity of a glucose biosensor (*85*). GOx was immobilized by crosslinking with glutaraldehyde. It was found that the electrode fabricated by incorporating Au_{coll} within the PVC/TTF-TCNQ matrix (PVC/TTF-TCNQ-Au_{coll}) exhibited higher sensitivity to glucose than that fabricated by immobilizing GOx and Au_{coll} on a PVC/TTF-TCNQ electrode. In the presence of Au_{coll}, the biosensor sensitivity was 45 ± 0.5 mA M^{-1} while in the absence of the gold colloids, the sensitivity was 3.5 ± 0.4 mA M^{-1} which is one order of magnitude lower. In other studies it was found that incorporating Au nanoparticles in a polypyrrole polymer improved the sensitivity of the GOx biosensor over others reported in literature (*81*). In this case a generic method was developed for immobilizing enzymes in a chemically synthesized gold polypyrrole (Au-PPY) composite in which Au nanoparticles were sequestered in the PPY polymer. When it comes to providing electron transfer pathways (*i.e.* electron relays), nanorods, nanowires and nanotubes would work in a manner similar to nanoparticles. They too can be incorporated into conductive polymers or combined with nanoparticles to form nanocomposites with similar functions.

Sensitivity in sensors or biosensors can also be improved by direct electron communication between an enzyme prosthetic group and the electrode surface as in third generation biosensors. Although these are the most selective of biosensors they too can suffer from sensitivity problems especially in cases where the enzyme's active site is buried deep within the protein globule. The sensitivity of these biosensors can also be improved by incorporating nanomaterials (*86*),

nanocomposites or polymers into the biosensor matrix to provide a conduit for faster electron transfer. However these direct-electron- transfer bio-sensing devices are still at the developmental stage and are yet to be realized for real time measurements in physiological systems because the environment can significantly alter their performance.

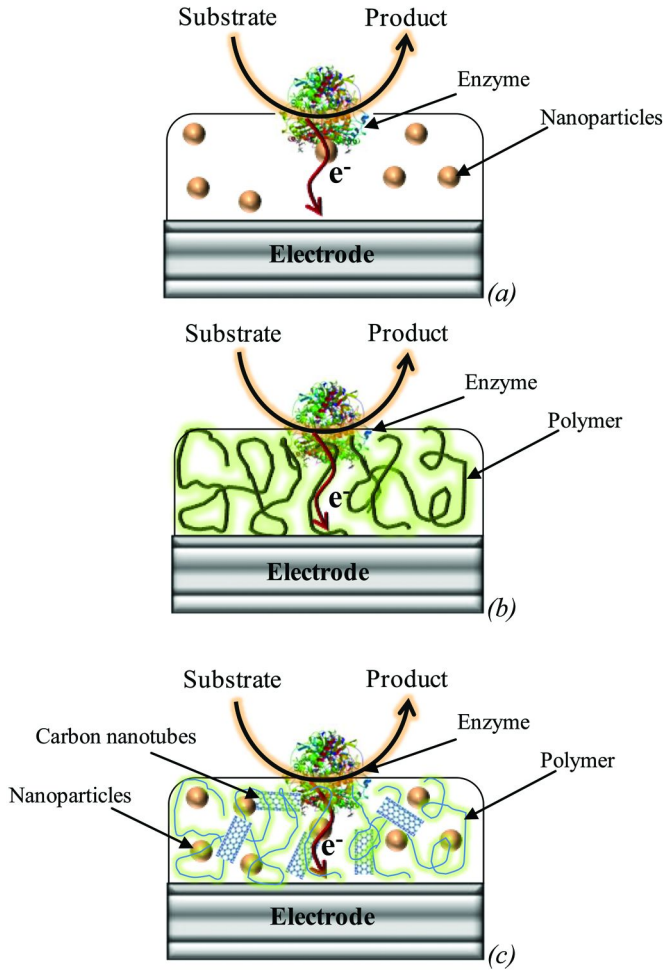

Figure 6. Schematic representation of electron relay between nanoparticles (a), conducting polymers which can also be mediators (b) and nanocomposites (c). (see color insert)

In Interfaces and Interphases in Analytical Chemistry; Helburn, R., et al.;
ACS Symposium Series; American Chemical Society: Washington, DC, 2011.

4. Other Challenges

An additional challenge for all sensors and biosensors in real time physiological applications involves designing them in such a way that they mimic the environment in which they are implanted. Just like any other foreign body, when a sensing device is implanted it will evoke a physiological inflammatory response resulting in the formation of a dense avascular collagen capsule around the electrode (*87*). When this occurs, biosensor sensitivity is reduced and response time is increased due to diffusion constraints of the analyte to and from the capsule wall. Moreover, the materials used to enhance the performance of the sensor or biosensor (such as mediators) may leach around the implantation site causing other unintended consequences.

5. Concluding Remarks and Future Perspective

Sensors and biosensors have revolutionalized the field of analytical chemistry in that they have provided an interface between the universally accepted but complicated classical analytical procedures and simple screening tools. They have also provided the ability for continuous real time measurement especially in physiological environments, affording opportunity for therapeutic intervention in the pathology of physiological conditions such as ischemia, Parkinson's disease and schizophrenia. However, sensors and biosensors in physiological applications still have significant challenges that need to be addressed before they can be reliably used as analytical tools that fully aid the decision making process with respect to physiopathology. For example even though the glucose monitor is a success story of a biosensor that has been utilized as a diagnostic tool, there is concern that the currently allowed 20 % error on the part of these monitors is too lenient and can lead to ambiguity in the self diagnosis of blood sugar levels where the measurement lies on a border line.

This chapter has provided an overview of some of the physical / chemical surface modification techniques that are used in the enhancement of selectivity and sensitivity of sensors and biosensors. It has further highlighted concerns and challenges that come with each of those techniques. With continued research in this field we could see new classes of sensors and biosensors used for identifying and quantifying a large diversity of analytes with applications in clinical diagnosis, quality control, or environmental monitoring. Nonetheless, while several real-time sensors have been reported in literature, their implementation into routine reliable functional devices still remains a great challenge.

Acknowledgments

I wish to thank Dr. Boniface Mailu for his useful and thorough suggestions in the writing of this chapter.

References

1. Amine, A.; Mohammadi, H.; Bourais, I.; Palleschi, G. *Biosens. Bioelectron.* **2006**, *21*, 1405–1423.
2. Castillo, J.; Gáspár, S.; Leth, S.; Niculescu, M.; Mortari, A.; Bontidean, I.; Soukharev, V.; Dorneanu, S. A.; Ryabov, A. D.; Csöregi, E. *Sens. Actuators, B* **2004**, *102*, 179–194.
3. Thévenot, D. R.; Toth, K.; Durst, R. A.; Wilson, G. S. *Biosens. Bioelectron.* **2001**, *16*, 121–131.
4. Andreescu, S.; Marty, J.-L. *Biomol. Eng.* **2006**, *23*, 1–15.
5. Chaubey, A.; Malhotra, B. D. *Biosens. Bioelectron.* **2002**, *17*, 441–456.
6. Pearson, J. E.; Gill, A.; Vadgama, P. *Ann. Clin. Biochem.* **2000**, *37*, 119–145.
7. Andreescu, S.; Njagi, J.; Ispas, C.; Victor, E.; Manoj Kumar, R.; Ozlem, Y. In *The New Frontiers of Organic and Composite Nanotechnology*; Elsevier: Amsterdam, 2008, pp 355−394.
8. Njagi, J.; Erlichman, J. S.; Aston, J. W.; Leiter, J. C.; Andreescu, S. *Sens. Actuators, B* **2010**, *143*, 673–680.
9. Choi, H. N.; Han, J. H.; Park, J. A.; Lee, J. M.; Lee, W. Y. *Electroanalysis* **2007**, *19*, 1757–1763.
10. Maalouf, R.; Chebib, H.; Saïkali, Y.; Vittori, O.; Sigaud, M.; Jaffrezic-Renault, N. *Biosens. Bioelectron.* **2007**, *22*, 2682–2688.
11. Pan, S.; Arnold, M. A. *Talanta* **1996**, *43*, 1157–1162.
12. Yang, L.; Ren, X.; Tang, F.; Zhang, L. *Biosens. Bioelectron.* **2009**, *25*, 889–895.
13. Hascup, K. N.; Rutherford, E. C.; Quintero, J. E.; Day, B. K.; Nickell, J. R.; Pomerleau, F.; Huettl, P.; Burmeister, J. J.; Gerhardt, G. A. In *Electrochemical Methods for Neuroscience*; Michael, A. C., Borland, L. M., Eds.; CRC Press: Boca Raton, FL, 2007.
14. Volotovsky, V.; Soldatkin, A. P.; Shul'ga, A. A.; Rossokhaty, V. K.; Strikha, V. I.; El'skaya, A. V. *Anal. Chim. Acta* **1996**, *322*, 77–81.
15. Vaidya, R.; Wilkins, E. *Med. Eng. Phys.* **1994**, *16*, 416–421.
16. Marcela, C. R.; Gustavo, A. R. *Electroanalysis* **2004**, *16*, 1717–1722.
17. Zhang, Z.; Liu, H.; Deng, J. *Anal. Chem.* **1996**, *68*, 1632–1638.
18. Friedemann, M. N.; Robinson, S. W.; Gerhardt, G. A. *Anal. Chem.* **1996**, *68*, 2621–2628.
19. McMahon, C. P.; O'Neill, R. D. *Anal. Chem.* **2005**, *77*, 1196–1199.
20. Malitesta, C.; Palmisano, F.; Torsi, L.; Zambonin, P. G. *Anal. Chem.* **1990**, *62*, 2735–2740.
21. Palmisano, F.; Guerrieri, A.; Quinto, M.; Zambonin, P. G. *Anal. Chem.* **1995**, *67*, 1005–1009.
22. Sasso, S. V.; Pierce, R. J.; Walla, R.; Yacynych, A. M. *Anal. Chem.* **1990**, *62*, 1111–1117.
23. Chen, X.; Matsumoto, N.; Hu, Y.; Wilson, G. S. *Anal. Chem.* **2002**, *74*, 368–372.
24. Jung, S.-K.; Wilson, G. S. *Anal. Chem.* **1996**, *68*, 591–596.
25. Sternberg, R.; Bindra, D. S.; Wilson, G. S.; Thevenot, D. R. *Anal. Chem.* **1988**, *60*, 2781–2786.

26. Clark, L. C.; Lyons, C. *Ann. N. Y. Acad. Sci.* **1962**, *102*, 29–45.
27. Njagi, J. I. Clarkson University, Potsdam, 2009.
28. Ivanova, E.; Schuhmann, W.; Ryabov, A. *J. Anal. Chem.* **2009**, *64*, 404–409.
29. Wang, J. *Chem. Rev.* **2007**, *108*, 814–825.
30. Muguruma, H.; Kase, Y.; Uehara, H. *Anal. Chem.* **2005**, *77*, 6557–6562.
31. Schuhmann, W.; Ohara, T. J.; Schmidt, H. L.; Heller, A. *J. Am. Chem. Soc.* **1991**, *113*, 1394–1397.
32. Hogan, C. F.; Forster, R. J. *Anal. Chim. Acta* **1999**, *396*, 13–21.
33. Kulagina, N. V.; Shankar, L.; Michael, A. C. *Anal. Chem.* **1999**, *71*, 5093–5100.
34. Trudeau, F.; Daigle, F.; Leech, D. n. *Anal. Chem.* **1997**, *69*, 882–886.
35. Vago, J. M.; Campo Dall'Orto, V.; Forzani, E.; Hurst, J.; Rezzano, I. N. *Sens. Actuators, B* **2003**, *96*, 407–412.
36. Ozoemena, K. I.; Nyokong, T. *Electrochim. Acta* **2006**, *51*, 5131–5136.
37. Ohara, T. J.; Rajagopalan, R.; Heller, A. *Anal. Chem.* **1994**, *66*, 2451–2457.
38. Diab, N.; Schuhmann, W. *Electrochim. Acta* **2001**, *47*, 265–273.
39. Karyakin, A. A.; Karyakina, E. E.; Gorton, L. *Anal. Chem.* **2000**, *72*, 1720–1723.
40. Silber, A.; Hampp, N.; Schuhmann, W. *Biosens. Bioelectron.* **1996**, *11*, 215–223.
41. Yao, H.; Li, N.; Xu, S.; Xu, J.-Z.; Zhu, J.-J.; Chen, H.-Y. *Biosens. Bioelectron.* **2005**, *21*, 372–377.
42. Boguslavsky, L. I.; Geng, L.; Kovalev, I. P.; Sahni, S. K.; Xu, Z.; Skotheim, T. A.; Laurinavicius, V.; Persson, B.; Gorton, L. *Biosens. Bioelectron.* **1995**, *10*, 693–704.
43. Pereira, A. C.; Aguiar, M. R.; Kisner, A.; Macedo, D. V.; Kubota, L. T. *Sens. Actuators, B* **2007**, *124*, 269–276.
44. Vasilescu, A.; Andreescu, S.; Bala, C.; Litescu, S. C.; Noguer, T.; Marty, J.-L. *Biosens. Bioelectron.* **2003**, *18*, 781–790.
45. Kulys, J.; Wang, L.; Maksimoviene, A. *Anal. Chim. Acta* **1993**, *274*, 53–58.
46. Liu, B.; Yan, F.; Kong, J.; Deng, J. *Anal. Chim. Acta* **1999**, *386*, 31–39.
47. Ghica, M. E.; Brett, C. M. A. *Anal. Chim. Acta* **2005**, *532*, 145–151.
48. Tangkuaram, T.; Wang, J.; Rodríguez, M. C.; Laocharoensuk, R.; Veerasai, W. *Sens. Actuat., B* **2007**, *121*, 277–281.
49. Campuzano, S.; Pedrero, M.; Montemayor, C.; Fatás, E.; Pingarrón, J. M. *Electrochem. Commun.* **2006**, *8*, 299–304.
50. Pandey, P. C.; Glazier, S.; Weetall, H. H. *Anal. Biochem.* **1993**, *214*, 233–237.
51. Rasa, P.; Albertas, M.; Gleb, Z.; Ursula, E. S.-K. *Electroanalysis* **2007**, *19*, 2491–2498.
52. Cao, Z.; Jiang, X.; Xie, Q.; Yao, S. *Biosens. Bioelectron.* **2008**, *24*, 222–227.
53. Kataky, R.; Bryce, M. R.; Goldenberg, L.; Hayes, S.; Nowak, A. *Talanta* **2002**, *56*, 451–458.
54. Palmisano, F.; Zambonin, P. G.; Centonze, D.; Quinto, M. *Anal. Chem.* **2002**, *74*, 5913–5918.
55. Csoeregi, E.; Schmidtke, D. W.; Heller, A. *Anal. Chem.* **1995**, *67*, 1240–1244.

56. Willner, B.; Katz, E.; Willner, I. *Curr. Opin. Biotechnol.* **2006**, *17*, 589–596.
57. Deng, C.; Chen, J.; Chen, X.; Xiao, C.; Nie, L.; Yao, S. *Biosens. Bioelectron.* **2008**, *23*, 1272–1277.
58. Xiliang, L.; Anthony, J. K.; Malcolm, R. S. *Electroanalysis* **2006**, *18*, 1131–1134.
59. Wang, W.; Wang, F.; Yao, Y.; Hu, S.; Shiu, K.-K. *Electrochim. Acta*, in press.
60. O'Neill, R. D.; Chang, S.-C.; Lowry, J. P.; McNeil, C. J. *Biosens. Bioelectron.* **2004**, *19*, 1521–1528.
61. Anzai, J.-i.; Takeshita, H.; Kobayashi, Y.; Osa, T.; Hoshi, T. *Anal. Chem.* **1998**, *70*, 811–817.
62. Choi, S. H.; Lee, S. D.; Shin, J. H.; Ha, J.; Nam, H.; Cha, G. S. *Anal. Chim. Acta* **2002**, *461*, 251–260.
63. Cui, G.; Kim, S. J.; Choi, S. H.; Nam, H.; Cha, G. S.; Paeng, K.-J. *Anal. Chem.* **2000**, *72*, 1925–1929.
64. Xu, J.-J.; Luo, X.-L.; Du, Y.; Chen, H.-Y. *Electrochem. Commun.* **2004**, *6*, 1169–1173.
65. Ansari, A. A.; Kaushik, A.; Solanki, P. R.; Malhotra, B. D. *Electrochem. Commun.* **2008**, *10*, 1246–1249.
66. Baby, T. T.; Ramaprabhu, S. *Talanta* **2010**, *80*, 2016–2022.
67. Wang, J.; Liu, J.; Chen, L.; Lu, F. *Anal. Chem.* **1994**, *66*, 3600–3603.
68. Huang, J.; Li, J.; Yang, Y.; Wang, X. S.; Wu, B. Y.; Anzai, J. I.; Osa, T.; Chen, Q. *Mater. Sci. Eng., C* **2008**, *28*, 1070–1075.
69. McLamore, E. S.; Mohanty, S.; Shi, J.; Claussen, J.; Jedlicka, S. S.; Rickus, J. L.; Porterfield, D. M. *J. Neurosci. Methods* **2010**, *189*, 14–22.
70. Harris, D. C. *Quantitative Chemical Analysis*, 7th ed.; W. H. Freeman and Company: New York, 2007.
71. Chen, C.; Jiang, Y.; Kan, J. *Biosens. Bioelectron.* **2006**, *22*, 639–643.
72. Tang, H.; Chen, J.; Yao, S.; Nie, L.; Deng, G.; Kuang, Y. *Anal. Biochem.* **2004**, *331*, 89–97.
73. Yu, J.; Yu, D.; Zhao, T.; Zeng, B. *Talanta* **2008**, *74*, 1586–1591.
74. Yu, J.; Zhao, T.; Zeng, B. *Electrochem. Commun.* **2008**, *10*, 1318–1321.
75. Vamvakaki, V.; Tsagaraki, K.; Chaniotakis, N. *Anal. Chem.* **2006**, *78*, 5538–5542.
76. Deng, C.; Chen, J.; Nie, Z.; Si, S. *Biosens. Bioelectron.*, in press.
77. Fu, Y.; Zou, C.; Xie, Q.; Xu, X.; Chen, C.; Deng, W.; Yao, S. *J. Phys. Chem. B* **2009**, *113*, 1332–1340.
78. Hoa, D. T.; Kumar, T. N. S.; Punekar, N. S.; Srinivasa, R. S.; Lal, R.; Contractor, A. Q. *Anal. Chem.* **1992**, *64*, 2645–2646.
79. Sangodkar, H.; Sukeerthi, S.; Srinivasa, R. S.; Lal, R.; Contractor, A. Q. *Anal. Chem.* **1996**, *68*, 779–783.
80. Claussen, J. C.; Franklin, A. D.; ul Haque, A.; Porterfield, D. M.; Fisher, T. S. *ACS Nano* **2009**, *3*, 37–44.
81. Njagi, J.; Andreescu, S. *Biosens. Bioelectron.* **2007**, *23*, 168–175.
82. Ren, X.; Meng, X.; Chen, D.; Tang, F.; Jiao, J. *Biosens. Bioelectron.* **2005**, *21*, 433–437.
83. Njagi, J.; Chernov, M. M.; Leiter, J. C.; Andreescu, S. *Anal. Chem.* **2010**, *82*, 989–996.

In Interfaces and Interphases in Analytical Chemistry; Helburn, R., et al.;
ACS Symposium Series; American Chemical Society: Washington, DC, 2011.

84. Ramanavicius, A.; Kausaite, A.; Ramanaviciene, A. *Sens. Actuators, B* **2005**, *111-112*, 532–539.
85. Sánchez-Obrero, G.; Cano, M.; Ávila, J. L.; Mayén, M.; Mena, M. L.; Pingarrón, J. M.; Rodríguez-Amaro, R. *J. Electroanal. Chem.* **2009**, *634*, 59–63.
86. Liu, Y.; Wang, M.; Zhao, F.; Xu, Z.; Dong, S. *Biosens. Bioelectron.* **2005**, *21*, 984–988.
87. Wilson, G. S.; Johnson, M. A. *Chem. Rev.* **2008**, *108*, 2462–2481.

Chapter 12

Smart Interfacial Layers: Sorption-Reinforced Catalytic Substrates for Detection and "Self-Decontamination"

Yongwoo Lee, Ph.D.*

QinetiQ North America, Inc., Technology Solutions Group, 360 Second Ave., Waltham, MA 02451
***Yongwoo.Lee@QinetiQ-NA.com**

The long term objectives of this research are to develop regenerative, sorption-reinforced catalytic substrates capable of detecting and decomposing a range of warfare chemicals including organophosphorus (OP) nerve agents and sulfur mustard compounds. Our approach consists of embedding a biocatalytic composite into the desired substrate (particles, glass beads, fabrics) to create a durable material that detects and fully degrades toxic chemicals, and sequesters the degradation products so that the material can be recycled or safely disposed. Active enzymes against nerve agent compounds that comprise this composite include organophosphorous hydrolase (OPH) and organophosphorous acid anhydrolase (OPAA). In this work, OPH was incorporated into highly absorbing polymeric particles and then into fabric layers to create the catalytic composite. It was demonstrated that the enzyme-bearing polymeric materials were capable of rapid response to and degradation of the OP surrogates methyl parathion and methyl paraoxon.

Design Concept for Material Layers

The proposed design for a laminate system that detects and protects against toxic warfare chemicals is shown in Figure 1. The trilayer laminate consists of nanoreticulated textile and microporous membranes, and includes: 1 a textile outer layer, 2 a membrane middle layer, and 3 an inner liner layer. The outer

In Interfaces and Interphases in Analytical Chemistry; Helburn, R., et al.;
ACS Symposium Series; American Chemical Society: Washington, DC, 2011.

layer is a textile created from very high surface area reactive fibers. These fibers are embedded with catalytic materials, where the reactive fiber layer is intended for the catalytic degradation of toxic chemical compounds. The second layer is a membrane with a pore size that can be manipulated such that aerosols are entrapped, preventing chemical species from reaching the interior. The membrane is treated with catalytic polymers to add a secondary level of biocatalytic protection. Finally, an inner lining layer contains activated carbon to serve as a backup layer (against the body) in the event a toxic species passes through the first two layers.

In this chapter, we present a series of studies aimed at developing composite materials to be used as part of the outer catalytic layers (Figure 1). Specifically, these are materials designed for the catalytic and biocatalytic degradation of nerve agent chemicals. An additional goal for these materials is their ability to sequester the products of the degradation reactions so that the "self decontaminated" composite material can be recycled or safely disposed.

Warfare Chemicals and Their Modes of Degradation

Chemical warfare agents can be divided into four categories based on their mode of action and degradation. Choking agents such as phosgene ($COCl_2$), chlorine (Cl_2), and chloropicrin (Cl_3CNO_2) have been detoxified via acid-base interactions and nucleophilic displacements. Blood agents, such as cyanogen chloride (CNCl) and chloroacetophenone, have been detoxified through the use of activated carbon treated with metal-amine catalysts. Blister agents, which are sulfur mustards (*e.g.*, bis-2-chloroethyl sulfide) (Figure 2a) can be decomposed via inorganic compounds such as polyoxometalates (POM) or TiO_2 nanoparticles. These materials are highly effective when used in conjunction with surfactants or UV light. Nerve agents such as sarin, soman, tabun, and VX, which are organophosphorus (OP) compounds (Figure 2b), have also been reported to be decomposed by inorganic catalysts, although extremely slowly.

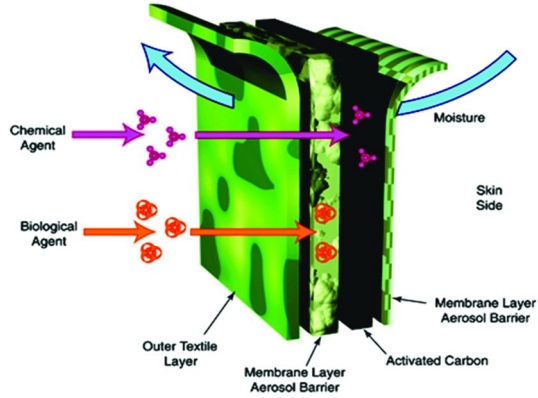

Figure 1. Design concept for interfacial layers for detection, catalytic degradation and self decontamination. (see color insert)

In Interfaces and Interphases in Analytical Chemistry; Helburn, R., et al.;
ACS Symposium Series; American Chemical Society: Washington, DC, 2011.

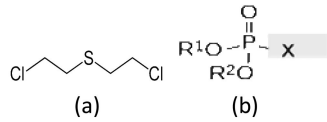

Figure 2. General structure of a sulfur mustard (a) and organophosphates (b); for sarin and soman x = F, R^1 and R^2 = alkyl groups.

Owing to high turnover rate, two enzymes, organophosphorus hydrolase (OPH) and organophosphorous acid anhydrolase (OPAA) have been developed with hydrolytic activity against chemical nerve agents (Figure 2b). LinB enzyme, a haloalkane dehalogenase (HD), has been developed to degrade sulfur mustards (Figure 2a). The enzyme facilitates C-Cl bond-breaking by hydrolysis (turnover rate: 6.9 s^{-1}), a desirable breakdown mechanism that prevents formation of highly toxic sulfone and/or sulfonium intermediates that form during conventional oxidative degradation. All three enzymes are compatible in solution and can be stabilized to avoid deactivation upon prolonged exposure to UV irradiation, rain or excessive heat. Some stabilization methods include: 1 encapsulation in phospholipid-based liposomes (*1*) or polymers encased within chemically modified shells (*2*), 2 physisorption to polymers such as poly-β-cyclodextrin (PCD) particles (*2*), and 3 layer-by-layer techniques (*3*). In this work we employ methods 2 and 3 to create OPH impregnated particles and fabrics (*4*).

Incorporating Enzymes into a Material Composite: Strategies for Enzyme Stabilization

An ideal catalytic system for chemical decontamination should provide full protection against nerve agent and sulfur mustard compounds. OPH and OPAA, organophosphate-hydrolyzing enzymes, are the most effective biocatalysts, degrading chemical nerve agents rapidly (at ~50 s^{-1}). HD is the first enzyme developed to degrade sulfur mustard within a few seconds. In addition to rapid decontamination, it has been shown that the decomposed byproducts of this enzymatic reaction are not toxic or genotoxic, containing none of the aforementioned oxidized intermediates formed through conventional slow abiotic hydrolysis (~ 0.0046 s^{-1}). Thus, OPH, OPAA, and HD are good candidates for incorporation into polymeric particles within a fabric.

The catalytic system we introduce here employs PCDs and poly(trehalose) (PTH) as polymeric supports, where the incorporated enzymes are able to repair themselves through refolding. The catalytic system is deposited on fibers and membranes using a layer-by-layer assembly technique (*4*).

Enzyme Immobilization via Layer-by-Layer Assembly

Enzymes are generally unstable and deactivate rapidly. They have limited shelf life in solution and their performance as a catalyst is limited to certain temperature and pH ranges. Many strategies for immobilization have been pursued in recent years to stabilize enzymes, and to retard their deactivation upon

exposure to stressful conditions such as rain, heat, and daylight. Layer-by-layer assembly via electrostatic, noncovalent adsorption has been an attractive process for this work, owing to its nonintrusive nature, simplicity, and the low cost of fabrication.

Layer-by-layer assemblies of enzymes have been reported to retain their catalytic activity over long periods (> 6 months). OPH (50 s^{-1}, 15 μg VX/ml) was immobilized between layers of buffered polyelectrolyte on silica microspheres (*3*). When so immobilized, OPH maintained higher catalytic activity compared to systems without immobilization, in which case it denatures within 62 h and all enzyme activity is lost. Cotton cloth with OPH enzyme fabricated by similar techniques retained its hydrolytic activity against methyl parathion (MPT) (Figure 3a) as measured by the formation of the hydrolysis degradation product *p*-nitro phenol (pNP) (Figure 3b). The intense yellow color due to pNP developed as a result of rapid catalytic degradation that occurred within five minutes of exposure (*2*, *3*). OPAA enzyme was also demonstrated to have exceptional hydrolytic activity against a VX simulant when immobilized onto sorptive polyurethane. HD-enzyme-immobilized cotton thread also facilitated release of HCl (hydrochloric acid) immediately upon exposure to chloroethyl methyl sulfide in aqueous medium under ambient conditions. The isoelectric points of the three enzymes lie between pH 6.4 and 7.5, meaning that all three could be incorporated sequentially into polymeric substrates in order to create materials that decontaminate multiple chemical agents simultaneously.

Enzymatic "Chaperones" Facilitate Enzyme Self-Repair

Though tuned favorably to the local microenvironment, the enzymes that we are immobilizing within the polymer matrix degrade gradually after cycled use over time under stressful conditions. Thus, the need exists to regain high turnover rates characteristic of their initial states for continuous catalytic degradation (Figure 4) (*5–7*). An enzyme chaperone is a species that assists the non-covalent folding or unfolding and the assembly or disassembly of another macromolecular structure, but does not occur in those structures when they are performing their normal biological functions. Artificial enzyme chaperones can be used to revive the lowered activity of denatured enzymes.

Enzymes are amphoteric by nature, having specific molecular domains and hydrophobic surfaces that trigger more complicated intermolecular or interdomain interactions, ultimately leading to denaturing. They tend to aggregate upon exposure to stressful conditions such as heat, light, salt, and extreme pH. For example, denatured lysozyme (hen egg white lysozyme) was found to regain 75% of its original enzyme activity from the use of ethylammonium nitrate as a chaperone (*8–11*). In Figure 4, we show the measured activity of OPH with and without the presence of a chaperone.

Other researchers have shown that β-cyclodextrin (β-CD) is useful as a chaperone when attached to nanoparticles of TiO_2 via an aminosilyl spacer, or that detergents can be combined with β-CD derivatives to accomplish similar goals. One group has patented certain cyclodextrin derivatives. In addition, refolding kits are available for renaturization even after enzymes have been exposed to

thermal stress. Other proteins can act as chaperones, and organic salts and ionic liquids have been used as well. In our laboratory, we observed that cotton threads coated with OPH and poly-β-CD (PCD, Figure 5) had much greater activity after being renatured in buffered solution mixtures. After 48 h, when stored at 7°C in the presence of a CHES (cyclohexyl-2-aminoethanesulfonic acid) buffered solution, the used thread was withdrawn from the refrigerator and exposed to a fresh 10 mL MPT solution to monitor the subsequent catalytic degradation capability of the used OPH thread. Surprisingly, the amount of *p*-nitrophenol (pNP) produced in the bulk solution increased enormously, almost by a factor of 5 (~100 μM after 30 min), indicating that OPH cotton thread was reactivated using CHES buffer and poly-β-cyclodextrin as a chaperone at low temperature (7°C), as seen by the data in Figure 4.

This experimental result of enhanced activity using the poly-β-CD and layer-by-layer assembly was also reproduced on OPH-coated nylon substrates (Biodyne B-membrane procured from Pall corporation). It may be premature, but it could be concluded that once enzymes are immobilized in a molecular assembly of polyelectrolyte, an artificial chaperone could serve to renature them within the catalytic multilayer system.

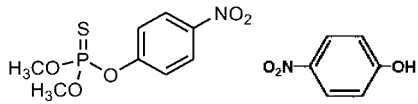

Figure 3. Methyl parathion is used as an OP surrogate in this work (a);the yellow hydrolysis product pNP is montored (b).

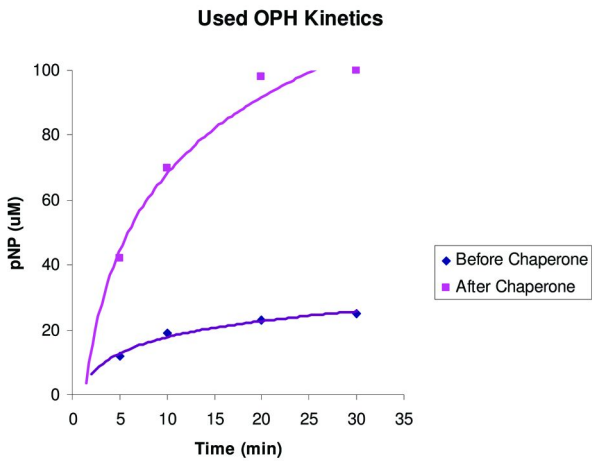

Figure 4. Catalytic kinetics of used OPH cotton thread before (purple, lower) and after (pink, upper) chaperone treatment: Increase of p-nitrophenol (pNP) concentration is indicative of continuous enzyme activity. (see color insert)

In Interfaces and Interphases in Analytical Chemistry; Helburn, R., et al.;
ACS Symposium Series; American Chemical Society: Washington, DC, 2011.

Absorptive Polymer Particles as Physical Supports of Enzymes

Synthesis and Characterization of Poly-β-cyclodextrin Derivatives (Poly-β-CD)

Absorptive polymer particles containing β-CD were chosen to serve as a physical support for enzymes as they possess strong sorption capability toward toxins and are safe for disposal. PCD (*12*) particles were prepared by coupling β-CD with hexyl diisocyanate (HDI) in dimethylformamide (DMF) at 70°C over 14 hours (Figure 5). PCDs are known to catalyze ester hydrolysis and are capable of forcing chemical species into their hydrophobic cavities for host-guest complexation. In that manner, PCD could sequester target comounds and their degradation products. As anticipated, the particles we obtain have a high sorption capacity for the OP surrogate MPT and its breakdown product pNP. The crosslinking of β-CD with HDI produced robust PCD particles (*13*), which were then taken up into the cotton thread. The β-CD content of the particles imbibed on fabrics was believed to determine their sorption capacity toward MPT and pNP. Figure 6 shows how the adsorbed amount (%) and sorption preference (*i.e.*, MPT vs. pNP) for poly-β-CD-functionalized cotton thread varies with the β-CD content generated *in situ* from the different ratio of HDI to corresponding β-CD in the coupling reaction.

The PCD particles were characterized by FT-IR [CO_2 group at 1715 cm^{-1}], BET surface area 10.2 m^2/g, and the total pore volume 0.06 cm^3/g. Species such as MPT and pNP were sequestered by forming inclusion complexes with poly-(β-CD) with pNP having a formation constant (K) = 10^9. The formation constant for pNP on β-CD is K = 10^2. Conveniently, enzymatic status was recovered and regenerated by simple immersion in buffer. Note that preferential sorption of MPT over pNP was also observed in batch mode. These polymeric particles were shown to be chemically inert and robust enough to endure extended exposure to highly acidic and highly alkaline media alike.

Similarly, each poly-β-CD impregnated cotton string was coated with OPH under the same condition and its enzymatic activity was assayed using UV-VIS absorption measurements of pNP [$A_{405\ nm}$] (Figure 8). The amount of enzyme loaded could also be maximized in this controlled quantitative deposition method.

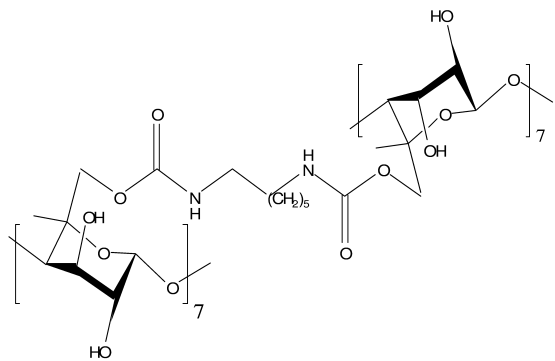

Figure 5. Structure of poly- β-cyclodextrin.

In Interfaces and Interphases in Analytical Chemistry; Helburn, R., et al.;
ACS Symposium Series; American Chemical Society: Washington, DC, 2011.

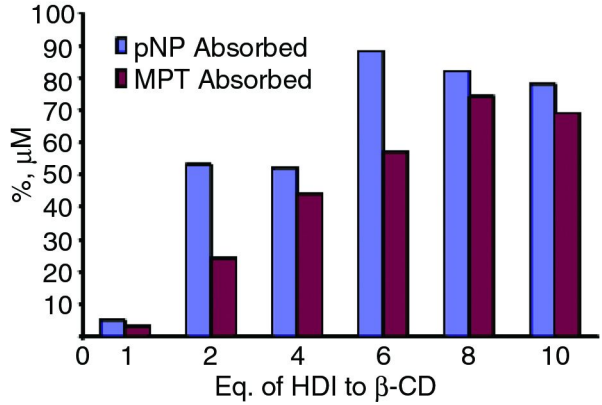

Figure 6. pNP and MPT absorption behavior by cotton thread coated with poly (β-cyclodextrin) as a function of hexyl diisocyanate ratio. (see color insert)

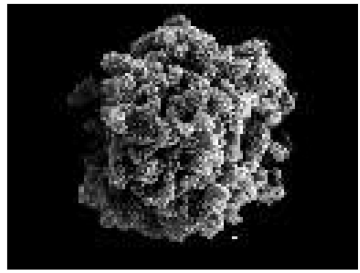

Figure 7. SEM image of sieved poly-β-CD particles with large surface area [~10 µ].

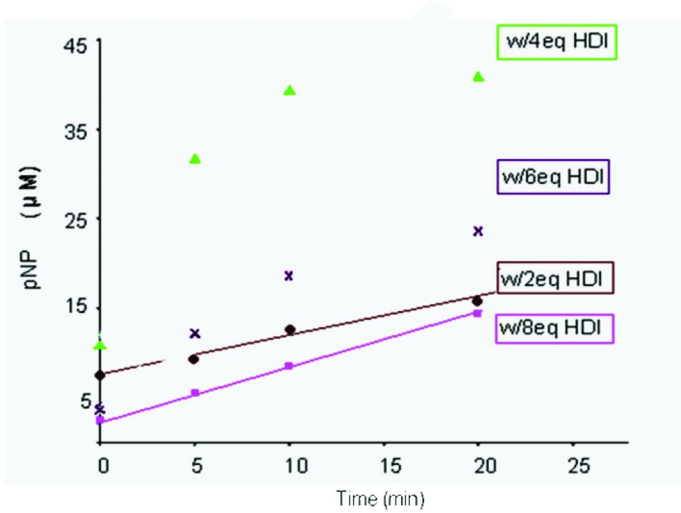

Figure 8. OPH-coated poly-β-CD cotton fibers for catalytic MPT degradation; results as a function of ratio of β-CD to HDI. (see color insert)

In Interfaces and Interphases in Analytical Chemistry; Helburn, R., et al.;
ACS Symposium Series; American Chemical Society: Washington, DC, 2011.

Maximized catalytic degradation is desired and could be achieved from maximum loading of enzyme by monitoring maximum absorption of MPT and the occurrence of the degradation product pNP. *In situ* modification of cotton threads (1 m long) was carried out, and coupling of β-CD with 4 equivalents of HDI produced the best sorption and catalytic capability (twice the previous condition of 8 equivalents of HDI employed). Based on these experimental results, the optimal equivalent molar ratio of β-CD to HDI was determined to be 1:4 (Figure 8), and this optimized reaction system was reproduced onto cotton threads, erkol-treated PTFE membranes, and fibrous cellulose.

Catalytic Behavior of the Polymeric Particles with and without OPH: Inter-Laboratory Comparison

The coupling reaction (*i.e.*, coupling of β-CD with DI in DMF) is highly exothermic, and sometimes gelation occurs via random exhaustive crosslinking with HDI. BET analysis of PCD produced by known protocol shows that the surface area is relatively small (1.7-1.9 m^2/g), in contrast to the total pore volume (0.06cm^3/g), indicating that those PCD particles should have a highly tortuous matrix. The QinetiQ North America (QNA) PCD particles, however, showed an unexpected ability to absorb and hydrolyze MPT within 14 h, even in the absence of any enzyme catalyst. Figure 9 shows samples of poly-β-CD exposed to MPT for six days for: 1 a sample prepared at the Naval Research Laboratory (NRL), 2 a sample obtained from Los Alamos National Laboratory (LANL), 3 the QNA sample (our lab), and 4 a control of stock MPT. Only the QNA material developed the characteristic yellow color of pNP as a result of degradation, albeit over a much longer timeframe than in the presence of enzyme (6 days).

In addition to their reactive capability, when coated with OPH and then exposed to MPT vapor in the presence of water vapor (100 μg), a QNA cotton cloth functionalized with β-CD turned yellow over 8 h at 40°C, indicative of the qualitative breakdown of MPT (Figure 10).

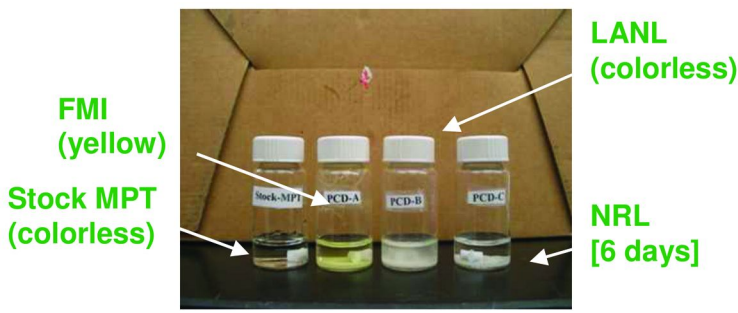

Figure 9. Interlaboratory comparison: unexpected hydrolytic capability of QNA (here labeled FMI)poly(β-CD) particles when exposed to a solution of colorless MPT. (see color insert)

In Interfaces and Interphases in Analytical Chemistry; Helburn, R., et al.;
ACS Symposium Series; American Chemical Society: Washington, DC, 2011.

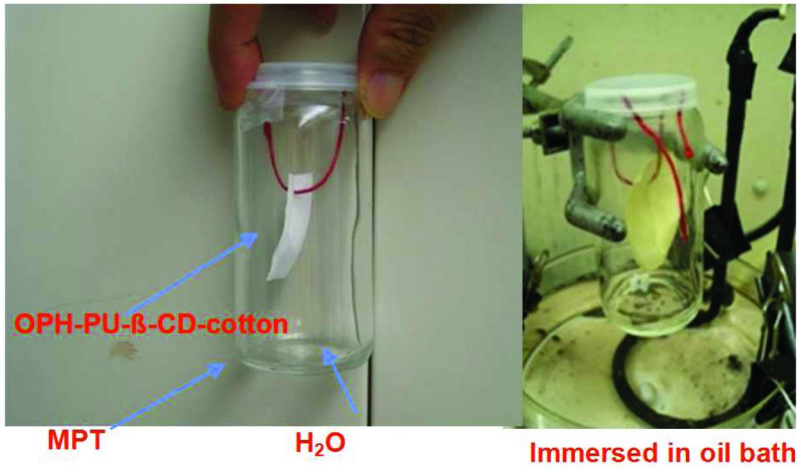

Figure 10. Breakdown of MPT to produce pNP by poly(β-cyclodextrin)-functionalized cotton cloth. (see color insert)

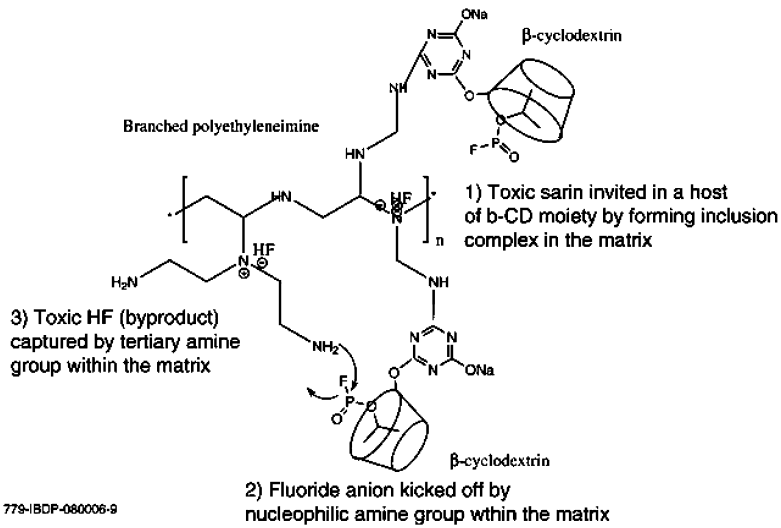

Figure 11. Potential mode of action of β-cyclodextrin functionalized branched poly(ethylene imine) against sarin.

β-CD-bonded poly(ethylene imine) (β-CD-BPEI) was also proposed as a pore-forming reactive polymer with potential for OP detoxification. The β-CD-BPEI was prepared in an aqueous medium at 70°C from reaction of branched poly(ethyleneimine) (BPEI) with monochlorotriazinyl-β-cyclodextrin (MCT-β-CD). Figure 11 illustrates a hypothetical mechanism of performance of this absorptive nucleophilic polymer, which could act as a sorbent for sarin, trapping the compound in the hydrophobic β-CD bucket. This would allow for subsequent nucleophilic attack on the phosphorus by a nearby primary amine,

eventually followed by sequestration of the fluoride by a tertiary amine on the polymer backbone.

This particular example (β-CD-BPEI) was prepared as electrospun nanofiber mats co-spun with poly(ethylene oxide) in a 1:1 ratio as shown in Figures 12 and 13. Lyophilization of the mat allowed much of the open structure to be maintained (200 nm fiber diameter).

PCD Coatings on Nylon

Nylon fabric is a common shell for outdoor clothing. We obtained a sample of grooved C-CP nylon cloth from Specialty Customer Fiber. It has a surface area almost three times that of a conventional round fiber. When coated with polymeric β-cyclodextrin and then OPH as described above, degradation of MPT was observed within minutes, as seen in Figure 14.

Performance of Poly-β-CD as a Sorption Material for pNP and MPT

Crosslinked PCD has been shown to effectively absorb pNP from an aqueous medium (*15*). In batch mode, the absorbing properties of PCD were evaluated over a range of pNP concentrations (0.05-50 mM) at buffered solution pHs of 10.00 and 8.6. These experiments demonstrated maximum experimental capacities of 22 and 195 mg/g PCD, respectively. Under the conditions studied, pNP uptake could be accurately described using the Sipps equation ($R^2 \geq 0.998$), providing an average apparent binding affinity for pNP of 7.15 and 53.76 mM at pH 10.00 and 8.6, respectively. In a continuous flow-through system using a PCD-packed column that we describe in a later section of this chapter (Figure 32), PCD performed similarly as compared to the batch mode. Sorption capacity increased with increasing influent concentration of pNP and with decreasing pH. At slower flow rates (Figure 32), the poly-β-CD column exhibited a sharper breakthrough of pNP. Column regeneration was achieved by rinsing the packed poly-β-CD column with ethanol.

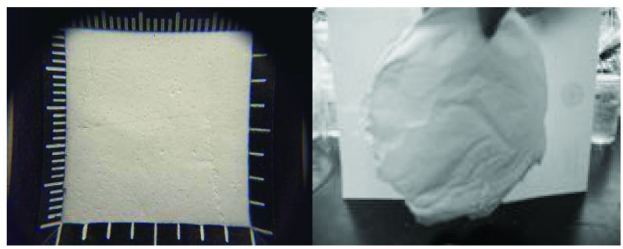

Figure 12. Electrospun nanofiber mats.

In Interfaces and Interphases in Analytical Chemistry; Helburn, R., et al.;
ACS Symposium Series; American Chemical Society: Washington, DC, 2011.

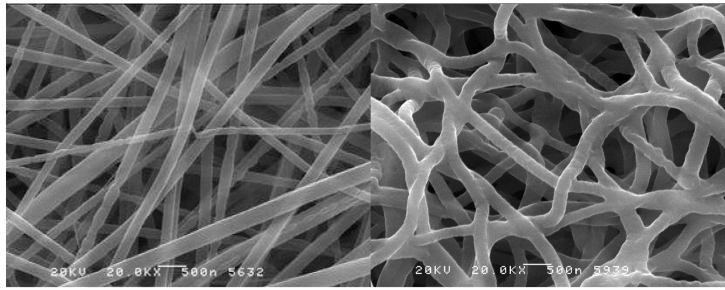

Figure 13. Electrospun nanofiber mats in closeup

Figure 14. Effectiveness of OPH coated poly(β-cyclodextrin)-functionalized nylon grooved fibers against MPT as opposed to stock MPT. (see color insert)

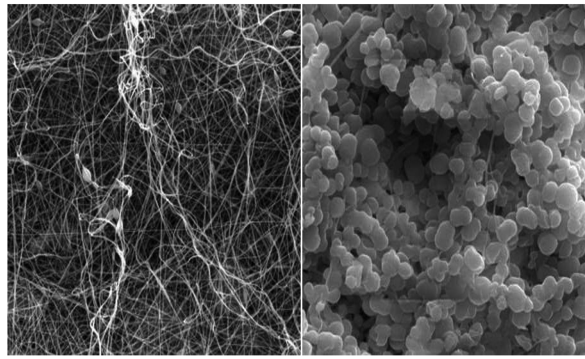

Figure 15. SEM of PVA electrospun fibers before (left) and after treatment with polymeric β-cyclodextrins (right).

From Microparticles to Nanoparticles of Poly-β-CD

Coupling reactions of crosslinkable monomeric units are hard to control because they are highly exothermic once they reach their activation energy, and the reaction can not be stopped as desired. Using optimized reaction conditions at dilute concentration in DMF, nanoparticles of poly-β-CD were produced and imbibed onto the nanofibrous polymeric mats over 14 h. With this protocol, we could have nanosized crosslinked polymeric β-CD particles fabricated using electrospun nanofibers as a template.

Super-absorbing poly-β-CD was intercalated between polyvinyl alcohol (PVA) electrospun nanofiber when treated *in situ* with a mixture of β-cyclodextrin hydrate and hexamethylene diisocyanate at 70°C. PVA nanofiber samples were electrospun onto aluminum foil. The sample was treated with polymeric cyclodextrins, similar to the above stated procedure, and rinsed with hot DMF. A large amount of poly-β-CD nanopororous particles was incorporated into the PVA nanofibers via a template-initiated polymerization process. The crosslinked PCD nanoparticles on PVA nanofibers were found to be insoluble, highly absorbing and of large surface area. When OPH was incorporated, they were highly catalytic towards MPT degradation. The particles could be recycled by rinsing in methanol.

Polymeric Trehalose

D-(+)-trehalose is a disaccharide that has been widely employed for enzyme stabilization. Trehalose has been reported to display chaperone-like activity by stabilizing the native conformation of enzymes and protecting them from various kinds of stress. In addition to its intrinsic protein-stabilizing activity, trehalose has been shown to regulate the activity of other molecular chaperones, and may stabilize the folded state of proteins involved in unfolding or misfolding diseases.

In this work, trehalose was incorporated into a polymeric matrix generated *in situ* on cotton thread by coupling reactions with alkyl (aryl) isocyanate derivatives. Like β-CD, when polymerization was carried out in the presence of cotton thread, coating of the thread occurred and a subsequent layer of OPH enzyme could then be applied (Figure 16). PTH (poly-trehalose) was prepared and optimized so as to maximize its catalytic properties and ability to sequester target compounds such as MPT. It was noted PTH particles have an intrinsic hydrolytic capability toward MPT in the absence of OP hydrolyzing enzymes. These enzyme modified polymeric particles were also demonstrated to have high binding efficiency for the enzyme, a high resulting enzymatic activity, and the capability to efficiently hydrolyze and sequester substrates (*16*). In addition, PTH was observed to be insoluble in most organic and aqueous media. Its density was approximately one-third that of similar silica microspheres. Figure 16 shows the color change (due to presence of pNP) that happens when this treated thread is exposed to MPT. Unlike PCD cotton thread, the recovery of pNP adsorbed to the OPH enzyme-coated poly(trehalose) cotton thread was not completely reversible, owing to higher binding affinity than that of PCD (*17*).

Figure 16. MPT degradation by OPH-coated poly(D-(+)-trehalose cotton thread withdrawn after exposure to MPT (right), as opposed to control poly(trehalose) cotton thread (left side). (see color insert)

Catalytic and Enzyme Stabilizing Properties of the OPH-PTH Cotton Thread: Comparison to PCD

The PTH functionalized cotton threads were chemically inert and robust with respect to exposure to stressful conditions. They were demonstrated to absorb both MPT and pNP in aqueous media. Upon exposure of the treated threads to methanol, compounds were quickly de-sorbed and the functionalized cotton threads were recovered for reuse. The degradation of MPT was assayed as a function of the amount of pNP produced in the bulk solution; 42 μM was the maximum pNP produced and 58 μM pNP was believed to be adsorbed to the surface of the thread via inclusion phenomena and hydrophobic interactions. A higher binding affinity was also demonstrated in OPH-coated poly(trehalose) particles.

With respect to enzyme stabilization, it should be noted that *bound* OPH (either to PCD or PTH) displays a sustained activity of 5% of its initial value after being immersed in NaCl for 2 h, 11% of its initial value after 2 h immersion in methanol, 9% following 2 h immersion in acetone, 58% for 24 h immersion in tapwater, and showed an increase to 300% of its initial activity for an acidic condition (pH 5.5), which was unexpected. These results are in support of the chaperone-like role played by PTH and PCD in maintaining enzyme activity (through OPH-PCD and OPH-PTH molecular interactions), even when the composite is exposed to stressful conditions such as those of high ionic strength and organic solvents. In that respect, we note that OPH is more strongly bound to PTH than to PCD; the absorbed pNP could not be completely washed out of the PTH particles. Another surprising result was the substantial hydrolytic capability of PTH on its own.

In Figure 17, the development of pNP in an MPT solution treated with 100 mg OPH-coated PTH particles is compared with the performance of 100 mg of poly-β-

CD particles exposed to MPT, demonstrating that most were bound and degraded near the surface of PTH cotton thread. When OPH-coated PCD particles (100 mg) and OPH-coated PTH particles (100 mg) were exposed to 10 mL of 100 µM MPT, pNP rapidly appeared in solution, with the entire reaction being complete in about 15 minutes. The decreasing concentration of MPT was monitored as A_{275nm}, but there was substantial inaccuracy in the data due to interference by other compounds. The concentration of MPT in the supernatant was confirmed to be zero, from adding known-active OPH to it and observing no increase in the absorbance of pNP (A_{405nm}). Because of the complete removal of MPT from the solution, it is clear that some of the product (and possibly some of the starting material) was absorbed onto the PTH particles.

Comparison of Sorption Behavior among Several Polymeric Support Materials

In order to study the effect of sorption behavior by various polymeric particles on particle catalytic activity, samples of five particle types *without* enzyme were exposed to solutions of 100 µM pNP and 100 µM MPT. Figure 18 shows how the relative absorption of pNP and MPT changes with the type of particle. In particular, the simple polyurethane made from the autoreaction of HDI with water and a polyacrylate sample showed much greater relative absorption of pNP relative to hydrophobic MPT. Conversely, polyurethane samples based on hexyl diisocyanate reacted with β-CD and/or calix[8]arene had lower equilibrium uptake of pNP relative to MPT, presumably due to the presence of hydrophobic pockets in the latter. The relative absorption of MPT vs. pNP is an important piece of information that determines whether the resulting catalytic composite will engage in continuous catalytic activity and consume all of the parent compound. MPT should be preferentially absorbed so that it will displace the formed pNP in a catalytic "pocket". This concept is addressed in an upcoming section.

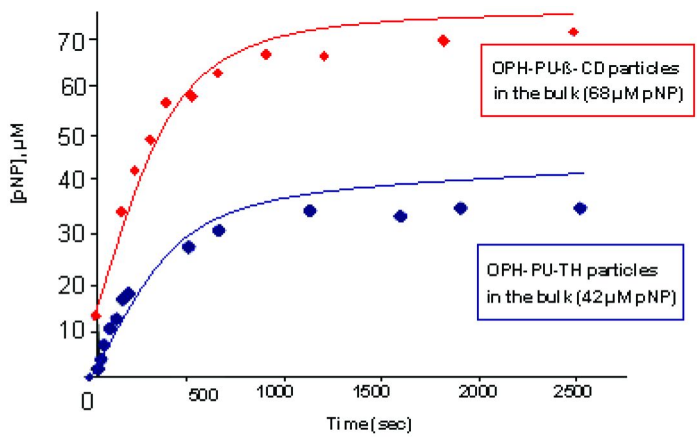

Figure 17. MPT degradation kinetics; comparison of OPH coated poly-β-CD to OPH coated PTH particles. (see color insert)

In Interfaces and Interphases in Analytical Chemistry; Helburn, R., et al.;
ACS Symposium Series; American Chemical Society: Washington, DC, 2011.

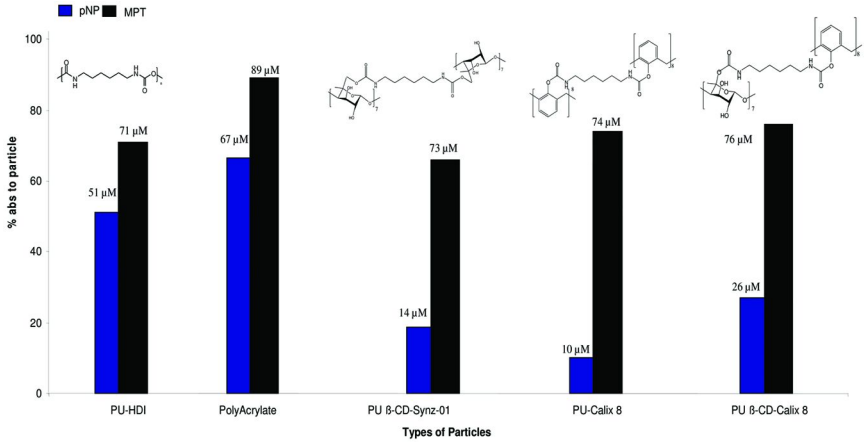

Figure 18. MPT and pNP sorption behavior on different absorptive polymeric particles. (see color insert)

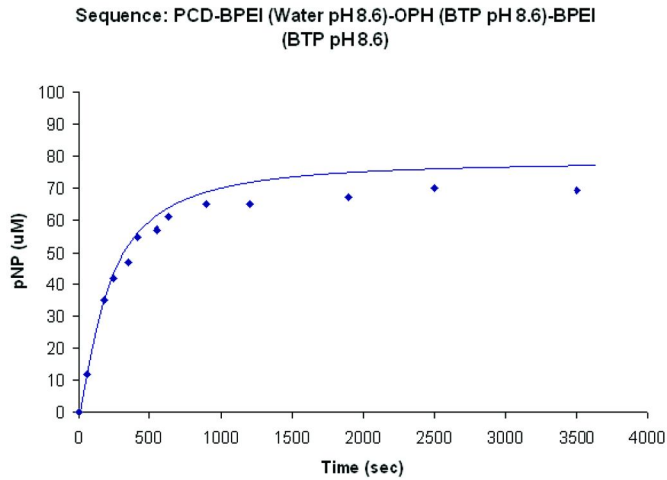

Figure 19. Enzyme kinetics of OPH-PCD as amount of pNP produced in the bulk liquid only.

Kinetic Studies of the OPH Catalyzed Degradation of MPT: Comparison of PTH and PCD

PCD particles were employed as a physical support on which OPH enzyme was immobilized. When OPH-PCD particles (100 mg) (protein content: 7.8 mg / g PCD) were immersed in a 10 mL solution of 100 µM MPT, within 5 min, ~55% MPT was hydrolyzed, and within 10 min, hydrolysis was completed. Interestingly, out of 100 µM MPT, only 70 µM pNP produced was monitored in the solution, indicating that the other 30 µM pNP was absorbed by particles as an inclusion complex. The strongly colored yellow particles were washed to

In Interfaces and Interphases in Analytical Chemistry; Helburn, R., et al.;
ACS Symposium Series; American Chemical Society: Washington, DC, 2011.

recover the absorbed pNP and reused over several cycles. No MPT was detected in the recovered solution, only pNP . The solutions were analyzed for MPT and pNP by HPLC with UV/vis detection (A_{275nm} and A_{405nm}, respectively). Figure 19 illustrates the amount of pNP produced vs. time for this experiment.

The enzyme kinetics of OPH-PCD and OPH-PTH particles are very complex owing to the ability of PCD and PTH to absorb pNP present in the bulk solution. For that reason, the initial rate (V_o) measured could be even higher, considering the additional amount of pNP adsorbed to PTH (or PCD) particles during the overall process.

Sorption-Reinforced Catalytic Systems: Summary and Proposed Mechanisms

Several versions of the catalytic materials have been prepared and tested against the nerve agent surrogate MPT. OPH-enzyme-modified C-CP (nylon) fibers and OPH-enzyme-modified nylon membranes also show rapid hydrolytic degradation of MPT. PTH particles were prepared which have further advantages: for example, D-(+)-trehalose-stabilized enzymes can hydrolyze MPT within the crosslinked polymeric substrates, unlike PCDs, and they have higher sorption capacity for both MPT and pNP. The advantage of the composite architectures (Figure 21) that we have employed is that as more-efficacious catalysts are discovered, they can be easily incorporated into the nanocomposite. The porosity of the nanocomposite material can be manipulated to accommodate different size target molecules.

Our enzyme-based catalytic system was demonstrated to be promising when coupled with absorbing polymeric crosslinked particles. It was further demonstrated to be highly catalytic under such stressful conditions characterized by the presence of salts or organic solvents, ionic strength, and aciditic and alkaline conditions. These results suggest that stressful conditions can be overcome by the molecular interaction of enzymes with absorbing polymeric particles, and that their performance as a catalytic system could be improved by chemical modification of supporting polymeric materials.

Figure 21 illustrates the catalytic breakdown and sequestration of OP compounds within material surface layers. As an example, incoming surrogate MPT is attracted to and included into the exterior layer of a poly-β-CD host through the hydrophobic interactions and by interaction with the enzyme-harboring polymeric CD via host-guest-complex formation. As MPT is biocatalytically degraded, an intense color change is observed, indicating the appearance of pNP. Although the CD bucket has the capacity to hold the degraded, nontoxic breakdown product (pNP), its preferential sorption toward MPT results in displacement of pNP by MPT (*14*), thus facilitating continuous catalytic activity and complete decomposition. This is the basis of the "self-decontamination" process.

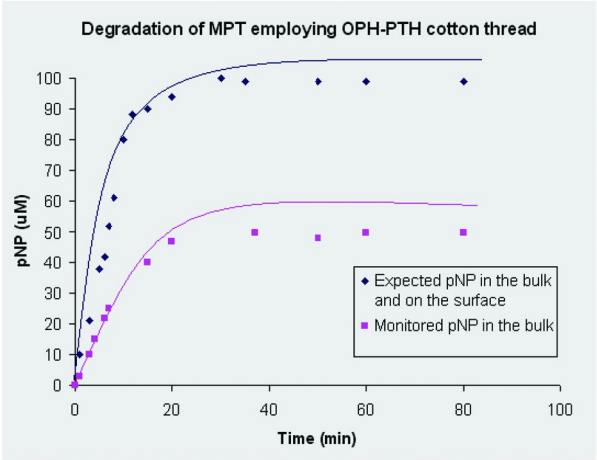

Figure 20. Catalytic degradation of MPT employing OPH-PTH cotton thread. (see color insert)

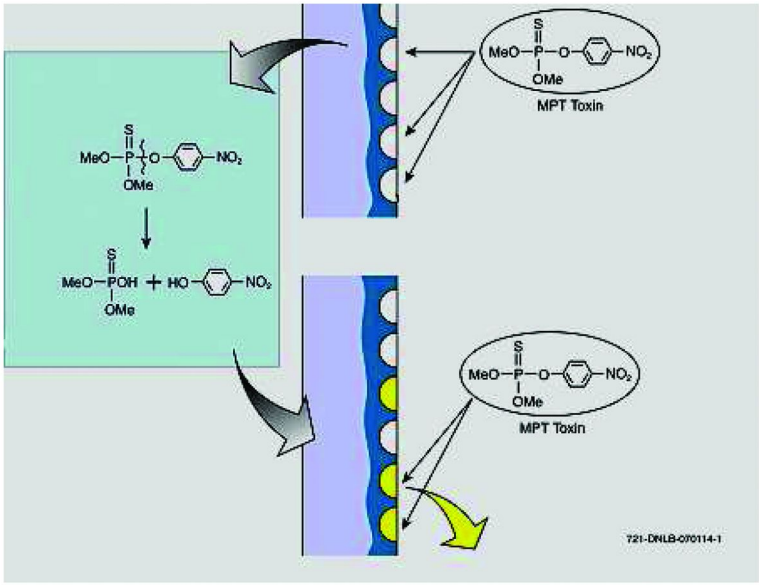

Figure 21. Nanocomposite catalytic system showing the decomposition of MPT; mechanism of the "smart" self-cleaning composite layer. (see color insert)

Coating Meltblown Nanofibers with Poly-β-CD

Melt blowing (MB) is a process for producing fibrous webs from polymers using high-velocity hot air or another appropriate force to attenuate the filaments. MB fiber-based fabrics have fiber diameters $\geq$ 1μm. Electrospinining, by comparison, produces individual fibers in a smaller range of sizes (10 - 500 nm, Figures 13 and 15). Given our success with coating natural fibers, nylon, and electrospun PVA nanofiber (Figure 15), we explored the coating of MB synthetic fibers as well. Figure 22 shows scanning-electron micrographs (SEM) of coated meltblown fibers. Micron-sized polypropylene polyethylene (PP/PE) fibermat and polypropylene sulfide (PPS) fiber mat were procured from Silver Star. They were coated with PCD over a period of 8 h at 70°C. Of particular interest are the smooth coatings on the poly(propylene sulfide) fibers, which show that coatings can be achieved without clogging or blinding the pores in the fibermat, and that particle formation is not a necessary consequence of the polymerization conditions (compare to Figure 15, right). As is demonstrated in the SEM images, absorptive PCDs were implemented along the axis of fibers under our deposition protocols, covered in specific locals most likely near the surface of polyethylene unit, as in case of the PP/PE fabrics, and fully covered, as in PPS fibermats.

Additional Catalytic Supports: Synthesis and Characterization of Reactive Metal-Organic Frameworks

Introduction

A metal-organic framework (MOF) is a crystalline compound consisting of metal ions or clusters coordinated (often) to rigid organic molecules to form one- two-, or three-dimensional structures. These materials are porous, light and highly adsorbing especially toward gaseous species. Most MOFs are not stable in water. However, this limitation is being overcome through incorporation of $Cu_2(COO)_4$ clusters into the structure, an investigation that is ongoing in our lab. These experiments have produced MOFs that are resistant to hydrolysis in addition to having an ability to take up significant amounts of small gases and organic species (*18*, *19*).

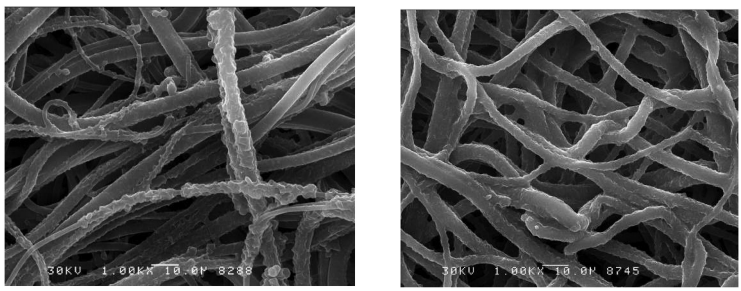

Figure 22. SEM of meltblown fiber: (left) poly-β-CD coated PP/PE (1k x); (right) poly-β-CD FMI-PPS (1k x).

In Interfaces and Interphases in Analytical Chemistry; Helburn, R., et al.;
ACS Symposium Series; American Chemical Society: Washington, DC, 2011.

Current Projects

At present we have developed a suite of *reactive* (*i.e.*, self-decontaminating) MOFs (SD-MOFs) via a chelating reaction of copper (II) nitrate (CN) with linear acetylenedicarboxylic acid (ADA) and organic 4,4′-bipyridyl linkers. The linkers that we have used are pyrazine and its derivatives, bipyridyl ethylene, and 4,4′-bipyridyl. A current *series* (organized by groups of linkers) consists of (1) SDMOF-FM02-Pyz (pyrazine and its derivatives), (2) SDMOF-FM01-BPe (bipyridyl ethylene) and (3) SDMOF-FM03-BPl (4,4′-bipyridyl). An important feature with respect to the reactivity of these MOFs is their metal-to-amine ratio. Initial studies show that these materials, in the absence of enzymes, have the ability to degrade MPT and methyl paraoxon (MPO, Figure 23) in both liquid and gas environments, respectively, and to subsequently capture their breakdown products through the open pores of the MOFs. We have begun examining the response of these materials to the toxic OP sarin.

Specific Reactive MOF Structures

We examined the amine-based linker chemistries in conjunction with the more traditionally employed linker acetylenedicarboxylic acid (ADA). The materials were prepared through the chelating reaction (Cu^{2+} and linker) in either water or a 1:1:1 mixture of N,N′-dimethyl formamide (DMF):methanol:water at 90-100°C. Examples of active pyridinyl amine linkers, shown in Figure 24, include pyrazine (Pyz) and its derivatives, 4,4′-dipyridyl (Dpl), and trans-1,2-bis(4-pyridyl)-ethylene(DPe). The resulting MOFs can have a Cu:pyridyl amine molar ratio that approaches 1:1. The nature of chemical linkers is such that they can be used to alter adsorbent selectivity as well as activity.

Examples of the MOF particles are given in Figure 25. The chemical linker ratios used in the individual syntheses are also provided.

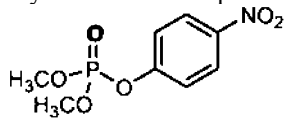

Figure 23. Methyl paraoxon; the hydrolysis product is the same as for MPT, i.e., pNP. See Figure 3.

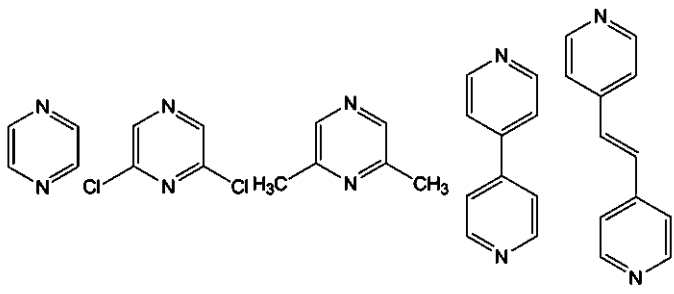

Figure 24. Pyridinyl amine linkers.

In Interfaces and Interphases in Analytical Chemistry; Helburn, R., et al.;
ACS Symposium Series; American Chemical Society: Washington, DC, 2011.

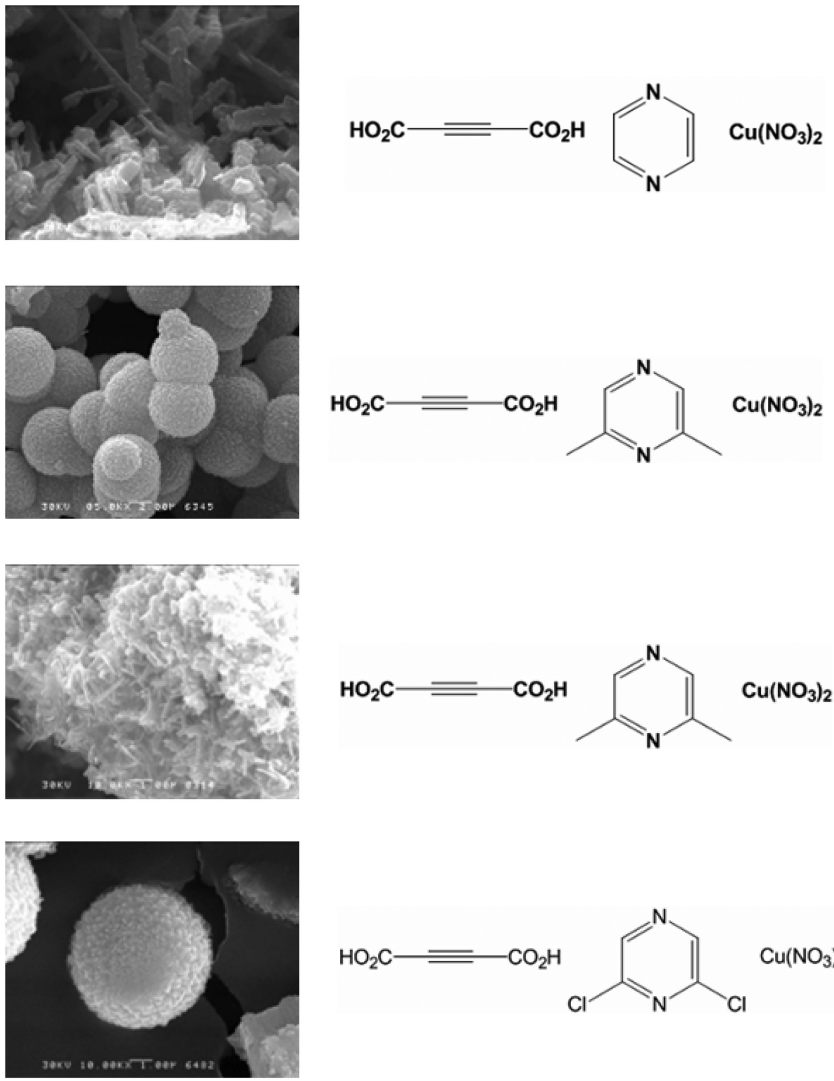

Figure 25. SEM images for SD-MOFs (prepared in water, or in formulated solvent); ratio of carboxylic acid (as ADA) to amine functionalized linker is 1:1.

Studies on the Reactivity and Sorption Capability of the Prepared MOFs

The MOFs created with either solvent system (*i.e.,* water or the 1:1:1 mixture of DMF, methanol and water) both resulted in a final product that showed activity against MPT and MPO. Reactivity, of the bare MOF was observed for both a liquid environment (a solution of MPT and MPO) and gas environment (flowing a stream of N_2 spiked with MPO vapors at ambient condition). As an example, interaction of MPT with MOF-FM1 (*ADA-Pyz*-Cu$(NO_3)_2$) showed evidence of degradation products as illustrated in Figure 26. A concentrated yellow-green color rapidly

developed in the reaction mixture, indicating the presence of pNP. The reaction was monitored via Uv/vis absorption (disappearance of MPT as A_{275nm}, appearance of pNP as A_{405nm}). Visual observations are given in Figure 26. Additional work will be required to understand if the MOF is being consumed in the reaction or is acting catalytically. The reaction was reproduced several times with no observable loss in the quantity of the MOF, indicating, at a minimum, a large capacity toward this reaction.

The chemical activity of MOF-FM1 toward MPT hydrolysis was also observed via Uv/vis. The appearance of pNP was monitored immediately when 100 μM MPT solution was exposed to 100 mg of MOF-FM1. It was noticed that the amount of pNP was less than 100% conversion, indicating partial sorption of MPT to MOF powders during decontamination. To this solution, NaOH was added with no further pNP production observed; thus it was concluded that the solution had no residual MPT present in the bulk liquid, and 100% conversion was indicated. Next, the particles were collected from solution and washed with either DMF or acetone. Additional pNP was collected, indicating that the missing pNP was actually present but adsorbed in the MOF structure (Figure 27). MPT was not found in the rinsed SD-MOF powders, but the pNP degradation product was observed in the powders in an adsorbed form, providing evidence of complete "decontamination" through the open pores of SD-MOFs.

Kinetic Studies on MOFs with and without Enzyme

The kinetics of the MPT hydrolysis was next examined. Without the incorporated OPH, degradation of MPT by MOF-FM1 was found to be complete within ~3 h, much faster than that shown by other known catalytic particles (Figure 28). The material was also found to be hypersorptive toward degradation products. Out of 100 μM MPT, about 20%, measured either as MPT or pNP depending on the material and the experiment, was found to be adsorbed to the powders. Interestingly, MOF-FM1 can be reused many times. In Figure 29, MOF-FM1 was reused four times. In that experiment, the particles were rinsed with acetone between applications to fresh MPT solution. Each replicate experiment was run for 30 minutes.

Relative reactivities of SD-MOFs were demonstrated in a reaction carried out under ambient conditions for 2 h (Figure 30). Among those SD-MOFs that were examined, 2,6-dimethyl pyrazine (w/ ADA-CN) was demonstrated to have the highest activity toward MPT, followed by the pyrazine (w/ ADA-CN) MOF, and three additional MOFs (Figure 30). Figure 31 illustrates several sets of kinetic data on the degradation of MPT for several reactive materials. Note, one plot is MOF-FM1 used as a support for OPH. A substantial increase in activity was demonstrated for that system. Untreated PCD did not produce pNP in the solution, under the conditions of that experiment (Figure 31).

Sorption of the MPT by SD-MOFs is close to 20% while 80% of the MPT was degraded, out of 100 μM MPT in the solution. The pyrazine-based SD-MOF had little sorption capability; its activity can be attributed to the degradation of unadsorbed (solution phase) MPT.

In Interfaces and Interphases in Analytical Chemistry; Helburn, R., et al.;
ACS Symposium Series; American Chemical Society: Washington, DC, 2011.

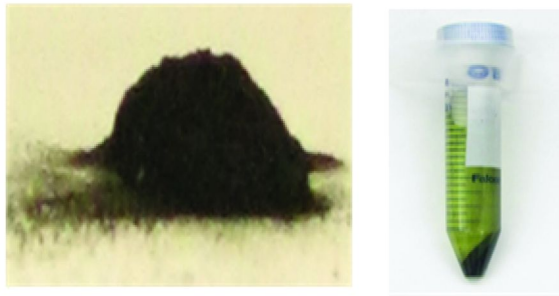

Figure 26. (left) MOF-FM1 adsorbent is crystalline and contains high Cu:amine molar content. (right) Room-temperature decomposition of simulant methyl parathion is demonstrated over MOF-FM1 at room temperature, producing a yellow-green decomposition product pNP. (see color insert)

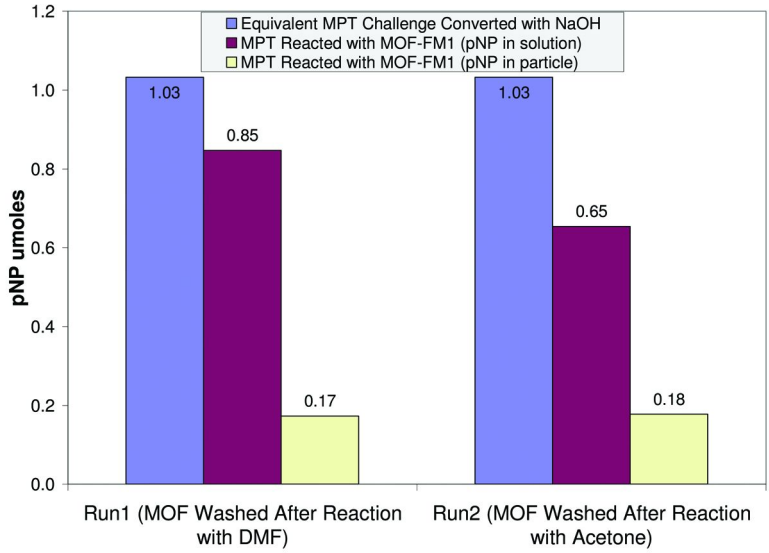

Figure 27. MOF-FM1 particle is able to "decontaminate" the MPT from a 15% methanol aqueous solution. The difference between the observed pNP concentration in the bulk solution and what is retrieved from the same 100 μM MPT solution, treated with NaOH; recovered from the MOF-FM1 particles using DMF or acetone rinses. (see color insert)

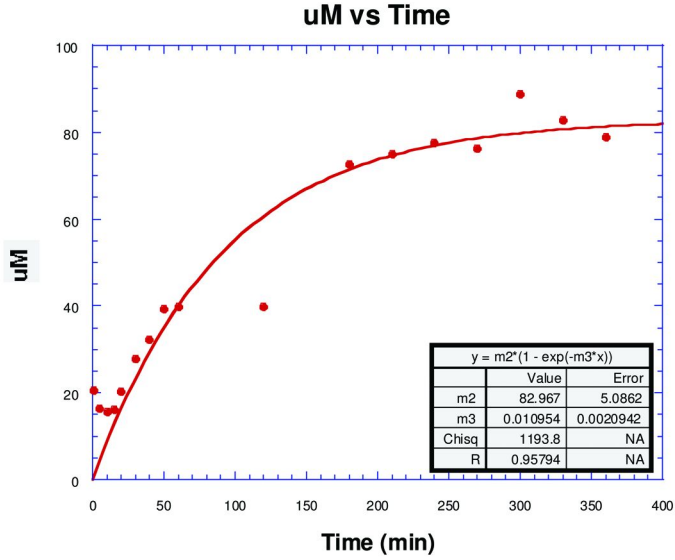

Figure 28. uM pNP produced vs. time; MOF-FM1 particle is able to "decontaminate" the MPT in a 15% methanol aqueous solution. The difference between the observed pNP concentration in the bulk liquid and the expected 100μM pNP can be attributed to sorption of pNP onto MOF-FM1 particles. Each reaction used 100 mg of MOF-FM1 per 100 μM MPT.

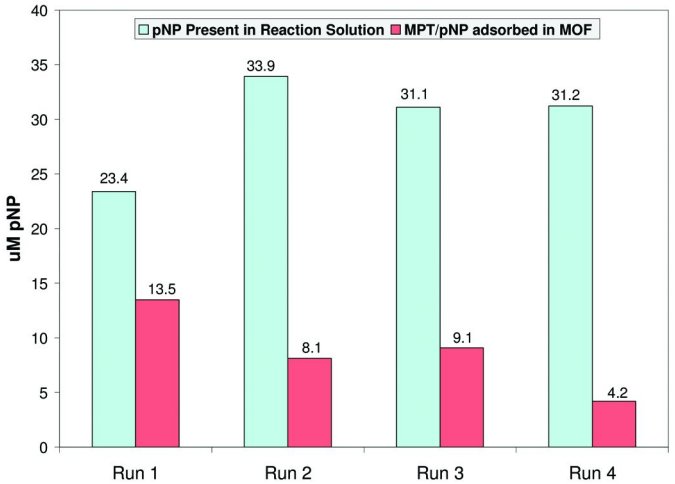

Figure 29. MOF-FM1 particle is able to decontaminate MPT in a 15% methanol aqueous solution and be reused many times. In this experiment, the MOF-FM1 was rinsed with acetone after each reaction. Each reaction used 100 mg of MOF-FM1 per 100 μM MPT; reaction time was 30 min. (see color insert)

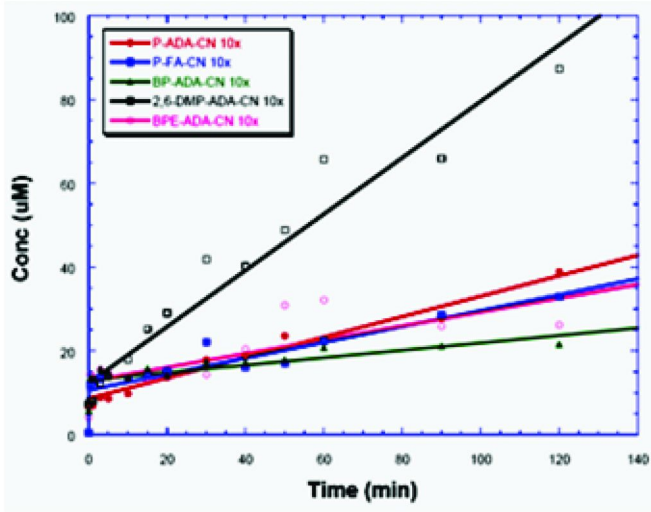

Figure 30. pNP formed vs. time; MOF kinetics and the effect of the linker chemistry on reactivity of amine-containing MOFs. (P: pyrazine, CN: copper nitrate, FA: fumaric acid, BP: 4,4'-bipyridyl,2,6, DMP: 2,6-dimethyl pyrazine, BPE: bipyridyl ethylene (BPe). (see color insert)

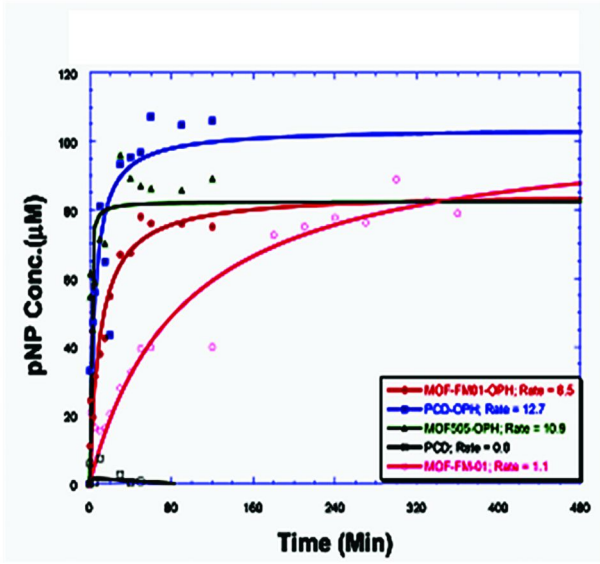

Figure 31. Activity of enzyme-supported reactive adsorbents based on either MOF or PCD; OPH enzyme enhances the activity of MOF-FM1. Each reaction used 100 mg of reactive adsorbent per 10 mL MPT (100 µmolar). (see color insert)

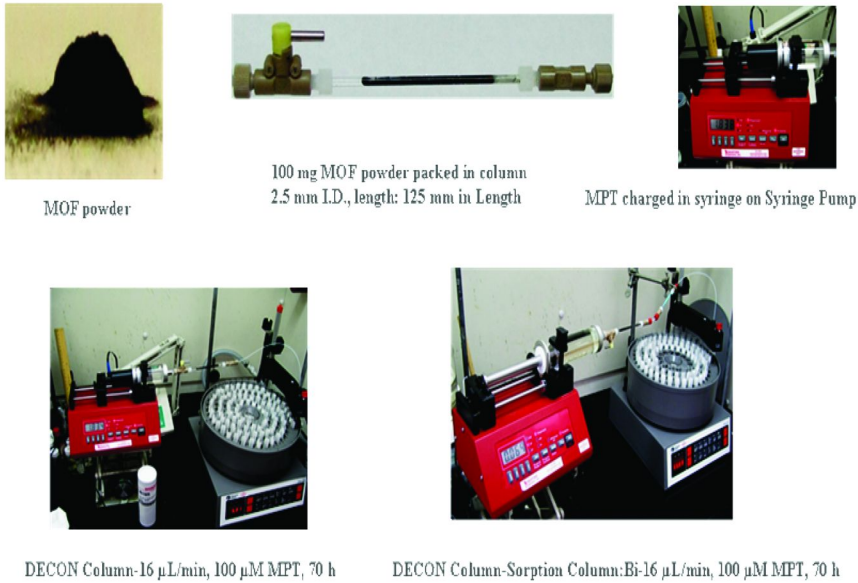

Figure 32. Packed bed gas phase reactor to test for MOF reactivity. (see color insert)

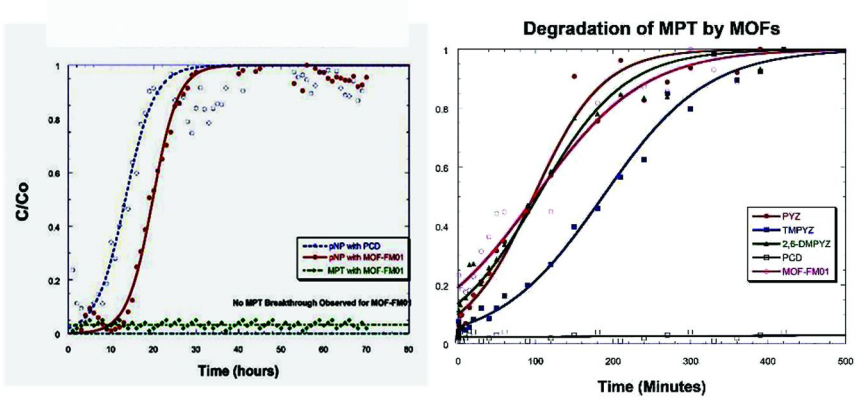

Figure 33. Breakthrough of degradation product pNP in packed bed reactor containing SD-MOFs ; Left plot: pNP degradation product breakthrough over SD-MOF-FM1. The blue line as a control represents pNP solution passed through a column of nonreacting PCD powders; the red line shows pNP resulting from MPT simulant solution passed through a column of SD-MOF; the green line is the measured MPT reactant. Right plot: MPT degradation kinetics by SD MOFs: degraded MPT-measured as pNP appearing in solution over pyrazine-, tetramethyl pyrazine-, 2,6-dimethyl-pyrazine, BPE-based MOFs respectively, over a period of 8 h (untreated PCD was a nonreactive adsorbent control). (see color insert)

In Interfaces and Interphases in Analytical Chemistry; Helburn, R., et al.;
ACS Symposium Series; American Chemical Society: Washington, DC, 2011.

Gas Phase Studies Using a Packed Bed Reactor

Gas-phase reactivity of the MOF-FM1 was also observed. Significant quantities of pNP were able to be extracted from the MOF-FM1 powder sample after 24 h exposure to MPO in a gas stream containing no moisture. For MPT, the amount of pNP produced varied depending on the experimental conditions, and this aspect needs more investigation. Continuous decontamination of MPT (liquid phase application) was demonstrated at the flow rate of 1mL/h in the MOF-powders packed bed reactor (PBR) (Figure 32). The column was packed with SD-MOF powders, and the released pNP was collected in individual vials, the solutions of which were separately analyzed.

For a complete and compact decontamination system, hypersorptive MOF-505 was filled in a second column, connected to the first SD-MOF column, which was used as a safeguard to sequester the less toxic pNP.

The observed activity (using the PBR) of selected SD-MOFs is given in Figure 33 (left) and compared with that of untreated (non catalytic) PCD powders in terms of the column's ability to elute pNP. Control experiments verified that the reactivity toward MPT and MPO was not significant for MOF materials that did not include di-pyridinyl functionality. The carboxylic-coordinated MOF-505 demonstrated only hypersorptive activity toward MPT and MPO. As shown in Figure 33 (right) over a period of 8 h interval, all SD-MOFs degraded MPT with different reactivities, releasing pNP out to the individually collected bulk solution samples.

Conclusions

QNA has developed novel self-decontaminating polymeric particulate materials for use in laminates. Specifically, we have developed reactive / catalytic materials based on 1 MOFs and 2 polymeric crosslinked particles prepared from β-cyclodextrin (poly β-CD, PCD), trehalose (poly-trehalose, PTH), calix[8]arene, and absorbing polyurethane substrates. We have demonstrated the ability to apply the enzymes OPH to these materials to create a catalytic composite that effectively degrades OP surrogate compounds such as methyl parathion and methyl paraoxon (MPT and MPO). Some important features of these materials include an ability to preferentially absorb MPT over the hydrolysis product pNP. This allows for continuous uptake of MPT into the layered composite so as to promote complete degradation, resulting in a final material that contains sequestered degradation products. Another important feature is the ability of the polymeric support to assist in maintaining the enzyme in an active form, through repair and re-naturing. Large surface areas available on meltblown and nanofiber mats coated with PCD make these materials especially attractive; their performance as a catalytic system could be further improved by chemical modification of the supporting polymeric material. An advantage of the type of architecture that we employ is that as more efficacious catalysts are discovered, they may be easily incorporated into the nanocomposite. Porosity of the material can also be manipulated to accommodate different sizes of target toxins.

In Interfaces and Interphases in Analytical Chemistry; Helburn, R., et al.;
ACS Symposium Series; American Chemical Society: Washington, DC, 2011.

The work described in this chapter has been focused on the use of organophosphorus degrading enzymes. Future work will be devoted to the HD sulfur mustard degrading enzymes, so as to create a more comprehensive self-decontaminating system. The application is in the development of protective garments.

Acknowledgments

I wish to acknowledge QNA-TSG colleagues Dr. Steven E Weiss, Dr. Thomas Phely-Bobin, Tomasz Modzelewski, and Anastasia Manesis for technical contributions, and the generous support of Tom Campbell. I also thank Dr. Alok Singh and Walter Dressick at the Naval Research Laboratory (Washington, DC) for earlier contributions to our decontamination research.

References

1. Lawson, G. E.; Lee, Y.; Singh, A. *Science* **1997**, *277*, 1232.
2. Lee, Y.; Stanish, I.; Rastogi, V.; Cheng, T.-C.; Singh, A. *Langmuir* **2003**, *19*, 1330.
3. (a) Singh, A.; Lee, Y.; Dressick, W. J. *Adv. Mater.* **2004**, *16*, 2112. (b) Singh, A.; Lee, Y.; Dressick, W. J. *Adv. Mater.* **2005**, *17*, 392.
4. Zhang, X.; Chen, H.; Zhang, H. *Chem. Commun.* **2007**, *14*, 1395–1405.
5. Sampedro, J. G.; Uribe, S. *Mol. Cell Biochem.* **2004**, *256-257*, 319.
6. Hevehan, D. L.; Clark, E. D. B. *Biotechnol. Bioeng.* **2000**, *54*, 221.
7. Buchanan, S.; Menze, M.; Hand, S.; Pyatt, D.; Carpenter, J. *Cell Preserv. Technol.* **2005**, *3*, 212.
8. Dong, X. Y.; Shi, Y. H.; Sun, Y. *Biotechnol. Progr.* **2002**, *18*, 663.
9. Haines, A. H. *Biomol. Chem.* **2006**, *4*, 702.
10. Sharma, A.; Karuppiah, N. U.S. Patent 5,728,804, 1998.
11. Wang, J.; Lu, D.; Lin, Y.; Liu, Z. *Biochem. Eng. J.* **2005**, *24*, 269.
12. Ma, M.; Li, D. *Chem. Mater.* **1999**, *11*, 872.
13. Mercier, L. *Chem. Mater.* **2001**, *13*, 4512.30.
14. Singh, A.; Lee, Y.; Zabetakis, D.; Dressick, W. D. *Proc. Chem. Biol.* Defense Conference, MD, 2005.
15. Lee, Y.; Singh, A. *Mater. Res. Soc. Symp. Proc.* **2003**, *774*, O7.32.1–O7.32.6.
16. Dressick, W. J.; Lee, Y., Singh, A. *NRL Review* 2004.
17. Kurita, K.; Hirakawa, N.; Morinaga, H.; Iwakura, Y. *Makromol. Chem.* **1979**, *180*, 2769.
18. Zhang, Z.; Xiang, S.; Chen, Y.-S.; Ma, S.; Lee, Y.; Phely-Bobin, T.; Chen, B. *Inorg. Chem.* **2010**, *49* (18), 8444.
19. Chen, B.; Ma, S.; Zapata, F.; Fonczek, F. R.; Lobkovsky, E. B.; Zhou, H.-C. *Inorg. Chem.* **2007**, *46*, 1233.

Subject Index

A

Absorptive polymer particles
  catalytic behavior, 256
  enzymes, physical support, 254
  OPH, 256
Acetophenones, 43*f*
AFP. *See* Alpha-fetoprotein
Alkyl chain assemblies and interphase, 3
  bonded monolayers, 7
  micelle/buffer interface, 5
  mounted bilayers, 6
Allyl-monolith, 126
  hydrosilylation, 127, 129*f*, 131*f*
Allylorgano-silica monoliths, 127*f*
Allyl-silica hybrid monolithic, 127*f*, 128*f*, 131*f*
Allyl-trimethoxysilane, 127*f*, 128*f*
Allyl-TrMOS. *See* Allyl-trimethoxysilane
Alpha-fetoprotein, 210*f*
3-Aminopropyltriethoxysilane
  films
    amino groups, surface modification, 156
    carboxyfluorescein conjugated, 151*t*
    characterization, 146
    curing conditions, 151, 152*f*, 152*t*, 153*f*, 154*f*, 155*f*
    deposition solution and reaction time, 147, 149*f*, 151*t*, 160*f*
    EDC, 156
    hydrazine, 156
    modification, 145, 156, 157*t*
    NHS, 158*f*
    PBS, 148*t*, 150*f*, 151*t*, 159*f*
    preparation, 144
    silicon substrates, 145*s*
    silicon wafer, 8*f*, 159*f*
    SMCC, 158*f*
    succinic anhydride, 158*f*
    toulene, 148*f*, 148*t*
    water contact angles, 151*t*
Amino-terminated organic films and silicon substrates, 141
Analytical chemistry
  historical sketch, 2
  interface, 1, 3, 4*f*
Analytical interface and materials
  carbon nanotubes, 10
  gel pseudophases, 11
  layer-by-layer, 9
  silica, 10, 11
Anionic micelle, 43*t*
Anionic surfactants
  head groups, multiple, 71*f*
  and LSER, 67
APTES. *See* 3-Aminopropyltriethoxysilane

B

Benzophenones, 43*f*
Benzyl-DMS, 129*f*, 130*f*
Bile salts, 70
Biomolecule analyte, 7*f*
Biomolecules in membranes
  electrokinetic motion modeling
    drag force, 112
    electric field force, 113
    forces in bilayers, 110
    hydrodynamic force, 111
Bio-reactive materials
  interface, incorporation, 12
    biosensing interfaces in clinical analysis, 13
    history, 12
    smart interfacial layers, 13
Biosensor
  glucose oxidase, 230*f*
  oxidase enzymes, 231*f*
  selectivity, 225, 227
    electro-reduction potential, 237
    permselective membranes, 228, 235
    pre-oxidizing layer, coating, 236
    self referencing, 238
    sensor or biosensor detection potential, 231
  sensitivity, 225, 240
4,4′-Bipyridyl, 272*f*
Bipyridyl ethylene, 272*f*
Blotting techniques, 102
Bonded monolayers, 7
Bovine β-casein tryptic digest and HfO_2, 137*f*
Bovine serum albumin, 116*f*, 203*f*
BP. *See* 4,4′-Bipyridyl
BPE. *See* Bipyridyl ethylene
Brij-35 micellar systems, 76, 77*t*
BSA. *See* Bovine serum albumin
Buffer interface and micelle, 5

In Interfaces and Interphases in Analytical Chemistry; Helburn, R., et al.;
ACS Symposium Series; American Chemical Society: Washington, DC, 2011.

C

Capillary electrochromatography, 136*f*
Capillary gel electrophoresis, 218*f*, 220*f*
Capillary liquid chromatography, 130*f*
Capillary zone electrophoresis, 218*f*, 220*f*
Carbon nanotubes and magnetoresistance, 185, 187, 188
Cationic micelle, 43*t*
Cationic surfactants and LSER, 72, 73, 74*f*
β-CD-bonded poly(ethylene imine), 257*f*
β-CD-BPEI. *See* β-CD-bonded poly(ethylene imine)
C_8-DMCS. *See* Octyldimethylchlorosilane
CEC. *See* Capillary electrochromatography
Cell membrane biomolecules
  role
    biological function, 100
    disease, 100
    inter-membrane protein reactions, 102*f*
  and supported lipid bilayer electrophoresis, 99
C8E5 micelles, 25*f*, 36*f*
Cesium perfluorooctanoate micelles, 38*f*, 39
Cetyltrimethylammonium bromide
  micelles, 60*t*
  sodium octylsulfate, 91*t*
  structure, 21*f*
  vesicle systems, 91*t*
CGE. *See* Capillary gel electrophoresis
Chaperones
  enzyme self-repair, 252
  OPH cotton thread, 253*f*
Cholesterol and LSER, 93*t*
CLC. *See* Capillary liquid chromatography
CMC. *See* Critical micelle concentration
CNTS. *See* Carbon nanotubes
Copper nitrate, 272*f*
Critical micelle concentration, 25*f*
CTAB. *See* Cetyltrimethylammonium bromide
Cytochrome c-oxidase, 6*f*
CZE. *See* Capillary zone electrophoresis

D

Decyltrimethylammonium chloride micelles, 32, 34*f*, 35*f*
DeTAC micelles. *See* Decyltrimethylammonium chloride micelles
$DHP_{70}Chol_{30}$ liposomes, 88*f*
Di-8-ANEPPS, 88*f*, 89*f*
1,2-Dilauroyl-*sn*-glycero-3-phosphocholine, 109*f*
1-(3-Dimethylaminopropyl)-3-ethylcarbodiimide hydrochloride, 158*f*
2,6-Dimethyl pyrazine, 272*f*
Dimyristoylphosphatidylcholine vesicles, 88*f*
Dipalmitoyl-L-α- phophatidylcholine, 93*t*
Dipalmitoyl-L-α-phosphatidylglycerol, 93*t*
Disease and cell membrane species, 100
DLPC. *See* 1,2-Dilauroyl-*sn*-glycero-3-phosphocholine
DMF. *See* N,N′-dimethyl formamide
DMP. *See* 2,6-Dimethyl pyrazine
DMPC vesicles. *See* Dimyristoylphosphatidylcholine vesicles
DNA
  guanosine gels, 215
  76-mer strands, 221, 221*f*
  separations, 215
DNAP. *See* N,N-dialkyl-4-nitroaniline indicators
Dodecylphosphocholine micelles, 36*f*, 38*f*
Dodecyltrimethylammonium bromide, 58*t*, 59*t*
Dodecyltrimethyl-ammonium ion micelle, 24*f*
Double cushion strategy and transmembrane protein mobility, 116*f*
DPC micelles. *See* Dodecylphosphocholine micelles
DPPC. *See* Dipalmitoyl-L-α-phophatidylcholine
DPPG. *See* Dipalmitoyl-L-α-phosphatidylglycerol
Drugs separation and monolithic columns, 130*f*
DTAB. *See* dodecyltrimethylammonium bromide

E

EDC. *See* 1-(3-Dimethylaminopropyl)-3-ethylcarbodiimide hydrochloride
Electrokinetic motion modeling
  biomolecules in membranes, 110
    drag force, 112
    electric field force, 113
    hydrodynamic force, 111
Electrospun nanofiber mats, 258*f*, 259*f*
Enzymes
  and absorptive polymer particles

In Interfaces and Interphases in Analytical Chemistry; Helburn, R., et al.;
ACS Symposium Series; American Chemical Society: Washington, DC, 2011.

OPH, 256
poly-β-cyclodextrin, 254, 258, 260
material composite, incorporation, 251
chaperones and self-repair, 252
immobilization, 251
layer-by-layer assembly, 251
stabilization, 251
and metal-organic framework, 269
physical supports, 254
reactive adsorbents, supported, 272*f*

F

Fluorescence and nitrocellulose, 202*f*
Fumaric acid, 272*f*

G

Gel pseudophases, 11
G-gels. *See* Guanosine gels
Glucose oxidase
biosensor, 230*f*
electrical wiring, 236*f*
glucose sensor, amperometric, 14*f*
Glucose test strip, disposable, 239*f*
GMP. *See* Guanosine 5′-monophosphate
GOx. *See* Glucose oxidase
Graphene sheet, 187*f*
G-tetrads, 12*f*, 217*f*
Guanosine, 12*f*
Guanosine gels, 12*f*
CGE, 218*f*, 220*f*, 222*f*
and DNA separations, 215
formation, 217
Guanosine 5′-monophosphate, 217*f*, 218*f*

H

Hafnia
and bovine β-casein tryptic digest, 137*f*
monolithic capillary column, 136*f*
and zirconia monoliths
morphology, 132
NMF, 133*f*, 135, 135*f*
surface area and porosity, 132, 135*f*, 136*f*
synthesis, 130, 133*f*
uses, 134
HED. *See* Heptaethylene glycol monododecyl ether
Heme copper enzyme and silver electrode, 6*f*
Heptaethylene glycol monododecyl ether, 60*t*
Hexadecylpyridinium chloride micelles, 76
Hexadecyltrimethylammonium bromide micelles, 73*t*
Hexafluoroisopropoanol and MST, 83*f*
Hexyl diisocyanate, 255*f*
HFIP. *See* Hexafluoroisopropoanol
HfO_2. *See* Hafnia
Homodimers, separation, 218*f*, 219
Homopentamers, separation, 219, 220*f*
HTAB. *See* Hexadecyltrimethylammonium bromide; *N*-hexadecylammonium bromide
Hydrosilylation
and allyl-monolith, 127, 129*f*, 131*f*
and benzyl-DMS, 129*f*

I

Indium tin oxide
POM, 9*f*, 171*s*, 177*f*
porphyrin, 178*f*
porphyrin and POM, 167
fluorescence spectra, 182*f*
UV-visible studies, 181*f*
$SiW_{12}O_{40}^{4-}$, 173*f*, 175*f*, 176*f*, 182*f*, 183*f*
$TMPyP^{4+}$, 9*f*, 171*s*, 173*f*, 175*f*, 176*f*, 182*f*, 183*f*
Interface
analytical chemistry, 1, 3, 4*f*
and bio-reactive materials, 12
Interfacial layers, design concept, 249, 250*f*
Interphase
and alkyl chain assemblies, 3
modeled images, 4*f*
C_{18}-on-silica RPLC interphase, 4*f*
micelles, 4*f*
polymers, condensed, 4*f*
RPLC stationary-mobile phase system, 4*f*
ITO. *See* Indium tin oxide

K

Kamlet-Taft solvatochromic studies, 52
α and β scales, 54
π* scale, 53
vesicles, 85

In Interfaces and Interphases in Analytical Chemistry; Helburn, R., et al.;
ACS Symposium Series; American Chemical Society: Washington, DC, 2011.

L

Laaksonen and Rosenholm simulation, 29*f*
Layer-by-layer, 9
LBL. *See* layer-by-layer
LDS. *See* Lithium dodecyl sulfate
Linear solvation energy relationships, 51, 63
  anionic surfactants, 67, 71*f*
  bile salts, 70
  Brij-35, 76, 77*t*
  cationic surfactants, 72, 73, 74*f*
  cyclic head group surfactants, 75*f*
  hexadecylpyridinium chloride, 76
  hexadecyltrimethylammonium bromide micelles, 73*t*
  linear head group surfactants, 75*f*
  lithium dodecyl sulfate, 68
  lithium perfluorooctanesulfonate, 68, 68*f*, 69*t*
  MEKC, 76, 79
  micellar liquid chromatography, 79
  micellar selectivity triangle, 80
  micellar systems, 64, 70
  modifiers, 77
  nonionic micelles, 76
  SDS, 64, 78*f*
  sodium alkyl sulfate, 67
  tetradecyltrimethyl ammonium bromide, 73*t*
  and vesicles, lipid, 82, 90
    cetyltrimethylammonium bromide and sodium octylsulfate, 91*t*
    cholesterol, 93*t*
    dipalmitoyl-L-α- phophatidylcholine, 93*t*
    dipalmitoyl-L-α-phosphatidylglycerol, 93*t*
    octyltrimethylammomium bromide and sodium dodecylsulfate, 91*t*
LiPFOS. *See* Lithium perfluorooctanesulfonate
Lipids
  bilayer
    heme—copper protein cytochrome c-oxidase, 6*f*
    silver electrodes, 6*f*
  fluorescent, separation, 109*f*
  isomers and SLBE, 107
  membrane biomolecule and electric field, 111*f*
Lithium dodecylsulfate
  linear solvation energy relationships, 68
  and lithium perfluorooctanoate mixed micellar, 68*f*, 69*f*
Lithium perfluorooctanesulfonate, 59*t*, 68, 69*t*
Lithium perfluorooctanoate, 68*f*, 69*f*
LPFOS. *See* Lithium perfluorooctanesulfonate
LSER. *See* Linear solvation energy relationships

M

Magnetoresistance
  carbon nanotubes, 187, 188
  single wall carbon nanotubes, 185, 194*f*
Material composite and enzymes, 251
Materials and analytical interface
  carbon nanotubes, 10
  layer-by-layer, 9
  silica, 10
MB. *See* Melt blowing
MD simulation. *See* Molecular dynamics simulation
MEKC. *See* Micellar electrokinetic chromatography
Melt blowing, 266
Meltblown nanofibers
  poly-β-CD coated, 266
    FMI-PPS, 266*f*
    polypropylene/polyethylene, 266*f*
Metal-organic framework
  amine containing, 272*f*
  enzymes, 269
  and FM1, 270*f*, 271*f*
    OPH, 272*f*
    PCD, 272*f*
  gas phase reactivity, 274
  reactivity and sorption capability, 268
  self-decontaminating, 268*f*
  structures, 267
  synthesis and characterization, 266
Methyl paraoxon, 267*f*
Methyl parathion, 253*f*, 255*f*, 267*f*
  decomposition, 265*f*
  degradation, 261*f*, 265*f*
  nanocomposite catalytic system, 265*f*
  OPH coated
    poly-β-CD particles, 259*f*, 262*f*
    PTH particles, 262*f*, 265*f*
  poly-β-cyclodextrin, 258
  poly(D-(+)-trehalose cotton thread, 261*f*
  QinetiQ North America particles, 256*f*
  reaction, 15*f*
Micellar electrokinetic chromatography, 68*f*, 69*f*, 75*f*, 76, 79, 83*f*, 84*f*
Micellar liquid chromatography, 79

In Interfaces and Interphases in Analytical Chemistry; Helburn, R., et al.;
ACS Symposium Series; American Chemical Society: Washington, DC, 2011.

Micellar selectivity triangle
hexafluoroisopropoanol, 83*f*
linear solvation energy relationships, 80
micellar systems, 81*f*, 84*f*
pentanol, 83*f*
SDS LSER, 82*f*
Micelle, 40
and buffer interface, 5
interphase, modeled images, 4*f*
LSER, 64
solvatochromic parameters, 56
structure, 5*f*
structure and representations, 20
anionic, 23*f*
$CH_3(CH_2)_7$-$(OCH_2CH_2)_5$-OH monomers, 25*f*
dodecyltrimethyl-ammonium ion, 24*f*
molecular dynamics simulation, 25*f*, 26*f*
spherical, 24*f*
and water interface, 19, 26, 51
acetophenones, solubilization sites, 43*f*
anionic, 43*t*
benzophenones, solubilization sites, 43*f*
bromide, 32
cationic, 43*t*
cesium perfluorooctanoate micelles, 38*f*, 39
decyltrimethylammonium chloride, 32, 34*f*, 35*f*
non-ionic micelle, 37
penetration, computational studies, 27
SDS, 30*f*, 32*f*
sodium octanoate, 28, 29*f*, 30*f*
zwitterionic micelle, 37
Microorganisms and sensing interface, 13*f*
Modifiers
linear solvation energy relationships, 77
and SDS LSER coefficients, 78*f*
MOF. *See* Metal-organic framework
Molecular dynamics simulation, 25*f*, 26*f*
Monolithic columns, 123
Mounted bilayers, 6
MPT. *See* Methyl parathion
MR. *See* Magnetoresistance
MST. *See* Micellar selectivity triangle

N

Nanocomposite
catalytic system and MPT decomposition, 265*f*
electron relay, 242*f*
Nanoparticles, electron relay, 242*f*
N-hexadecylammonium bromide, 59*t*
NHS. *See N*-hydroxysuccinimide
N-hydroxysuccinimide, 158*f*
Nitrocellulose
BSA, 203*f*
microarray, 202*f*
polymer, protein microarray, 201*f*, 202*f*
N-methylformamide and hafnia and zirconia monoliths, 133*f*, 135*f*
NMF. *See* N-methylformamide
N,N-dialkyl-4-nitroaniline indicators, 33, 86*f*, 87*f*, 88*f*
N,N′-dimethyl formamide, 270*f*
N,N-dimethyl-4-nitroaniline, 52*f*, 53*f*
Nonionic micelles, 37, 43*t*, 76
Nylon and PCD coatings, 258

O

Octyldimethylchlorosilane, 125*f*, 131*f*
Octyltrimethylammomium bromide and sodium dodecylsulfate, 91*t*
OP. *See* Organophosphorus
OPH. *See* Organophosphorus hydrolase
Organic solvents, π* values, 55*t*
Organophosphates, 251*f*
Organophosphorus, 253*f*
Organophosphorus hydrolase, 15*f*
absorptive polymer particles, 256
cotton thread and chaperone treatment, 253*f*
and MOF-FM1, 272*f*
and MPT, 259*f*, 262*f*, 264
poly-β-cyclodextrin
cotton fibers, 255*f*
enzyme kinetics, 263*f*
functionalized nylon grooved fibers, coated, 259*f*
MPT degradation, 262*f*
poly(D-(+)-trehalose cotton thread, coated, 261*f*
PTH, 262*f*
catalytic and enzyme stabilizing properties, 261
MPT, catalytic degradation, 265*f*
Oxidase enzymes and biosensor, 231*f*

P

Packed bed reactor
gas phase studies, 274

In Interfaces and Interphases in Analytical Chemistry; Helburn, R., et al.;
ACS Symposium Series; American Chemical Society: Washington, DC, 2011.

MOF reactivity, 273*f*
SD-MOF, 273*f*
1-Palmitoyl-2-oleoyl-*sn*-glycero-3-phosphocholine, 108*f*, 109*f*
PBR. *See* Packed bed reactor
PBS. *See* Phosphate buffered saline
PCD. *See* Poly-β-cyclodextrin
PEG. *See* Polyethylene glycol
Pentanol and MST, 83*f*
PeOH. *See* Pentanol
$PG_{24}PC_{46}Chol_{30}$ liposomes, 86*f*, 87*f*
Phenyl bonded quartz fiber and SWCNTs, 10
Phosphate buffered saline and 3-APTES, 148*t*, 150*f*, 151*t*, 159*f*
P-nitro phenol, 253*f*, 255*f*, 257*f*, 263*f*, 267*f*
MOF kinetics, 272*f*
poly-β-cyclodextrin, 258
pNP. *See P*-nitro phenol
Poly-β-CD. *See* Poly-β-cyclodextrin
Poly-β-cyclodextrin, 15*f*, 254, 260
cotton fibers and OPH, 255*f*
and cotton thread, 255*f*
functionalized cotton cloth, MPT breakdown, 257*f*
and meltblown nanofibers, 266
and MOF-FM1, 272*f*
MPT degradation, 263
nylon, coatings, 258
OPH, 263
PVA electrospun nanofiber, 259*f*
sieved particles, 255*f*
sorption material
MPT, 258
pNP, 258
structure, 254*f*
Poly(D-(+)-trehalose cotton thread
MPT degradation, 261*f*
OPH-coated, 261*f*
Polyethylene glycol, 116*f*, 128*f*
Polymeric support materials
MPT and pNP sorption behavior, 263*f*
sorption behavior, 262
Polymers
interphase, modeled images, 4*f*
mediators, 242*f*
Polyoxometalates, 9*f*, 167, 168*s*, 171*s*, 182*f*, 183*f*
films, 179*f*
ITO, 177*f*
Polypropylene sulfide, 266*f*
Polypropylene/polyethylene, 266*f*
Poly-trehalose, 261, 263
Polyvinyl alcohol
electrospun nanofiber, 259*f*
polymeric β-cyclodextrins, 259*f*
POM. *See* Polyoxometalates
POPC. *See* 1-Palmitoyl-2-oleoyl-*sn*-glycero-3-phosphocholine
Porphyrin
films, 179*f*
ITO, 108*f*
and POM layers, 181*f*, 182*f*
Porphyrin–polyoxometalate films
electrochemical studies, 167
indium-tin oxide, 167
PP/PE. *See* Polypropylene/polyethylene
PPS. *See* Polypropylene sulfide
Protein microarray, 198, 199*f*
nitrocellulose coating, 201*f*
silica colloidal crystals, 197, 207
silica particles substrate, sub-micron, 11*f*
types
antibody array, 199*f*
reverse protein array, 199*f*
Protein purification and assay, 101
biophysical approaches, 103
blotting techniques, 102
PTH. *See* Poly-trehalose
PVA. *See* Polyvinyl alcohol
Pyrazine, 272*f*
Pyridinyl amine linkers, 267*f*

Q

QinetiQ North America particles, 256*f*
QNA particles. *See* QinetiQ North America particles

R

Reversed phase liquid chromatography, 4*f*
RPLC. *See* Reversed phase liquid chromatography

S

SAM. *See* Self assembled monolayer
Sarin, 251*f*, 257*f*
SC. *See* Sodium cholate
SD-MOF. *See* Self-decontaminating-MOF
SDS. *See* Sodium dodecylsulfate
Self assembled monolayer
metal surface, 8*f*
thiol and Au suface, 8*f*
Self-decontaminating-MOF, 268*f*, 273*f*
Sensing interface and microorganisms, 13*f*

In Interfaces and Interphases in Analytical Chemistry; Helburn, R., et al.;
ACS Symposium Series; American Chemical Society: Washington, DC, 2011.

Silanes, 191*t*
Silanols, 190*f*
Silica
  analytical interface and materials, 10, 11
  colloidal crystals, 205*f*, 206*f*, 207*f*
    binding, nonspecific, 211*f*
    protein microarrays, 197, 207, 209*f*
    streptavidin, biotin capturing labeled, 208*f*
    and surface coatings, 204
  fibers and SWCNT coated, 185, 189, 191*f*
  monolith synthesis, 125*f*
  protein microarray, 11*f*
Silica hybrid monoliths, 124
  allyl-monolith, 126
    allyl-silica hybrid monolithic, 127*f*
    hydrosilylation, 127, 129*f*
Silicon
  and carbon linkage, 7*f*
  substrates
    and amino-terminated organic films, 141
    APTES film, 145*s*
  wafer and APTES, 8*f*
Siloxane linkage, 7*f*
Silver electrode
  and cytochrome c-oxidase, 6*f*
  and heme copper enzyme, 6*f*
Single wall carbon nanotubes
  applications, 186
  graphene sheet, 187*f*
  magnetoresistance, 185
  and phenyl bonded quartz fiber, 10
  properties, interfacial, 186
  silica fibers, coated, 185
    C_{18} modification, 190*f*
    light microscopy, 191
    magnetoresistance, 194*f*
    oxidized, 192*f*
    preparation, 189, 191*f*
    resistance measurements, 193
    SEM microscopy, 191
    temperature dependent resistance, 185, 194*f*
    un-oxidized, 192*f*, 193*f*
$SiW_{12}O_{40}^{4-}$ and ITO, 173*f*, 175*f*, 176*f*, 182*f*, 183*f*
SLBE. *See* Supported lipid bilayer electrophoresis
Small unilamellar vesicles
  and solvatochromic π* indicators, 86*f*, 87*f*, 88*f*
  and supported lipid bilayer, 106*f*
Smart interfacial layers, 249
SMCC. *See* Succinimidyl-4-(*N*-maleimidomethyl)cyclohexane-1-carboxylate
Sodium alkyl sulfate micelles, 67
Sodium cholate, 59*t*
Sodium dodecylsulfate, 21*f*
  LSER
    coefficients and modifiers, 78*f*
    micellar selectivity triangle, 82*f*
  micelles, 30*f*, 31, 33*f*
    solvatochromic parameters, 60*t*
    and solvent, 59*t*
    and water, 58*t*
  molecular dynamics simulation, 32*f*
  solvatochromic parameters, 59*t*
Sodium octanoate micelles, 28, 29*f*, 30*f*
Sodium tetradecylsulfate, 60*t*
Solvatochromism, 51
  Kamlet-Taft parameters, 85
  micelles, 56
  vesicles, lipid, 82, 85, 89
Soman, 251*f*
Sorption-reinforced catalytic systems, 249, 264
Succinimidyl-4-(*N*-maleimidomethyl)cyclohexane-1-carboxylate, 158*f*
Sulfur mustard, 251*f*
Supported lipid bilayer electrophoresis
  assay platform, 105
  and cell membrane biomolecules, 99
  double cushion strategy, 116*f*
  formation, 106*f*
  lipid isomers, separation, 107
  and membranes, 105
  preparation, 106
  proteins separation, 104*f*
  sample preparation and implementation, 107*f*
  and small unilamellar vesicles, 106*f*
  transmembrane protein, 115, 116*f*
  tuning membrane composition aids separation, 110
Surface chemistry, 3
SUV. *See* Small unilamellar vesicles
SWCNT. *See* Single wall carbon nanotubes

T

Tetradecyltrimethyl ammonium bromide micelles, 73*t*
5,10,15,20-Tetrakis(4-methylpyridinium) porphyrin, 9*f*
  indium-tin oxide, 171*s*, 173*f*, 175*f*, 176*f*, 182*f*, 183*f*

In Interfaces and Interphases in Analytical Chemistry; Helburn, R., et al.;
ACS Symposium Series; American Chemical Society: Washington, DC, 2011.

tosylate salt, 168*s*
Tetramethoxysilane, 125*f*, 127*f*, 128*f*
Texas red 1,2-dihexadecanoyl-*sn*-glycero-3-phosphoethanolamine, triethyl ammonium salt, 108*f*
Texas red isomers
and DLPC, 109*f*
and POPC, 109*f*
separation, 109*f*
Thiol and self assembled monolayer, 8*f*
TMOS. *See* Tetramethoxysilane
$TMPyP^{4+}$. *See* 5,10,15,20-Tetrakis(4-methylpyridinium) porphyrin
Toluene and 3-APTES films, 148*f*, 148*t*, 151*t*, 152*f*, 152*t*, 153*f*, 154*f*, 155*f*, 160*f*
Tosylate salt, 168*s*
Transmembrane protein
and SLBE
challenges, 115
double cushions bolster transmembrane protein mobility, 116
mobility, 115
TR-DHPE. *See* Texas red 1,2-dihexadecanoyl-sn-glycero-3-phosphoethanolamine, triethyl ammonium salt
Triton X-100, 21*f*, 60*t*
TTAB. *See* Tetradecyltrimethyl ammonium bromide micelles

V

Vesicles, lipid
formation, 84*f*
Kamlet-Taft parameters, 85
linear solvation energy relationships, 82, 90
solvatochromic studies, 82, 85, 89
water interface, 51

W

Warfare chemicals, 250
Water interfacial and micelles, 26

Z

Zirconia
and hafnia monoliths
morphology, 132
surface area and porosity, 132, 135*f*, 136*f*
synthesis, 130, 133*f*
uses, 134
Zwitterionic micelle, 37

In Interfaces and Interphases in Analytical Chemistry; Helburn, R., et al.;
ACS Symposium Series; American Chemical Society: Washington, DC, 2011.